

Faculty of Science and Engineering

Department of Chemistry

**In-Silico Prediction of the Physical Performance
of Pharmaceutical Crystals**

Mustafa Hamad

This thesis is presented for the Degree of

Doctor of Philosophy

of

Curtin University

July 2021

Declaration

To the best of my knowledge and belief this thesis contains no material previously published by any other person except where due acknowledgment has been made.

This thesis contains no material which has been accepted for the award of any other degree or diploma in any university.

I warrant that I have obtained, where necessary, permission from the copyright owners to use any third-party copyright material reproduced in the thesis.

Date: 18-06-2021

Dedication

To the freedom of Palestine

To my devoted wife for her support and patience

To my dear family

Acknowledgements

The research activities of this PhD started in July 2017 and concluded in July 2021. The four years of diligent work were rife with challenges and critical decisions. I am very pleased to have successfully completed my PhD degree resulting in this thesis which i hope, would be of great benefit to the scientific advancements in the field.

Without reservation, i would like to express my acknowledgement and gratitude to my main supervisor Professor Andrew Rohl, and co-supervisors Professor Julian Gale and Professor Victor Calo. I would like to thank Professor Andrew Rohl for steering this research in the most effective and efficient way, and for the several key discussions which gave me inspiration to interpret, achieve and complete this research. Also, i would like to thank Professor Julian Gale for his time and effort invested in developing the variety of methods (reported and unreported) used in this thesis, for the theory discussions related to the methods and the results, and for his criticism and sharp observations that were essential in completing this research. Last but not least, i would like to thank Professor Victor Calo for his critical insights into the continuum mechanics aspects of our atomistic simulations, for the several discussions and tasks given in relation to this research, and for his advice and recommendations.

Also, I would like to express my acknowledgement and gratitude to my thesis co-supervisors Dr. Sten Nilsson Lill and Associate Professor Catherine Boissier from the industry partner AstraZeneca R&D, Gothenburg, Sweden. I would like to thank Associate Professor Catherine Boissier for elucidating the research problem, following up on the results, and providing literature data on pharmaceuticals. I would like to thank Dr. Sten Nilsson Lill for his regular and persistent follow up of the latest results, his critical comments, and for providing literature articles related to this research. I would like to thank both co-supervisors for assisting me during my visits to AstraZeneca R&D. They introduced me to several AstraZeneca R&D colleagues, and thus gave me the chance to

have insightful multi-disciplinary discussions with different groups working on different projects.

I would like to duly acknowledge and thank, Curtin University for supporting and funding my Phd studies through the award of Curtin International Postgraduate Research Scholarship (CIPRS) and research stipend scholarship, AstraZeneca R&D for financial support, Industrial Doctoral Training Centre (IDTC), directed by, Associate Professor Charles Lawoko for the professional development seminars and conferences, Pawsey Supercomputing Centre for providing computational resource, and Curtin Institute for Computation.

Finally, I would like to express my pleasure for being a member of Curtin's Computational Materials and Minerals Group. I also would like to thank, Associate Professor Paolo Raiteri for using his General Purpose Trajectory Analysis (GPTA) program, Associate Professor Nigel Marks for pointing to us to use OVITO software, and all the members of Curtin's Computational Materials and Minerals Group, past and present.

Abstract

The pharmaceutical industry is a multi-trillion dollar industry and is expected to grow further during the post-pandemic period. A significant production cost is the large scale manufacturing of drug tablets, with processes such as milling and compaction inducing defects and disorder in the active pharmaceutical ingredient (API) and potentially causing production problems and delays. The mechanical property of hardness is useful in describing the plastic deformation. Hardness is defined by the ease of the activation of deformation mechanisms (slip barriers for dislocation slip, twinning, etc.) along several slip systems and studies have shown that medium hardness APIs correlate with successful tableting. There are two main categories of methods to study deformation in ideal defect-free materials, the generalized stacking fault energy (GSFE), and affine shear deformation methods. Both methods, even with their significant limitations, are still used in understanding and describing idealized deformation in the absence of defects and heterogeneities.

In this thesis, we propose two new computational methods: the rigid block shearing method (RBSM), an extension of the GSFE method where a block of fully relaxed atoms is added between two rigid blocks, and the tensor based shearing method (TBSM), an affine shear deformation method with the major advance of using finite strain derivatives. The other major improvement to existing methods is the use of the Rational Function Optimizer (RFO), which ensures the Hessian always has the required structure and the optimized structures are stable throughout the deformation simulation. We chose to study FCC metals first to verify our methods before studying materials with increasing complexity up to organic molecular crystals.

GSFE calculations were performed on FCC Au, Pb, Pd, Pt, Ag, Al, Ni, Cu, and the beta phase of O₂, finding their deformation barriers. Then, RBSM was applied to study the deformation of FCC Au and other FCC metals to find the slip barriers, which provided critical insights about the activation of several deformation mechanisms, and in particular, twinning deformation. RBSM

barriers were found to be much lower than those calculated via GSFE. An atomistic definition of strain is proposed which enabled the calculation of internal strain, multiplicity of slip models, periodicity of the deformation, and ideal shear stress. Further, TBSM was applied to FCC Au with two control simulations performed using Newton-Raphson and RFO energy minimizers, showing that the RFO ensures all the deformed configurations are physically stable, i.e. phonon frequencies are real. TBSM deformation results and barriers were consistent with those found by RBSM. To the best of our knowledge, TBSM is the first affine shear deformation method to simulate twinning deformation in detail, including twinning deformation pathways. A geometric procedure is provided to determine the direction of the easiest slip.

RBSM and TBSM were used to shear MgO, an ionic crystal. Both methods predict the ranking of slip systems and ideal shear stress consistent with experiment. In addition, TBSM finds that the deformation outcome of the $(\bar{1}10)[110]$, but not the $(001)[110]$, depends on the algorithm used to evaluate the electrostatic interactions with two possibilities, phase change or slip deformation.

Our methods were also applied to study the deformation of solid diatomic oxygen. Several slip systems were sheared and our results showed a coupling between shear deformation and rotations of the molecules, in addition to unveiling rotational twinning deformation. Finally, RBSM and TBSM were used to shear anthracene crystals. Both methods predicted slip along the $(001)[010]$ and $(001)[110]$, consistent with experiment, although both also suggested that slip along $(001)[100]$ might be possible, which requires experimental verification.

Table of Contents

Declaration	i
Dedication	ii
Acknowledgements	iii
Abstract	v
Chapter 1 Background	1
1.1 Perspective	1
1.2 Introduction	2
1.3 Pharmaceutical Significance	3
1.4 Mechanical Performance and Properties	5
1.4.1 Stress-Strain Diagrams	6
1.4.2 Experimental Hardness Measurements	7
1.4.3 Theoretical Hardness Calculations	11
1.5 Introduction to Deformation Mechanisms	13
1.5.1 Deformation Mechanism Maps	13
1.5.2 Theory of Dislocations	16
1.5.3 Characteristics of Dislocations	18
1.6 Slip Deformation	21
1.6.1 Slip Systems in Metals	22
1.6.2 Slip in Ionic Crystals	26
1.6.3 Slip in Organic Molecular Crystals	28
1.7 Twinning Deformation	30
1.8 Generalized Stacking Fault Energy: Application to Plastic Deformation	32
1.8.1 Active Deformation Mechanism Predictions	33

1.8.2	GSFE-Based Extended Theories	35
1.8.3	Hybrid-Dislocation Models	38
1.9	Affine Shear Deformation Methods	40
1.10	Differential Displacement Proposals	42
1.11	Literature Gaps	43
Chapter 2	Methods	61
2.1	Introduction	61
2.2	Introduction to Force Fields	61
2.3	Force Field Examples	64
2.3.1	Force Fields for Metals	64
2.3.2	Force Field Models for MgO	65
2.3.3	Force Field for O ₂	66
2.3.4	General Amber Force Field For Anthracene	67
2.4	Energy Minimization Techniques	68
2.5	Introduction to Molecular Dynamics	70
2.6	Method 1: The Rigid Block Shearing Method	71
2.7	Method 2: The Tensor Based Shearing Method	74
Chapter 3	Generalized Fault Energies	84
3.1	Introduction	84
3.2	Deformation Mechanisms of FCC Au	85
3.2.1	Full Dislocation Without Dissociation	86
3.2.2	Stacking Fault Emission	87
3.2.3	A-A Stacking Deformation	87
3.2.4	Full Dislocation by Partial Dislocations Dissociation	88
3.2.5	Twinning Deformation	88
3.3	GPFE Barriers For a List of FCC Metals	90
3.4	GPFE Curve of The New Twinning Route	92
3.5	GPFE Curve of β -Oxygen	95
3.6	Summary	97
Chapter 4	Rigid Block Shearing Method: Application to FCC Metals	101
4.1	Introduction	101

4.2	Methodology	102
4.3	Deformation in the $(111)[\bar{1}10]$ System	103
4.3.1	Convergence as a Function of System Size	103
4.3.2	Convergence as a Function of Step Size	104
4.3.3	Slip Phenomena	105
4.3.4	Site Energies and Differential Displacement	110
4.3.5	Multiplicity of Slip	112
4.3.6	Partial Dislocation Slip	118
4.4	Deformation in the $(111)[\bar{2}11]$ System	120
4.4.1	Convergence Analysis	120
4.4.2	Twinning Deformation Mechanism	121
4.4.3	Twinning Deformation Analysis	123
4.4.4	Alternative Twinning Deformation Mechanisms	124
4.5	Atomistic Definition of Strain	127
4.6	Ideal Shear Strength and Application to FCC Metals	129
4.6.1	Shear Stress Versus Strain in FCC Au	129
4.6.2	Slip Barriers and Ideal Shear Strength of FCC Metals	130
4.7	Summary	130
Chapter 5 Tensor-Based Shearing Method: Application to FCC metals		136
5.1	Introduction	136
5.2	Methodology	137
5.3	Influence of the Energy Minimization Algorithm	138
5.4	Shearing the $(111)[\bar{2}11]$ System in FCC Au	139
5.4.1	Convergence: System and Step Size Variables	140
5.4.2	Deformation of the Lattice Vectors	141
5.4.3	Twinning Deformation Mechanism	143
5.4.4	Twinning Deformation Analysis	144
5.4.5	Multiplicity of Slip: Alternative Twinning Routes	146
5.5	Shearing the $(111)[\bar{1}10]$ System in FCC Au	150
5.5.1	Convergence Analysis: System and Step Sizes	150
5.5.2	Deformation of the Lattice Vectors	151
5.5.3	Slip Deformation Mechanisms	153

5.5.4	Dislocation Slip By Partial Dislocations	154
5.6	TBSM Strain Versus Green-Lagrange	156
5.7	Ideal Shear Strengths and Slip Barriers of FCC Metals	157
5.7.1	Stress Tensor in TBSM: Ideal Shear Strength of FCC Au	157
5.7.2	Slip barriers and Ideal Shear Strength for FCC Metals	158
5.8	Finding the Easiest Slip Direction	160
5.9	Summary	162
Chapter 6	Deformation in MgO	166
6.1	Introduction	166
6.2	Geometry and Setup Details	168
6.3	Application of RBSM to MgO Slip Systems	169
6.4	Application of TBSM to MgO Slip Systems	171
6.5	Summary	174
Chapter 7	Deformation of Simple Molecular Solids: the Case of Diatomic Oxygen	178
7.1	Introduction	178
7.2	Methodology	179
7.2.1	Force Field and Crystal Structure	179
7.2.2	Slip Systems and Geometry	179
7.3	Convergence Analysis	183
7.3.1	RBSM Convergence	183
7.3.2	TBSM Convergence	183
7.4	Deformation Results	184
7.4.1	Slip in (111)	184
7.4.2	Slip in Higher Index Planes	188
7.4.3	Twinning Deformation in the (110) Plane: Rotational Twinning	189
7.5	Summary	193
Chapter 8	Slip Barriers in Anthracene	196
8.1	Introduction	196
8.2	Methodology	196
8.3	Convergence Analysis	198
8.4	Slip Barriers	199

8.5 Summary	201
Chapter 9 Conclusions and Future Outlook	205
Appendix A Finding The Easiest Slip Direction	213
Appendix B MgO Convergence Analysis	215
B.1 RBSM Convergence Results	215
B.2 TBSM Convergence Results	216
Appendix C Copyrights and Permission	218

Chapter 1

Background

1.1 Perspective

The physical performance of crystalline materials, the response of a material to external mechanical stimulus, is a broad topic. A geometric description of a material is a prerequisite to quantify its deformation. There are two popular ways to connect geometry and mechanics. One approximates a material body as a continuum, defined by the enclosure of a density within a surface boundary, within which physical processes act using integrodifferential equations. Continuum mechanics¹ introduces constitutive assumptions which lead to elastoplastic theories. These heuristic theories ignore the material's microstructure, characterizing the material response using an elasticity tensor (elastic deformation is reversible). A plastic material response indicates irreversible deformation and requires coefficients beyond the elastic constants to parametrize the deformation.² This elastoplastic theory provides the macro-scale description of the physical performance of a material. An alternative to elastoplastic theory is dislocation density crystal plasticity theory³, which is able to simulate the microstructure and its evolution during the plastic deformation, but nevertheless, requires a constitutive model and several assumptions about the system.

An alternative connection between mechanics and geometry is via the material's microstructure, especially its atomic structure. In this case, the material density enclosed within a surface becomes composed of atoms interacting with each other via a potential. By utilizing a force field approximation of the potential energy, such as a Lennard-Jones potential,⁴ the material performance is described, for instance, using molecular dynamics⁴ which integrates Newton's equation of motion. In principle, the detailed description that molecular dynamics provides allows it to describe continuum mechanics outcome. Calculating the phonon spectrum of any configuration allows the

determination of the system's physical stability.⁵ In addition, the elasticity tensor can be readily calculated from the atomistic description.⁵

Atomistic modeling of materials is computationally demanding and limited to tiny system sizes (roughly 50 by 50 by 50 nm^3) and extremely short time scales (μs). This description does not require calibration or constitutive assumptions, beyond selecting the potential model, to simulate many physical problems elusive to a continuum description such as anharmonic effects.⁶ Nevertheless, continuum mechanics can successfully investigate how tectonic plates move kilometers over the course of thousands of years.⁷ The multiscale modeling of materials performance is a promising field, where the nanoscale performance of the material informs its bulk performance at the macroscale.

Another class of continuum mechanics theories take into account the microstructure of the material. Perhaps the most popular among them are the 3M (micropolar, microstretch, micromorphic) theories developed by Eringen.⁸ Such theories divide the continuum into infinitesimal subvolumes or microelements. Each micro-element itself has a continuum description that adds extra degrees of freedom to the system that can accommodate different physical processes (material coefficients) such as those describing the micro-stretching and micro-rotations of micro-elements. These coefficients may be few in number if isotropy is assumed.

Barbagallo *et al.*⁹ briefly described the complexity of the generalized continuum theories produced in recent decades. For example, the anisotropic micromorphic elasticity theory by Mindlin and Eringen⁹ requires 498 material coefficients to describe general anisotropic material deformation. Thus, they devised an anisotropic relaxed micromorphic theory to model the deformation of material with a microstructure with a minimal number of additional material coefficients; namely six. Such simplification is highly desirable in describing real-life physical experiments. For example, in the near future, a micromorphic elasticity theory may accurately describe the deformation of organic molecular crystals where the microstructure is well-defined, including bond rotations, dihedral molecular deformations, different conformations; nevertheless, these lofty goals seem a long way off.

1.2 Introduction

This dissertation is the outcome of a collaboration between Curtin University and AstraZeneca Research and Development in Sweden. An understanding of the physical performance of crys-

talline material via computational methods is sought; this background chapter outlines the research achievements in the literature to date. The scope of plasticity is very broad, can be approached at several scales, and strongly influenced by defects and heterogeneities. Thus, the scope of this dissertation mainly targets ideal defect-free materials. However, particular topics related to experiment are discussed in the introduction, in order to showcase the multi-disciplinary nature of this research. The first part describes the pharmaceutical significance of the crystal mechanical properties and the importance of hardness, and reviews the mechanical performance and properties via stress-strain diagrams emphasizing the multiscale nature of hardness and the underlying plastic deformation. Next, deformation mechanisms maps are described fitting them within dislocation theory as it carries into the macroscale description of plastic deformation. Next, two dislocation mechanisms are discussed: slip (in metals, ionic crystals, and organic molecular crystals) and twinning deformation. Then, the two prevalent quasistatic computational methods to plastic deformation are reviewed; namely the generalized stacking fault energy (GSFE) and affine shear deformation methods. Then the literature findings regarding differential (relative) displacement are briefly reviewed, a vital component of the atomistic strain definition utilized in subsequent thesis chapters. To conclude, the critical gaps in the literature relevant to GSFE and affine shear deformation methods are collated.

1.3 Pharmaceutical Significance

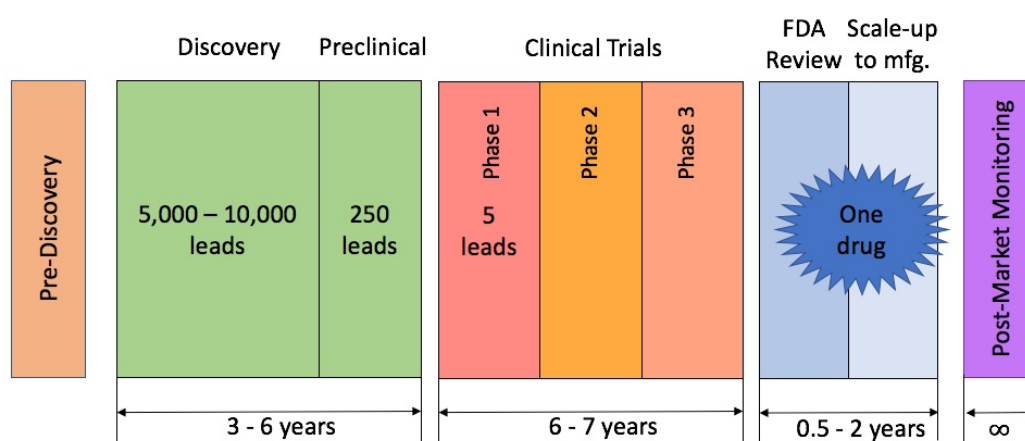


Figure 1.1: The genesis of a drug diagram depicting several stages, average times and lead numbers. Adapted from reference.¹⁰

Figure 1.1 shows the stages of drug production. There are seven with an average completion time of, at best, nine-and-a-half years and, at worst, fifteen years. The starting number of drug candidates is usually between 5,000 and 10,000 at the discovery stage, sifted down to about 250 at

the preclinical stage, and only five will reach the clinical trials, whilst a single drug will pass to the large-scale manufacturing stage.

The outcomes of this PhD research contribute to the large-scale manufacturing of drug tablets. Amongst all the oral dosage forms of drugs, tablets account for nearly 80%¹¹ because of their chemical stability, ease of administration, ability to be manufactured at large-scale economically, and control of drug release.

Tableting is the process responsible for drug pill production and involves two primary operations. First, micronization mills a pure active pharmaceutical ingredient (API) from a single crystal to produce a drug powder, inducing defects and disorder in the crystalline API¹² of some organic molecular crystals and amorphization and polymorphic transition¹³ in others. Second, compaction¹⁴ where the API and a binder/excipient are compacted together to produce the final drug tablet. Compaction is a complicated process that depends on several physical parameters: porosity, particle size and shape, tableting speed, compression force, and induces defects in the crystalline structure.¹⁵ Often, problems arise in the large-scale manufacturing of drug tablets due to their mechanical integrity, such as capping, lamination, chipping, stress cracking, and picking (Figure 1.2). We believe that we can avoid such problems by using prior knowledge of the API's mechani-

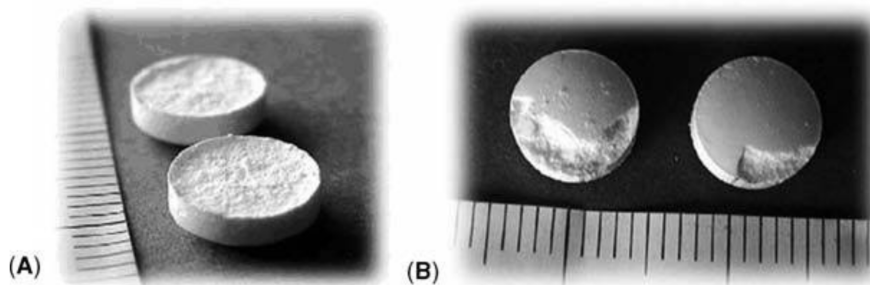


Figure 1.2: Examples of failed tablet samples, (A) Capping, (B) Chipping. Republished with permission of Taylor & Francis Group LLC - Books, from reference;¹⁵ permission conveyed through Copyright Clearance Center, Inc.

cal properties, namely the hardness, defined as the material's resistance to plastic deformation.¹⁶ Nanoindentation experiments have been used to measure the hardness of various API crystals¹⁷ and shown that medium hardness delivers optimum compaction performance for APIs. The question becomes: where does "hardness" fit in the spectrum of a material's mechanical properties?

1.4 Mechanical Performance and Properties

One of the first recorded experiments to study mechanical performance is the one designed by Leonardo Da Vinci in the 1500s.¹⁸ In his experiment, Da Vinci claims to have used the setup shown in Figure 1.3 to determine the strengths of iron wires as a function of length and found that the strength of short wires is higher than those of long ones. This is the opposite result to what should have been observed and Lund and Byrne¹⁸ suggest that the material heterogeneity is a possible cause for such questionable results. However, there is no doubt that Da Vinci's general experimental setup is an inspiration for international standards¹⁹ to experimentally determine mechanical material properties.

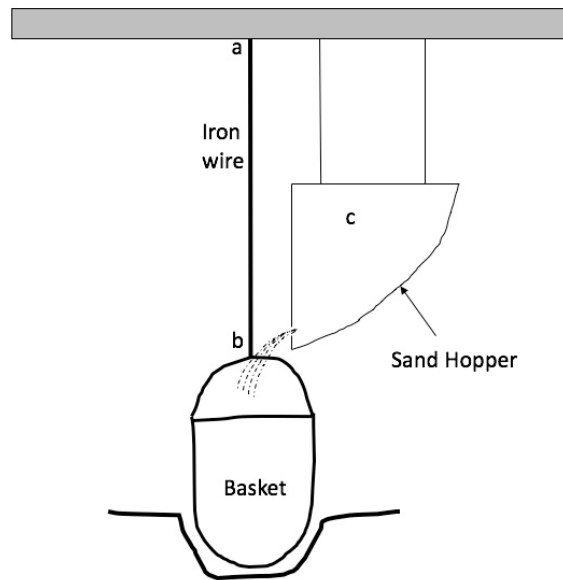


Figure 1.3: Setup used by Leonardo Da Vinci to determine the strength of metallic wires. The wire is placed between points *a* and *b*. Sand is fed into the bucket from hopper *c* which has a spring attached to it to close the sand feed as soon as the wire fails. Adapted from reference.¹⁸

Elastoplasticity describes the Newtonian reaction of a material specimen to an external stress field.²⁰ Such a theory applies a constitutive approximation to relate deformation to stress. Figure 1.4 serves as an introduction to the concepts of tensile and shear stresses in experiments, and shows the view along the *z* axis of a cubic material (although the subsequent definitions equally apply to all crystal systems). Tensile stresses act perpendicular to the cube's surface along the positive material axis (elongation stress $\sigma_{yy,t}$ in Figure 1.4). If the same stress acts in the negative direction it is called compressive stress, $\sigma_{yy,c}$ in Figure 1.4. Shear stress acts parallel to the surface, denoted by $\sigma_{yx,s}$ in Figure 1.4. The order of *yx* in the subscript denotes that the shear stress is acting in the direction perpendicular to *y* and along *x*. Strain is defined as a measure of the deformation of the geometry. Additional information can be found in Chapter 6, reference.¹⁶

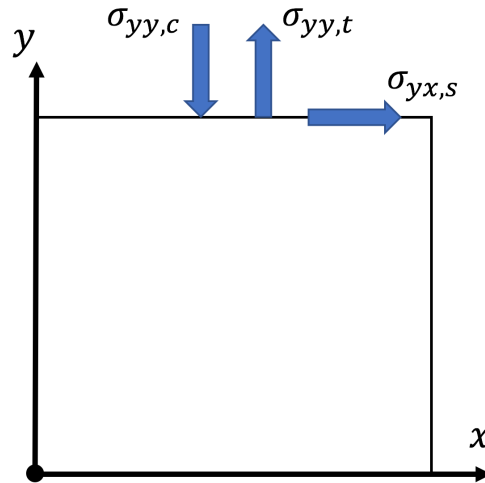


Figure 1.4: xy view with z pointing out of page of a three-dimensional cubic material subjected to three different stress modes. Subscripts c , t , and s represent compressive, tensile and shear respectively.

1.4.1 Stress-Strain Diagrams

A commonly used constitutive plot in materials science and engineering is the stress versus strain diagram.¹⁶ Such diagrams usually depict tensile or shear deformation experiments and provide information on the deformation of a material under a set of conditions that can then be used to guide design projects. Figure 1.5 shows qualitative examples of typical stress versus strain diagrams for a BCC metal,²¹ FCC metal,²² organic molecular crystal,²³ alloy (steel),²⁴ and ideal plastic material.²⁵

In the special case of linear elasticity, elastic deformation in crystalline materials is where the

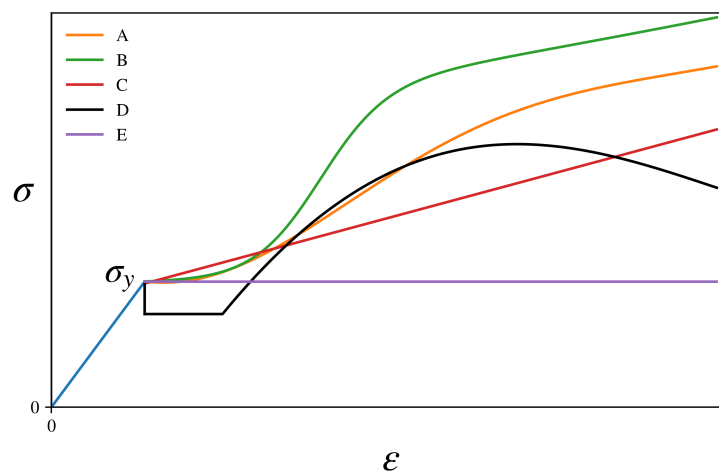


Figure 1.5: Several qualitative stress versus strain diagrams for different classes of crystalline material: BCC metal (A), FCC metal (B), organic molecular crystal (C), alloy (steel) (D), and ideal plastic material (E). The slope of the elastic regime is normalized so the curves lie on top of each other.

stress relates linearly to strain, i.e. the portion in Figure 1.5 connecting the zero point of stress

and strain to the yield stress σ_y , defined as the limit marking the onset of plastic deformation.¹⁶ σ_y is not equal for different classes of crystalline material, nor is the slope of the linear elastic curve, but were made equal in the plot for simplicity. Elastic deformation is reversible such that when the applied load is released, the material returns to its original configuration, i.e. Hooke's law applies in this regime.²⁶ Elastic constants of materials are determined both experimentally²⁷ from single-crystal data and computationally^{5, 28-31} based on ideal crystal structures. With the elasticity tensor, the material's elastic deformation under the influence of an external stress can be calculated analytically or numerically.

Figure 1.5 also shows the stress as a function of strain beyond the elastic limit, i.e. the plastic deformation zone. Ideally, plastic deformation should proceed at constant stress as shown by curve (E).²⁵ However, the actual deformation proceeds differently according to the class of crystalline material. The plastic stress versus strain curve of single-crystal deformations is so complicated because it is affected by many factors³² such as size, alloying, temperature, crystallographic orientation, and a variety of heterogeneities and defects.³³ The main features of the plastic deformation regime are the irreversibility demonstrated by permanent damage and distortion should the applied load be released and the absence of a comprehensive descriptive theory encompassing all the unique aspects.³³ Indeed, some of the outcomes of this thesis will be the interpretation of some particular plastic deformation events characteristic of defect-free materials such as high purity single crystals and nanowires. The hardness property is quantified based on the plastic deformation of a material. As will be briefly reviewed in later sections, some of the complexity of plastic deformation is due to the involvement of dislocation theory³⁴ leading to nucleation, interaction and multiplication of defects in crystallographic planes and directions, which explains why hardness has been elusive to first-principles calculations.

1.4.2 Experimental Hardness Measurements

There are several internationally recognized standards to experimentally measure the hardness of a material, such as: Rockwell hardness tests,³⁵ Brinell hardness tests,³⁶ and Knoop and Vickers hardness tests³⁷ and their micro-hardness implementations³⁸ with a small range of test force between 9.8×10^{-3} and 9.8 N applicable for the micro-tests as compared to the macro-tests (test force greater than 9.8 N). Such standards are mainly developed for hardness testing of metallic materials, with the exception of Knoop and Vickers micro-hardness.³⁸ In hardness tests, an indenter of a specific geometry is forced into the material's surface at one particular standardized load, causing a

surface impression due to plastic deformation. The three procedures above give hardness numbers derived from the indentation load and geometry, except the Rockwell hardness test, whose hardness number is found based on the indentation depth. Figure 1.6 provides a summary of several

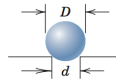
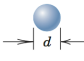
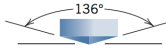
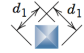
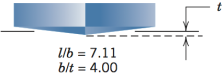
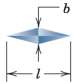
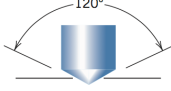



Test	Indenter	Shape of Indentation		Load	Formula for Hardness Number ^a
		Side View	Top View		
Brinell	10-mm sphere of steel or tungsten carbide			P	$HB = \frac{2P}{\pi D[D - \sqrt{D^2 - d^2}]}$
Vickers microhardness	Diamond pyramid			P	$HV = 1.854P/d_1^2$
Knoop microhardness	Diamond pyramid			P	$HK = 14.2P/l^2$
Rockwell and Superficial Rockwell	{ Diamond cone; $\frac{1}{16}, \frac{1}{8}, \frac{1}{4}, \frac{1}{2}$ in. diameter steel spheres			60 kg } 100 kg } Rockwell 150 kg }	
				15 kg } 30 kg } Superficial Rockwell 45 kg }	

Figure 1.6: Summary of the hardness test type, indenter shape, dimensions and geometry, and the formulae used to derive the hardness number for several hardness tests. ^a P is the applied load in kg, D, d, d₁, and l are in mm. Republished with permission of John Wiley & Sons - Books from reference;¹⁶ permission conveyed through Copyright Clearance Center, Inc.

hardness-test types, the indenters used along with their shapes and dimensions, and the formulae to derive the hardness number. Each hardness test provides a scale of its own; for example, Brinell hardness in units of HB, Vickers hardness in HV. The range of hardness values covered by each scale is different (see Figure 6.18 in reference¹⁶), implying that some tests are better suited for a specific material than others. Broitman³⁹ provides a critical overview of multiscale hardness tests, including the applicable load ranges and indentation dimensions. Broitman also discusses why it is impossible to precisely convert hardness from one scale to the other, such as using the exact indentation area in some tests or the projected area in other tests.

Micro-hardness measurement experiments have been performed on several pharmaceutical single crystals. Ichikawa *et al.*⁴⁰ measured the hardness by indenting the broadest face of the crystals, the face that slowly grows during crystallization, for three different loads. Ridgway *et al.*⁴¹ measured the hardness of randomly oriented crystals but ensured their faces had no visible irregularities and possessed uniform and parallel orientations. Ridgway *et al.* performed 325 indentations on aspirin and obtained a hardness of 0.085 GPa with a standard deviation of 0.03 GPa. Ichikawa *et al.* performed two indentations at different loads (where three indentations were used on all the other materials in their paper;⁴⁰ presumably, aspirin could not yield a clean indentation surface at higher

loads) and obtained an average hardness of 0.0955 GPa with average standard deviation of 0.0135 GPa. Both references yield hardness values of aspirin of the same order of magnitude. However, the standard deviations in both cases are significant, which shows that micro-hardness measurement tests on pharmaceutical crystals is possible but with limited accuracy and requires careful specimen and setup preparation. Micro-hardness testing is limited when applied to soft pharmaceutical crystals since the required loads become decreasingly small while higher magnification is required to measure the indented geometry.

The technical problems in calculating the hardness of organic (pharmaceutical) molecular crystals have been tackled since the start of the 21st century. Figure 1.7 shows the number of publica-

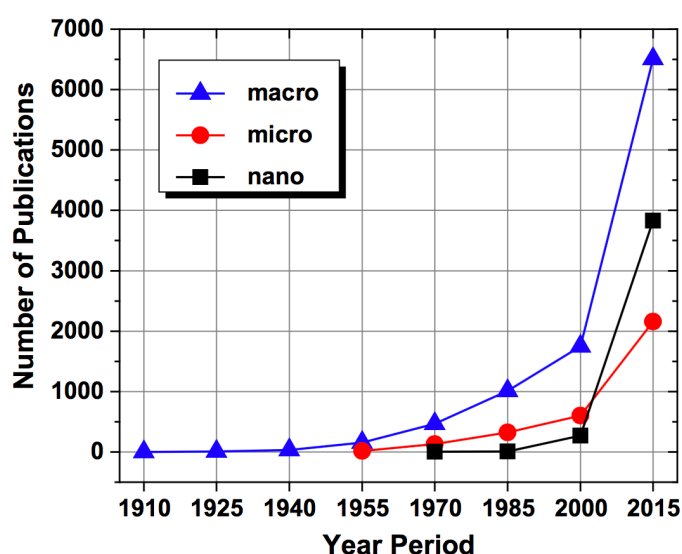


Figure 1.7: Number of publications reporting the hardness of materials at different scales: macro, micro and nano. Reproduced from article³⁹ which is distributed under the terms of the Creative Commons Attribution 4.0 International License (<http://creativecommons.org/licenses/by/4.0/>).

tions reporting the hardness of materials using different scales, with nano-hardness measurement techniques overtaking the micro-techniques and is likely to overtake the macro. At the nano-scale, hardness is measured using the nano-indentation technique. The main difference of this technique to the micro- and the macro-hardness measurements techniques is that the load and indentation depth are monitored in real-time. Figure 1.8 shows an example of the surfaces of a sucrose single crystal before and after indentation, in addition to the force-displacement diagram. The applied forces are in μN , and the obtained depth is in nm , indicating the high precision of nano-indentations. The Oliver-Pharr⁴³ method calculates the hardness based on the force-displacement plot and the geometry of the indenter. Masterson and Cao⁴² performed nano-indentation hardness measurement on a series of pharmaceutical crystals by varying the indentation depth (force) and found that hard-

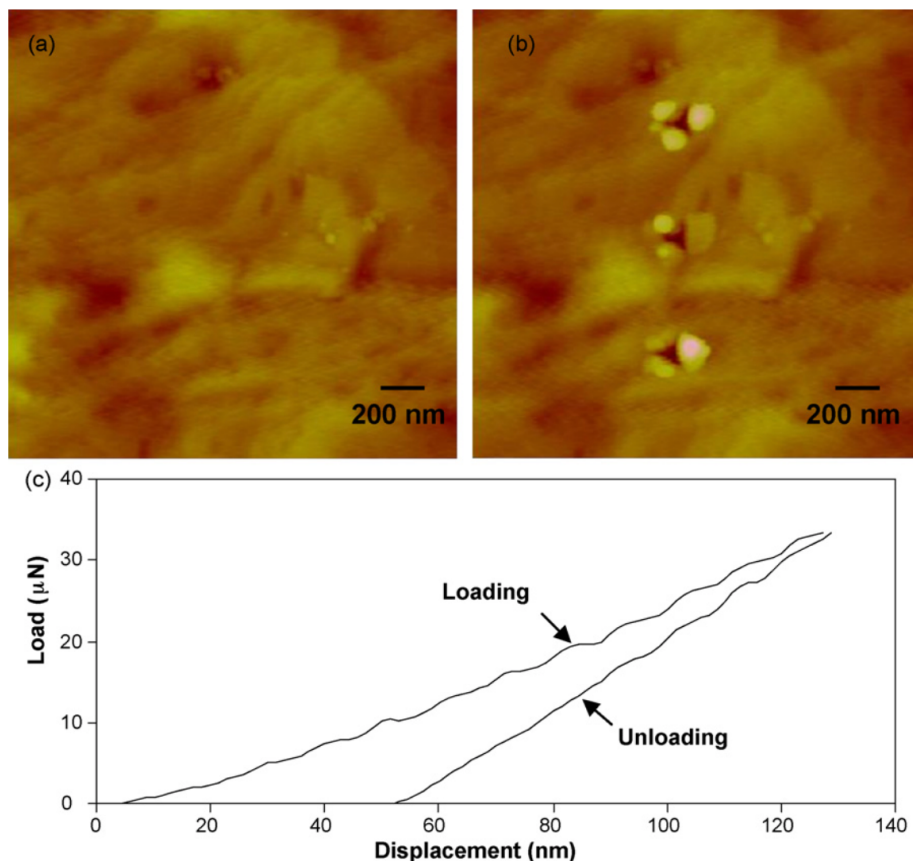


Figure 1.8: AFM Nano-indentation of a sucrose crystal, (a) before indentation, (b) after indentation (c) typical force versus displacement curve. Reprinted from reference,⁴² with permission from Elsevier.

ness varied as a function of indentation depth, even at the same peak force due to the inhomogeneity of the samples. We note that the standard deviation in some of these measurements can be as high as 40% (Table 4 reference⁴²). Mannepalli and Mangalampalli review on indentation plasticity of organic crystals⁴⁴ shows that hardness measurement is affected by several factors such as size effect, thermal drift, material pile-up/sink-in, making the actual process of measuring hardness very challenging.

Experimental hardness measurements of single crystals of pharmaceuticals reveal anisotropy in different crystallographic faces.⁴⁴ For paracetamol, Finnie *et al.*⁴⁵ measured the indentation hardness of several crystal faces and found a link between the ease of slip (a form of deformation mechanisms that will be introduced in the upcoming sections) and the anisotropic hardness of the crystal. Kiran *et al.*⁴⁶ studied nano-indentation hardness anisotropy in saccharin indented on two different planes and found that the hardness varied by 10%, while the plastic deformation was remarkably different as evident in the force-displacement graphs (see Figure 2 in reference⁴⁶). There were pop-in events in the force-displacement graph of the softer crystallographic face by integer

multiples of 18 *nm* corresponding to the unique plastic deformation mechanism compared to the other crystallographic face indentation. In summary, these reviews show that crystal anisotropy is dominant in pharmaceutical crystals and is reflected in the hardness measurement of the different crystallographic faces. This anisotropy in the hardness of organic molecular crystals raises concerns as to whether a single crystallographic face hardness measurement represents the bulk deformation of a single crystal, as hardness impacts the compactibility of drug tablets.¹⁷

1.4.3 Theoretical Hardness Calculations

Attempts to predict the hardness of materials based on lattice energies, such as Roberts and Rowe⁴⁷ proposed the model below to find the hardness of pharmaceutical crystals;

$$H = K.CED \quad (1.1)$$

where *K* depends on the crystal structure and explicitly assumes the slip ratio (the ratio of the Burger's vector to the unit cell vector, a quantity related to the deformation mechanism), and *CED* is the cohesive energy density (defined as the energy required to convert the solid into the gas phase). Roberts and Rowe⁴⁷ used the above model to estimate and compare the hardness of several pharmaceutical crystals, yielding successful predictions for four compounds but poor ones for ibuprofen and α -lactose. Roberts and Rowe acknowledged the importance of determining the active slip system for the model to provide successful predictions. However, *CED* is a volumetric quantity, and it is not clear how it relates to the hardness of the material. Even the more specialized attachment energy calculations (defined as the energy per molecule released due to the growth of the surface by one layer) predict the slip systems in organic crystals with a success rate below 50%.⁴⁸ Shariare *et al.*⁴⁹ explored interplanar d-spacing and surface energies to predict the mechanical properties of organic molecular crystals, including hardness. Their results gave a weak correlation as well as significant outliers (paracetamol and sucrose). Shariare *et al.* reasoned their model gave a weak correlation due to surface corrugations of crystallographic planes and those surface energies calculate vertical displacements while, in reality, lateral-displacement (shear) barriers are required.

Can plastic properties be derived based on elastic ones? Sun *et al.*⁵⁰ first addressed this question by performing mechanical property measurements on pharmaceutical tablets of varying composition between the plastic (microcrystalline cellulose- MCC) and brittle (dibasic calcium phosphate anhydrate- DPCA) as a function of compaction pressure. They found that irrespective of the composition or the compaction force; there is a linear relationship between hardness and Young's modulus

($H = 0.036E - 0.0018$, $R^2 = 0.955$); where Young's modulus is the constant of proportionality between stress and strain within the elastic limit.¹⁶ The same group extended their investigations⁵¹ and studied the relationship between hardness and Young's modulus of 256 molecular crystals. They found the linear regression $E/H_c=23.4$ GPa, with R^2 of 0.98, with some significant outliers proposing various reasons for error sources such as temperature, size effects and crystallographic orientation. While this finding may be a good first-order approximation, any anisotropic effects are absent. Young's modulus and hardness measurements are derived from the indented face of the crystal. Other faces may yield varying results depending on the level of anisotropy. We also note the error bars representation can be very large for some measurements. It remains to be verified experimentally whether such first-order approximations can assist in choosing candidates for the tableting process.

We note that for certain materials, it is possible to estimate the hardness theoretically. Tian *et al.*⁵² reviewed bond resistance, bond strength and electronegativity models. The common feature that all these models implicitly define hardness as the resistance of the chemical bonds to localized indentation. Tian *et al.* showed that such models could successfully predict the hardness for a variety of covalent, polar covalent and ionic crystals. This success owes to the localization of the chemical bonds and is inapplicable to crystalline material with delocalized bonds such as metals and the weak long-range forces that hold organic molecular crystals together. Meanwhile, Tse⁵³ suggests that first-principles computer simulations of the ideal stress and shear strength are the most accurate and reliable to compare predicted hardness values against experiments. However, this proposal needs to be verified for organic molecular crystals.

To summarize, the property of hardness with two definitions according to the macro¹⁶ and micro⁵² scales has been introduced. There are a variety of techniques at multiple scales to measure the hardness of material.³⁹ The smaller and more accurate the measurement procedure becomes, the more complicated the measurement process and underlying physics becomes.⁴⁴ For single crystals of pharmaceutical compounds, hardness anisotropically operates via deformation mechanisms⁴⁵ and plastic deformation.⁴⁶ Simple models^{47,51} may work as first-order approximations, but care has to be taken because of outliers and large standard deviations in the experimental hardness measurements. The hardness of covalent and ionic crystals can be calculated using models of the chemical bonds,⁵² yet metallic and organic molecular crystals whose interactions are delocalized, or long-range, respectively, remain elusive.

The anisotropy of hardness in molecular crystals strongly questions if a single value is repre-

sentative of the bulk. In addition, indentation hardness explores the material's response to compressive stresses only, even though there are various ways to deform a crystal, including shear and tensile strains. A more accurate qualitative description of hardness will require the detailed investigation of plastic deformation mechanisms, coupled with consideration of ideal shear strengths of several crystallographic faces. Experimentally, finding the ideal shear strengths and investigating plastic deformation phenomena in single crystals is very challenging and time-consuming. Computational techniques that can simulate plastic deformation and describe the atomistic details of this deformation are required, particularly in the limit of ideal defect-free materials where a universal computational treatment can uncover intrinsic material properties without the need of explicit treatment of defects. Before reviewing some of the present computational methods in the literature, it is necessary to review some basic plastic deformation mechanisms of crystalline material.

1.5 Introduction to Deformation Mechanisms

1.5.1 Deformation Mechanism Maps

In 1972, Ashby⁵⁴ published the first deformation mechanism map for polycrystalline metals. Figure 1.9 shows a map for silver.

Such maps contain deformation mechanisms as a function of the applied stress and temperature for a particular critical strain rate $\dot{\epsilon}_c$ and grain size. The x -axis is defined in terms of the temperature T or the homologous temperature (T/T_m ; where T_m is the melting temperature). The y -axis is defined in terms of the applied tensile stress or, equivalently, the normalized tensile stress (σ/μ ; where μ is the shear modulus). In general, a selected point of σ and T at a specific strain rate for a given material grain size will fall within a particular region of Figure 1.9. Such graphs are generated based on the constitutive description⁵⁴ of the material performance. Some deformation regions are based on theory while others on experimental data fitting. The several relevant regions and their description as per Ashby⁵⁴ are:

1. Elastic regime: as defined in the previous section, this is the region where reversible deformation occurs should the applied load be released.
2. Defect-less flow: which is of the order of $\mu/20$ and is independent of temperature. A point that lies above the theoretical shear stress threshold characterizes the deformation of defect-free material. Ashby assumed that the planes of atoms in the crystal “bodily lift” over neigh-

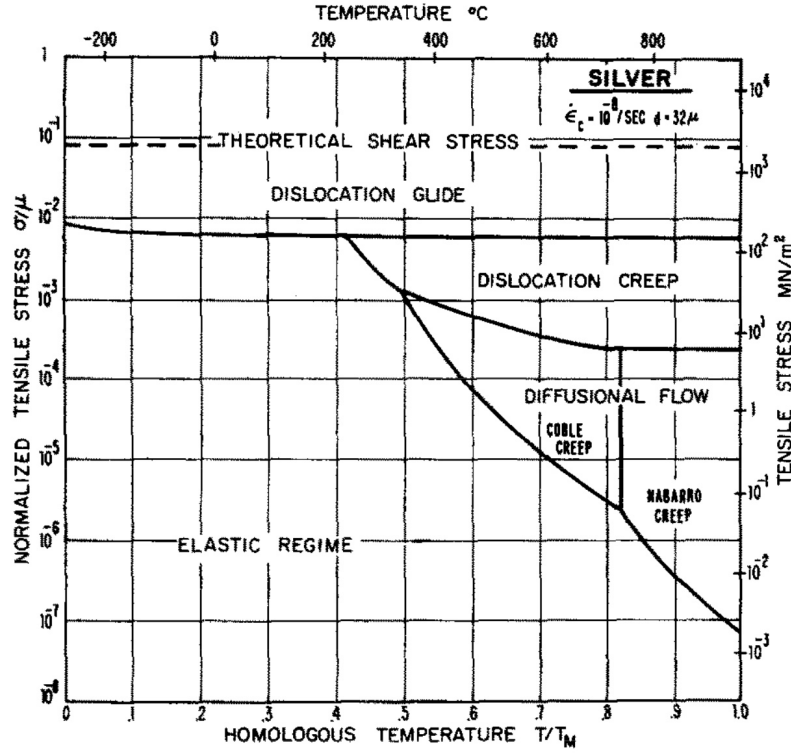


Figure 1.9: Deformation mechanism map of polycrystalline Ag of grain size of $32 \mu\text{m}$ and critical strain rate $\dot{\epsilon}_c$ of $10^{-8}/s$. Reprinted from reference,⁵⁴ with permission from Elsevier.

boring planes producing permanent deformation.

3. Dislocation glide: dislocation (type of line defect pre-existing in the crystal before deformation) glide mechanism activates when the experiment meets specific conditions such as threshold stress. The presence of obstacles in impurities, solute atoms or other dislocations limits this kind of slip plasticity. For FCC and HCP metals, the below constitutive equation⁵⁴ applies:

$$\dot{\epsilon}_2 = \dot{\epsilon}_0 e^{-\left[\frac{S-\sigma}{kT}\right]ba} \quad (1.2)$$

where $S = \frac{\mu b}{l}$ is the flow stress at absolute zero, b is the Burgers vector (a geometric quantity related to the structure of the dislocation), and l is the obstacle spacing; k is Boltzmann's constant, T the absolute temperature, a is the activation area and $\dot{\epsilon}_0$ is the strain rate when $\sigma = S$. Equation 1.2 is valid when $\sigma/\mu \geq \sigma_0/\mu$, and equals 0 otherwise; where σ_0 is the cut-off stress. Equation 1.2 is useful for delineating the limit line between dislocation glide and other deformation mechanisms. We note that the dislocation glide spans the whole homologous temperature range just like the theoretical shear stress deformation. For BCC

metals, the situation is more complicated. The whole BCC crystal resists dislocation motion resulting in a strengthening mechanism at low temperatures that is difficult to model. We note that in defect-free materials such as nanowires and whiskers, where pre-existing dislocations are not present, this mechanism does not apply in the early stages of plastic deformation.

4. At relatively higher homologous temperatures (well-above room temperature), the diffusional creep deformation mechanism¹⁶ dominates, which is a consequence of the exposure of a material to a static load at an elevated temperature for a prolonged duration of time. Creep strain is additive as a function of time and ultimately results in the rupture of the material. For FCC Ag in Figure 1.9, Ashby highlights three different creep deformation mechanisms. Dislocation creep occurs when dislocations diffuse through the crystal grains of the polycrystal to form cells. Nabarro-creep happens when the material diffuses in bulk following a Newtonian-viscous (fluid-like) motion. Coble-creep is similar to Nabarro-creep, except such diffusion occurs through the boundaries of the grains.

Ashby notes several advantages and disadvantages of deformation mechanism maps. Such maps can guide experimentalists to the correct parameters to further investigate particular deformation mechanisms. They can be helpful in engineering applications to study the deformation of mechanical components such as turbine blades in operation. On the other hand, some of the main disadvantages mentioned by Ashby are that other deformation mechanisms are not included in the map, such as deformation twinning and grain boundary sliding, because of the absence of their theoretical and constitutive understanding when this paper was published in 1972. Frost and Ashby, in 1982,⁵⁵ extended the deformation mechanism map to include more complex features such as dynamic recrystallization. In recent years, Meyers *et al.*⁵⁶ extended the deformation mechanism map by Frost and Ashby and proposed a constitutive modeling of twinning and slip deformation, thus adding these two regimes, as can be seen in Figure 13, reference.⁵⁶

Herein, we are interested in materials performance at room temperature and close to ideal conditions at zero Kelvin. Figure 1.2 shows that the possible deformation mechanisms are elastic or ideal theoretical shearing of the material, where the latter links to the nucleation of dislocations due to plastic deformation.⁵⁷ Thus in the next subsection, we introduce the subject of dislocations and reveal some of their correlations with deformation mechanisms.

1.5.2 Theory of Dislocations

Dislocation theory emanates from observations in the 19th century of slip bands in plastically deformed metals, followed by three central papers in 1934 developed by Orowan, Polanyi, and Taylor, and then in the early 1950s, the direct observation of dislocations via transmission electron microscopy.⁵⁸ Dislocation theory explained slip morphologies and helped solve the problem as to why crystalline material fails at stresses much lower than their ideal strengths. In a related matter, Frank⁵⁹ proposed nucleation and growth of a crystal via dislocations to be the reason why experimentally, the actual supersaturation is much lower than the theoretical prediction.

Dislocations were mentioned in earlier sections and defined as “line defects”. More precisely, simple dislocations correspond to an extra half-plane of atoms/molecules embedded within an ideal crystal.³⁴ Such line defects exist in crystalline materials in three possible configurations. Figure 1.10 shows an illustration of a typical dislocation. Following Hirth and Lothe,³⁴ let unit vector

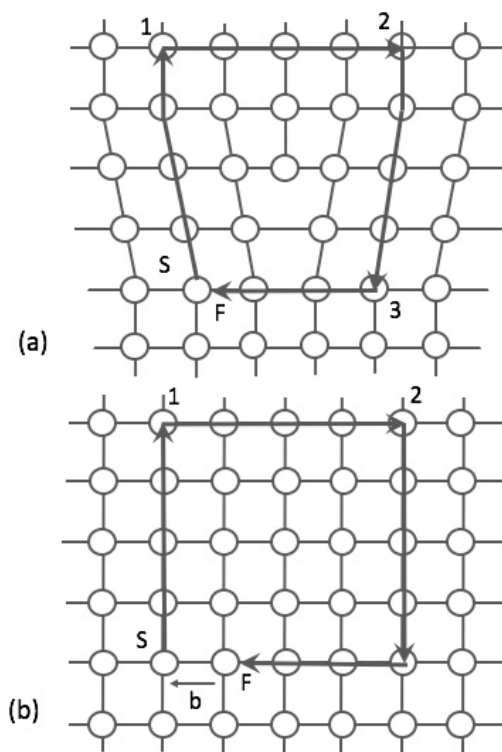


Figure 1.10: Schematic showing (a) a dislocation embedded in an ideal crystal, while noting the extra half-plane of atoms (b) Perfect reference crystal with Burger’s circuit constructed. Schematic adapted from reference.³⁴

ξ be the tangent to the dislocation line, which in Figure 1.10 is into the page. The displacement of a dislocation is described by constructing the Burger’s circuit³⁴ as Figure 1.10 (a) and (b) show, where in (a) the first circuit is constructed by connecting the points 1, 2, 3, F, and S (where F and S are superimposed), and then in (b) the new circuit is constructed after adding the missing half-

plane of atoms. The circuit does not close unless points F and S are connected, and this connecting vector denotes the Burger's vector. In metals, the Burger's vector (b) points in the crystallographic direction of the closest atomic packing and its magnitude is related to the interatomic distance.¹⁶ Three different types of dislocations³⁴ are differentiated based on Figure 1.10. If b is perpendicular to ξ , then we have an "edge" dislocation, if parallel to ξ , then we have a "screw" dislocation, and if it has components parallel and perpendicular to ξ , then we have a "curved" dislocation.

Deformation-induced dislocation motion has been experimentally observed in all classes of crystalline material: FCC Al,⁶⁰ BCC Mo,⁶¹ HCP Ti and Zr,⁶² the MgO ionic crystal,⁶³ the semiconductor Si,⁶⁴ organic molecular crystals pentaerythritol tetranitrate (PETN) and cyclotrimethylene trinitramine (RDX),⁶⁵ and even in diamond,⁶⁶ the hardest crystalline material. Following Hull and Bacon,⁶⁷ we assume a perfect crystal has a single edge dislocation. Shear stress is applied to the crystal as shown in Figure 1.11 where the edge dislocation moves from the interior to the right-hand side of the crystal. This idealized process leads to the formation of two perfect edges on each lateral side of the crystal. The dashed line indicates the slip plane and marks the plane of glide of the dislocation. Figure 1.12 illustrates a simplified movement of a screw dislocation. The

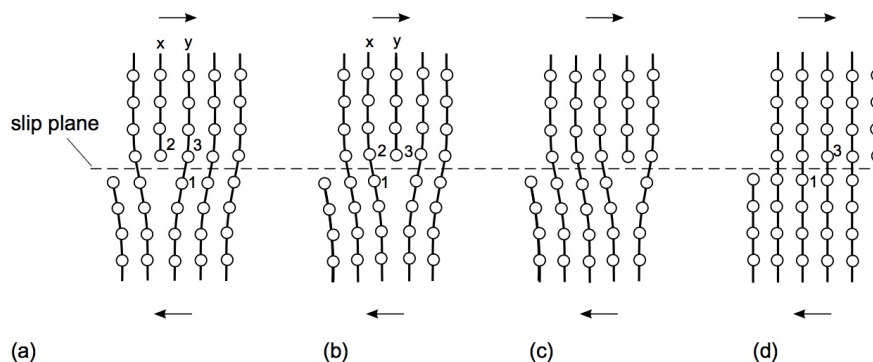


Figure 1.11: Illustration of the movement of an edge dislocation. The shear direction is parallel to the arrows. As the crystal shears, a dislocation moves to the exterior resulting in two perfect edges at the lateral sides of the crystal. Reprinted from reference,⁶⁷ with permission from Elsevier.

top and bottom sides of the crystal are sheared parallel to the LM direction (the line connecting points L and M in Figure 1.12). The dislocation originally terminated at AA' now propagates to BB'. The outcome of this motion is the formation of two edges on the lateral sides of the crystal. However, these motions are ideal, as in practice materials develop a rich pattern of plastic deformation manifested through nucleation, interaction and multiplication of dislocations⁶⁸ that can reach dislocation densities as high as 10^{14} m^{-2} at large plastic strain.

The high pre-existing and resulting dislocation densities⁶⁸ (except in whiskers and nano-wires, which are nearly defect-free) complicate the analysis of dislocations in materials. There is an exten-

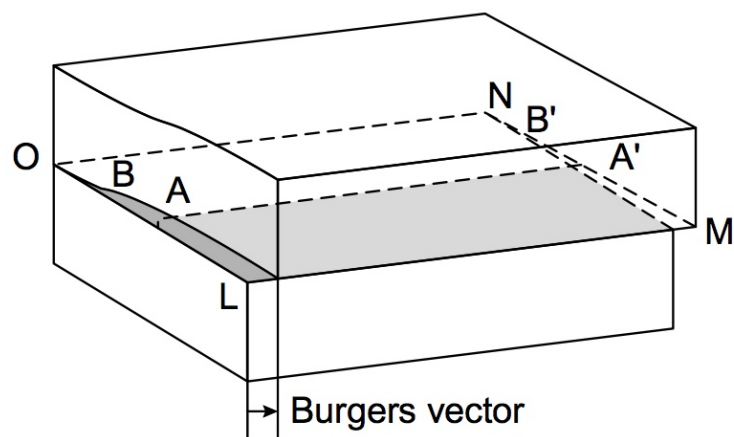


Figure 1.12: Illustration of the movement of a screw dislocation. The shear direction is parallel to LM; the line connecting points L and M. As the crystal shears, a dislocation moves to the exterior resulting in two edges at the lateral sides of the crystal. Reprinted from reference,⁶⁷ with permission from Elsevier.

sive body of theoretical developments in dislocations in hard materials such as metals. The Hirth and Lothe book on the Theory of Dislocations³⁴ is indispensable in the field as it covers a wide variety of topics, including dislocation types, elastic fields, dislocation dynamics, interactions, and energies. However, a similar theoretical exposure of dislocation theory in organic molecular crystals is absent from the literature, mainly due to their lower symmetry and the directionality of their interactions.⁶⁹ As will be seen in the forthcoming sections, this has not prevented applying the theoretical knowledge of dislocations in hard materials to molecular crystals.

1.5.3 Characteristics of Dislocations

At equilibrium, an ideal defect-free crystal adopts an energy minimum configuration. Any perturbation to the ideal packing of a crystal, such as the presence of dislocations, produces an elastic field and a disruption of crystallinity at the dislocation core. To demonstrate how dislocations statically perturb a crystal, we follow Hirth and Lothe³⁴ and assume there exists a straight edge dislocation embedded in an isotropic material, as shown in Figure 1.13. The straight dislocation is assumed to produce planar strain in the xy plane only. Hirth and Lothe³⁴ solved the equilibrium equation in

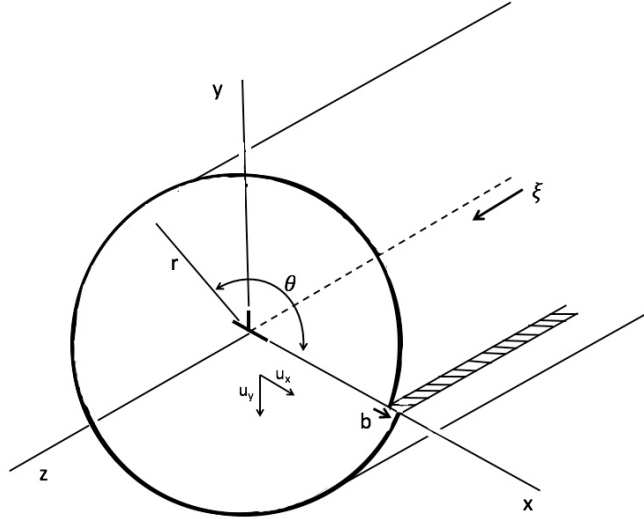


Figure 1.13: Schematic of an edge dislocation in an isotropic material. ξ is the dislocation line vector, b the Burger's vector, u the displacement, θ and r the cylindrical coordinate axis. Adapted from reference.³⁴

the form of the Airy stress function⁷⁰ and found the resulting stress field:

$$\sigma_{xx} = -\frac{\mu b}{2\pi(1-\nu)} \frac{y(3x^2 + y^2)}{(x^2 + y^2)^2} \quad (1.3a)$$

$$\sigma_{yy} = \frac{\mu b}{2\pi(1-\nu)} \frac{y(x^2 - y^2)}{(x^2 + y^2)^2} \quad (1.3b)$$

$$\sigma_{xy} = \frac{\mu b}{2\pi(1-\nu)} \frac{x(x^2 - y^2)}{(x^2 + y^2)^2} \quad (1.3c)$$

$$\sigma_{zz} = -\frac{\mu b\nu}{\pi(1-\nu)} \frac{y}{x^2 + y^2} \quad (1.3d)$$

$$\sigma_{xz} = \sigma_{yz} = 0 \quad (1.3e)$$

where μ is the shear modulus, b the Burger's vector, ν Poisson's ratio, x and y the Cartesian coordinates. The stress analytic solutions in 1.3 reveal some features of dislocations:

1. The self-stress (or similarly self-strain) obtained via isotropic elasticity solutions is undefined at $x = y = 0$; this undefined point of the material has a particular name in dislocation theory; the "dislocation core".
2. Self-stress fields vanish almost quadratically as the stress is calculated away from the dislocation core and dislocation line.

We highlight that even if the anisotropic elastic solution of the stress field of a dislocation⁷¹ is employed, there will still exist a singularity at the dislocation core. Dislocations are also characterized by an energy:⁷²

$$E_{total} = E_{core} + E_{elastic\ strain} \quad (1.4)$$

where E_{core} is the core energy of dislocation and $E_{elastic\ strain}$ is the elastic energy of a dislocation. For instance, Hirth and Lothe³⁴ found the isotropic elastic strain energy for the straight edge dislocation in Figure 1.13 to be;

$$E_{elastic\ strain} = L \frac{\mu b^2}{4\pi(1-\nu)} \left[\ln \frac{R}{r_0} - 1 \right] \quad (1.5)$$

where L is the length of the dislocation, R is the outer radius of the cylinder, and r_0 is the core radius. According to equation 1.5, the energy of dislocation is directly proportional to the square of the magnitude of Burger's vector. We show below that this dislocation theory result directly influences the prediction of slip systems in some materials.

The Peierls-Nabarro Dislocation Model (see reference³⁴ in Chapter 8) is able to describe the properties of ideal screw/edge dislocations in terms of dislocation core energy estimates, dislocation core width (proportional to the interplanar spacing and elastic properties), and the Peierls stress to move a dislocation. Lu⁷³ briefly reviewed the Peierls-Nabarro model and indicated some of its limitations and extensions, such as the Semi-Discrete Peierls-Nabarro Model which combines atomistic calculations (γ surface which will be introduced later) with the classical model, to obtain more accurate dislocation properties.

It is possible to calculate the core energy of a dislocation E_{core} using atomistic simulations.⁷⁴ In general, the proper configuration of a dislocated structure has to be constructed and its energy calculated. Then, the energy of a dislocation core is found by:

$$E_{core} = E_{disl} - E_{ideal} - E_{elastic\ strain} \quad (1.6)$$

where E_{disl} and E_{ideal} are the potential energies of the dislocated and the ideal structure, respectively.

The following sections discuss some of the important features of deformation mechanisms such as slip and twinning deformation. Although the scope of this dissertation mainly addresses deformation in ideal defect-free crystals i.e. no dislocation cores or dislocation glides, reference is made below to experiments and computational methods particularly focussed on elucidating and/or explaining certain features of deformation and slip barriers.

1.6 Slip Deformation

We described above that in dislocated ideal crystals, slip deformation corresponds to the movement of dislocation(s) from within the material to the boundaries forming edges on the lateral surfaces. Experiments have confirmed the formation of such edges. For instance, Gotoh⁷⁵ performed tensile deformation experiments on dislocation-free Cu whiskers and, using a differential interference contrast microscope, was able to image the whiskers during the course of deformation. Gotoh noted (in Figure 2 reference⁷⁵) the formation of slip lines as a consequence of the nucleation and movement of dislocations. These slip lines were geometrically related to the $\langle 011 \rangle$ crystallographic directions in the $\{111\}$ crystallographic planes of FCC Cu. Xia *et al.*⁷⁶ performed nanoindentation experiments on an FCC alloy to understand dislocation activity via slip steps in a material sample having a dislocation density of $10^{12} m^{-2}$. The authors used a scanning electron microscope (SEM)

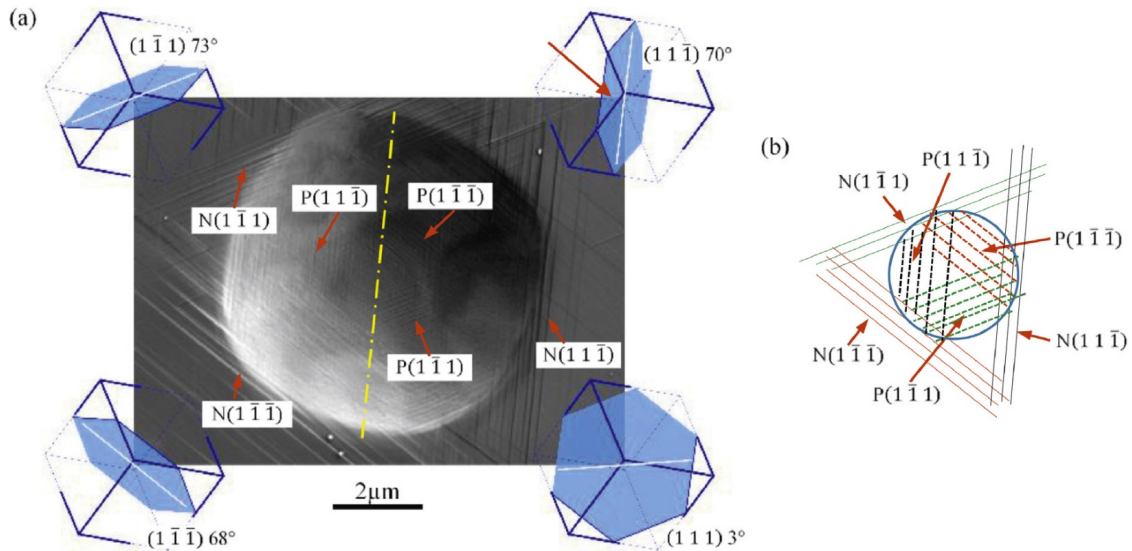


Figure 1.14: An image (a) and illustration (b) of the indented area of a $\{111\}$ grain. P and N represent positively and negatively inclined slip planes. Reproduced from article⁷⁶ which is distributed under the terms of the Creative Commons Attribution 4.0 International License (<http://creativecommons.org/licenses/by/4.0/>).

to photograph the indented area. Figure 1.14 shows that several slip lines (steps) appear as a consequence of $\{111\}$ plane indentation. The slip lines in the figure are parallel to the $(1\bar{1}1)$, $(11\bar{1})$, and $(1\bar{1}\bar{1})$ planes because they are at angles between 73° , 70° , and 68° with respect to the surface, but not the (111) plane because it is at 3° to the surface and thus received negligible shear stress. The terms positively and negatively inclined slip planes imply the slip step is either extruding outward of the material or intruding inward, respectively. Xia *et al.* attribute the formation of these slip lines to the movement of dislocations in the material.

A slip system¹⁶ is the combination of a crystallographic slip plane and a crystallographic direction. The main questions regarding slip systems are: How can the easiest slip system in a material be found? Is it possible to rank all the possible slip systems? There are three parts to the answer of these questions. First, it is possible to derive first-order theoretical insights into the ranking of slip systems from dislocation theory. We mentioned in earlier sections that the energy of an edge dislocation is directly proportional to the magnitude of the Burger's vector. The same proportionality applies to dislocations in general,³⁴ which implies that the energetically favorable dislocation will be the one corresponding to the shortest Burger's vector. The Interplanar spacing distance d appears in the Peierls-Nabarro model of dislocations such that the lowest dislocation energy (hence the easiest slip system) corresponds to the largest d .³⁴ Later sections will verify these first-order approximation. Second, it is possible to use experimental techniques to deform the material and then identify the resulting slip lines. Third, there exists an extensive body of atomistic computational research to address deformation aspects of crystalline material. In the following subsections, we elaborate on slip systems of metals, ionic crystals, and organic molecular crystals since our interest is in materials characterized by delocalized and long-range interactions.

1.6.1 Slip Systems in Metals

Metals slip in the plane of highest planar atomic density and the crystallographic direction of the closest packing of atoms,¹⁶ the latter being a consequence of the energy of a dislocation being proportional to the square of the magnitude of the Burger's vector.

FCC metals are characterized by a single family of slip systems, the $\langle 011 \rangle \{111\}$.¹⁶ Each $\{111\}$ plane contains three $\langle 011 \rangle$ directions. An FCC metal has four different $\{111\}$ planes implying twelve possible slip systems. The atomic arrangements in FCC metals have close-packed layers in $\{111\}$ stacked in ABC positions (see Chapter 3 for more details). Hull and Bacon⁷⁷ give the example of the $1/2 [10\bar{1}]$ dislocation and for now denoted by b_1 . Figure 1.15 shows the top view of the (111) plane for FCC metals. A, B, and C denote the stacking of atoms (layers) in the (111) plane. Atom A is shown as a solid circle while atoms B and C are shown by the position of their centers, atoms B are lower than atoms A, and atoms C are the lowest. The Burger's vector b_1 connecting A to an A, B to B or C to C, is representative of the dislocation with the lowest energy. Hull and Bacon⁷⁷ explain that if the crystal shears in the direction of b_1 at the interface between A and B to produce a displacement, then the crude illustration in Figure 1.15 shows that it is easier for B to pass through the valleys (B to C, then C to B - in a zigzag pathway, or equivalently in the direction of b_2

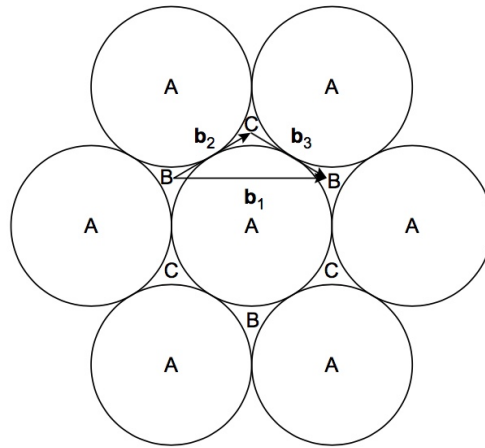


Figure 1.15: Visualization of the top view of the $\{111\}$ plane in FCC metals. A, B, and C indicate atomic stacking sequence. Arrows b_i represent Burger's vectors. Reprinted from reference,⁷⁷ with permission from Elsevier.

then b_3) than to directly move to the next B position over the top of A (along b_1). When B moves to C, it produces a stacking fault, defined as a disruption in the natural ABC stacking of atoms in the (111) plane. This stacking fault is characterized by a local minimum on the global potential energy hyper-surface called the intrinsic stacking fault energy. Hull and Bacon⁷⁷ support this dislocation propagation based on computer simulations; namely, γ surface calculations introduced by Vitek,⁷⁸ and defined as the excess surface energy resulting from the rigid translation of one rigid block on top of the other. Figure 1.16 forms the foundation of the zig-zag propagation of dislocations in

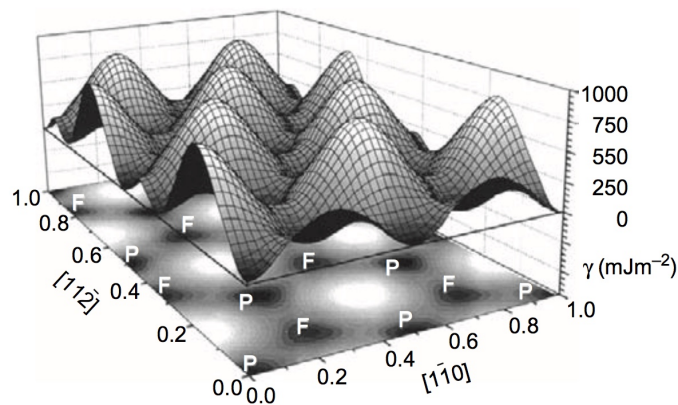


Figure 1.16: Plot of the γ surface in the (111) plane of Cu on the z axis, as a function of the rigid block displacements along the $[1\bar{1}0]$ and $[11\bar{2}]$ represented by the x - and y -axis, respectively. Point P represents the reference configuration with γ equals to 0, point F represents the intrinsic stacking fault energy. Reprinted from reference,⁷⁷ with permission from Elsevier.

FCC metals. The curve results from a computer simulation calculating the γ surface in FCC Cu in the (111) plane. The lowest energy path from point P to the next point P would be P to F, then F to P. Similar arguments for dislocation propagation in FCC metals have been made by Hirth and

Lothe³⁴ where the dislocation propagation from P to P would require larger dilatation normal to the slip plane than the propagation from P to F, then F to P.

Such zigzag motions of dislocations also originate from dislocation theory. Frank⁷⁹ proposed dislocation reactions in the form reactants and products ($b_1 = b_2 + b_3$) being proportional to the square of the magnitude of the Burger's vector. In FCC metals, for instance, b_1 is called a full dislocation that can dissociate according to:⁷⁷

$$\frac{1}{2}[10\bar{1}] = \frac{1}{6}[\bar{2}11] + \frac{1}{6}[\bar{1}\bar{1}2] \quad (1.7)$$

According to Frank's rule,⁷⁹ this dislocation dissociation reaction is energetically favourable. In terms of the square of the magnitude of the Burger's vector, the right-hand side has a magnitude of ($a^2/6 + a^2/6 = a^2/3$) which is less than that of the left-hand side ($a^2/2$). The products in 1.7 are called Shockley partials,^{34,77} which are partial dislocations because their Burger's vector is a fraction of half the lattice vector. Such partial dislocations being at 60° repel each other and produce a stacking fault ribbon, whose dimensions are used to estimate the intrinsic stacking fault energy according to,⁷⁷

$$d = \frac{Gb^2}{4\pi\gamma} \quad (1.8)$$

where d is the separation distance between the partials, G the shear modulus, γ the stacking fault energy. Equation 1.8 is the basis of the experimental measurement of the stacking fault energy.

The previous discussion shows that there are several combinations of dislocation mechanisms in FCC metals which depend⁸⁰ on the loading mode (tensile versus compressive) and crystallographic direction (the Schmid factor). Cao and Ma⁸¹ performed molecular dynamics simulations of tensile and compressive deformation on Cu nanopillars noting that the tensile case observed first the nucleation of a Shockley partial b_1 (not to be confused with earlier reaction in equation 1.7 where b_1 corresponded to the full dislocation, since Cao and Ma⁸¹ use b_1 and b_2 to denote Shockley partials and b_3 to denote the full dislocation) as shown in Figure 1.17 (a), followed by the propagation of this Shockley partial throughout the domain, Figure 1.17 (b) - (e), which results in slip by partial dislocations. The compressive deformation⁸¹ of the same geometry led to the propagation of a full dislocation via dissociated partials, as shown in Figure 1.18. First, a dislocation nucleation site is indicated in the corner of the geometry in (a), followed by the nucleation of a Shockley partial b_1 (the leading partial) (b), then the subsequent nucleation of Shockley partial b_2 (the trailing partial) (c), and its combination with b_1 to form a full dislocation b_3 , (c)-(f) the full dislocation propagates throughout the structure. The authors rationalize the switch in the deformation mecha-

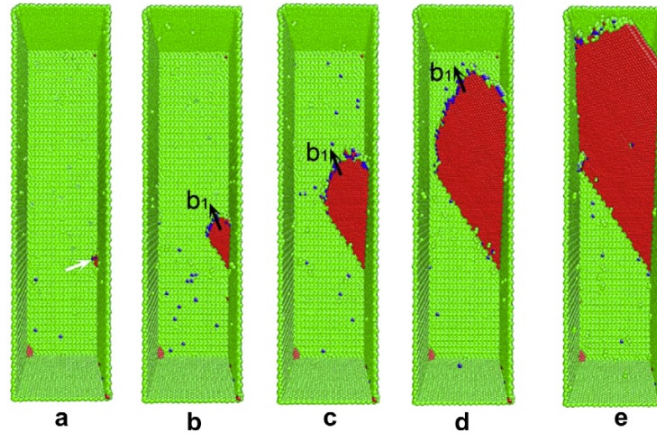


Figure 1.17: Trajectory snapshots of the molecular dynamics tensile deformation simulation performed by Cao and Ma, (a) the nucleation of a Shockley partial b_1 indicated by the white arrow, (b)-(e) the propagation of b_1 throughout the structure. To observe the defects inside the pillars (red color), surface atoms at the front having an FCC packing are hidden. Reprinted from reference,⁸¹ with permission from Elsevier.

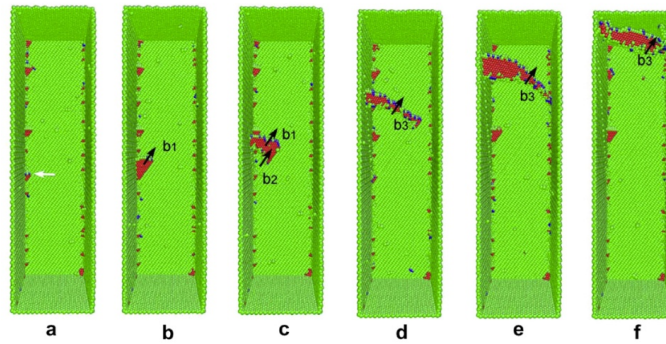


Figure 1.18: Trajectory snapshots of the molecular dynamics compressive deformation simulation performed by Cao and Ma, (a) white arrow indicates the dislocation nucleation site (b) the nucleation of Shockley partial b_1 from the corner, (c) the nucleation of the subsequent Shockley partial b_2 from the corner and combining with b_1 to form full dislocation, (d)-(f) full dislocation propagation in the nanopillar. Reprinted from reference,⁸¹ with permission from Elsevier.

nism due to the different Schmid factors when the stress acts in tension or compression. Xu *et al.*⁸² performed molecular dynamics simulations mimicking the experiments of compressive deformation of Al nanopillars to understand the plastic deformation as a function of size and orientation. They found that different deformation mechanisms activate when the orientation of the deformation changes. The authors⁸² also confirmed the well-known trend of smaller-diameter nanopillars being stronger than larger-diameter ones. The presence of size-effects combined with the Schmid law makes finding the critical strength of the nanopillars challenging and, accordingly, the barriers to activating different deformation mechanisms.

1.6.2 Slip in Ionic Crystals

Ionic crystals are held together by Coulomb interactions between the cationic and anionic species. Due to strong charges within the crystal, its plastic deformation is associated with specific electric phenomena. Urusovskaya⁸³ reviewed such effects and in summary:

1. Gyulai-Hartly effect:⁸⁴ it increases the ionic conductivity in rock-salt crystals upon plastic deformation, particularly along the slip planes and was found to be proportional to the applied load, diminishes with heat, is either weakened by cationic impurities or strengthened by anionic impurities, and decays with time at a constant load.
2. Stepanov's discovery:⁸⁵ an electric potential on the surface of plastically deformed rock salt specimens changes its magnitude; this change is maximum if the stress maximizes the slip in the material. Such a charge disappears upon unloading.

Urusovskaya⁸³ concluded that movement of charged dislocations in ionic crystals and their interaction with charged defects (e.g. vacancies) are the reasons behind these electric effects.

This brief account of aspects of plasticity in ionic crystals shows that there exist a number of complexities in describing their plastic deformation. The first is the prediction of the active slip systems. We mentioned earlier that slip in metals happens in the plane of highest planar density and the crystallographic direction of the closest packing of atoms, as defined in reference.¹⁶ Similarly, Hirth and Lothe³⁴ highlighted that the planes characterized by the largest d (interplanar) spacing are the closest-packed planes, where d for cubic materials is defined by;

$$d_{hkl} = \frac{a_0}{\sqrt{h^2 + k^2 + l^2}} \quad (1.9)$$

where, a_0 is the lattice constant, and h , k , and l are the Miller indices of the plane. In rock-salt structures,³⁴ the operative slip system is $\{110\}\langle 110\rangle$ while $\{001\}\langle 110\rangle$ becomes active at high temperatures. According to equation 1.9, the opposite is expected. Amodeo *et al.*⁸⁶ mentions that in ionic crystals, an additional rule has to be taken into account regarding the impossibility of shearing planes that would bring the ions of the same charge closer together, e.g. the (111) plane in rock-salt structures. Amodeo *et al.* summarized the possible slip systems in MgO, as illustrated in Table 1.1. We use the VESTA⁸⁷ program to visualize an equilibrated MgO lattice in Figure 1.19. The $(\bar{1}10)$ slip plane is indicated in pink while the brown arrow represents the slip direction $[110]$. Focussing on a corner Mg ion in the pink plane, note that there is a possible shorter Burger's vector in $(\bar{1}10)$, i.e. the vector connecting Mg to the closest O ion in the same plane (along the cyan arrow

Index	Plane	\vec{b}	Index	Plane	\vec{b}
1	($\bar{1}10$)	$\frac{1}{2}[110]$	7	(001)	$\frac{1}{2}[110]$
2	(110)	$\frac{1}{2}[1\bar{1}0]$	8	(001)	$\frac{1}{2}[1\bar{1}0]$
3	(0 $\bar{1}1$)	$\frac{1}{2}[011]$	9	(100)	$\frac{1}{2}[011]$
4	(011)	$\frac{1}{2}[01\bar{1}]$	10	(100)	$\frac{1}{2}[01\bar{1}]$
5	($\bar{1}01$)	$\frac{1}{2}[101]$	11	(010)	$\frac{1}{2}[101]$
6	(101)	$\frac{1}{2}[10\bar{1}]$	12	(010)	$\frac{1}{2}[10\bar{1}]$

Table 1.1: List of the $1/2\langle 110 \rangle\{110\}$ and $1/2\langle 110 \rangle\{100\}$ slip systems in MgO. Adapted from reference.⁸⁶

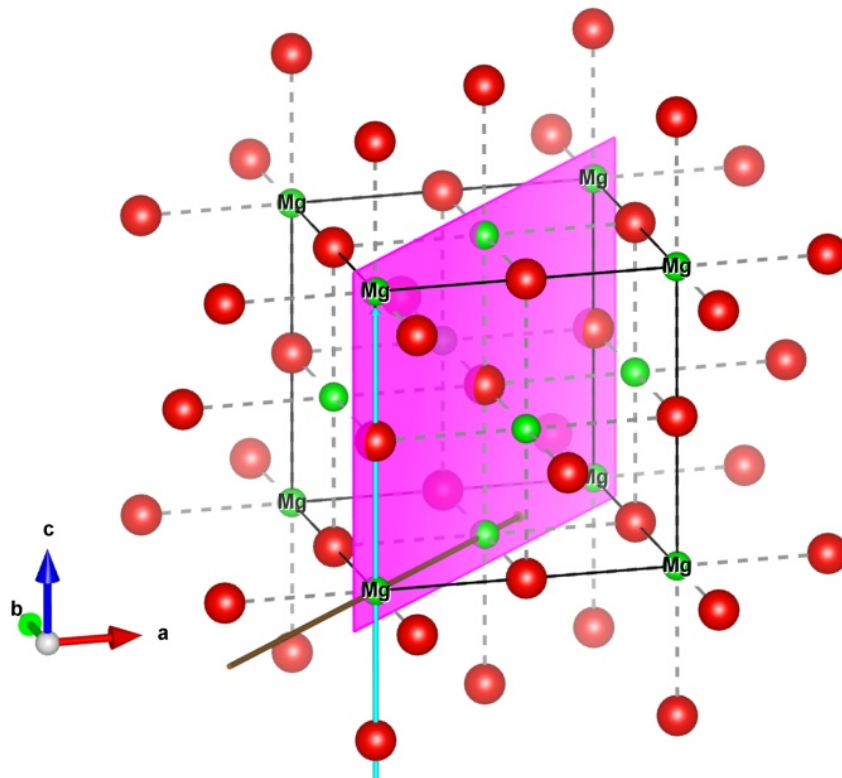


Figure 1.19: Visualization of the rock-salt structure of MgO. Index 1 slip system from Table 1.1 is visualized. The pink plane corresponds to the ($\bar{1}10$). The $[110]$ crystallographic direction is indicated by the brown arrow while the $[001]$ direction is indicated by the cyan one.

in Figure 1.19, i.e. the a lattice vector is shorter than the $[110]$). Yet, slip happens along the $[110]$ direction. Hirth and Lothe³⁴ suggest that the most consistent rationalization of such active slip systems in rock-salt structures derives from the numerical calculations of dislocation core energies by Huntington and Dickey.⁸⁸ Hirth and Lothe calculated that the core energy of an edge dislocation $\{001\}\langle 110 \rangle$ is 2.5 times higher than $\{110\}\langle 110 \rangle$ in NaCl. This may explain why slip does not happen in the $\langle 001 \rangle$ closest-packed direction but rather in the $\langle 110 \rangle$, which in turn shows that as we depart from metal crystals, the use of dislocation theory to predict the active slip systems

becomes less applicable.

Organic molecular crystals include in their composition functional groups and hydrogen bonds that can carry strong partial or full charges. Thus, it would appear to be even more complicated to treat via dislocation theory. In the following subsections, we visit slip deformation in organic molecular crystals.

1.6.3 Slip in Organic Molecular Crystals

Experimental methods such as micro and nanoindentation are frequently used to study the active slip systems in organic molecular crystals.⁶⁹ Kojima⁸⁹ reviewed growth and defects in molecular crystals, including a summary of the main slip systems determined experimentally for anthracene, naphthalene, p-terphenyl, stearic acid, and the PTS monomer. Focussing on anthracene (monoclinic lattice parameters as reported in:⁸⁹ $a=8.56 \text{ \AA}$, $b=6.04 \text{ \AA}$, $c=11.16 \text{ \AA}$, $\beta=124.4^\circ$), the main slip systems are the (001)[010] and (001)[110]. Kojima⁸⁹ reports that such active slip systems in anthracene (and the rest of the molecular crystals studied) are consistent with dislocation theory.³⁴

Gallagher *et al.*⁹⁰ performed micro-indentation experiments combined with etching pit and x-ray topography to analyze the active slip systems in cyclotrimethylene trinitramine (RDX) and pentaerythritol tetranitrate (PETN), finding that the active slip system in PETN is (110)[$\bar{1}\bar{1}$]. Gallagher *et al.* remarks that $\langle 111 \rangle$ is not the lowest possible Burger's vector, yet it is the active system. Therefore, the authors⁹⁰ assume that bond anisotropy, hydrogen bonding, or permanent dipole-dipole interactions are all additional factors to the close-packing conditions that influence the activation of slip in organic molecular crystals. They also propose and define steric hindrance effects that could arise from the lattice translations on a given plane containing irregularly-shaped molecules, leading to very high energies should atoms or functional groups overlap/collide.

Historically, there have been several controversies regarding the active slip systems in some molecular crystals. Kojima⁹¹ mentioned a discrepancy in the determination of slip systems of naphthalene between Kochendörfer⁹² and Gordon⁹³ which was resolved by Robinson and Scott.⁹⁴ Kochendörfer⁹² proposed that slip occurred in the [101](001) system and also in the (010) plane in an unknown direction. On the other hand, Gordon's⁹³ deformation experiments on naphthalene showed that only the [010](001) slip system is active. To solve this discrepancy, Robinson and Scott⁹⁴ performed tensile deformation tests by varying the orientation on three grades of naphthalene with different levels of purity. They discovered that high purity grades deformed along [110](001) and [010](001) systems while the commercial-grade deformed plastically only in the

[010](001) system.

Another controversy exists in the literature on the identification of the active slip systems in RDX.⁶⁹ Connick and May⁹⁵ used a compressive load combined with etch pits and x-ray analysis and determined that $\{001\}$ is the active slip plane. Gallagher *et al.*⁹⁰ used the microhardness indentation technique combined with etch pits and x-ray analysis to determine that in RDX (010), $\{021\}$ are the active slip planes. Ramos *et al.*,⁹⁶ using nanoindentation experiments combined with both the indenter's tip scan and AFM to characterize the topology of deformed RDX indents, found that three slip planes activate simultaneously, (010), $\{011\}$, and $\{021\}$ for indentations of specific crystallographic faces. These findings are striking in that if more than a single slip system activates upon nanoindentation, how is it possible to rank the slip systems?

The above-mentioned examples of complexities in the experimental determination of the active slip systems of organic molecular crystals necessitates a revisit of the theoretical modeling of such materials. Classical elasticity dislocation theory solutions of the strain field as provided in references^{34,72,73} do not consider the microstructure of the continuum; atoms are assumed as solid spheres and only the elasticity tensor determines the constitutive relations while molecular crystals can have conformational change, and dihedral and angular distortions. Po *et al.*⁹⁷ developed a non-singular theory of dislocations in anisotropic crystals as a version of Mindlin's anisotropic gradient elasticity theory. Their formulation invoked higher-order material tensors,⁹⁷ and their proposed solutions under a set of approximations, including centrosymmetry, relied on finding the higher-order material coefficients using computer algorithms employing force field potential models.⁹⁸ Po *et al.* found their solutions of the stress fields for HCP Mg and BCC Fe were much improved compared to the singular stress field solutions and much closer to the atomistic description of the dislocation core energy. In related research, Moosavian and Shodja⁹⁹ applied Mindlin-Eringen anisotropic micromorphic elasticity, another version of higher-order theories beyond classical elasticity by incorporating additional material constants (tensors) to the formalism and studied the phonon dispersion curves for centrosymmetric diamond and silicon. They calculated the higher-order material constants using density functional perturbation theory (DFPT). Their calculated phonon dispersion curves, using Mindlin-Eringen anisotropic micromorphic elasticity, were consistent with both experiments and those directly calculated using DFPT. We highlight that contributions in references^{97,99} are essential to progress and explore the applicability of higher-order elasticity theories to interpret experimental findings. Their use of computer software to calculate the higher-order material constants is remarkable given the algebraic formulations' complexity. Yet, the centrosym-

metric assumption implies a drastic reduction in the additional material constants to be found numerically, limiting the applicability to relatively simple structures such as diamond and Mg. Many organic molecular crystals are not centrosymmetric, where this assumption is invalid, but perhaps future developments may enable the prediction of intramolecular distortions of organic crystals and establish a correlation with slip and deformation.

Some simple first-order computational and hybrid methods are proposed in the literature to predict the active slip systems in organic molecular crystals. Wang and Sun¹⁰⁰ proposed that visual inspection of the crystal structure combined with attachment energy calculations should give the active slip systems in organic molecular crystals. They based their findings on three pharmaceutical compounds and their polymorphs. In a subsequent publication,¹⁰¹ they found that their earlier methodology needs further improvement to rank the active slip systems in anhydrous and dihydrate α -oxalic acid. Therefore, they added an extra ingredient to their predictive procedure, the 3D distribution of Young's modulus found via dispersion corrected DFT methods. It remains to be verified whether such a modified procedure can successfully predict the active slip systems in organic molecular crystals in general.

1.7 Twinning Deformation

Deformation twinning is ubiquitous in crystalline materials and has been observed in BCC, HCP, FCC metals and alloys, intermetallic compounds, elemental semiconductors and compounds, and in minerals such as calcite.¹⁰² Recent publications indicate that twinning deformation also contributes to the plasticity of organic molecular crystals.^{103–107} Deformation twinning is defined as the homogeneous shape deformation of a crystalline material resulting in part of the deformed crystal being oriented differently to the parent one;¹⁰⁸ this can manifest itself experimentally as part of the crystal becomes a mirror reflection of the parent part. Early crystallographic theories, such as that of Bilby and Crocker,¹⁰⁸ attempted to find twinning by geometrically constructing the homogeneous deformation mapping from an ideal structure to a twinned structure, and then calculating the shear strain required to achieve twinning. Crocker¹⁰⁹ proposed another crystallographic twinning theory to explain the double twinning phenomena. Indeed, Crocker¹⁰⁹ highlights two major assumptions in all such theories:

1. “The magnitude of the twinning shear of an operative mode should be small”.
2. “A large proportion of the points of the Bravais space lattice on which the structure is based

should shear directly to points of the twin lattice thus minimizing the extent of any atomic shuffling”.

The second assumption is surprising, given that plastic deformation events such as slip and twinning induce a sharp drop in the stress-strain diagram.¹¹⁰ Mahajan and Chin¹¹¹ highlighted that the mechanisms of twinning nucleation and growth are not yet fully understood, as one school of thought argues twins nucleate homogeneously in crystals while the other proposes that twinning nucleates from heterogeneities. Advocates of heterogeneous nucleation of twins near defects rely on dislocation reactions in terms of dissociation and combination¹⁰² or grain boundaries as sources.¹¹²

Twinning deformation in nanocrystalline FCC metals¹¹² occurs in $\{111\}\langle 112\rangle$ and has been extensively studied using both experiments and numerical simulations. Several twinning mechanisms have been identified such as overlapping stacking fault ribbons, and partial emission from grain boundaries. Such mechanisms involve Shockley partials.⁷⁷ In contrast to crystallographic theories of twinning, several models use energy calculations, mainly those computing the γ surface⁷⁸ in FCC metals. Generalized planar fault energy models (GPFE), first introduced by Tadmor and Hai¹¹³ to model the nucleation of a two-layer micro-twin near a crack tip, are commonly used to study deformation twinning aspects and mechanisms.

Perhaps an important matter in the twinning of FCC metals is its relationship to stacking fault energies and competition with slip deformation. Deformation twinning is affected by several factors¹¹² such as temperature, high strain rate (shock-loading), grain size, and particularly in FCC metals with high stacking fault energies, twinning deformation should not occur.^{56, 102, 112} Yet, deformation twinning has been observed in Al alloys under cryogenic shock-loading conditions,¹¹⁴ in nanocrystalline Al,¹¹⁵ Al single crystals¹¹⁶ quasi-statically deformed at an orientation where the twinning system receives the maximum stress, and shock-loaded specimens.¹¹⁷ The recently discovered new twinning route of Wang et al.¹¹⁸ provides alternative pathways to explain twinning in high-stacking fault energy FCC metals.

Theoretical treatment of twinning deformation in molecular crystals is under-developed. Takamizawa and Takasaki¹⁰⁴ report on the superelastic response of 3, 5-difluorobenzoic acid ($C_7H_4F_2O_2$) upon mechanical deformation. The authors applied load to a specific slip system and observed that the crystal deforms by twinning while it recovers its original dimensions upon releasing the load. Figure 1.20 shows some of their results, including snapshots of the deformation process and the force-displacement diagram of the jig (stress-strain diagram). The authors assume the source of such superelastic behaviour to be the molecular distortions at the twin interfaces. This twinning is

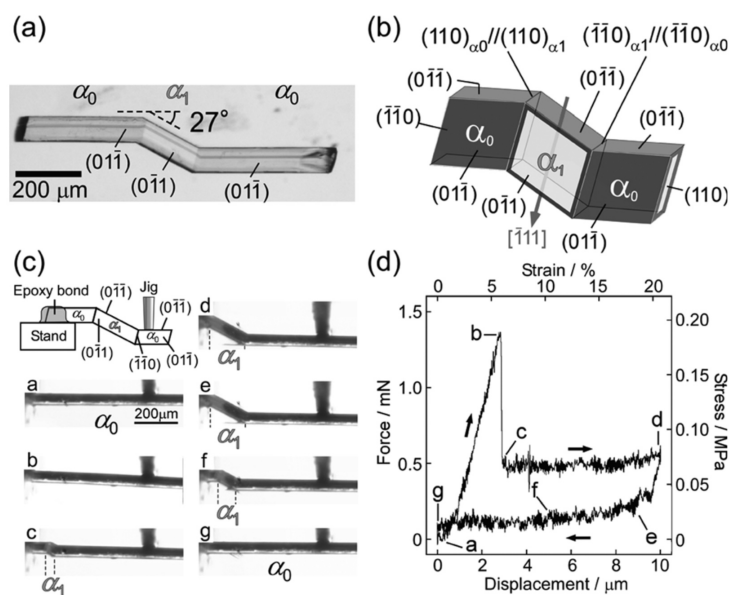


Figure 1.20: Illustrations of the (a) twinned crystal, (b) indices of the crystal faces, (c) snapshots of the bent crystal, the first figure describes the experimental settings, subsequent snapshots describe the sequence of events throughout the loading and unloading whose points are marked on the (d) stress-strain curve of loading and unloading the sample. Note that the process is reversible. Reprinted from reference,¹⁰⁴ with permission from John Wiley and Sons.

apparently related to the intramolecular distortion of molecules, which is related to the microstructure of the continuum. As mentioned earlier, higher order elasticity methods and micromorphic models have not yet matured to the state of describing this twinning phenomena. These experimental results push our understanding of plasticity to the limit, as it invokes the need for a theoretical understanding of such mechanisms in organic molecular crystals beyond conventional elasticity.

Because plasticity is relatively well developed for FCC metals, and since our proposed computational methods are expected to simulate such phenomena, the next few sections will deal with computational methods in the literature applied to study the deformation of FCC metals.

1.8 Generalized Stacking Fault Energy: Application to Plastic Deformation

The generalized stacking fault energy (GSFE) theory, also known as γ surface calculations, was first introduced by Vitek⁷⁸ in his quest to find stable stacking faults in FCC and BCC metals. Vitek's⁷⁸ computer simulations found stable stacking faults in FCC but not BCC metals. The 3-D γ surface of the (111) plane of Cu in Figure 1.16 shows that barriers to the deformation mechanisms can be readily extracted. Chapter 3 discusses GSFE/GPFE calculations applied to FCC metals to

calculate the barriers of the different deformation mechanisms. One strong assumption of GSFE simulations is that the rigid translation of two blocks past each other provides useful energetic quantities. Due to the simplicity of this assumption, an extensive body of publications exist in the literature utilizing GSFE calculations to study the deformation of FCC metals and other materials, as will be discussed below. For instance, computational techniques involving rigid/non-rigid blocks (the “supercell approach”) are being effectively used to calculate the stacking fault energies of materials.^{119–122} Stacking fault energies can also be calculated using the Axial Interaction Model (AIM).¹²³ Still, unlike the supercell approach, AIM does not provide information on the barriers along deformation paths. The Nudged Elastic Band method and its variants have been used to calculate the GSFE curves of FCC metals, and have been shown¹²⁴ to provide consistent quantitative and qualitative results with those obtained via the supercell approach.

GSFE barriers and energy minima (stacking faults or twinning faults) find applications in various deformation-related models. Here, we focus on a few related examples: prediction of the active deformation mechanism, GSFE-based theories of plasticity in FCC metals, and hybrid dislocations models to predict critical stresses.

1.8.1 Active Deformation Mechanism Predictions

Shearing of rigid blocks past each other while calculating lattice energies based on an atomistic potential (i.e. force field or high accuracy computational methods such as DFT) inspired several scientists to establish relationships between non-equilibrium (or meta-stable equilibria) lattice energies and material response.

Rice¹²⁵ studied the problem of dislocation nucleation near a crack tip by combining a Peierls¹²⁶ concept of periodic stress as a function of slip displacement and fracture mechanics. In his development, he identified a new solid-state parameter, the unstable stacking fault energy (γ_{us}), defined as the maximum energy per unit area resulting from the rigid-block shearing of one half of a crystal to the other along the Burger’s vector of a lattice dislocation. In other words, γ_{us} can be directly obtained from GSFE analysis, i.e. the peaks in Figure 1.16. Rice’s work showed that the resistance of dislocation nucleation near a crack-tip is directly proportional to γ_{us} . A few assumptions were needed: shear deformation is negligibly affected by normal stresses, and that γ_{us} and the stacking fault energy found based on the supercell shear approach are accurate.

Tadmor and Hai,¹¹³ following Rice’s criterion, investigated the onset of dislocation twinning at a crack tip. They based their models on the fracture mechanics concepts of stress intensity factors

combined with a proposed new material parameter, the unstable twinning energy γ_{ut} , defined as the maximum energy barrier for an intrinsic stacking fault to grow by one additional layer. γ_{ut} is similar to γ_{us} such that it can be calculated using the GPFE approach; see Chapter 3 for the calculation details. γ_{ut} represents the resistance of the lattice to the nucleation of a microtwin (two adjacent stacking faults). Tadmor and Hai¹¹³ defined the twinning tendency T ;

$$T = \lambda_{crit} \sqrt{\frac{\gamma_{us}}{\gamma_{ut}}} \quad (1.10)$$

such that, if $T > 1$, the model predicts dislocation twinning, and if $T < 1$, it indicates dislocation emissions where λ_{crit} is a parameter that describes the extra load necessary to nucleate a trailing partial relative to a leading partial. Building on their previous model, Tadmor and Bernstein¹²⁷ proposed a homogenization of equation 1.10 particularly for polycrystalline FCC metals, and obtained an approximate qualitative twinning tendency measure, τ_a , applicable at a temperature of 0 K and under quasi-static loading conditions:

$$\tau_a = \left[1.136 - 0.151 \frac{\gamma_{sf}}{\gamma_{us}} \right] \sqrt{\frac{\gamma_{us}}{\gamma_{ut}}} \quad (1.11)$$

Equation 1.11 shows that the twinning tendency in polycrystalline FCC metals is a function of three different GSFE energy quantities. Bernstein and Tadmor¹²⁸ used computational techniques to calculate GSFE energy quantities and applied equation 1.11 to rank the twinnability of eight FCC metals. Bernstein and Tadmor¹²⁸ wrote that several extensions of this twinnability criterion would be required, such as the inclusion of the effects of strain rate, finite temperature, and expansion to other crystal structures. Furthermore, the grain size effect¹¹² is not included in the twinnability criterion. In addition, the recent proposal of the experimentally observed new twinning route in FCC metals¹¹⁸ is at odds with the twinnability criterion, perhaps due to the involvement of grain boundaries as sources of partial dislocations. Also, given the rigid-block approximation to calculate γ_{ut} , it remains unknown so far whether fully relaxed simulations would yield higher or lower barriers than γ_{ut} .

Molecular dynamics (MD) simulations are powerful tools to simulate the dynamics of a system; we detail how molecular dynamics simulations work in Chapter 2. MD simulations permit the numerical exploration of a system exposed to external stimulus. For instance, Yamakov *et al.*¹²⁹ proposed a deformation mechanism map based on MD tensile deformation numerical experiments of a high- and a low-stacking fault energy nanocrystalline metal. They found that the high stacking fault energy metal for the same grain size was deformed by full dislocation propagation via dissociated partials (perfect dislocation slip), while the low stacking fault energy metal deformed

only via the propagation of partial dislocations (partial slip). The authors¹²⁹ extrapolated their results and proposed a dimensionless deformation map which depended mainly on the stacking fault energy of the FCC metal (γ_{sf}). For a fixed grain size, high values of γ_{sf} would promote perfect dislocation slip, while low values of γ_{sf} would promote partial slip. In addition, they mentioned the limitation of the MD deformation simulation approach in that the typical achievable strain rates are usually greater than 10^7 s^{-1} . A few months later, Swygenhoven *et al.* published an article¹³⁰ on the stacking fault energy and slip in nanocrystalline material, where they indicate the transition in deformation mechanism for Cu and Ni were in disagreement with the proposal of Yamakov *et al.*¹²⁹ Furthermore, they analyzed the switch in the dislocation mechanism between perfect dislocation and partial dislocation using the ratio of γ_{sf}/γ_{usf} and found that when this ratio approaches unity, full dislocation slip is observed in MD, and when it is much less than unity, partial dislocation slip is observed.

Warner *et al.*¹³¹ reported their results using a finite-temperature multi-scale atomistic-continuum approach to analyze the transition of the deformation mechanism between slip deformation and twinning near the crack tip of FCC metals. Supplemented with an analytic model based on fracture mechanics, they found that the transition in the deformation mechanism near a crack tip is rate dependent. One of the predictions is that cracks in aluminum are not expected to twin at room temperature except at very high strain rates. Yet, micro-twins and stacking faults have been detected in aluminum deformed at room temperature within the quasi-static limit.¹¹⁶ Furthermore, Yamakov and Glaessgen¹³² discussed the results of reference¹³¹ and suggested that a correlation does exist between the rate effects and the switch of the deformation mechanism near a crack tip, but is not definitive and requires further investigation.

1.8.2 GSFE-Based Extended Theories

There are attempts in the literature to understand the deformation of FCC metals by using modified versions of the conventional GSFE theory. Herein, we focus on three main proposals: the theory of plasticity in FCC metals,¹³³ the surface stacking fault energy approach,¹³⁴ and the model proposed by Osetsky and Bacon.¹³⁵

Jo *et al.*¹³³ constructed a deformation map of several FCC metals, which is based on the orientation of the applied stress to the twinning direction. In their development, they performed MD shear simulations on 2-D periodic systems of FCC metals containing $\approx 140,000$ atoms and two-line

defects as partial dislocation sources in the supercell. The simulations were performed at a temperature of 10 K and a strain rate $\approx 10^7 \text{ s}^{-1}$, though the authors statically relaxed the system after each step to remove the effect of strain rate. In each simulation, they varied the direction of shear between 0° and 60° to the $[11\bar{2}]$ direction in the (111) plane, and then they observed the deformation mechanism (slip, twinning, or stacking fault emission) as they measure its generalized planar fault energy (GPFE) curve. For stable FCC metals sheared at 0° , they always observe twinning deformation, at 60° , full slip. For angles between 0° and 60° , they observed the switch in the deformation mechanism (twinning versus slip), which happens at a different angle for each metal. To interpret their MD results, they geometrically transformed the intrinsic energy barriers obtained from GPFE to effective energy barriers. Their analysis culminated in the deformation map as shown in Fig-

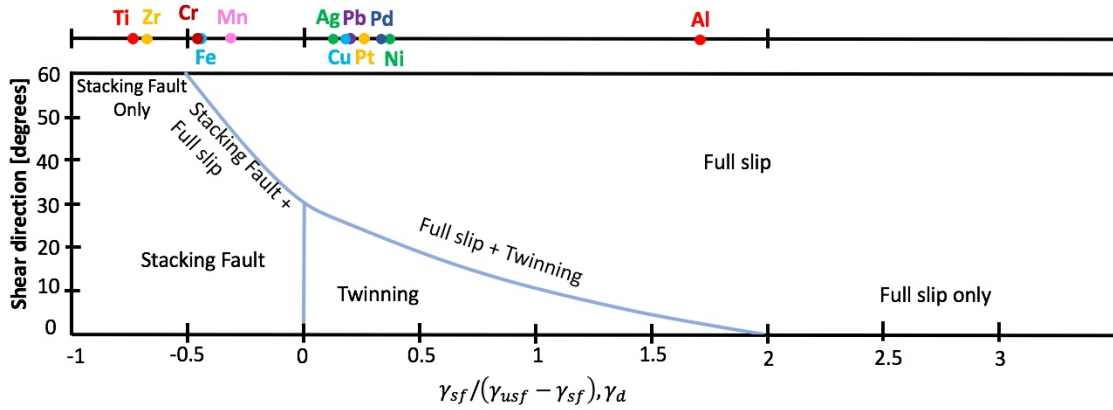


Figure 1.21: Normalized deformation mode map as a function of the shear angle and γ_d for a set of FCC metals drawn on the top axis of the figure. Adapted from reference.¹³³

ure 1.21 which shows that for some materials, there exists a tendency to activate more than a single deformation mechanism depending on the orientation of the shear stress to the twinning direction. As the authors suggest,¹³³ it is necessary to experimentally verify such a proposed theory of plasticity in FCC metals. There is also a scope for generalizing this theory to FCC alloys. It is not clear if such a theory is equally applicable to homogeneous defect-free material such as nanowires and whiskers. Finally, the inclusion of size-effects on the switch of deformation mechanism would be highly insightful.

Jiang *et al.*¹³⁴ proposed a surface stacking fault energy (SSFE) approach to predict the active deformation mechanism in surface-dominated structures as a function of the cross-section type and dimensions of nanowires. Instead of shearing the bulk, e.g. γ surface calculations, the nanowire is split into two blocks and sheared along the twinning (or slipping) direction to produce the surface stacking fault (SSF) energy curve. Figure 1.22 shows an example of the results obtained for a

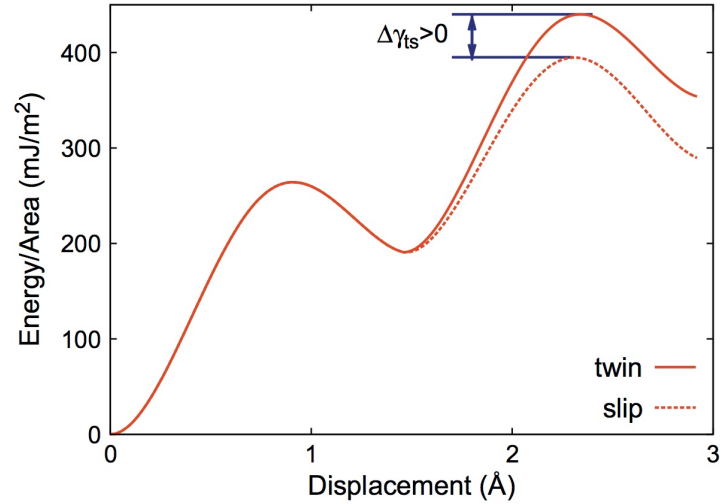


Figure 1.22: Surface-stacking fault energy curves obtained for a 40x4x4 unit cell Cu nanowire. The solid line is the curve produced to form a two-layer micro-twin, while the dashed line is for slip deformation. The gap in the barriers is represented by $\Delta\gamma_{ts}$, which is positive for this setup. Reprinted from reference,¹³⁴ with permission from Elsevier.

square Cu nanowire of length 40 lattice vectors. The SSFE criterion predicts that slip is the incipient deformation mechanism for this particular geometry. The authors¹³⁴ tested several other geometries and different dimensions of Cu nanowires. They verified their results by comparing their SSFE criterion to low temperature (0.1 K) high strain (10^9 s^{-1}) rate MD simulations. The results of Jiang *et al.*¹³⁴ highlight the importance of surface effects in the incipient plastic deformation of surface-dominated structures.

Osetsky and Bacon¹³⁵ proposed an extended method to GSFE based on rigid blocks; Figure 1.23 shows a schematic of the simulated geometry. The first step of the method is to divide the system into regions. Blocks B and F are rigid, while the atoms in block A are fully relaxed. Block A contains a dislocation and is neighbored by regions P, representing part of the image whose atoms interact with region A, e.g. through periodic boundary conditions in x and z . No periodic boundary condition applies in the y direction. Osetsky and Bacon propose two schemes to simulate the deformation in the system: the first is to apply a shear force to block B, and the second is to apply a rigid displacement of block B. Conjugate gradients were used to perform the energy minimization. We note that because the method proposed in reference¹³⁵ simulates dislocations, it requires a large supercell to obtain converged properties.

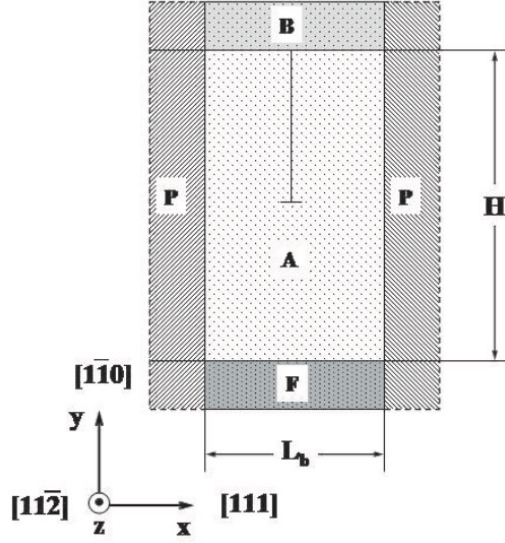


Figure 1.23: Geometry of the setup simulated by the method proposed in reference.¹³⁵ The setup is divided into several blocks: blocks P are the periodic images in the x - z planes, blocks B and F are rigid, block A contains an edge dislocation. H and L_b are the dimensions of block A. x , y , and z directions are aligned along $[111]$, $[1\bar{1}0]$, and $[11\bar{2}]$ directions in the BCC lattice. Republished with permission of IOP Publishing, Ltd, from reference,¹³⁵ permission conveyed through Copyright Clearance Center, Inc.

1.8.3 Hybrid-Dislocation Models

Hybrid-dislocation models^{136–139} employ a mix of dislocation theory description of a slip/twin with GSFE/GPFE energy quantities.

Kim *et al.*¹³⁶ performed quasi-static *in-situ* TEM tensile deformation experiments on a $\langle 110 \rangle$ oriented Al nanowire. The authors were able to continuously take TEM images of the wire during the deformation process and synchronously record the stress versus strain curve. As a result of tensile deformation, the Al nanowire deformed via twinning bands formed in a zig-zag pattern along $\{111\}$ planes. Kim *et al.* proposed the model below;

$$\sigma = \sigma_{mis} + \sigma_{el} = \frac{1}{m} \left[\frac{\gamma}{b_p} + \frac{Gb_p}{2\pi R} \left(\frac{(2-\nu)}{(1-\nu)} \right) \ln \frac{8\alpha R}{e^2 r_0} \right] \quad (1.12)$$

where σ is the applied normal stress, m is the Schmid factor, σ_{mis} is the misfit stress; the stress to generate and move a partial dislocation in the direction of the Burger's vector b_p , γ is the energy from the GSFE/GPFE curves, σ_{el} is the elastic strain due to the dislocation, whose parameters G , R , ν , e^2 , α , r_0 represent the elastic and geometric parameters of the dislocation, more details are found in reference.¹³⁶ Kim *et al.* used this model to generate stress curves along with the twinning and slipping pathways by substituting γ from GSFE and GPFE curves in addition to the Schmid factors m . They obtained a dislocation twinning stress less than dislocation slip in agreement with their experimental results.

Kibey *et al.*¹³⁷ proposed a more sophisticated hybrid-dislocation model to solve the long-standing unresolved issue of finding the critical twinning stress in FCC metals. According to the authors, their proposed theory is devoid of empiricism and solely based on analytic expressions. We mention below some of the general assumptions and features of their theory:¹³⁷

1. Twinning is initiated in FCC metals by pre-existing dislocation configurations.
2. The theory applies to bulk coarse-grained, not nanocrystalline, FCC metals, where twinning ensues in the proximity of pre-existing defects, not grain boundaries. Therefore, the theory addresses only the heterogeneous nucleation model of twinning, not homogeneous.
3. Although there may exist heterogeneous defects in the structure, the proposed theory uses energy values obtained from the GPFE curve, which is based on an ideal defect-free crystal structure.
4. An assumption is made that both edge and screw dislocation components are present and contribute to twinning deformation.

The derivation of the critical stress equation is lengthy and can be found in details in reference.¹³⁷ Herein, we briefly describe how the model is derived. The main governing equation is;

$$E_{total} = E_{edge} + E_{screw} - W_{\tau} + E_{GPFE} \quad (1.13)$$

where the total energy of the system E_{total} is divided into the energies of edge, E_{edge} , and screw, E_{screw} , dislocations, W_{τ} is the work done in displacing the twinning partials through width d , and E_{GPFE} is the energy contribution from the GPFE curve, which is further expressed as the difference between the energy required to nucleate a twin and the energy required to create an intrinsic stacking fault. Analytic expressions for the elasticity solutions of dislocations are readily available. However, analytic cosine functions having normalized displacement as arguments are proposed for γ_{sf} and γ_{twin} to add their contribution to the energy equation 1.13 via integration as a function of displacement. Once all the components of equation 1.13 are assembled, the total energy function is minimized with respect to the twinning width d and the number of twin layers N ($\frac{\partial E_{total}}{\partial d} = 0$, $\frac{\partial E_{total}}{\partial N} = 0$). Ultimately, the critical stress reads as:

$$\tau = \tau(\gamma_{isf}, \gamma_{tsf}, \gamma_{us}, \gamma_{ut}, G_{\{111\}}, N, d). \quad (1.14)$$

The full expression for 1.14 is found in reference.¹³⁷ Indeed, the analytic expression of stress in 1.14 is mainly a function of N and d , where N is known for FCC metals to be three.¹³⁷ Kibey *et al.*

obtained the twinning stress by numerically minimizing equation 1.14 with respect to d subject to the condition that ($d \geq b_{twin}$), obtaining critical twinning stresses that are comparable to four FCC metal experimental critical stresses. The Kibey *et al.* model is strongly based on GPFE and twinning width d , where GPFE energy quantities are obtained from the rigid-block approximation. The main success of their proposed model is the order of magnitude of the critical twinning stress being comparable to that of experiments.

Meanwhile, Huang *et al.*¹³⁸ have developed another hybrid-dislocation model to study the critical stress for twinning nucleation in medium and high entropy CrCoNi-based alloys. In summary, the authors adopt a total energy formalism similar to equation 1.13 with a few differences. They consider only edge dislocations to contribute to twinning deformation. Similarly to,¹³⁷ they describe the GSFE quantities with analytic harmonic functions whose arguments are the disregistry function (a function describing the relative displacement of the atoms near the cores of the three dislocations of a three-layer twin, see¹³⁸ for more details). In total, four parametric equations describe all GPFE contributions over four different displacement intervals, which is a major difference compared to the formalism in.¹³⁷ The critical twinning stress is obtained by differentiating the total energy function of the three-layer twin with respect to the position of the partial dislocation. By numerically evaluating the critical stress equation, the authors¹³⁸ found the critical twinning stress for CrCoNi alloy is very similar to experimental values.¹⁴⁰ Huang *et al.*¹³⁸ also applied Kibey *et al.*'s model and found that it underestimates the critical twinning stress of CrCoNi-based alloys. In a subsequent publication, Abuzaid and Patriarca¹⁴¹ performed tensile deformation experiments on polycrystalline and single-crystalline CoCrNi medium entropy alloy. They found that CoCrNi deformed by slip with a critical slip stress much lower than that found by Huang *et al.* Abuzaid and Patriarca¹⁴¹ also cites another publication¹⁴² where experimental investigation of the deformation of CoCrNi medium entropy alloy led to critical stresses less than those found by Huang *et al.*¹³⁸ and the other experimental group in.¹⁴⁰

1.9 Affine Shear Deformation Methods

Affine shear deformation methods constrain the system by fixing a strain component and then performing static energy minimizations under this constraint.

Perhaps one of the earliest versions dates back to 1970 when F. Milstein¹⁴³ proposed a method to calculate the theoretical strength of crystals by combining force fields, Born stability criteria, and

affine shear deformation. Axial load was applied to the system along one particular lattice vector while relaxing the strains along the other two, and progressively calculating the strain derivatives of energy necessary to evaluate the stability of the system, enabling the estimation of the theoretical strength and stability limits. Paxton *et al.*¹⁴⁴ used quantum mechanical calculations to find the ideal twinning stresses in some BCC and FCC metals. The strain was applied by transforming the lattice vector(s) to deform the system along the twinning direction. Energy profiles were then calculated for several points, and the slope of the energy as a function of strain yielded the stress. They found that relaxation had a negligible impact on the critical twinning stress, and their calculated twinning stresses were in agreement with the classical Frenkel model ($\sigma_{crit} \approx G/10$, G is the shear modulus).

The next major update to Paxton *et al.*'s work was proposed by Roundy *et al.*,¹⁴⁵ where the authors used pseudopotential density functional theory to shear an ideal crystal along the twinning direction. The major steps are:

1. Construction of the initial energy-minimum geometry of the atomistic system.
2. Application of a Cartesian deformation tensor (D_{ij}) to the lattice vectors to obtain the desired deformed state.
3. Use of a Newton-Raphson energy minimizer on the system subject to the constraint that the fixed component of strain cannot be relaxed, while the other five components must relax. This step constitutes the main advance over Paxton *et al.*'s procedure.
4. Repeat steps 2 and 3 as many times to generate sufficient energy points.
5. Find the stress versus strain profile using the energy derivatives and geometry.
6. The maximum value of the stress from stress-strain curves is the ideal stress of the material.

Roundy *et al.* fitted the energy profile to a cosine series to calculate the stress using energy derivatives. Reference¹⁴⁵ compared Cu and Al in relaxed and unrelaxed simulations and found that the relaxed simulations yielded about half the unrelaxed stress. Also, the authors in¹⁴⁵ mention that owing to the quasi-static calculations, simulations do miss phonon instabilities near the critical state and thus may overestimate the ideal shear stress.

Clatterbuck *et al.*¹⁴⁶ analyzed the phonon instability due to the application of affine shear deformation¹⁴⁵ to FCC Al. Their results, as shown in Figure 1.24, indicate that the phonon instability occurs before the maximum stress is reached. The twinning direction in FCC metals should be the

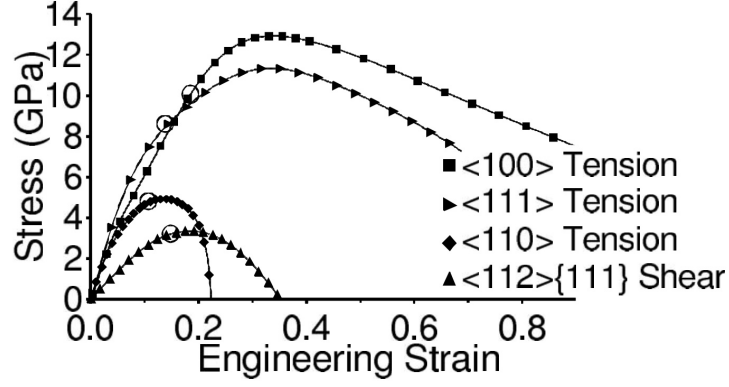


Figure 1.24: Stress-strain curves for FCC Al sheared using affine shear deformation method along different crystallographic directions and using different deformation modes. Open circles indicate the position of the phonon instability. Reprinted with permission from reference¹⁴⁶ by the American Physical Society.

easiest direction of deformation, as per discussions in previous sections. For the $\{111\}\langle 112\rangle$ shear in Figure 1.24, the position of the instability is very close to the maximum shear stress. There are other deformation directions, such as the $\langle 100\rangle$ tensile deformation, where the phonon instability occurs at a stress much less than the maximum stress (9.20 GPa compared to 12.92 GPa as calculated in¹⁴⁶). Clatterbuck *et al.* show that the ideal shear stresses obtained based on the maximum shear stress along the stress-strain curve, see Figure 1.24, not the phonon instability position, becomes an upper bound approximation which deteriorates as deformation is analyzed for systems other than the easiest slip one.

1.10 Differential Displacement Proposals

Vitek *et al.*¹⁴⁷ investigated the core of dislocations in BCC metals, where they construct a “displacement-map”¹⁴⁷ based on the difference between the vector connecting two atoms in the dislocated structure and the same vector connecting the same atoms in the ideal crystal. The differential displacement analysis method proposed by Sempere *et al.*¹⁴⁸ employed geometric elements such as the relative displacement across the slip interface to investigate dislocation properties in rare-gas crystals. Zimmerman *et al.*¹⁴⁹ proposed the slip vector metric to study the properties of slip, including crystallographic direction and slip magnitude, from the data obtained from MD simulations. The slip vector is defined according to to;¹⁴⁹

$$s^\alpha = -\frac{1}{n_s} \sum_{\beta \neq \alpha}^n (x^{\alpha\beta} - X^{\alpha\beta}) \quad (1.15)$$

where s^α is the slip vector of atom α , n is the number of nearest neighbors to atom α , n_s is the number of slipped neighbors, $x^{\alpha\beta}$ and $X^{\alpha\beta}$ are the vector differences of atoms α and β current and reference positions, respectively.

The above-mentioned models are successful and useful in providing quantitative details about the geometry of dislocation cores, associated elastic fields, and slip properties.

1.11 Literature Gaps

In the course of briefly reviewing the literature on the mechanical performance of crystalline materials, we have touched upon several topics and, highlighted the most critical outcomes relevant to this dissertation. Below, we summarize a few gaps in the literature that are addressed in this thesis.

Our review of the active deformation mechanism prediction (section 1.8.1) implies that a re-examination of the influence of full relaxation (including normal stress), as opposed to rigid block shearing- on γ_{us} and γ_{ut} , should provide new insights into the applicability of Rice's model and the twinnability criterion.¹¹³ Imposing constraints on the system might lead to physically unstable structures with imaginary phonons, which should not be the case under full relaxation. A possible development is sandwiching an extra block of atoms that is fully relaxed between the rigid blocks used in GSFE. We address this point in Chapter Four as we apply one of our proposed computational methods to FCC metals.

For both studies^{129, 130} to predict the transition in the deformation mechanism (section 1.8.1), MD simulations were performed on nanocrystalline metals. However, the structure of the grain boundaries were most probably different, which may justify some differences in the results. MD simulations are still far from the quasi-static limit of deforming an appreciable system size within reasonable time limits with the current computational capacity. The high strain rate^{112, 131} is also a key dynamic variable that would influence the deformation in the system. A quasi-static approach that can overcome both size and strain rate effects, would enable a broader insight into how different deformation mechanisms activate and interact.

Building on the brief review of section 1.8.3, there seems to be a discrepancy in both experimental and theoretical methods in predicting the active deformation mechanism and critical twinning stress in FCC metals and alloys. We believe that the emphasis on the GPFE quantities beyond a first-order approximation may not be accurate. A fully consistent theoretical approach should discern and break down all aspects of deformation mechanisms and their detailed geometric and

energetic treatment.

There have been significant contributions in the literature which use the proposed affine shear deformation method¹⁴⁵ or its variants (e.g. different energy minimizer, system size, etc.)^{150–157}

Some general common observations around such publications:

1. The stress and energy curves as a function of strain lack the sudden drop as a function of strain (known in the literature as “pop-in” events in the force versus displacement curve). Any computational method that accurately describes the true deformation path of a crystalline material should exhibit such drop in the stress and energy curves due to the nucleation of defects and dislocations,^{57, 110, 158} which does not preclude a computational method to predict the critical point just before the “pop-in” event by locating the phonon instability in the structure. Still, this task is generally ignored, presumably due to the higher computational resources required to achieve this step.
2. We cannot find any critical analysis of the variables convergence of affine shear deformation methods. The original implementation¹⁴⁵ used a single atom per unit cell and the Newton-Raphson energy minimizer to find ideal shear strengths. The following publications^{155–157} use different system sizes and even generalize some of the conclusions to dislocations movement and slip, without due consideration of the significance of the phonon instability, the influence of the system size on the results, and the impact of the energy minimizer. Even though some results in references^{155–157} show a sudden drop in stress as a function of strain, the results are not definitive because phonon frequency calculations are absent.
3. Because of the underdevelopment of the affine shear deformation methods, many questionable results are present in literature. For instance, Jahnátek *et al.*¹⁵⁵ claims that stacking fault energies and configurations can be measured in the stressed material configuration, which may be true for a single-layered system in periodic boundary conditions but is not correct for the many-layered systems, as stacking faults should emerge upon relaxation. Jahnátek *et al.* also argue that alias shear deformation methods (analogous to GSFE calculations with a single layer relaxed in 3D space) are better suited to describing a material’s deformation than affine shear deformation methods. We believe that regardless of the method used; the main physical phenomena must be reproducible in a single computational framework.
4. Although many implementations of affine shear deformation methods have been applied to the twinning direction in FCC metals; none has yet successfully simulated deformation twin-

ning. Probably, the general thought is that such simulations are not achievable using affine shear deformation methods, however, they almost certainly were not looking for twinning deformation since their objective was calculating ideal shear strengths. We think this has a strong relationship to the type of the energy minimizer and the size of the system coupled to the phonon instability and deformation path, as we will show in subsequent chapters of this thesis.

In this thesis, we will propose and apply two computational methods that can combine several deformation aspects such as ideal shear strength, stacking faults, partial dislocation, slip, and twinning deformation in ideal defect-free materials. We will show that the energy and configurational parameters converge as a function of the system size. We also explore the use of different energy minimizers. We can perform such a thorough analysis quickly because we use a force field approximation rather than the commonly used density-functional theory (DFT). Even though force fields can be quantitatively less accurate than DFT, the higher accuracy of the latter methods is lost when the system traverses an energy path that is not the minimum energy one.

Bibliography

- ¹ O. Gonzalez and A. M. Stuart, *A First Course in Continuum Mechanics*. Cambridge Texts in Applied Mathematics, Cambridge University Press, 2008.
- ² R. I. Borja, *Plasticity: Modeling and Computation*. Berlin, Heidelberg: Berlin, Heidelberg: Springer Berlin / Heidelberg, 2013.
- ³ A. Ma, F. Roters, and D. Raabe, “A dislocation density based constitutive model for crystal plasticity fem including geometrically necessary dislocations,” *Acta Materialia*, vol. 54, no. 8, pp. 2169–2179, 2006.
- ⁴ D. C. Rapaport, *The Art of Molecular Dynamics Simulation*. Cambridge University Press, 2 ed., 2004.
- ⁵ J. D. Gale and A. L. Rohl, “The general utility lattice program (gulp),” *Molecular Simulation*, vol. 29, no. 5, pp. 291–341, 2003.
- ⁶ A. McGaughey and M. Kaviany, “Phonon transport in molecular dynamics simulations: Formulation and thermal conductivity prediction,” vol. 39 of *Advances in Heat Transfer*, pp. 169–255, Elsevier, 2006.
- ⁷ E. Choi, E. Tan, L. L. Lavier, and V. M. Calo, “Dynearthsol2d: An efficient unstructured finite element method to study long-term tectonic deformation,” *Journal of Geophysical Research: Solid Earth*, vol. 118, no. 5, pp. 2429–2444, 2013.
- ⁸ A. Eringen, *Microcontinuum Field Theories: I. Foundations and Solids*. Springer New York, 2012.
- ⁹ G. Barbagallo, A. Madeo, M. V. d’Agostino, R. Abreu, I.-D. Ghiba, and P. Neff, “Transparent anisotropy for the relaxed micromorphic model: Macroscopic consistency conditions and long

- wave length asymptotics,” *International Journal of Solids and Structures*, vol. 120, pp. 7 – 30, 2017.
- ¹⁰ E. Petrova, *Innovation in the Pharmaceutical Industry: The Process of Drug Discovery and Development*, pp. 19–81. New York, NY: Springer New York, 2014.
- ¹¹ C. C. Sun, “Microstructure of tablet—pharmaceutical significance, assessment, and engineering,” *Pharmaceutical research*, vol. 34, no. 5, pp. 918–928, 2017.
- ¹² S. P. Chamarthy and R. Pinal, “The nature of crystal disorder in milled pharmaceutical materials,” *Colloids and Surfaces A: Physicochemical and Engineering Aspects*, vol. 331, no. 1, pp. 68 – 75, 2008. *Frontiers in Formulation Science (Formula V - 2007)*.
- ¹³ M. Descamps, J. Willart, E. Dudognon, and V. Caron, “Transformation of pharmaceutical compounds upon milling and comilling: The role of tg,” *Journal of Pharmaceutical Sciences*, vol. 96, no. 5, pp. 1398 – 1407, 2007.
- ¹⁴ M. Çelik, *Pharmaceutical powder compaction technology / [edited by] Metin Çelik*. New York: New York : Informa Healthcare, 2011.
- ¹⁵ S. W. Hoag, V. S. Dave, and V. Moolchandani, “Compression and compaction,” in *Pharmaceutical dosage forms-tablets*, pp. 571–646, CRC Press, 2008.
- ¹⁶ W. D. Callister, *Materials science and engineering : an introduction / William D. Callister, Jr.* Hoboken, NJ: Hoboken, NJ : John Wiley & Sons, 2007.
- ¹⁷ X. Cao, M. Morganti, B. C. Hancock, and V. M. Masterson, “Correlating particle hardness with powder compaction performance.,” *J Pharm Sci*, vol. 99, pp. 4307–4316, Oct 2010.
- ¹⁸ J. R. LUND and J. P. BYRNE, “Leonardo da vinci’s tensile strength tests: Implications for the discovery of engineering mechanics,” *Civil Engineering and Environmental Systems*, vol. 18, no. 3, pp. 243–250, 2001.
- ¹⁹ ASTM E8 / E8M-16ae1, “Standard test methods for tension testing of metallic materials,” standard, ASTM International, West Conshohocken, PA, 2016.
- ²⁰ K. Hashiguchi and S. O. service), *Elastoplasticity Theory / by Koichi Hashiguchi*. Berlin, Heidelberg: Berlin, Heidelberg : Springer Berlin Heidelberg, 2009.

- ²¹ T. Takeuchi, “Orientation dependence of work-hardening in iron single crystals,” *Japanese Journal of Applied Physics*, vol. 8, pp. 320–328, mar 1969.
- ²² P. Haasen, “Plastic deformation of nickel single crystals at low temperatures,” *The Philosophical Magazine: A Journal of Theoretical Experimental and Applied Physics*, vol. 3, no. 28, pp. 384–418, 1958.
- ²³ P. M. Robinson, “The work-hardening of anthracene single crystals,” *Acta metallurgica*, vol. 16, no. 4, pp. 545–551, 1968.
- ²⁴ E. Hall, *Yield Point Phenomena in Metals and Alloys*. Springer US, 2012.
- ²⁵ W. Han and B. D. Reddy, “Elastoplastic media,” in *Plasticity: Mathematical Theory and Numerical Analysis*, pp. 41–94, New York, NY: Springer New York, 2013.
- ²⁶ a. Vannucci, Paolo, *Anisotropic elasticity / Paolo Vannucci*. Singapore : Springer, 2018.
- ²⁷ D. B. Sirdeshmukh and K. G. Subhadra, “Consistency checks on elastic properties of crystals,” *Journal of Materials Science*, vol. 40, no. 7, pp. 1553–1570, 2005.
- ²⁸ W. Perger, J. Criswell, B. Civalieri, and R. Dovesi, “Ab-initio calculation of elastic constants of crystalline systems with the crystal code,” *Computer Physics Communications*, vol. 180, no. 10, pp. 1753 – 1759, 2009.
- ²⁹ R. Golesorkhtabar, P. Pavone, J. Spitaler, P. Puschnig, and C. Draxl, “Elastic: A tool for calculating second-order elastic constants from first principles,” *Computer Physics Communications*, vol. 184, no. 8, pp. 1861 – 1873, 2013.
- ³⁰ S. Smidstrup, T. Markussen, P. Vancraeyveld, J. Wellendorff, J. Schneider, T. Gunst, B. Verstichel, D. Stradi, P. A. Khomyakov, U. G. Vej-Hansen, M.-E. Lee, S. T. Chill, F. Rasmussen, G. Penazzi, F. Corsetti, A. Ojanperä, K. Jensen, M. L. N. Palsgaard, U. Martinez, A. Blom, M. Brandbyge, and K. Stokbro, “QuantumATK: an integrated platform of electronic and atomic-scale modelling tools,” *Journal of Physics: Condensed Matter*, vol. 32, p. 015901, oct 2019.
- ³¹ S. Plimpton, “Fast parallel algorithms for short-range molecular dynamics,” *Journal of Computational Physics*, vol. 117, no. 1, pp. 1 – 19, 1995.
- ³² L. M. Brown, “Constant intermittent flow of dislocations: central problems in plasticity,” *Materials Science and Technology*, vol. 28, no. 11, pp. 1209–1232, 2012.

- ³³ J. Lubliner, *Plasticity Theory*. Dover books on engineering, Dover Publications, 2008.
- ³⁴ J. P. Hirth and J. Lothe, *Theory of Dislocations (2nd ed.)*. New York: Wiley, 1982.
- ³⁵ ASTM E18-20, “Standard test methods for rockwell hardness of metallic materials,” standard, ASTM International, West Conshohocken, PA, 2020.
- ³⁶ ASTM E10-18, “Standard test method for brinell hardness of metallic materials,” standard, ASTM International, West Conshohocken, PA, 2018.
- ³⁷ ASTM E92-17, “Standard test methods for vickers hardness and knoop hardness of metallic materials,” standard, ASTM International, West Conshohocken, PA, 2017.
- ³⁸ ASTM E384-17, “Standard test method for microindentation hardness of materials,” standard, ASTM International, West Conshohocken, PA, 2017.
- ³⁹ E. Broitman, “Indentation hardness measurements at macro-, micro-, and nanoscale: A critical overview,” *Tribology Letters*, vol. 65, no. 1, p. 23, 2016.
- ⁴⁰ J. Ichikawa, K. Imagawa, and N. Kaneniwa, “The effect of crystal hardness on compaction propensity,” *Chem Pharm Bull (Tokyo)*, vol. 36, pp. 2699–2702, Jul 1988.
- ⁴¹ K. RIDGWAY, E. SHOTTON, and J. GLASBY, “The hardness and elastic modulus of some crystalline pharmaceutical materials,” *Journal of Pharmacy and Pharmacology*, vol. 21, no. S1, pp. 19S–23S, 1969.
- ⁴² V. M. Masterson and X. Cao, “Evaluating particle hardness of pharmaceutical solids using afm nanoindentation,” *International Journal of Pharmaceutics*, vol. 362, no. 1, pp. 163 – 171, 2008.
- ⁴³ W. Oliver and G. Pharr, “An improved technique for determining hardness and elastic modulus using load and displacement sensing indentation experiments,” *Journal of Materials Research*, vol. 7, no. 6, pp. 1564–1583, 1992.
- ⁴⁴ S. Mannepalli and K. Mangalampalli, “Indentation plasticity and fracture studies of organic crystals,” *Crystals (Basel)*, vol. 7, no. 11, p. 324, 2017.
- ⁴⁵ S. Finnie, K. V. R. Prasad, D. B. Sheen, and J. N. Sherwood, “Microhardness and dislocation identification studies on paracetamol single crystals,” *Pharmaceutical Research*, vol. 18, no. 5, pp. 674–681, 2001.

- ⁴⁶ M. S. R. N. Kiran, S. Varughese, C. M. Reddy, U. Ramamurty, and G. R. Desiraju, “Mechanical anisotropy in crystalline saccharin: Nanoindentation studies,” *Crystal Growth & Design*, vol. 10, pp. 4650–4655, 10 2010.
- ⁴⁷ R. J. Roberts, R. C. Rowe, and P. York, “The relationship between indentation hardness of organic solids and their molecular structure,” *Journal of Materials Science*, vol. 29, no. 9, pp. 2289–2296, 1994.
- ⁴⁸ C. C. Sun and Y.-H. Kiang, “On the identification of slip planes in organic crystals based on attachment energy calculation,” *J Pharm Sci*, vol. 97, pp. 3456–3461, Aug 2008.
- ⁴⁹ M. H. Shariare, F. J. J. Leusen, M. de Matas, P. York, and J. Anwar, “Prediction of the mechanical behaviour of crystalline solids,” *Pharmaceutical Research*, vol. 29, no. 1, pp. 319–331, 2012.
- ⁵⁰ W.-J. Sun, S. Kothari, and C. C. Sun, “The relationship among tensile strength, young’s modulus, and indentation hardness of pharmaceutical compacts,” *Powder Technology*, vol. 331, pp. 1 – 6, 2018.
- ⁵¹ C. Wang and C. C. Sun, “The landscape of mechanical properties of molecular crystals,” *CrystEngComm*, vol. 22, pp. 1149–1153, 2020.
- ⁵² Y. Tian, B. Xu, and Z. Zhao, “Microscopic theory of hardness and design of novel superhard crystals,” *International Journal of Refractory Metals and Hard Materials*, vol. 33, pp. 93 – 106, 2012.
- ⁵³ J. S. Tse, “Intrinsic hardness of crystalline solids,” *Journal of Superhard Materials*, vol. 32, no. 3, pp. 177–191, 2010.
- ⁵⁴ M. Ashby, “A first report on deformation-mechanism maps,” *Acta Metallurgica*, vol. 20, no. 7, pp. 887 – 897, 1972.
- ⁵⁵ H. J. Frost and M. F. Ashby, *Deformation-mechanism maps : the plasticity and creep of metals and ceramics / by H.J. Frost and M.F. Ashby*. Oxford Oxfordshire: Oxford Oxfordshire : Pergamon Press, 1982.
- ⁵⁶ M. Meyers, O. Vöhringer, and V. Lubarda, “The onset of twinning in metals: a constitutive description,” *Acta Materialia*, vol. 49, no. 19, pp. 4025 – 4039, 2001.

- ⁵⁷ C. L. Kelchner, S. J. Plimpton, and J. C. Hamilton, “Dislocation nucleation and defect structure during surface indentation,” *Phys. Rev. B*, vol. 58, pp. 11085–11088, Nov 1998.
- ⁵⁸ J. P. Hirth, “A brief history of dislocation theory,” *Metallurgical Transactions A*, vol. 16, no. 12, pp. 2085–2090, 1985.
- ⁵⁹ F. C. Frank, “The influence of dislocations on crystal growth,” *Discuss. Faraday Soc.*, vol. 5, pp. 48–54, 1949.
- ⁶⁰ P. B. Hirsch, R. W. Horne, and M. J. Whelan, “Direct observations of the arrangement and motion of dislocations in aluminium,” *Philosophical Magazine*, vol. 86, no. 29-31, pp. 4553–4572, 2006.
- ⁶¹ H. Matsui and H. Kimura, “Dislocation configurations and work hardening in molybdenum single crystals deformed in tension at 77 and 293 k,” *Transactions of the Japan Institute of Metals*, vol. 22, no. 7, pp. 481–492, 1981.
- ⁶² E. Clouet, D. Caillard, N. Chaari, F. Onimus, and D. Rodney, “Dislocation locking versus easy glide in titanium and zirconium,” *Nature Materials*, vol. 14, no. 9, pp. 931–936, 2015.
- ⁶³ A. S. Keh, “Dislocations in indented magnesium oxide crystals,” *Journal of Applied Physics*, vol. 31, no. 9, pp. 1538–1545, 1960.
- ⁶⁴ A. Danilewsky, J. Wittge, A. Croell, D. Allen, P. McNally, P. Vagovič, T. dos Santos Rolo, Z. Li, T. Baumbach, E. Gorostegui-Colinas, J. Garagorri, M. Elizalde, M. Fossati, D. Bowen, and B. Tanner, “Dislocation dynamics and slip band formation in silicon: In-situ study by x-ray diffraction imaging,” *Journal of Crystal Growth*, vol. 318, no. 1, pp. 1157 – 1163, 2011. The 16th International Conference on Crystal Growth (ICCG16)/The 14th International Conference on Vapor Growth and Epitaxy (ICVGE14).
- ⁶⁵ P. J. Halfpenny, K. J. Roberts, and J. N. Sherwood, “Dislocations in energetic materials,” *Journal of Materials Science*, vol. 19, no. 5, pp. 1629–1637, 1984.
- ⁶⁶ A. Nie, Y. Bu, J. Huang, Y. Shao, Y. Zhang, W. Hu, J. Liu, Y. Wang, B. Xu, Z. Liu, H. Wang, W. Yang, and Y. Tian, “Direct observation of room-temperature dislocation plasticity in diamond,” *Matter*, vol. 2, no. 5, pp. 1222 – 1232, 2020.

- ⁶⁷ D. Hull and D. Bacon, “Chapter 3 - movement of dislocations,” in *Introduction to Dislocations (Fifth Edition)* (D. Hull and D. Bacon, eds.), pp. 43 – 62, Oxford: Butterworth-Heinemann, fifth edition ed., 2011.
- ⁶⁸ D. Hull and D. Bacon, “Chapter 8 - origin and multiplication of dislocations,” in *Introduction to Dislocations (Fifth Edition)* (D. Hull and D. Bacon, eds.), pp. 157 – 169, Oxford: Butterworth-Heinemann, fifth edition ed., 2011.
- ⁶⁹ I. A. Olson, A. G. Shtukenberg, B. Kahr, and M. D. Ward, “Dislocations in molecular crystals,” *Reports on Progress in Physics*, vol. 81, p. 096501, jul 2018.
- ⁷⁰ M. H. Sadd, “Chapter 7- airy stress function,” in *Elasticity - Theory, Applications, and Numerics (2nd Edition)*, Elsevier, 2009.
- ⁷¹ D. M. Barnett and L. A. Swager, “The elastic energy of a straight dislocation in an infinite anisotropic elastic medium,” *physica status solidi (b)*, vol. 48, no. 1, pp. 419–428, 1971.
- ⁷² D. Hull and D. Bacon, “Chapter 4 - elastic properties of dislocations,” in *Introduction to Dislocations (Fifth Edition)* (D. Hull and D. Bacon, eds.), pp. 63 – 83, Oxford: Butterworth-Heinemann, fifth edition ed., 2011.
- ⁷³ G. Lu, *The Peierls-Nabarro Model of Dislocations: A Venerable Theory and its Current Development*, pp. 793–811. Dordrecht: Springer Netherlands, 2005.
- ⁷⁴ A. M. Walker, J. D. Gale, B. Slater, and K. Wright, “Atomic scale modelling of the cores of dislocations in complex materials part 1: methodology,” *Phys. Chem. Chem. Phys.*, vol. 7, pp. 3227–3234, 2005.
- ⁷⁵ Y. Gotoh, “Slip patterns of copper whiskers subjected to tensile deformation,” *physica status solidi (a)*, vol. 24, no. 1, pp. 305–313, 1974.
- ⁷⁶ W. Xia, G. Dehm, and S. Brinckmann, “Unraveling indentation-induced slip steps in austenitic stainless steel,” *Materials & Design*, vol. 183, p. 108169, 2019.
- ⁷⁷ D. Hull and D. Bacon, “Chapter 5 - dislocations in face-centered cubic metals,” in *Introduction to Dislocations (Fifth Edition)* (D. Hull and D. Bacon, eds.), pp. 85 – 107, Oxford: Butterworth-Heinemann, fifth edition ed., 2011.

- ⁷⁸ V. Vitek, “Intrinsic stacking faults in body-centred cubic crystals,” *The Philosophical Magazine: A Journal of Theoretical Experimental and Applied Physics*, vol. 18, no. 154, pp. 773–786, 1968.
- ⁷⁹ N. Mott, “Mechanical properties of metals,” *Physica*, vol. 15, no. 1, pp. 119 – 134, 1949.
- ⁸⁰ C. R. Weinberger and W. Cai, “Plasticity of metal nanowires,” *J. Mater. Chem.*, vol. 22, pp. 3277–3292, 2012.
- ⁸¹ A. Cao and E. Ma, “Sample shape and temperature strongly influence the yield strength of metallic nanopillars,” *Acta Materialia*, vol. 56, no. 17, pp. 4816 – 4828, 2008.
- ⁸² S. Xu, Y. Guo, and A. Ngan, “A molecular dynamics study on the orientation, size, and dislocation confinement effects on the plastic deformation of al nanopillars,” *International Journal of Plasticity*, vol. 43, pp. 116 – 127, 2013.
- ⁸³ A. A. Urusovskaya, “Electric effects associated with plastic deformation of ionic crystals,” *Soviet Physics Uspekhi*, vol. 11, pp. 631–643, may 1969.
- ⁸⁴ Z. Gyulai and D. Hartly, “Elektrische leitfähigkeit verformter steinsalzkristalle,” *Zeitschrift für Physik*, vol. 51, no. 5, pp. 378–387, 1928.
- ⁸⁵ A. W. Stepanow, “Über den mechanismus der plastischen deformation,” *Zeitschrift für Physik*, vol. 81, no. 7, pp. 560–564, 1933.
- ⁸⁶ J. Amodeo, S. Merkel, C. Tromas, P. Carrez, S. Korte-Kerzel, P. Cordier, and J. Chevalier, “Dislocations and plastic deformation in mgo crystals: A review,” *Crystals (Basel)*, vol. 8, no. 6, pp. 240–53, 2018.
- ⁸⁷ K. Momma and F. Izumi, “VESTA: a three-dimensional visualization system for electronic and structural analysis,” *Journal of Applied Crystallography*, vol. 41, pp. 653–658, Jun 2008.
- ⁸⁸ H. B. Huntington, J. E. Dickey, and R. Thomson, “Dislocation energies in nacl,” *Phys. Rev.*, vol. 100, pp. 1117–1128, Nov 1955.
- ⁸⁹ K. Kojima, “Crystal growth and defect control in organic crystals,” *Progress in Crystal Growth and Characterization of Materials*, vol. 23, pp. 369 – 420, 1992.
- ⁹⁰ H. G. Gallagher, P. J. Halfpenny, J. C. Miller, J. N. Sherwood, J. E. Field, and P. Gray, “Dislocation slip systems in pentaerythritol tetranitrate (petn) and cyclotrimethylene trinitramine (rdx),”

- Philosophical Transactions of the Royal Society of London. Series A: Physical and Engineering Sciences*, vol. 339, no. 1654, pp. 293–303, 1992.
- ⁹¹ K. Kojima, “Slip systems in deformed anthracene crystals,” *physica status solidi (a)*, vol. 51, no. 1, pp. 71–78, 1979.
- ⁹² A. Kochendörfer, “Zur dynamik der plastischen verformung: Untersuchungen an naphthalinkristallen,” *Zeitschrift für Kristallographie - Crystalline Materials*, vol. 97, no. 1, pp. 263 – 299, 01 Dec 1937.
- ⁹³ R. Gordon, “Plastic flow of naphthalene,” *Acta Metallurgica*, vol. 13, no. 3, pp. 199 – 203, 1965.
- ⁹⁴ P. M. Robinson and H. G. Scott, “The effect of impurities on the deformation behaviour of naphthalene,” *Acta metallurgica*, vol. 15, no. 7, pp. 1230–1231, 1967.
- ⁹⁵ W. Connick and F. May, “Dislocation etching of cyclotrimethylene trinitramine crystals,” *Journal of Crystal Growth*, vol. 5, no. 1, pp. 65 – 69, 1969.
- ⁹⁶ K. J. Ramos, D. E. Hooks, and D. F. Bahr, “Direct observation of plasticity and quantitative hardness measurements in single crystal cyclotrimethylene trinitramine by nanoindentation,” *Philosophical Magazine*, vol. 89, no. 27, pp. 2381–2402, 2009.
- ⁹⁷ G. Po, M. Lazar, N. C. Admal, and N. Ghoniem, “A non-singular theory of dislocations in anisotropic crystals,” *International Journal of Plasticity*, vol. 103, pp. 1 – 22, 2018.
- ⁹⁸ N. C. Admal, J. Marian, and G. Po, “The atomistic representation of first strain-gradient elastic tensors,” *Journal of the Mechanics and Physics of Solids*, vol. 99, pp. 93 – 115, 2017.
- ⁹⁹ H. Moosavian and H. M. Shodja, “Mindlin–eringen anisotropic micromorphic elasticity and lattice dynamics representation,” *Philosophical Magazine*, vol. 100, no. 2, pp. 157–193, 2020.
- ¹⁰⁰ C. Wang and C. C. Sun, “Identifying slip planes in organic polymorphs by combined energy framework calculations and topology analysis,” *Crystal Growth & Design*, vol. 18, pp. 1909–1916, 03 2018.
- ¹⁰¹ C. Wang and C. C. Sun, “Computational techniques for predicting mechanical properties of organic crystals: A systematic evaluation,” *Molecular Pharmaceutics*, vol. 16, pp. 1732–1741, 04 2019.

- ¹⁰² J. Christian and S. Mahajan, “Deformation twinning,” *Progress in Materials Science*, vol. 39, no. 1, pp. 1 – 157, 1995.
- ¹⁰³ R. Bandyopadhyay and D. J. W. Grant, “Plasticity and slip system of plate-shaped crystals of l-lysine monohydrochloride dihydrate,” *Pharmaceutical Research*, vol. 19, no. 4, pp. 491–496, 2002.
- ¹⁰⁴ S. Takamizawa and Y. Takasaki, “Superelastic shape recovery of mechanically twinned 3,5-difluorobenzoic acid crystals,” *Angewandte Chemie International Edition*, vol. 54, no. 16, pp. 4815–4817, 2015.
- ¹⁰⁵ E. R. Engel, Y. Takasaki, S. H. Mir, and S. Takamizawa, “Twinning ferroelasticity facilitated by the partial flipping of phenyl rings in single crystals of 4,4'-dicarboxydiphenyl ether,” *Royal Society Open Science*, vol. 5, no. 1, p. 171146, 2018.
- ¹⁰⁶ E. R. Engel and S. Takamizawa, “Versatile ferroelastic deformability in an organic single crystal by twinning about a molecular zone axis,” *Angewandte Chemie International Edition*, vol. 57, no. 37, pp. 11888–11892, 2018.
- ¹⁰⁷ S. H. Mir, Y. Takasaki, E. R. Engel, and S. Takamizawa, “Enhancement of dissipated energy by large bending of an organic single crystal undergoing twinning deformation,” *RSC Adv.*, vol. 8, pp. 21933–21936, 2018.
- ¹⁰⁸ B. A. Bilby and A. G. Crocker, “The theory of the crystallography of deformation twinning,” *Proceedings of the Royal Society of London. Series A, Mathematical and Physical Sciences*, vol. 288, pp. 240–255, 2021/01/21/ 1965.
- ¹⁰⁹ A. G. Crocker, “Double twinning,” *The Philosophical Magazine: A Journal of Theoretical Experimental and Applied Physics*, vol. 7, no. 83, pp. 1901–1924, 1962.
- ¹¹⁰ A. Gouldstone, H.-J. Koh, K.-Y. Zeng, A. Giannakopoulos, and S. Suresh, “Discrete and continuous deformation during nanoindentation of thin films,” *Acta Materialia*, vol. 48, no. 9, pp. 2277 – 2295, 2000.
- ¹¹¹ S. Mahajan and G. Chin, “Formation of deformation twins in f.c.c. crystals,” *Acta Metallurgica*, vol. 21, no. 10, pp. 1353 – 1363, 1973.

- ¹¹² Y. Zhu, X. Liao, and X. Wu, “Deformation twinning in nanocrystalline materials,” *Progress in Materials Science*, vol. 57, no. 1, pp. 1 – 62, 2012.
- ¹¹³ E. Tadmor and S. Hai, “A peierls criterion for the onset of deformation twinning at a crack tip,” *Journal of the Mechanics and Physics of Solids*, vol. 51, no. 5, pp. 765 – 793, 2003.
- ¹¹⁴ G. Gray, “Deformation twinning in al-4.8 wt% mg,” *Acta Metallurgica*, vol. 36, no. 7, pp. 1745 – 1754, 1988.
- ¹¹⁵ M. Chen, E. Ma, K. J. Hemker, H. Sheng, Y. Wang, and X. Cheng, “Deformation twinning in nanocrystalline aluminum,” *Science (American Association for the Advancement of Science)*, vol. 300, no. 5623, pp. 1275–1277, 2003.
- ¹¹⁶ W. Z. Han, G. M. Cheng, S. X. Li, S. D. Wu, and Z. F. Zhang, “Deformation induced microtwins and stacking faults in aluminum single crystal,” *Phys. Rev. Lett.*, vol. 101, p. 115505, Sep 2008.
- ¹¹⁷ F. Zhao, L. Wang, D. Fan, B. X. Bie, X. M. Zhou, T. Suo, Y. L. Li, M. W. Chen, C. L. Liu, M. L. Qi, M. H. Zhu, and S. N. Luo, “Macrodeformation twins in single-crystal aluminum,” *Phys. Rev. Lett.*, vol. 116, p. 075501, Feb 2016.
- ¹¹⁸ L. Wang, P. Guan, J. Teng, P. Liu, D. Chen, W. Xie, D. Kong, S. Zhang, T. Zhu, Z. Zhang, E. Ma, M. Chen, and X. Han, “New twinning route in face-centered cubic nanocrystalline metals,” *Nature Communications*, vol. 8, 12 2017.
- ¹¹⁹ S. Kibey, J. B. Liu, D. D. Johnson, and H. Sehitoglu, “Generalized planar fault energies and twinning in cu–al alloys,” *Applied Physics Letters*, vol. 89, no. 19, p. 191911, 2006.
- ¹²⁰ X.-M. Wei, J.-M. Zhang, and K.-W. Xu, “Generalized stacking fault energy in fcc metals with meam,” *Applied Surface Science*, vol. 254, no. 5, pp. 1489 – 1492, 2007.
- ¹²¹ X.-Z. Wu, R. Wang, S.-F. Wang, and Q.-Y. Wei, “Ab initio calculations of generalized-stacking-fault energy surfaces and surface energies for fcc metals,” *Applied Surface Science*, vol. 256, no. 21, pp. 6345 – 6349, 2010.
- ¹²² S. Ogata, J. Li, and S. Yip, “Energy landscape of deformation twinning in bcc and fcc metals,” *Phys. Rev. B*, vol. 71, p. 224102, Jun 2005.

- ¹²³ R. Li, S. Lu, D. Kim, S. Schönecker, J. Zhao, S. K. Kwon, and L. Vitos, “Stacking fault energy of face-centered cubic metals: thermodynamic and ab initio approaches,” *Journal of Physics: Condensed Matter*, vol. 28, p. 395001, aug 2016.
- ¹²⁴ P. Tu, Y. Zheng, C. Zhuang, X. Zeng, and H. Zhu, “A high-throughput computation framework for generalized stacking fault energies of pure metals,” *Computational Materials Science*, vol. 159, pp. 357–364, 2019.
- ¹²⁵ J. R. Rice, “Dislocation nucleation from a crack tip: An analysis based on the peierls concept,” *Journal of the Mechanics and Physics of Solids*, vol. 40, no. 2, pp. 239 – 271, 1992.
- ¹²⁶ R. Peierls, “The size of a dislocation,” *Proceedings of the Physical Society*, vol. 52, pp. 34–37, jan 1940.
- ¹²⁷ E. Tadmor and N. Bernstein, “A first-principles measure for the twinnability of fcc metals,” *Journal of the Mechanics and Physics of Solids*, vol. 52, no. 11, pp. 2507 – 2519, 2004.
- ¹²⁸ N. Bernstein and E. B. Tadmor, “Tight-binding calculations of stacking energies and twinnability in fcc metals,” *Phys. Rev. B*, vol. 69, p. 094116, Mar 2004.
- ¹²⁹ V. Yamakov, D. Wolf, S. R. Phillpot, A. K. Mukherjee, and H. Gleiter, “Deformation-mechanism map for nanocrystalline metals by molecular-dynamics simulation,” *Nature Materials*, vol. 3, no. 1, pp. 43–47, 2004.
- ¹³⁰ H. Van Swygenhoven, P. M. Derlet, and A. G. Frøseth, “Stacking fault energies and slip in nanocrystalline metals,” *Nature Materials*, vol. 3, no. 6, pp. 399–403, 2004.
- ¹³¹ D. H. Warner, W. A. Curtin, and S. Qu, “Rate dependence of crack-tip processes predicts twinning trends in f.c.c. metals,” *Nature Materials*, vol. 6, no. 11, pp. 876–881, 2007.
- ¹³² V. I. Yamakov and E. H. Glaessgen, “To twin or not to twin,” *Nature Materials*, vol. 6, no. 11, pp. 795–796, 2007.
- ¹³³ M. Jo, Y. M. Koo, B.-J. Lee, B. Johansson, L. Vitos, and S. K. Kwon, “Theory for plasticity of face-centered cubic metals,” *Proceedings of the National Academy of Sciences*, vol. 111, no. 18, pp. 6560–6565, 2014.

- ¹³⁴ J.-W. Jiang, A. M. Leach, K. Gall, H. S. Park, and T. Rabczuk, “A surface stacking fault energy approach to predicting defect nucleation in surface-dominated nanostructures,” *Journal of the Mechanics and Physics of Solids*, vol. 61, no. 9, pp. 1915 – 1934, 2013.
- ¹³⁵ Y. N. Osetsky and D. J. Bacon, “An atomic-level model for studying the dynamics of edge dislocations in metals,” *Modelling and Simulation in Materials Science and Engineering*, vol. 11, pp. 427–446, may 2003.
- ¹³⁶ S.-H. Kim, H.-K. Kim, J.-H. Seo, D.-M. Whang, J.-P. Ahn, and J.-C. Lee, “Deformation twinning of ultrahigh strength aluminum nanowire,” *Acta Materialia*, vol. 160, pp. 14–21, 2018.
- ¹³⁷ S. Kibey, J. Liu, D. Johnson, and H. Sehitoglu, “Predicting twinning stress in fcc metals: Linking twin-energy pathways to twin nucleation,” *Acta Materialia*, vol. 55, no. 20, pp. 6843 – 6851, 2007.
- ¹³⁸ H. Huang, X. Li, Z. Dong, W. Li, S. Huang, D. Meng, X. Lai, T. Liu, S. Zhu, and L. Vitos, “Critical stress for twinning nucleation in crconi-based medium and high entropy alloys,” *Acta Materialia*, vol. 149, pp. 388 – 396, 2018.
- ¹³⁹ P. Chowdhury and H. Sehitoglu, “Atomistic energetics and critical twinning stress prediction in face and body centered cubic metals: Recent progress,” *Journal of engineering materials and technology*, vol. 140, no. 2, 2018.
- ¹⁴⁰ G. Laplanche, A. Kostka, C. Reinhart, J. Hunfeld, G. Eggeler, and E. George, “Reasons for the superior mechanical properties of medium-entropy crconi compared to high-entropy crmnfeconi,” *Acta Materialia*, vol. 128, pp. 292–303, 2017.
- ¹⁴¹ W. Abuzaid and L. Patriarca, “A study on slip activation for a coarse-grained and single crystalline cocrni medium entropy alloy,” *Intermetallics*, vol. 117, p. 106682, 2020.
- ¹⁴² B. Uzer, S. Picak, J. Liu, T. Jozaghi, D. Canadinc, I. Karaman, Y. Chumlyakov, and I. Kireeva, “On the mechanical response and microstructure evolution of nicocr single crystalline medium entropy alloys,” *Materials Research Letters*, vol. 6, no. 8, pp. 442–449, 2018.
- ¹⁴³ F. Milstein, “Theoretical strength of a perfect crystal,” *Phys. Rev. B*, vol. 3, pp. 1130–1141, Feb 1971.

- ¹⁴⁴ A. T. Paxton, P. Gumbsch, and M. Methfessel, “A quantum mechanical calculation of the theoretical strength of metals,” *Philosophical Magazine Letters*, vol. 63, no. 5, pp. 267–274, 1991.
- ¹⁴⁵ D. Roundy, C. R. Krenn, M. L. Cohen, and J. W. Morris, “Ideal shear strengths of fcc aluminum and copper,” *Phys. Rev. Lett.*, vol. 82, pp. 2713–2716, Mar 1999.
- ¹⁴⁶ D. M. Clatterbuck, C. R. Krenn, M. L. Cohen, and J. W. Morris, “Phonon instabilities and the ideal strength of aluminum,” *Phys. Rev. Lett.*, vol. 91, p. 135501, Sep 2003.
- ¹⁴⁷ V. Vitek, R. C. Perrin, and D. K. Bowen, “The core structure of $\frac{1}{2}(111)$ screw dislocations in b.c.c. crystals,” *The Philosophical Magazine: A Journal of Theoretical Experimental and Applied Physics*, vol. 21, no. 173, pp. 1049–1073, 1970.
- ¹⁴⁸ S. Sempere, A. Serra, J. Boronat, and C. Cazorla, “Dislocation structure and mobility in hcp rare-gas solids: Quantum versus classical,” *Crystals*, vol. 8, no. 2, 2018.
- ¹⁴⁹ J. A. Zimmerman, C. L. Kelchner, P. A. Klein, J. C. Hamilton, and S. M. Foiles, “Surface step effects on nanoindentation,” *Phys. Rev. Lett.*, vol. 87, p. 165507, Oct 2001.
- ¹⁵⁰ S. Ogata, J. Li, and S. Yip, “Ideal pure shear strength of aluminum and copper,” *Science*, vol. 298, no. 5594, pp. 807–811, 2002.
- ¹⁵¹ S. Ogata, J. Li, N. Hirotsuki, Y. Shibutani, and S. Yip, “Ideal shear strain of metals and ceramics,” *Phys. Rev. B*, vol. 70, p. 104104, Sep 2004.
- ¹⁵² D. Roundy, C. R. Krenn, M. L. Cohen, and J. W. M. Jr., “The ideal strength of tungsten,” *Philosophical Magazine A*, vol. 81, no. 7, pp. 1725–1747, 2001.
- ¹⁵³ W. Luo, D. Roundy, M. L. Cohen, and J. W. Morris, “Ideal strength of bcc molybdenum and niobium,” *Phys. Rev. B*, vol. 66, p. 094110, Sep 2002.
- ¹⁵⁴ X. Li, S. Schönecker, W. Li, L. K. Varga, D. L. Irving, and L. Vitos, “Tensile and shear loading of four fcc high-entropy alloys: A first-principles study,” *Phys. Rev. B*, vol. 97, p. 094102, Mar 2018.
- ¹⁵⁵ M. Jahnátek, J. Hafner, and M. Krajčí, “Shear deformation, ideal strength, and stacking fault formation of fcc metals: A density-functional study of al and cu,” *Phys. Rev. B*, vol. 79, p. 224103, Jun 2009.

- ¹⁵⁶ S.-L. Shang, J. Shimanek, S. Qin, Y. Wang, A. M. Beese, and Z.-K. Liu, “Unveiling dislocation characteristics in Ni₃Al from stacking fault energy and ideal strength: A first-principles study via pure alias shear deformation,” *Phys. Rev. B*, vol. 101, p. 024102, Jan 2020.
- ¹⁵⁷ G. Li, Q. An, U. Aydemir, S. I. Morozov, B. Duan, P. Zhai, Q. Zhang, and W. A. Goddard, “Intrinsic mechanical behavior of mgagsb thermoelectric material: An ab initio study,” *Journal of Materiomics*, vol. 6, no. 1, pp. 24–32, 2020.
- ¹⁵⁸ J. Li, K. J. Van Vliet, T. Zhu, S. Yip, and S. Suresh, “Atomistic mechanisms governing elastic limit and incipient plasticity in crystals,” *Nature*, vol. 418, no. 6895, pp. 307–310, 2002.

Every reasonable effort has been made to acknowledge the owners of copyright material. I would be pleased to hear from any copyright owner who has been omitted or incorrectly acknowledged.

Chapter 2

Methods

2.1 Introduction

This thesis explores the development and application of two quasi-static computational methods to study the deformation and mechanical performance of ideal defect-free materials. There are several topics that need to be visited before presenting the proposed methods. First, force fields are introduced, which are a set of mathematical functions that calculate the potential energy of material as a function of coordinates. Having defined how force fields work, a few examples of force fields for metals, MgO, O₂, and anthracene are given as these materials are simulated in this thesis. We have seen in Chapter 1 that GSFE and affine shear deformation methods strongly depend on energy minimization. Furthermore, constrained energy minimization is an essential factor in our proposed methods. Therefore, a section is dedicated to energy minimization techniques and algorithms. Then molecular dynamics simulations in terms of the working principles is introduced as this technique is used to further study some of the minima found in this work. Finally, the two proposed computational methods are described, which have been coded into the General Utility Lattice Program (GULP)¹ by Professor Julian Gale.

2.2 Introduction to Force Fields

The previous chapter discussed investigations of deformation at two different scales. Continuum mechanics always requires material coefficients (elasticity tensor, thermal conductivity, fluid viscosity, specific heat) to either analytically or numerically compute the response of a material to external stimulus. However, this does not account explicitly for the atomistic nature of the sys-

tems.

As the name implies, a force field is a set of mathematical functions from which atomistic forces are derived in the form of a field that depends on atomic coordinates. The simplest force field assumes that all interactions in a system can be expressed as a sum of two-body interactions;

$$V = \sum_{i=1}^N \sum_{j>i}^N V(r_{ij}) \quad (2.1)$$

where V is the total potential energy in a system of N atoms, and r_{ij} is the position vector between atoms i and j , and $V(r_{ij})$ is the functional form. Equation 2.1 has the units of energy (e.g. eV, kJ/mol). By finding the negative derivative of equation 2.1 with respect to position vectors r_{ij} , the forces on each atom can be calculated;

$$\vec{F} = - \sum_{j=1}^N \frac{\partial V}{\partial r_j} \hat{r}_j \quad (2.2)$$

Once the functional form is known, how are the parameters for these functions determined?

There are two main approaches:¹

1. The potential energy hypersurface (of $3N$ dimensions, where N is the number of atoms in the system) is calculated using a high-accuracy quantum mechanics method followed by the fitting of this surface to a set of mathematical functions to reproduce the result.
2. An inverted approach where the force field parameters are varied by trial-and-error until one or more experimental properties of the material are reproduced.

Determination of the mathematical functions of a force field depends strongly on the type of material. In general, atomic interactions are divided² into bonded and non-bonded interactions. Non-bonded interactions are those that act on the atom through a field i.e. such interactions are the strongest around an atom within a specific spherical cut-off, and are divided into van der Waals and Coulombic interactions. Van der Waals interactions³ play a critical role in the binding of molecular and rare-gas crystals and are divided into attractive and repulsive contributions. Mathematically, they can be modeled in several forms, such as the Lennard-Jones (LJ) potential;^{4,5}

$$V_i = 4\varepsilon \left[\left(\frac{\sigma}{r_{ij}} \right)^{12} - \left(\frac{\sigma}{r_{ij}} \right)^6 \right] \quad (2.3)$$

where ε and σ are material-specific constants.

Coulombic interactions describe forces arising from the interaction of charged species. They are

often stronger than van der Waals interactions and are characterized by the longest range of all possible interactions. They are readily calculated according to Coulomb's law.⁴

On the other hand, bonded interactions are those corresponding to covalently-bonded atoms. Consider the sketch in Figure 2.1 showing two atoms covalently bonded together. It is possible to

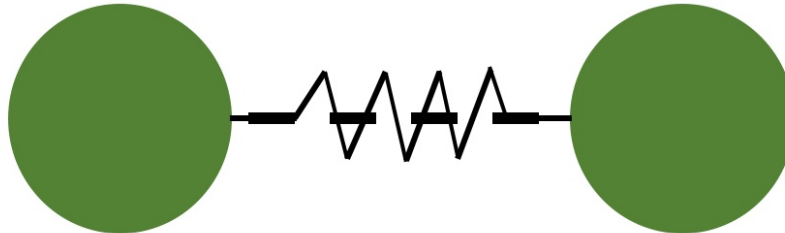


Figure 2.1: Schematic showing two covalently bonded atoms - dashed line represents the bond. The analogous stiffness of the bond is modeled by a harmonic spring.

model the covalent bond between the two atoms by a spring.² In reality, there are no springs between atoms, but within the limit of the harmonic approximation, interactions between atoms resemble oscillations about an equilibrium position;

$$U = \frac{1}{2}k(r - b)^2 \quad (2.4)$$

where U is the potential energy of the atoms in Figure 2.1, k is the stiffness, r and b are the displacement and the equilibrium bond length, respectively.

There are a variety of bonded interactions dependent on the number of atoms bonded together and the shape of the geometry, such as harmonic angle potential, dihedrals, etc. The reader is referred to the GULP documentation¹ for a comprehensive list of common and uncommon force field formalisms.

While it is possible to derive a specific force field for every material, very often the task is challenging and time consuming. To this end, there is a huge number of force fields in the literature, as can be verified by visiting the OpenKIM project (<https://openkim.org>), which aims to provide a repository of tested force fields, transferable across several simulation software. Some force fields are designed for categories of material such as the Modified Embedded Atom Method Second Nearest Neighbor (MEAM-2NN)⁶ for metals, General Amber Force Field (GAFF)⁷ for organic molecular crystals, Chemistry at Harvard Molecular Mechanics (CHARMM36)⁸ for folded and intrinsically disordered proteins, etc.

2.3 Force Field Examples

The previous section discussed the force field concept from a high level without recourse to the details. Hence this section gives examples of force field models to describe the interactions in metals, MgO, O₂, and anthracene.

2.3.1 Force Fields for Metals

The classical picture of metallic bonds can be described through the Drude theory of metals⁹ as positive ions immersed in a sea of electrons, implying that valence electrons are not bound to their atoms but are rather free to move in the material. The presence of this sea of electrons implies there should be a special treatment in modeling metal force fields. The simplest mathematical form of a metallic force field is a two-body Lennard-Jones potential, e.g. see reference.¹⁰ However, two-body potentials are unable to reproduce the Cauchy violation in the elastic constants ($C_{11} \neq C_{14}$).¹¹ To resolve this shortcoming, many-body interactions are needed leading to the advent of several many-body potentials.¹¹⁻¹³ For instance, Daw *et al.*¹⁴ developed the many-body (originating from inclusion of a density term in the lattice energy) embedded atom method (EAM) permitting the simulation of defects and surfaces in Ni and Pd metals more accurately than with two-body potentials. The basic EAM equation is:¹⁴

$$E_{tot} = \sum_i F_i(\rho_{h,i}) + \frac{1}{2} \sum_{\substack{i,j \\ i \neq j}} \phi_{ij}(R_{ij}) \quad (2.5)$$

where E_{tot} is the total energy, F_i is the embedding energy as a function of $\rho_{h,i}$, the total host electron density at atom i , ϕ_{ij} is the short-range pairwise potential, and R_{ij} is the distance between atoms i and j . Equation 2.5 shows that in addition to the two-body terms ϕ_{ij} , many-body terms contribute to the energy via the F_i functional of the density. Later, Baskes¹⁵ expanded the original EAM into a modified embedded-atom method first-nearest-neighbor (MEAM-1NN). The inclusion of a directional term in the formalism (i.e. an expansion of the many-body term in equation 2.5 by adding terms proportional to the cosines, cosines squared and cosines cubed of the angles, see reference¹⁵) led to elastic constants calculations and stacking fault energies consistent with experiment. Lee *et al.*⁶ highlighted some shortcomings in MEAM-1NN, for instance, the finite temperature instability of some FCC metals, and thus developed the modified embedded atom method second-nearest neighbor (MEAM-2NN). Therefore, we use the MEAM-2NN⁶ force field to model the interactions in FCC Ag, Al, Ni, Pd, Pt, Pb and Cu, and the modified version by Ryu *et al.*¹⁶ to model FCC Au

interactions.

2.3.2 Force Field Models for MgO

There are several force fields to model the interactions in ionic crystals. The simplest of these is the rigid ion model where the van der Waals and electrostatic interactions (via fixed-charges) determine the energy of the crystal. Namjoshi *et al.*¹⁷ proposed a rigid ion model yielding phonon dispersion curves of NaCl in agreement with experiments. Yet, Verma¹⁸ highlighted that rigid ion models lack the capability to simulate electronic polarization, and thus would fail to reproduce many important crystal properties. Dick and Overhauser¹⁹ developed the theory of dielectric constants for alkali halide crystals and proposed the shell model as a means to model electronic polarization in ionic crystals. Their theoretical treatment was unable to explain some experimental results regarding the compressibility,¹⁹ but was the basis for the development of further complicated models such as the breathing shell model by Schröder.²⁰

MgO adopts a rock-salt structure and is characterized¹ by a Cauchy violation such that elastic constant $C_{12} \neq C_{44}$. To accurately model this violation, we need a force field that has a many-body interaction term and thus we use the breathing shell model (BSM) for MgO developed by Rohl and Gale.¹

Mg is modeled using a core only and has a positive elementary charge of 2.0. O is modeled using

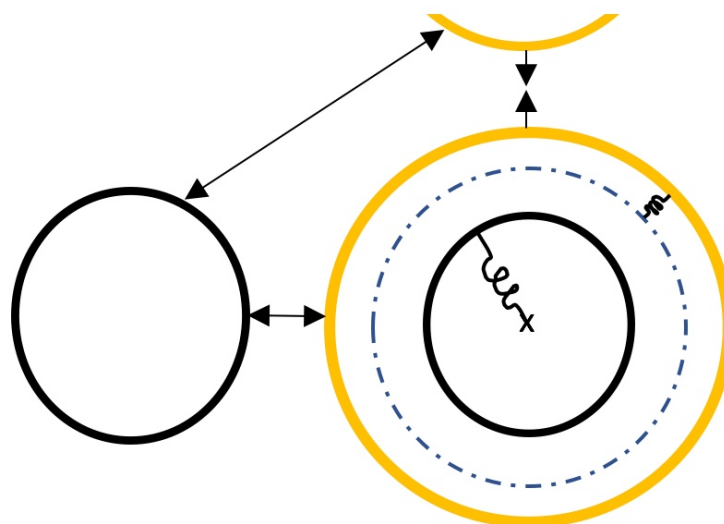


Figure 2.2: The breathing shell model interactions in MgO. Solid black circles represent Mg (left) and O cores (right). There are no shells for Mg. The solid orange circle represents the O breathing shell, the dashed blue circle is the reference radius for the O breathing shell, outward arrows represent repulsive interactions, inward arrows represent attractive interactions, spring symbols represent harmonic potentials connecting two entities.

a core (+0.8 charge) and a shell (-2.8 charge), as shown in Figure 2.2. Attractive and repulsive

interactions are modeled via a Buckingham potential;¹

$$V = Ae^{-\frac{r}{\rho}} - \frac{C}{r^6} \quad (2.6)$$

where V is the potential energy, A , C , and ρ , are parameters, r is the distance between interacting atoms. All the charges in the system interact with each other via Coulomb's law. The Buckingham potentials only interact between Mg cores and O breathing shells and the O breathing shells themselves. The O core interacts harmonically with the center of the ion, while the O breathing shell interacts harmonically with a reference radial distance as indicated in Figure 2.6; the O breathing shell can increase/decrease its radius. The O core interacts with Mg core and O breathing shell only via Coulomb interactions. By taking into account the possibility of the change in the radius of the O breathing shell, O possesses polarizability. This complexity of many-body interactions can potentially lead to macroscopic polarization in the system and thus allows for the computation¹ of the Cauchy violation in the elastic constants of MgO and hence is better force field than rigid-ion or shell models for this system.

2.3.3 Force Field for O₂

Kobashi *et al.*²¹ reviewed several O₂ force fields and compared their results to experiment. Here, we use the one devised by Cheung²² as it is simple and reproduces some experimental properties of β -oxygen. Cheung's force field²¹ consists of a Lennard-Jones potential (see equation 2.3) and a harmonic bond (see equation 2.4).

There are few publications on the solid state material properties of low-pressure β oxygen. The below table compiles the list of our calculated parameters versus those found in literature. We note

Properties	Our calculation	Literature Data	Reference
Lattice parameter a_0 (Å)	3.333	3.272	21
Lattice parameter C_0 (Å)	10.771	11.277	21
Low frequency (cm^{-1})	46.46	51	23
High frequency (cm^{-1})	1552.5	1552.5	23
E_{static} (kJ/mol)	-9.3510	-8.7864	21
Density (kg/cm^3)	1.538	1.495	24

Table 2.1: List of $\beta - O_2$ properties obtained from our calculations, versus the corresponding data from literature.

that there is a reasonable agreement between our calculated properties of β oxygen and those found

in literature. The lattice parameters correspond to the hexagonal representations of the (111) plane of a rhombohedral cell (space group $R\bar{3}m$), as shown in Figure 1 (b) reference.²¹ The calculated lattice static energy ($E_{static} = -9.3510 \text{ kJ/mol}$) is lower than the same calculated in reference²¹ using Cheung's model, presumably because of the large potential cut-off radius of 20 Å used here.

2.3.4 General Amber Force Field For Anthracene

At ambient conditions, anthracene crystallizes in a monoclinic unit cell (space group P21/a) with two molecules per unit cell.²⁵ We have used the GAFF⁷ to model the interactions in anthracene. The maximum cut-off in GAFF force field is set to 10 Å. To find the partial charges of the carbon and hydrogen atoms in anthracene, A/Prof. Paolo Raiteri used Gaussian²⁶ employing the HF/6-311G(1d,1p) method to find the ESP derived charges and provided the output file (private communication). The charges for anthracene are summarized in Figure 2.3. Table 2.2 shows that the calculated lattice parameters following optimization with the present force field are in good agreement with those reported from experiment.²⁵

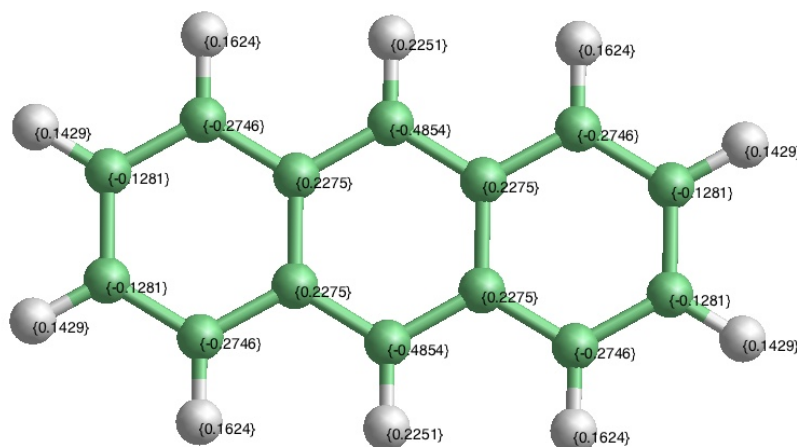


Figure 2.3: View of a single anthracene molecule with all the partial charges (a.u.) indicated for carbon (green) and hydrogen (white) atoms.

Lattice Parameters	a (Å)	b (Å)	c (Å)	α °	β °	γ °
GAFF	8.257	5.929	10.914	90.00	124.48	90.00
Exp. ²⁵	8.561	6.036	11.163	90.00	124.42	90.00

Table 2.2: Comparison of the lattice parameters calculated using the General Amber Force Field (GAFF) and from experiment.

2.4 Energy Minimization Techniques

The main objective is to find stationary point(s) on the potential energy hyper-surface. That is, a multi-variable quadratic function is a minimum (or a maximum) when the gradients (opposite sign of forces) along all the degrees of freedom are zero. If the Hessian is positive-definite, then the stationary point is a minimum. The minimization problem can be formulated algebraically¹ by performing a second order Taylor series expansion of the internal energy as a function of coordinates and truncating the expansion beyond the second-order term;

$$U(x + \delta x) \approx U(x) + \frac{\partial U}{\partial x} \delta x + \frac{1}{2} \frac{\partial^2 U}{\partial x^2} \delta x^2 \quad (2.7)$$

where U is the internal energy, x represents the coordinates and δx is the differential displacement. Equation 2.7 can further be manipulated to get the below general form:

$$\Delta x = -\alpha H^{-1} g \quad (2.8)$$

where Δx is a $3N + 6$ displacement and strain vector in a 3D periodic system, α is a scalar coefficient, H^{-1} is a $(3N + 6)$ by $(3N + 6)$ energy second derivatives inverse matrix, and g is the $3N + 6$ gradient vector (first derivative of energy), N represents the number of atoms in the system and the $+6$ denote the strain degrees of freedom.

Optimization algorithms can be divided into first-order and second-order methods. For instance, steepest descent (SD) and conjugate gradient (CJ)²⁷ are first-order methods that search for stationary points using information based on the gradients. The following general form applies for SD:

$$x_{k+1} = x_k + \alpha_k g_k \quad (2.9)$$

where x_{k+1} and x_k are the new and old coordinate vectors, respectively, α_k is a scaling coefficient, and g_k is the gradient vector.

Second-order expansion methods, such as Newton-Raphson (NR) and the Rational Function Optimizer (RFO),²⁸ seek to solve equation 2.8 by utilizing both the gradients and the Hessian, are thus more efficient in terms of the number of cycles than first-order methods but at the expense of higher computational cost.¹ In atomistic simulations, the internal energy (potential) is defined as a function of coordinates. Therefore, depending on the complexity of the potential function, it is possible to calculate the Hessian and the gradient analytically, increasing the accuracy and speed of the calculation. To understand the main differences between NR and RFO in solving equation

2.8, it is necessary to elaborate on the Hessian in more detail and to show its significance. Consider the generic Hessian matrix given below having $N + 6$ by $N + 6$ dimensions;²⁹

$$H = \begin{bmatrix} \frac{\partial^2 U}{\partial r_{1x}^2} & \cdots & \frac{\partial^2 U}{\partial r_{1x} \partial r_{Nz}} & \frac{\partial^2 U}{\partial r_{1x} \partial \varepsilon_1} & \cdots & \frac{\partial^2 U}{\partial r_{1x} \partial \varepsilon_6} \\ \vdots & \ddots & \vdots & \vdots & \ddots & \vdots \\ \frac{\partial^2 U}{\partial r_{Nz} \partial r_{1x}} & \cdots & \frac{\partial^2 U}{\partial r_{Nz}^2} & \frac{\partial^2 U}{\partial r_{Nz} \partial \varepsilon_1} & \cdots & \frac{\partial^2 U}{\partial r_{Nz} \partial \varepsilon_6} \\ \frac{\partial^2 U}{\partial \varepsilon_1 \partial r_{1x}} & \cdots & \frac{\partial^2 U}{\partial \varepsilon_1 \partial r_{Nz}} & \frac{\partial^2 U}{\partial \varepsilon_1^2} & \cdots & \frac{\partial^2 U}{\partial \varepsilon_1 \partial \varepsilon_6} \\ \vdots & \ddots & \vdots & \vdots & \ddots & \vdots \\ \frac{\partial^2 U}{\partial \varepsilon_6 \partial r_{1x}} & \cdots & \frac{\partial^2 U}{\partial \varepsilon_6 \partial r_{Nz}} & \frac{\partial^2 U}{\partial \varepsilon_6 \partial \varepsilon_1} & \cdots & \frac{\partial^2 U}{\partial \varepsilon_6^2} \end{bmatrix} \quad (2.10)$$

where r is the vector connecting two atoms, subscript in r denotes the index of the atom with x , y , and z being the Cartesian components, ε_i is the Voigt strain tensor where i takes indices 1, 2, ..., 6, corresponding to Cartesian components xx , yy , zz , yz , xz , and xy , respectively. There are several observations regarding the Hessian in 2.10:

1. The Hessian is composed of four quadrants, the first being the second derivative of energy with respect to Cartesian coordinates, the second and third quadrants are the mixed derivatives of energy with respect to strain and Cartesian coordinates, and the fourth contains the second derivatives of energy with respect to strain. Upon the proper manipulation, quadrant one can be used to find the phonons and the whole matrix to find the elastic constants of the material in general.
2. Owing to the symmetry of the potential such that the potential energy between atoms, e.g. one and three, and the energy between atoms three and one are equivalent, the Hessian is symmetric.
3. The Hessian at equilibrium has to be positive-definite, i.e. the curvature of the potential energy hypersurface is positive.
4. Since the Hessian is symmetric and positive-definite, then there exists a spectral decomposition yielding the eigenvalues and eigenvectors of the Hessian. This implies that numerical operations on the Hessian can be transformed into a different frame of reference using its normal coordinates decomposition.

We note that although the inverse Hessian appears explicitly in equation 2.8, there is no need for its exact calculation at every step. There are many algorithms in literature, such as the Broyden-Fletcher-Goldfarb-Shanno (BFGS),³⁰ that are able to numerically calculate the Hessian and its inverse, increasing the computational speed without resort to the exact analytical solution.

The NR procedure explicitly solves equation 2.8 to find the coordinates of the energy-minimum configuration. On the other hand, RFO drives the system toward having a required number of positive eigenvalues. If this number is correct but the structure is not at a minimum, then RFO pushes the system along the eigenvector of the lowest eigenvalue of the Hessian iteratively until an energy minimum is located. If the number of positive eigenvalues is incorrect, then RFO keeps driving the system along the eigenvector of the negative/zero eigenvalue of the Hessian iteratively until the correct number is achieved and the energy minimum is located. Therefore, RFO is superior to the NR algorithm especially in calculations involving transition states.

This thesis, and publications in literature, use quasi-static computational methods to simulate the deformation in crystalline systems. Physically, constraints such as rigid blocks or homogeneous shear deformation are enforced in the system by manipulating equation 2.8. Some degrees of freedom can be fixed and thus are excluded from the minimization procedure in order to calculate the metastable constrained energy minima of shear deformation. This allows for the exploration of the potential energy hypersurface and the system response to external excitations.

2.5 Introduction to Molecular Dynamics

Molecular dynamics simulations are used to study the time evolution of the system via Newton's second law of motion. The primary steps in MD simulations are:

1. Generation of the initial geometry of the system. Velocities of the atoms are then initialized, based on a Maxwell-Boltzmann distribution for the desired temperature.
2. Computation of the forces on every atom from the derivative of the potential energy with respect to displacement vectors (equation 2.2). This and the previous steps permit the calculation of the potential and kinetic energies of the system, and the pressure tensor.
3. Update the configuration by numerically solving Newton's equation of motion;

$$\frac{d^2 r_i}{dt^2} = \frac{F_i}{m_i} \quad (2.11)$$

where r_i is the position, F_i is the force, and m_i is the mass of atom i , for all the atoms in the system. This poses a limitation on the size of the system. Recall that a mole of material contains Avogadro's number 6.02×10^{23} of atoms. Typical achievable system sizes depending on the complexity of the force field fall in the range of 10^2 and 10^9 .³¹

4. Output new coordinates and velocities (optional). Repeat steps 2, 3 and 4 as required.

We note that the above is a generic introduction to molecular dynamics, which is used in this thesis solely as a mechanism to perturb minima before re-optimizing them. Other relevant important topics are statistical ensembles, integrators, barostats and thermostats, and are modeled extensively in the literature.⁴

2.6 Method 1: The Rigid Block Shearing Method

We propose the Rigid Block Shearing Method (RBSM) to simulate the deformation of crystalline material. RBSM is an extension of the generalized stacking fault energy (GSFE) proposed by Vitek³² such that instead of having two rigid blocks shearing past each other, an extra region of atoms is placed in between and allowed to fully relax in three-dimensional space. We note that RBSM is similar to the method proposed by Osetsky and Bacon,³³ yet we start from ideal defect-free structures while Osetsky and Bacon start from dislocated structures, and since dislocations are involved their system sizes are much larger than ours. RBSM is a quasi-static approach, implying that constrained energy minimizations are performed to explore the potential energy hypersurface along a specific strain direction. We choose RFO²⁸ to perform energy minimizations. The starting point for RBSM is to generate a surface cell from an energy minimized bulk unit cell and divide it into three regions, as in Figure 2.4:

1. Region 2 is a rigid block of atoms fixed in x , y , and z (colored in green in Figure 2.4). Neither the block, nor the constituting atoms, are allowed to relax throughout the calculations.
2. Region 1 is a region of atoms fully relaxed in x , y , and z (colored in red in Figure 2.4). GSFE is a special case of RBSM where the size of region 1 is zero.
3. Region 3 is a rigid block translated in the shear direction of interest (colored in cyan in Figure 2.4).

RBSM applies to surface cells which are periodic in two dimensions (x and y axes in Figure 2.4). Shear deformation is simulated by the translation of region three relative to region two. The translation is achieved in a sequence of steps, e.g. translate region three along surface lattice vector a , which is aligned along x , for an overall magnitude of three times the lattice vector in 300 steps. Following every translation step, the energy is minimized in the system using RFO²⁸ subject to the

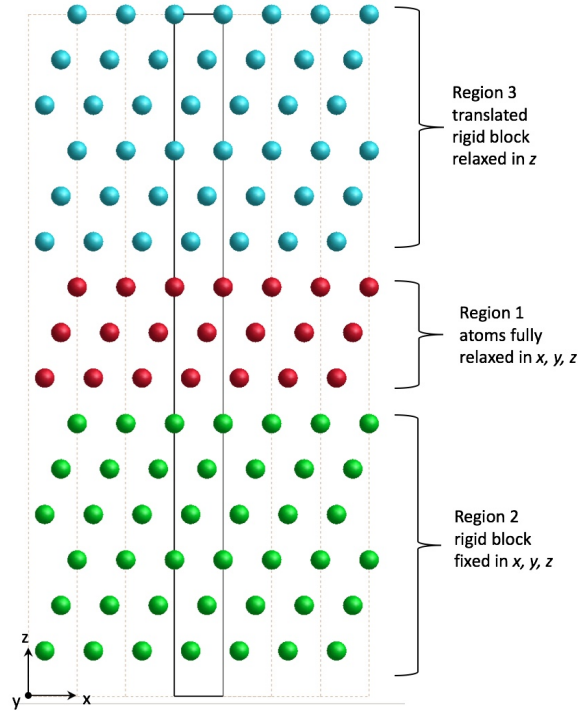


Figure 2.4: Schematic of the setup used in the rigid block shearing method simulations of deformation.

constraint that the region three can only relax orthogonal to the shear direction. The output frame becomes the input frame for the subsequent translation step and so on so forth. In this way, strain starts propagating throughout region one.

The outcome of the plastic deformation often cannot be determined *a priori*, and may manifest itself through stacking faults, twinned structures, phase transitions, etc. In order to determine whether the system is visiting any local energy minima, a re-optimization energy procedure needs to be performed for all RBSM frames by removing the constraint, i.e. region three can relax in all Cartesian dimensions. We will show in later chapters how this additional feature of RBSM makes it powerful in predicting several physical phenomena.

RBSM produces several important quantities that describe the process of deformation, both elastic and plastic. To analyze the energetics of the deformation, the dimensionless normalized strain energy barrier is defined;

$$U_{iN} = \frac{\Delta U}{N_a E_c} \quad (2.12)$$

where U_{iN} is the normalized strain energy of the i^{th} barrier, ΔU is the change in the potential energy between the strained and equilibrium surface cell, N_a is the number of atoms/molecules in region one, and E_c is the cohesive lattice energy per atom/molecule. These barriers, after converting to energy per interface per unit area, compare directly against GSFE curve barriers. The most critical barrier is the first one, since it coincides with the occurrence of the instability in the material,

or else known as the yield limit in continuum mechanics community. The instability is found using a purely atomistic treatment without the need of any constitutive assumption regarding the deformation process, nor what deformation mechanism triggers beyond the instability. In addition, it is possible to investigate the deformation of individual atoms/molecules in the system by plotting their site energies (defined as the potential energy per atom/molecule) as a function of strain. Furthermore, by recalling that the strain energy in GSF theory corresponds to that resulting from the relative displacement of two rigid blocks across a single interface, an atomistic definition of strain for multi-interfaces is proposed;

$$\gamma_a = \sum_{i=1}^{N_a+1} \frac{\Delta d_i}{h} \quad (2.13a)$$

$$\Delta d_i = d_i - d_{i+1} \quad (2.13b)$$

where γ_a is the atomistic strain, Δd_i is the differential (relative) displacement across interface i , d_i is the displacement vector of atom i , and h is the height of region one. Index i starts counting from the atom at the interface between region three and region one, and then increments by one until the atom in region two at the interface of region one. Our atomistic strain definition γ_a applies throughout the deformation path, even after the point of slip because within periodic boundary conditions, the relative displacement across a slipped interface between two atoms cannot exceed half the lattice vector. Thus if the actual calculated Δd_i is greater than half a lattice vector, then it needs to be adjusted by subtracting the corresponding lattice vector(s).

Equation 2.13a can be derived starting with the finite definition of strain ε_{xz} :

$$\varepsilon_{xz} = \frac{1}{2} \left(\frac{\partial d_x}{\partial z} + \frac{\partial d_z}{\partial x} + \left(\frac{\partial d_x}{\partial z} \frac{\partial d_x}{\partial x} + \frac{\partial d_y}{\partial z} \frac{\partial d_y}{\partial x} + \frac{\partial d_z}{\partial z} \frac{\partial d_z}{\partial x} \right) \right) \quad (2.14)$$

By neglecting the contribution of the higher order terms, and assuming that the relative displacement happens along one direction, then:

$$\gamma_{xz} = 2\varepsilon_{xz} = \frac{\partial d_x}{\partial z} \cong \frac{\sum \Delta d_i}{h} \quad (2.15)$$

By inspecting equation 2.15, it is clear that $\sum \Delta d_i$ equals to d_{R3} - the translation distance of region three. Indeed, our derivation shows that the proposed atomistic strain γ_a is based on an infinitesimal strain approximation in the vicinity of each atom. The continuum-based bulk definition of infinitesimal strain γ_b is expressed as;

$$\gamma_b = \tan^{-1} \left(\frac{d_{R3}}{h} \right) \cong \frac{d_{R3}}{h} \quad (2.16)$$

This analysis implies that γ_b and γ_a should be equal, at least until the frame before slip.

Shear stress can also be calculated in RBSM by employing γ_a such that:

$$\sigma = \frac{1}{V_0} \frac{dU}{d\gamma_a} = \frac{1}{V_0} \frac{\Delta U}{\Delta\gamma_a} \quad (2.17)$$

RBSM mimics an experiment where a test specimen is sheared by the translation of one region relative to a fixed one. In the literature, this is commonly known as a simple shear deformation experiment, e.g. see Figure 2 (c), reference.³⁴ One strength of RBSM is the relative ease of the construction of surface cells, e.g. using GDIS.³⁵ RBSM is coded into GULP¹ with an automatic scan feature. The use of RFO²⁸ energy minimization ensures that the system is physically stable throughout the deformation pathway. As the system size in RBSM is small compared to those used in conventional MD simulations,³³ it is relatively computationally easy to study deformation. The main disadvantage of using RBSM is the use of rigid blocks since they lead to heterogeneous strain distributions through the interfaces. The scope of plasticity is very broad and extends over several lengths scales. RBSM is unable to probe the plasticity related to full dislocation nucleation, dislocation loops³⁶, or phenomena that requires heterogeneities and their interactions. By construction, the rigid blocks forbid the formation of full dislocations and their associated dislocation cores as these require free rather than rigid surfaces. Yet, we show in this thesis that RBSM is a significant development in the field of quasi-static methods, and is able to simulate physical processes not seen before with similar methods.

2.7 Method 2: The Tensor Based Shearing Method

The motivation behind the Tensor Based Shear Method (TBSM) was to remove the strain heterogeneity of RBSM. TBSM belongs to the broad category of affine shear deformation methods popular in the literature.^{37,38} As the name suggests, shear deformation is quasi-statically applied to the system via a strain tensor. Figure 2.5 shows the application of a strain tensor to a two-dimensional hard sphere model. The axes and the atoms (solid circles) in the reference structure are colored in black. Upon the application of ε_{xz} to the system, axes x and z shear to new positions colored in cyan, as do the atoms. In the infinitesimal limit, the amount of shear ε_{xz} equals to the angle between the deformed and reference axes.

TBSM is applicable to 3D periodic systems. The starting point is to calculate the energy minimized unit cell. Then a supercell of a chosen number of layers in the specific crystallographic slip system of interest is constructed. The system is then sheared via the application of a strain tensor according

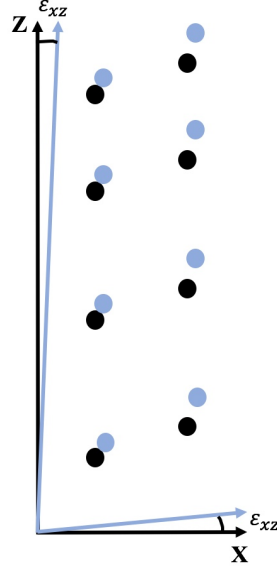


Figure 2.5: Example of the application of a strain tensor to a 2D system. Arrows represent axes and solid spheres represent atoms. Black colors refer to reference configuration while cyan colors to the deformed configuration.

to;

$$R = \varepsilon R_0 \quad (2.18)$$

where R is a 3 by 3 matrix of the deformed lattice vectors written column-wise, R_0 is the reference lattice of the same, and the Voigt strain tensor ε is;

$$\begin{bmatrix} 1 + \varepsilon_1 & \frac{1}{2}\varepsilon_6 & \frac{1}{2}\varepsilon_5 \\ \frac{1}{2}\varepsilon_6 & 1 + \varepsilon_2 & \frac{1}{2}\varepsilon_4 \\ \frac{1}{2}\varepsilon_5 & \frac{1}{2}\varepsilon_4 & 1 + \varepsilon_3 \end{bmatrix} \quad (2.19)$$

where strain subscripts 1, 2, 3, 4, 5, and 6 correspond to xx , yy , zz , yz , xz , and xy , respectively. Following the application of shear deformation via equation 2.18, the energy of the system is minimized such that the constrained strain component ε_{xz} is fixed and all the other five components and the internal coordinates of atoms are allowed to relax. TBSM has been coded into GULP¹ with an automatic scanning feature. For instance, an overall sum of $0.7 \varepsilon_{xz}$ can be applied in 2000 steps. Given equation 2.18, it is clear that TBSM is related to the Cauchy–Born approximation which relates the movement of atoms in a crystal to the overall deformation of the bulk solid. This treatment is well studied and has been applied to multi-scale deformation problems.^{39,40} Compared to TBSM, the CB approximation fixes the applied deformation and relaxes the internal coordinates, thereby producing an effective model of the response of the material⁴¹, while TBSM only fixes one or more components of the strain tensor and relaxes both the other components and the atomic positions allowing for the distortion of the bulk (lattice parameters) and the internal degrees of

freedom in a pure atomistic setting.

There are some caveats related to the implementation of affine shear deformation via incremental simple shear. For instance, Roundy *et al.*³⁷ suggested that the strain constraints be enforced by;

$$a_i^\alpha(n) = a_i^\alpha(m) + D_{ij}(n, m)a_j^\alpha(m) \quad (2.20)$$

where a_i^α is lattice vector (subscripts i and j are the Einstein notation of summations -1, 2, and 3 for x,y, and z-, and the superscript α is the indicator of the lattice vector), D_{ij} is the Cartesian tensor to apply deformation, n and m represent the new and old step. Expanding equation 2.20 for three steps:

$$a_i^\alpha(3) = a_i^\alpha(2) + D_{ij}(3, 2)a_j^\alpha(2) \quad (2.21a)$$

$$a_i^\alpha(3) = a_i^\alpha(2) + D_{ij}(3, 2)[a_i^\alpha(1) + D_{ij}(2, 1)a_j^\alpha(1)] \quad (2.21b)$$

$$a_i^\alpha(3) = a_i^\alpha(2) + D_{ij}(3, 2)a_j^\alpha(1) + D_{ij}(3, 2)D_{ij}(2, 1)a_j^\alpha(1) \quad (2.21c)$$

2.21c shows that deformation is applied via a power series expansion of tensor D_{ij} . The exponent is directly proportional to the number of steps used to apply the affine shear deformation. Second, there is no mention in the original references^{37, 38} of the deformation of the lattice vectors as a function of strain, which has an implication on the intended and actual directions of applied strain. TBSM is a major improvement to existing affine shear deformation methods in that the problem of the power series expansion of strain is resolved by always defining strain with respect to the reference structure. For example, strain steps in TBSM according to 2.18 follow:

$$R_1 = \varepsilon_1 R_0 \quad (2.22a)$$

$$R_2 = \varepsilon_2 R_0 \quad (2.22b)$$

$$R_3 = \varepsilon_3 R_0 \quad (2.22c)$$

i.e. subsequent configurations of the lattice vectors are dependent only on the reference structure. However, for this construction to work, the typical standard form of the infinitesimal strain derivatives of energy, ubiquitous in the literature e.g.,^{1, 26, 29, 42, 43} needs to be amended. Finite strain derivatives of energy have been analytically derived by Professor Julian Gale, and implemented in GULP¹ as an integral component of TBSM, such that strain is always applied to the reference structure. We note that because lattice vectors deform as a function of strain, this leads to a mismatch between the intended crystallographic direction of strain and the actual direction. This effect is expected to become pronounced at relatively large finite strain and will be examined in Chapter 5.

A procedure to align the lattice vectors in the deformed configuration along those in the reference structure will be proposed later in this section, being a pre-requisite to the differential displacement Δd_i analysis in Chapter 5.

We would like to introduce the Green-Lagrange strain tensor which defines the finite strain with respect to the reference structure, and under a Cartesian orthogonal basis takes the form;

$$E = \frac{1}{2}(C - I) \quad (2.23)$$

where I is the identity matrix and C is the Cauchy-Green deformation tensor defined as;

$$C = F^T F \quad (2.24)$$

where F is the deformation gradient. F is a rank 2 tensor which maps vectors from the undeformed configuration into the deformed configuration. Chapter 5 will compare the Voigt strain tensor defined in TBSM with the Green-Lagrange finite strain tensor.

TBSM can calculate properties in addition to those from RBSM such as stress-strain curves due to the tensor-based definition of stress, strain and geometry. For instance, stress is analytically calculated by evaluating the first derivative of energy with respect to strain, divided by the volume.¹ Phonon calculations at each strained configuration can be used to confirm the structural stability. The boundary conditions in TBSM are different than those in RBSM. Shearing the system by fixing a single strain component and relaxing the others is analogous to the homogeneous shear experiment on a material, also called pure shear deformation, see Figure 2 (a) in reference.³⁴ Because TBSM operates on 3D supercells, bulk properties can be determined in contrast to surface cell simulations in RBSM. The drawback is that the user needs to determine the proper cell representation to shear a particular material in a specific slip system (e.g., generating a (111) supercell in FCC Au).

Like RBSM, TBSM is unable to simulate plasticity associated with full dislocation nucleation and the formation of dislocation cores because relaxation of five components of strain in a 3D periodic boundary condition forbids such phenomena. However, we will show in Chapter 5 that TBSM is a much improved version of the affine shear deformation methods in the literature and that it is able to reveal particular interesting aspects of plasticity, not seen before with affine shear deformation methods.

Finally, the problem of performing differential displacement analysis Δd_i in TBSM is addressed. The deformation of the lattice vectors through the course of shearing causes a mismatch between crystallographic directions in the reference configuration and the deformed configuration. Such a

mismatch can be resolved by finding the three dimensional rotation tensor $T = T_z(\eta)T_y(\theta)T_x(\phi)$ that aligns the deformed lattice vectors along the Cartesian directions of the reference supercell;

$$R'_c = TR' \quad (2.25)$$

where R'_c and R' are the transformed and deformed lattice vectors written column-wise. T is the three dimensional rotation matrix, counter-clockwise in a right-handed frame of reference defined as;

$$T = \begin{bmatrix} \cos \eta \cos \theta & \sin \phi \sin \theta \cos \eta - \sin \eta \cos \phi & \cos \eta \cos \phi \sin \theta + \sin \eta \sin \phi \\ \sin \eta \cos \theta & \sin \phi \sin \theta \sin \eta + \cos \eta \cos \phi & \sin \theta \sin \eta \cos \phi - \cos \eta \sin \phi \\ -\sin \theta & \sin \phi \cos \theta & \cos \theta \cos \phi \end{bmatrix} \quad (2.26)$$

where η , θ , and ϕ represent the angles of rotations about z , y , and x axes, respectively. Solution of any system of equations in 2.25 requires the imposition of some constraints. For example, let there be a supercell that has lattice vector a aligned along x , lattice vector b having x and y components, and lattice vector c having three non-zero Cartesian components. Suppose the twinning direction lies originally along the vector $a + b$, i.e. in the xy plane. By deforming the supercell using TBSM, lattice vectors a and b start developing z components and the new twinning direction $a' + b'$ is not parallel to $a + b$. Re-writing equation 2.25 in component form yields;

$$\begin{bmatrix} a'_{xc} & b'_{xc} & c'_{xc} \\ 0 & b'_{yc} & c'_{yc} \\ 0 & 0 & c'_{zc} \end{bmatrix} = T \begin{bmatrix} a'_x & b'_x & c'_x \\ a'_y & b'_y & c'_y \\ a'_z & b'_z & c'_z \end{bmatrix} \quad (2.27)$$

Three constraints on equation 2.25 are imposed such that the transformed deformed lattice vectors have the same zero components as the reference lattice vectors, e.g. $a'_{yc} = a'_{zc} = b'_{zc} = 0$ in equation 2.27. For instance, $a'_{zc} = 0$ reads;

$$-\sin \theta a'_x + \sin \phi \cos \theta a'_y + \cos \theta \cos \phi a'_z = 0 \quad (2.28)$$

The other two equations can be found similarly. Given the three unknown angles in 2.26 and three equations equal to 0 in 2.27, non-linear optimization can be used to solve the system of equations. It is recommended that the initial guess of the three angles be zero such that solutions close to zero will be found first. Upon successfully transforming the deformed lattice vectors and atomic coordinates, differential displacement analysis proceeds in the same way explained in RBSM.

Bibliography

- ¹ J. D. Gale and A. L. Rohl, “The general utility lattice program (gulp),” *Molecular Simulation*, vol. 29, no. 5, pp. 291–341, 2003.
- ² K. Vanommeslaeghe, O. Guvench, and J. MacKerell, Alexander D, “Molecular mechanics,” *Current pharmaceutical design*, vol. 20, no. 20, pp. 3281–3292, 2014.
- ³ J. Patterson and B. Bailey, “Crystal binding and structure,” in *Solid-State Physics: Introduction to the Theory*, pp. 1–40, Berlin, Heidelberg: Springer Berlin Heidelberg, 2010.
- ⁴ D. C. Rapaport, *The Art of Molecular Dynamics Simulation*. Cambridge University Press, 2 ed., 2004.
- ⁵ J. E. Jones and S. Chapman, “On the determination of molecular fields ii. from the equation of state of a gas,” *Proceedings of the Royal Society of London. Series A, Containing Papers of a Mathematical and Physical Character*, vol. 106, no. 738, pp. 463–477, 1924.
- ⁶ B.-J. Lee, J.-H. Shim, and M. I. Baskes, “Semiempirical atomic potentials for the fcc metals cu, ag, au, ni, pd, pt, al, and pb based on first and second nearest-neighbor modified embedded atom method,” *Phys. Rev. B*, vol. 68, p. 144112, Oct 2003.
- ⁷ J. Wang, R. M. Wolf, J. W. Caldwell, P. A. Kollman, and D. A. Case, “Development and testing of a general amber force field,” *Journal of Computational Chemistry*, vol. 25, no. 9, pp. 1157–1174, 2004.
- ⁸ J. Huang, S. Rauscher, G. Nawrocki, T. Ran, M. Feig, B. L. de Groot, H. Grubmüller, and A. D. MacKerell, “Charmm36m: an improved force field for folded and intrinsically disordered proteins,” *Nature Methods*, vol. 14, no. 1, pp. 71–73, 2017.
- ⁹ N. W. a. Ashcroft and a. Mermin, N. David, *Solid state physics / Neil W. Ashcroft, N. David Mermin*. California, USA: California, USA : Brooks Cole/Cengage Learning, 1976.

- ¹⁰ T. Halicioğlu and G. M. Pound, “Calculation of potential energy parameters form crystalline state properties,” *physica status solidi (a)*, vol. 30, no. 2, pp. 619–623, 1975.
- ¹¹ M. W. Finnis and J. E. Sinclair, “A simple empirical n-body potential for transition metals,” *Philosophical Magazine A*, vol. 50, no. 1, pp. 45–55, 1984.
- ¹² J. Tersoff, “New empirical model for the structural properties of silicon,” *Phys. Rev. Lett.*, vol. 56, pp. 632–635, Feb 1986.
- ¹³ A. P. Sutton and J. Chen, “Long-range finnis–sinclair potentials,” *Philosophical Magazine Letters*, vol. 61, no. 3, pp. 139–146, 1990.
- ¹⁴ M. S. Daw and M. I. Baskes, “Embedded-atom method: Derivation and application to impurities, surfaces, and other defects in metals,” *Phys. Rev. B*, vol. 29, pp. 6443–6453, Jun 1984.
- ¹⁵ M. I. Baskes, “Modified embedded-atom potentials for cubic materials and impurities,” *Phys. Rev. B*, vol. 46, pp. 2727–2742, Aug 1992.
- ¹⁶ S. Ryu, C. R. Weinberger, M. I. Baskes, and W. Cai, “Improved modified embedded-atom method potentials for gold and silicon,” *Modelling and Simulation in Materials Science and Engineering*, vol. 17, p. 075008, aug 2009.
- ¹⁷ K. Namjoshi, S. Mitra, and J. Vetelino, “Rigid ion model of lattice dynamics - a re-evaluation,” *Solid State Communications*, vol. 9, no. 3, pp. 185–189, 1971.
- ¹⁸ M. Verma, “On rigid ion models of ionic solids,” *Journal of Physics and Chemistry of Solids*, vol. 33, no. 5, pp. 1166–1169, 1972.
- ¹⁹ B. G. Dick and A. W. Overhauser, “Theory of the dielectric constants of alkali halide crystals,” *Phys. Rev.*, vol. 112, pp. 90–103, Oct 1958.
- ²⁰ U. Schröder, “A new model for lattice dynamics (“breathing shell model”),” *Solid State Communications*, vol. 4, no. 7, pp. 347–349, 1966.
- ²¹ K. Kobashi, M. L. Klein, and V. Chandrasekharan, “Lattice dynamics in solid oxygen,” *The Journal of Chemical Physics*, vol. 71, no. 2, pp. 843–849, 1979.
- ²² J. Powles and K. Gubbins, “The intermolecular potential for nitrogen,” *Chemical Physics Letters*, vol. 38, no. 3, pp. 405–406, 1976.

- ²³ J. E. Cahill and G. E. Leroi, “Raman studies of molecular motion in condensed oxygen,” *The Journal of Chemical Physics*, vol. 51, no. 1, pp. 97–104, 1969.
- ²⁴ C. S. Barrett and L. Meyer, “Molecular Packing, Defects, and Transformations in Solid Oxygen,” *Physical Review*, vol. 160, pp. 694–697, Aug. 1967.
- ²⁵ R. Mason, “The crystallography of anthracene at 95 °k and 290 °k,” *Acta Crystallographica*, vol. 17, no. 5, pp. 547–555, 1964.
- ²⁶ M. J. Frisch, G. W. Trucks, H. B. Schlegel, G. E. Scuseria, M. A. Robb, J. R. Cheeseman, G. Scalmani, V. Barone, G. A. Petersson, H. Nakatsuji, X. Li, M. Caricato, A. V. Marenich, J. Bloino, B. G. Janesko, R. Gomperts, B. Mennucci, H. P. Hratchian, J. V. Ortiz, A. F. Izmaylov, J. L. Sonnenberg, Williams, F. Ding, F. Lipparini, F. Egidi, J. Goings, B. Peng, A. Petrone, T. Henderson, D. Ranasinghe, V. G. Zakrzewski, J. Gao, N. Rega, G. Zheng, W. Liang, M. Hada, M. Ehara, K. Toyota, R. Fukuda, J. Hasegawa, M. Ishida, T. Nakajima, Y. Honda, O. Kitao, H. Nakai, T. Vreven, K. Throssell, J. A. Montgomery Jr., J. E. Peralta, F. Ogliaro, M. J. Bearpark, J. J. Heyd, E. N. Brothers, K. N. Kudin, V. N. Staroverov, T. A. Keith, R. Kobayashi, J. Normand, K. Raghavachari, A. P. Rendell, J. C. Burant, S. S. Iyengar, J. Tomasi, M. Cossi, J. M. Millam, M. Klene, C. Adamo, R. Cammi, J. W. Ochterski, R. L. Martin, K. Morokuma, O. Farkas, J. B. Foresman, and D. J. Fox, “Gaussian 16 rev. c.01,” 2016.
- ²⁷ J. R. Shewchuk, “An introduction to the conjugate gradient method without the agonizing pain,” tech. rep., USA, 1994.
- ²⁸ A. Banerjee, N. Adams, J. Simons, and R. Shepard, “Search for stationary points on surfaces,” *The Journal of Physical Chemistry*, vol. 89, pp. 52–57, 01 1985.
- ²⁹ C. R. A. Catlow and W. C. Mackrodt, *Theory of simulation methods for lattice and defect energy calculations in crystals*, pp. 1–20. Berlin, Heidelberg: Springer Berlin Heidelberg, 1982.
- ³⁰ D. F. Shanno, “Conditioning of quasi-newton methods for function minimization,” vol. 24, pp. 647–656, 2021/06/02/ 1970.
- ³¹ M. E. Tuckerman, *Statistical Mechanics : Theory and Molecular Simulation*. Oxford, UNITED KINGDOM: Oxford University Press, Incorporated, 2010.
- ³² V. Vitek, “Intrinsic stacking faults in body-centred cubic crystals,” *The Philosophical Magazine: A Journal of Theoretical Experimental and Applied Physics*, vol. 18, no. 154, pp. 773–786, 1968.

- ³³ Y. N. Osetsky and D. J. Bacon, “An atomic-level model for studying the dynamics of edge dislocations in metals,” *Modelling and Simulation in Materials Science and Engineering*, vol. 11, pp. 427–446, may 2003.
- ³⁴ V. Segal, “Severe plastic deformation: simple shear versus pure shear,” *Materials Science and Engineering: A*, vol. 338, no. 1, pp. 331–344, 2002.
- ³⁵ S. Fleming and A. Rohl, “Gdis: A visualization program for molecular and periodic systems,” *Zeitschrift Fur Kristallographie - Z KRISTALLOGR*, vol. 220, pp. 580–584, 01 2005.
- ³⁶ S. Lee, A. Vaid, J. Im, B. Kim, A. Prakash, J. Guérolé, D. Kiener, E. Bitzek, and S. H. Oh, “In-situ observation of the initiation of plasticity by nucleation of prismatic dislocation loops,” *Nature Communications*, vol. 11, no. 1, p. 2367, 2020.
- ³⁷ D. Roundy, C. R. Krenn, M. L. Cohen, and J. W. Morris, “Ideal shear strengths of fcc aluminum and copper,” *Phys. Rev. Lett.*, vol. 82, pp. 2713–2716, Mar 1999.
- ³⁸ S. Ogata, J. Li, and S. Yip, “Ideal pure shear strength of aluminum and copper,” *Science*, vol. 298, no. 5594, pp. 807–811, 2002.
- ³⁹ J. Ericksen, “On the cauchy—born rule,” *Mathematics and Mechanics of Solids*, vol. 13, no. 3-4, pp. 199–220, 2008.
- ⁴⁰ E. B. Tadmor, M. Ortiz, and R. Phillips, “Quasicontinuum analysis of defects in solids,” *Philosophical Magazine A*, vol. 73, no. 6, pp. 1529–1563, 1996.
- ⁴¹ E. B. Tadmor, G. S. Smith, N. Bernstein, and E. Kaxiras, “Mixed finite element and atomistic formulation for complex crystals,” *Phys. Rev. B*, vol. 59, pp. 235–245, Jan 1999.
- ⁴² J. Zhao, J. M. Winey, and Y. M. Gupta, “First-principles calculations of second- and third-order elastic constants for single crystals of arbitrary symmetry,” *Phys. Rev. B*, vol. 75, p. 094105, Mar 2007.
- ⁴³ W. Perger, J. Criswell, B. Civalieri, and R. Dovesi, “Ab-initio calculation of elastic constants of crystalline systems with the crystal code,” *Computer Physics Communications*, vol. 180, no. 10, pp. 1753 – 1759, 2009.

Every reasonable effort has been made to acknowledge the owners of copyright material. I would be pleased to hear from any copyright owner who has been omitted or incorrectly acknowledged.

Chapter 3

Generalized Fault Energies

3.1 Introduction

The rigid block shearing method (RBSM) is an extension of the generalized stacking fault energy theory (GSFE, also known as the γ surface) by the inclusion of a region of atoms/molecules which are fully relaxed in 3-D space and the use of the rational function optimizer (RFO).¹ Setting aside RFO, this makes GSFE a special case of RBSM where the size of the fully flexible region is zero and only the rigid blocks are sheared. In Chapter One, the qualitative GSFE curves of FCC metals were discussed in relation to the deformation mechanisms in FCC metals. That review is not exhaustive, neither is the one presented below, as attention is focussed on calculating the energetics using the standard approach with the force fields that we have employed, so we can compare to the results from RBSM. In other words, before applying RBSM to selected FCC metals in the next chapter, it is important to perform GSFE curve calculations with the same force field, i.e. the modified embedded atom method second nearest neighbor (MEAM-2NN)² for all studied FCC metals except FCC Au whose MEAM-2NN parameters are taken from reference,³ so that the calculated deformation barriers between our methods and GSFE can be compared.

This chapter is organized in the following way. The major deformation mechanisms in FCC metal single crystals are briefly reviewed and the calculation of the corresponding GSFE curve is performed in detail for FCC Au. The energy barriers are also reported for Al, Pb, Pd, Pt, Cu, Ni, and Ag and some comments are made regarding the anomalous GSFE curve for FCC Pd. The generalized planar fault energy (GPFE) curve of the new twinning route proposed by Wang *et al.*⁴ is calculated starting from an ideal structure. Finally, because the (111) plane in β -oxygen has

the same ABC stacking as the (111) plane in FCC metals, the GSFE curves are calculated to be contrasted against the RBSM results applied to β -oxygen in Chapter Seven.

3.2 Deformation Mechanisms of FCC Au

Before describing the idealized deformation mechanisms in FCC Au, it is necessary to define the geometry and the methodology in general. Using the ideal defect-free energy minimized unit cell (space group $FM\bar{3}M$), a new cell is constructed such that the (111) plane in the original cell is in the ab plane of the new cell, as shown in Figure 3.1. This cell is composed of three atoms and the

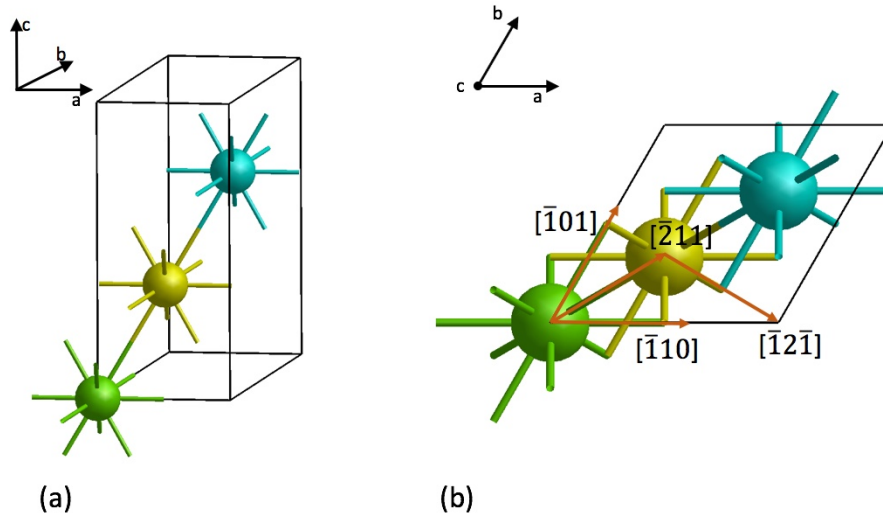


Figure 3.1: (a) 3-D Illustration of the cell with the close packed planes in the ab plane. (b) Top view of the cell with the main crystallographic directions indicated relative to the FCC unit cell. The different colors correspond to the ABC stacking sequence of the atoms.

close-packed layers stack in the c direction. Figure 3.1 (b) shows the top view of the (111) cell with the relevant crystallographic directions to investigate the deformation mechanisms using the GSFE and GPFE methods. We use a 3D periodic supercell composed of twelve atoms where the cell is extended in the c direction (Figure 3.1). The starting point of the calculations is the rigid translation of one block over the other in a sequence of steps where the energy is optimized after each step. Since the blocks are constrained in the ab plane, minimization only operates on the relaxed degrees of freedom. The bottom atom is always fixed in the x , y , and z directions. All the other atoms are allowed to relax in z during the optimization step. This implies the blocks are not perfectly rigid in our calculations. The atoms are relaxed in the vertical direction in order to obtain the lowest possible barriers⁵ while the γ_{isf} is unaffected. To ensure no stacking faults are produced between the top-most and bottom-most atoms through the periodic boundary condition e.g. see reference,⁶

the component of the c vector along the translation direction is also incremented by the translation distance after each translation step, as will be highlighted later. There are five possible idealized deformation mechanisms of FCC Au in the (111): full dislocation without dissociation, full dislocation by dissociation, twinning, stacking fault emission, and forced slip along the twinning direction (A-A stacking deformation).

3.2.1 Full Dislocation Without Dissociation

The supercell vectors were oriented with vector a aligned along x , vector b having x and y components, and vector c aligned along z . The first deformation mechanism corresponds to shearing the supercell along the closest contact direction of atoms, namely, the $[\bar{1}10]$ direction shown in Figure 3.1 (b). The lowest and highest energy configurations are depicted in Figure 3.2. The normalized translation distance d_{N1} is defined as the translation distance along the $[\bar{1}10]$ direction divided by the Burger's vector along the same direction, which coincides with the lattice vector a of the current cell representation. As the system shears, γ increases until point 1 is reached at $d_{N1}/2$ before going back to 0 after d_{N1} equals the lattice vector since atoms resume their commensurate lattice positions. The lattice vector c which is originally aligned along the $[111]$ direction, is also deformed along the direction of shear by the same increments as the translated rigid block, i.e. the configurations in Figure 3.2 where the small arrow indicates the shear of lattice vector c . We define the peak value on this curve as the unstable slipping energy (γ_{USE}). This value represents the barrier along this direction and for Au equals 289 mJ/m^2 .

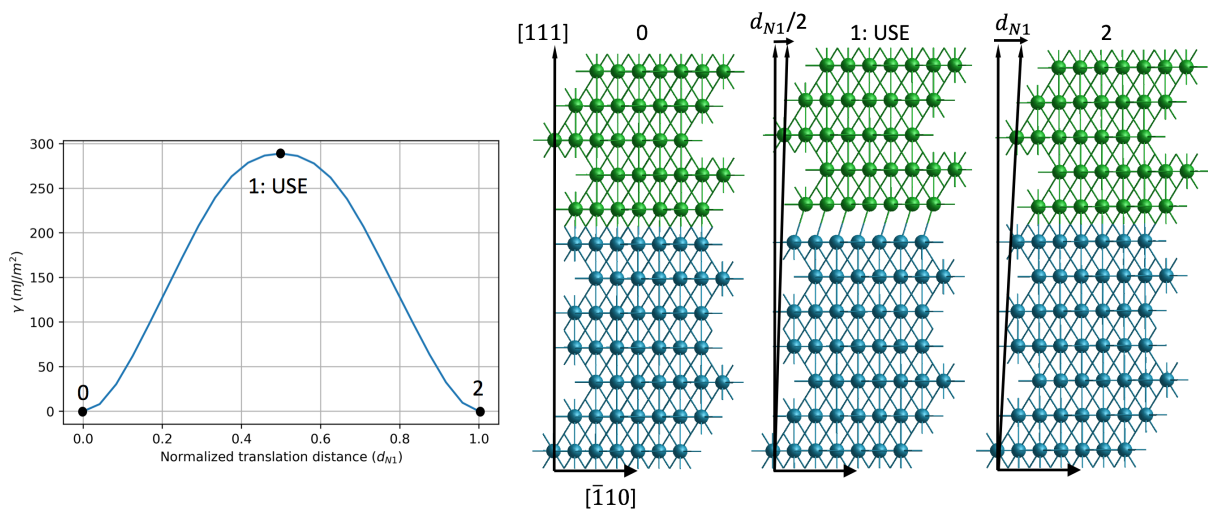


Figure 3.2: To the left, the γ surface as a result of shearing the $[\bar{1}10]$ direction. To the right, corresponding configurations at points 0, 1 and 2 on the GSFE plot. Atoms colored in green are translated while atoms in blue are fixed.

3.2.2 Stacking Fault Emission

To describe the energetic process of generating a stacking fault, the supercell used in subsection 3.2.1 was transformed using a 3-D rotation matrix such that the twinning direction ($[\bar{2}11]$) is aligned with the x axis. Herein, we define d_{N2} to be the translation distance normalized by the magnitude of the Burger's vector along the twinning direction, which equals $a_0 / \sqrt{6}$ (1.6628 Å), where a_0 is the lattice vector of the optimized FCC unit cell in Au. The GSFE curve and the important configurations along the pathway are shown in Figure 3.3. As the top rigid block (colored in green)

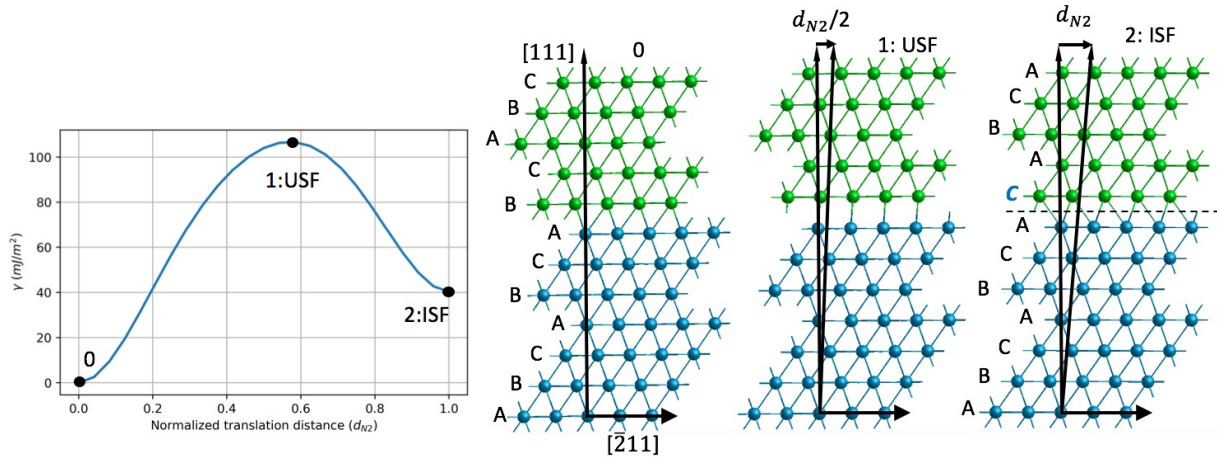


Figure 3.3: The γ surface as a result of shearing in the $[\bar{2}11]$ direction (left). Corresponding configurations at points 0, 1 (USF), and 2 (ISF) as denoted on the GSFE plot (right). Atoms colored in green are translated while atoms in blue are fixed. Stacking sequence is indicated with ABC to the left side. The blue, italic, and bold C denotes the stacking fault, and the dashed line the stacking interface.

translates, the strain energy increases until it reaches a maximum at the unstable stacking fault energy (USF).⁷ At a d_{N2} value of 1, the intrinsic stacking fault (ISF) is generated. The stacking of the layers is shown for points 0 and 2 in Figure 3.3, and changes from the ideal ABCABCABCABC to the ABCABCACBCA. Theoretically, if the shear applied to the supercell stops at the d_{N2} value of 1, then the deformation ends by the formation of a stacking fault. However, if the shear goes beyond the value of 1, three possible deformation paths can be simulated, as discussed in the forthcoming subsections. The calculated values of γ_{USF} and γ_{ISF} are 107 and 40 mJ/m², respectively.

3.2.3 A-A Stacking Deformation

The A-A stacking deformation is simulated by the additional shearing of the supercell in section 3.2.2 so that d_{N2} goes to 3. On the left side of Figure 3.4, beyond the ISF point on the GSFE curve, the energy increases sharply to a very high value at point 3, defined as UAA (unstable A-A

stacking). Observing the structure on the right-hand side of Figure 3.4 clearly indicates the peak in energy corresponds to the A-A stacking sequence (noting that A-A, B-B, and C-C stacking are all equivalent). At d_{N2} equals to 3, the reference structure is regenerated and the energy goes to zero.

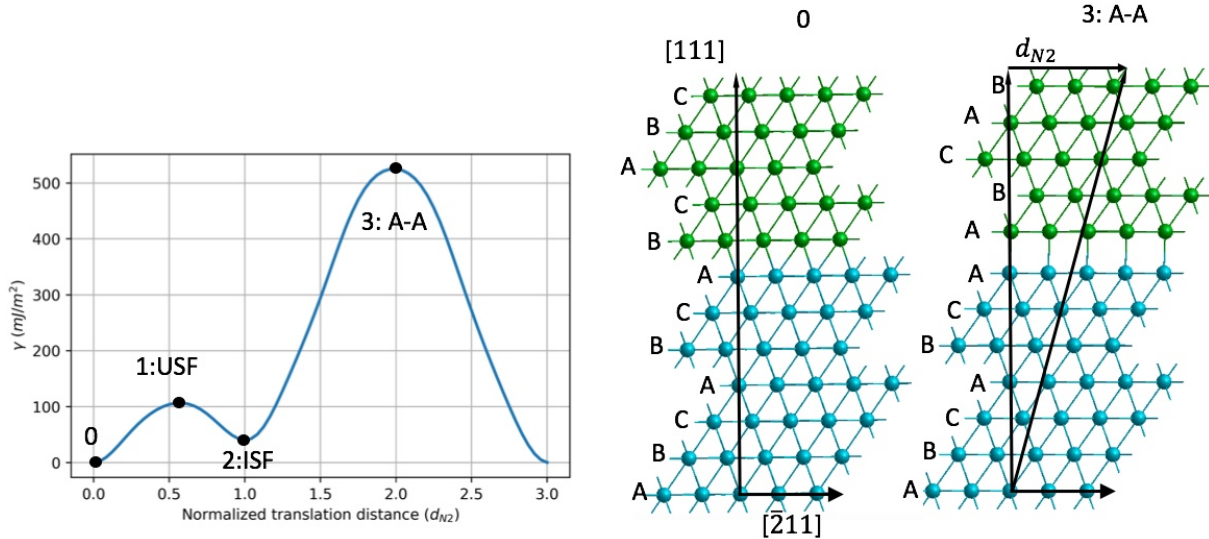


Figure 3.4: The γ surface as a result of shearing the supercell in the $[\bar{2}11]$ direction by a total of $3 d_{N2}$. The corresponding configurations at points 0 and 3 (A-A stacking) on the GSFE plot are shown to the right. Atoms colored in green are translated while atoms in blue are fixed.

3.2.4 Full Dislocation by Partial Dislocations Dissociation

One more deformation path is simulated by which the full dislocation propagates through the dislocation dissociation reaction. Along this path, the supercell is first sheared by d_{N2} along $[\bar{2}11]$ to generate the ISF structure. Then, the crystal is sheared again by d_{N2} but along the $[\bar{1}2\bar{1}]$ direction. The GSFE for this particular case is shown in Figure 3.5. At the end of the translation step, the reference structure is regenerated and the energy goes to zero.

3.2.5 Twinning Deformation

Finally, the last deformation mechanism, following the nucleation of a stacking fault, is twinning deformation. The particular GSFE curve to study twinning deformation is called the generalized planar fault energy curve (GPFE). The physics of the twinning process in GPFE assumes first the nucleation of a stacking fault (or its existence as a defect) in the material followed by a layer-by-layer growth. Figure 3.6 shows the calculated GPFE curve for FCC Au. Figure 3.7 shows the configurations of the point numbers shown in Figure 3.6

The generation of the stacking fault is as per section 3.2.2. The top 5 layers as indicated in Figure

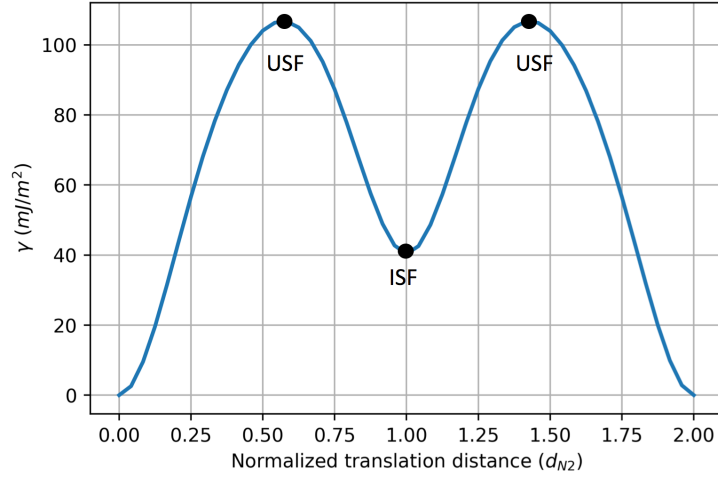


Figure 3.5: The γ surface calculation for simulating the full dislocation propagation by partial dislocations.

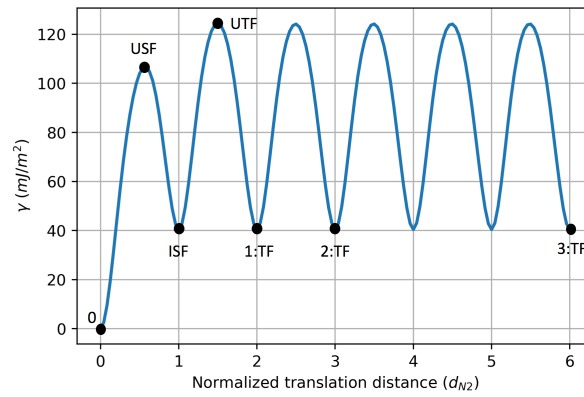


Figure 3.6: The GPFE calculations of twinning deformation.

3.7 are translated by d_{N2} along the $[\bar{2}11]$ direction. Next, the top four layers are translated by the same distance along the same direction. The structure obtained is the one indicated by point 1:TF in Figure 3.7. The growth of the ISF by one layer is observed by following the sequence of the stacking. Additional shearing of the remaining top layers in the supercell along the same direction leads to the formation of the three-layer twin (point 2:TF, Figure 3.7) until the translated structure is twinned (point 3:TF, Figure 3.7). The γ_{UTF} and γ_{TF} are calculated to be 125 and 40 mJ/m^2 , respectively.

Above, we have calculated the several GSFE curves for FCC Au. γ_{USF} is the most important barrier because it contributes to deformation mechanisms along the twinning directions. γ_{USE} is the second most important because it is the second easiest deformation barrier based on GSFE and contributes to slipping deformation. In Chapter Four, we compare the RBSM barriers against γ_{USF} and γ_{USE} .

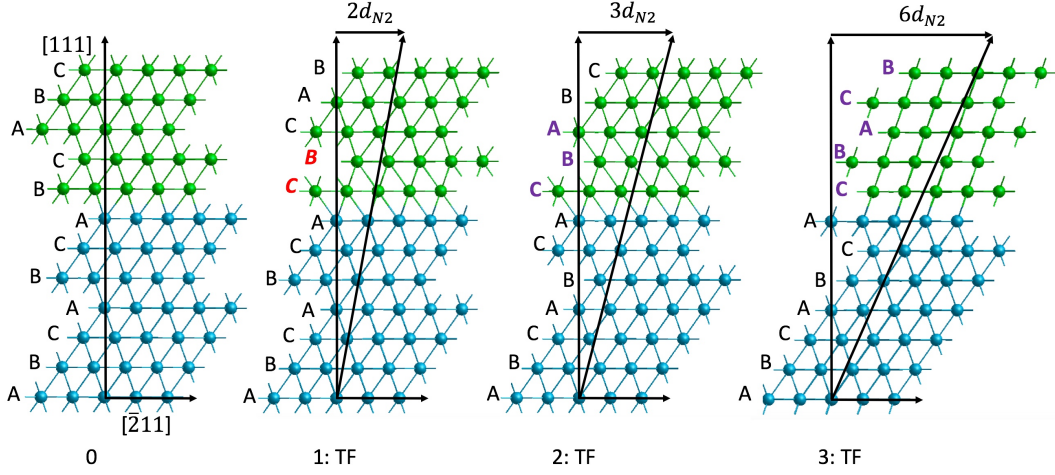


Figure 3.7: Configurations of the different points indicated on Figure 3.6. The green color corresponds to the translated layers, cyan color to the fixed atoms. The stacking sequence is indicated by ABC..., black for the default stacking, red, bold, and italic for the stacking faults, purple, and bold for the twinned portions.

3.3 GPFE Barriers For a List of FCC Metals

GPFE calculations have been performed for Ag, Pb, Pt, Pd, Cu, Ni and Al. The general trend of the GPFE curves are qualitatively the same as in the case of Au. The calculated energy barriers and

Metal	γ_{USF}	γ_{ISF}	γ_{UTF}	γ_{TF}	γ_{ISF} (ref ²)
Ag	203	21	210	21	21
Al	238	142	300	145	141
Cu	291	42	312	42	42
Ni	486	124	547	125	125
Pb	57	9	62	9	9
Pd	429	100	465	100	100
Pt	566	110	619	111	110

Table 3.1: Summary of the energy barriers and minima from the GPFE curves of a series of FCC metals. Units are in mJ/m^2 .

γ_{ISF} and γ_{TF} are reported in Table 3.1, which shows that γ_{USF} is always greater than γ_{ISF} , γ_{UTF} is always greater than the γ_{USF} , and γ_{TF} is equal to or greater than γ_{ISF} . Our calculated γ_{ISF} are very similar to those reported in the original force field paper.² An incidental finding was encountered in the case of Pd. For simplicity, only the A-A deformation path is plotted in Figure 3.8. Depending on whether our GSFE calculations involved relaxed atoms or rigid blocks (subsequently simulated to test the relaxation influence) in the vertical direction, the GSFE curves look different compared with the other FCC metals studied. For both cases in Figure 3.8, there are no clear points on the

curve for the USF barrier as the curve is nearly flat around the normalized displacement distance of 0.5. Beyond the ISF minimum and along the curve towards the A-A stacking (at a normalized displacement of two), the GSFE curve for the rigid block calculations shows a significant change of slope in the interval of normalized displacement between 1.5 and 2.5. For the relaxed case, the A-A stacking energy shows a minimum at a normalized displacement of two, preceded and followed by a shallow bowl-shaped profile of the curve, before tracing almost the same energy curve as that of the rigid case. Wei *et al.*⁸ performed MEAM-2NN GSFE calculations on a few FCC metals and observed a very similar result for Pd to our unrelaxed case. Our calculations indicate that there is a possible anomaly related to the GSFE and GPFE calculations of FCC Pd, with relaxation conditions strongly affecting the result.

Ryu *et al.*³ performed MEAM-2NN² force field-based A-A stacking GSFE calculations on FCC

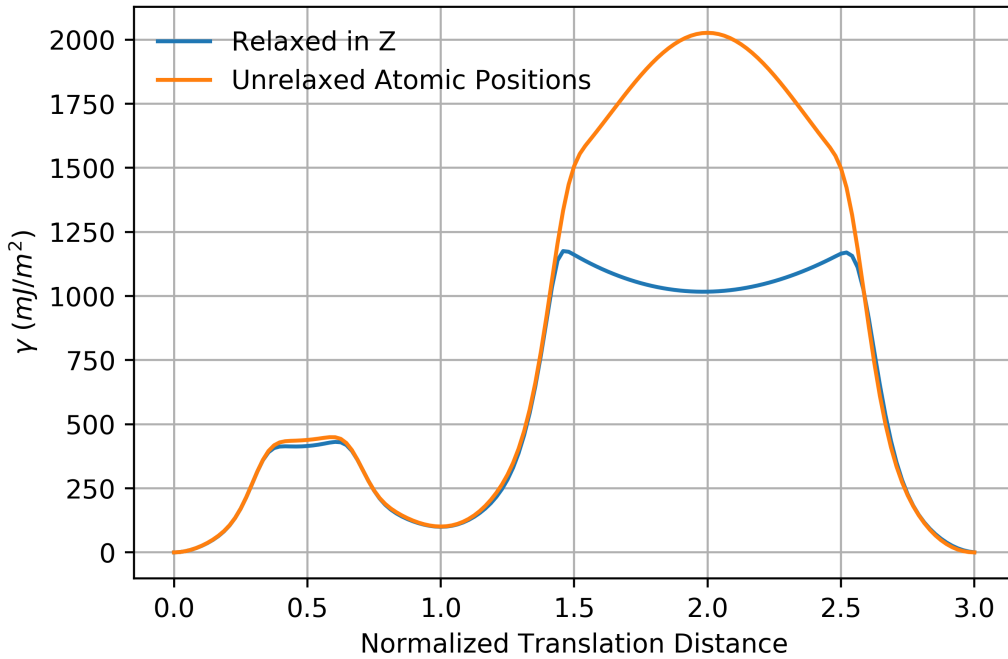


Figure 3.8: GSFE of FCC Pd for the cases of rigid blocks and relaxed atoms in the vertical direction

Au using the methodology proposed by Kang and Cai⁹ (relaxed γ -surface calculations) and calculated a curve for FCC Au very similar to the one we report for FCC Pd relaxed in z case in Figure 3.8. Ryu *et al.* suggested this is an artefact of FCC Au MEAM-2NN parameters and were able to resolve the shape of the curve by modifying the screening parameter for FCC Au, increasing the range of atomistic interactions. We have used Ryu *et al.*'s improved parameters throughout our calculations on FCC Au and MEAM-2NN parameters in² for the rest of FCC metals. This implies

that our MEAM-2NN results for FCC Pd may be improved if the force field parameters are properly adjusted.

Su *et al.*¹⁰ used DFT to calculate the GSFE of selected FCC metals. They used a specific computational procedure by which their twelve-layer supercell was bound by vacuum in the z direction, the top two and bottom two atoms were not relaxed throughout the calculations, and the atoms in between are allowed to relax only in z after translations. Their results indicate that Ir and Rh are characterized by similar energy cusps to the one we record in Figure 3.8, which led the authors to predict a novel dislocation dissociation in Ir and Rh.

Based on our results in Figure 3.8, and those of Ryu *et al.*³ and Su *et al.*,¹⁰ the cusp in the γ curve is closely related to the relaxation conditions. Since this result is reproduced by different levels of accuracy (DFT versus force field) and different GSFE calculation methods applied to different metals, it must be related to the metallic bond interactions and is perhaps not an anomaly. We emphasize because of the nature of constraints in GSFE calculations and the lack of phonon stability analysis of these novel structures, e.g. where Su *et al.* predicts a novel dislocation reaction, their physical significance remains unknown.

3.4 GPFE Curve of The New Twinning Route

The experimental results reported by Wang *et al.*⁴ suggest that their newly discovered twinning route could explain why twinning is observed in the FCC metals, with high stacking fault energies, such as Pt, Al, and Ni. Furthermore, they computed a twinning energy landscape to show that their proposed new twinning route is more favorable than the classical one, although molecular statics simulations applied to study deformation at a crack-tip for single and polycrystalline FCC metals¹¹⁻¹³ often show layer-by-layer nucleation and growth of deformation twins even in high stacking fault energy metals. Figure 3.9 is an excerpt from reference.⁴ The computational procedure is a variant of the GPFE calculations. However, the reference structures are either two stacking faults separated by five layers (Figure 3.9 (a), left hand side) or two stacking faults separated by a single layer (Figure 3.9 (b), left hand side). Their simulations involved the emission of a third stacking fault as shown in Figure 3.9 (a) and (b), right hand side. The energy landscapes are reported in Figure 3.9 (c). The barrier for the nucleation of the third stacking fault along path B, γ_{umtf} , is much lower than that along path, A γ_{utf} . Consequently, the authors explain their findings based on this energetic analysis, and propose that the source of the stacking faults (which are in

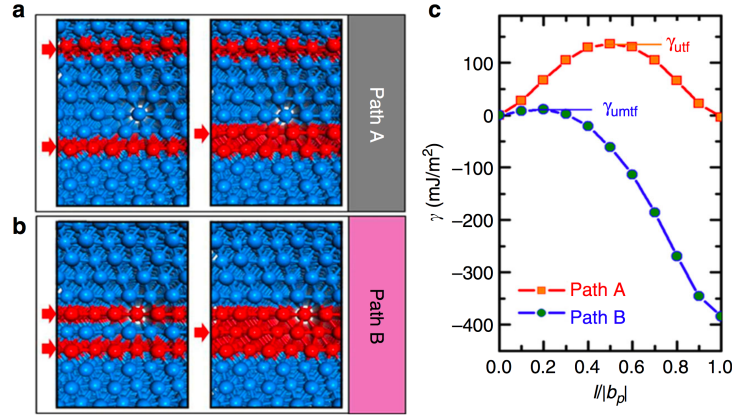


Figure 3.9: Twinning energy landscape from DFT calculations, (a) and (b) for twinning paths A and B. Left hand side, reference structures of two stacking faults separated by several layers or a single layer, respectively; right hand side, the nucleation of an additional stacking fault in the reference structures. (c) The calculated γ surface energies for shearing the crystal from the reference structures in (a) and (b) to the deformed configurations. The three-layer twin is obtained along path B, while the growth of one of the stacking faults by one layer is obtained along path A. Reproduced from article⁴ which is distributed under the terms of the Creative Common Attribution 4.0 International License (<http://creativecommons.org/licenses/by/4.0/>).

their reference structures, which is why the energy starts at 0 in Figure 3.9) are due to the steps on the grain boundaries of the nanocrystalline test specimen of Pt.

Here, we embark on simulating the new twinning route using the GPFE technique, except we assume the reference structure is defect-free. The supercell used is the same as the one used in section 3.2.5. The sequence of steps to analyze the new twinning route are shown in Figure 3.10. The GPFE of the new twinning route is shown in Figure 3.11.

To study the GPFE of the new twinning route, a stacking fault emission in an ideal crystal is simulated, and so we move from configurations (1) to (2) as per Figure 3.10. The energy curve in Figure 3.11 is the same as the one calculated in section 3.2.2, as are the USF and ISF surface energies. Next, we generate another stacking fault but this time separated by five layers for the classical route, and one layer for the new twinning route. We move from configurations (2) to (3) according to Figure 3.10. We define a new barrier, USF' , as the amount of surface energy required to generate a second stacking fault in an ideal crystal (Figure 3.11). We note that USF' values are equal (to within 0.3 mJ/m^2) for both twinning routes. USF' almost equals to the ISF plus the USF; the 0.3 mJ/m^2 difference is because the two stacking faults in the new twinning route configuration are close while they are distant in the classical case. Configuration 3 for both cases contains two separated stacking faults and therefore the energy minimum at 3 corresponds to 2 times the ISF. Finally, the simulation of the emission of the third stacking fault is calculated as the configurations change from configurations (3) to (4), in Figure 3.10. The energy change for the classical and new

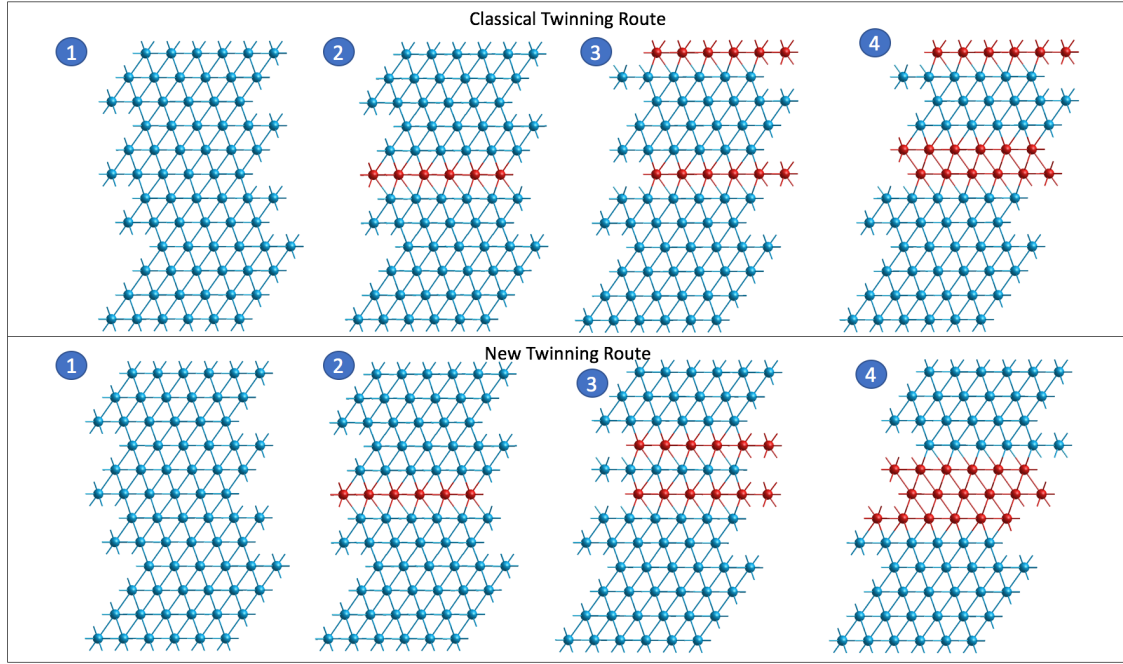


Figure 3.10: The schematic of the configurations used in the calculation of the GPFE curve of the new twinning route versus the classical approach. The images are sequenced from left to right. The numbers correspond to the configurations of the dashed lines on the GPFE curve in Figure 3.11. The red highlights the layers involved in the emission of the stacking fault.

twinning routes are different (Figure 3.11). The UTF barrier is encountered along the classical twinning route. UTF is used here as the designation of the twin nucleation barrier in Figure 3.11 because it was used by Wang *et al.* in their publication in addition to the UMTF (unstable middle twinning fault energy). However, the absolute value of UTF (Figure 3.11) is not to be confused with, and is not equal to, the absolute value of UTF in the GPFE (section 3.2.5, Figure 3.6). The physical significance is that the $(UTF - 2 ISF)$ is equal to 86 mJ/m^2 based on Figure 3.11, about 2 mJ/m^2 higher than the $(UTF - ISF, 84 \text{ mJ/m}^2)$ according to section 3.2.5, Figure 3.6. This small difference is due to the different relaxation conditions in each system because of the different distributions of the stacking faults. UTF describes the barrier to twin nucleation and growth in the structure with respect to the present stacking fault energy. On the other hand, the energy path for the new twinning route involves the UMTF barrier proposed by Wang *et al.*, which we found equals the USF' barrier to within 0.5 mJ/m^2 .

The final structure contains two stacking faults for the classical twinning route and a single stacking fault for the new twinning route, characterized by 2 ISF and ISF energies, respectively. Finally, the shape of the energy path for the new twinning route, starting from configuration (2) to (4), looks very similar to the shape of the full dislocation propagation by partial dislocation (Figure 3.5) shifted upward on the energy axis by the amount of energy for the ISF.

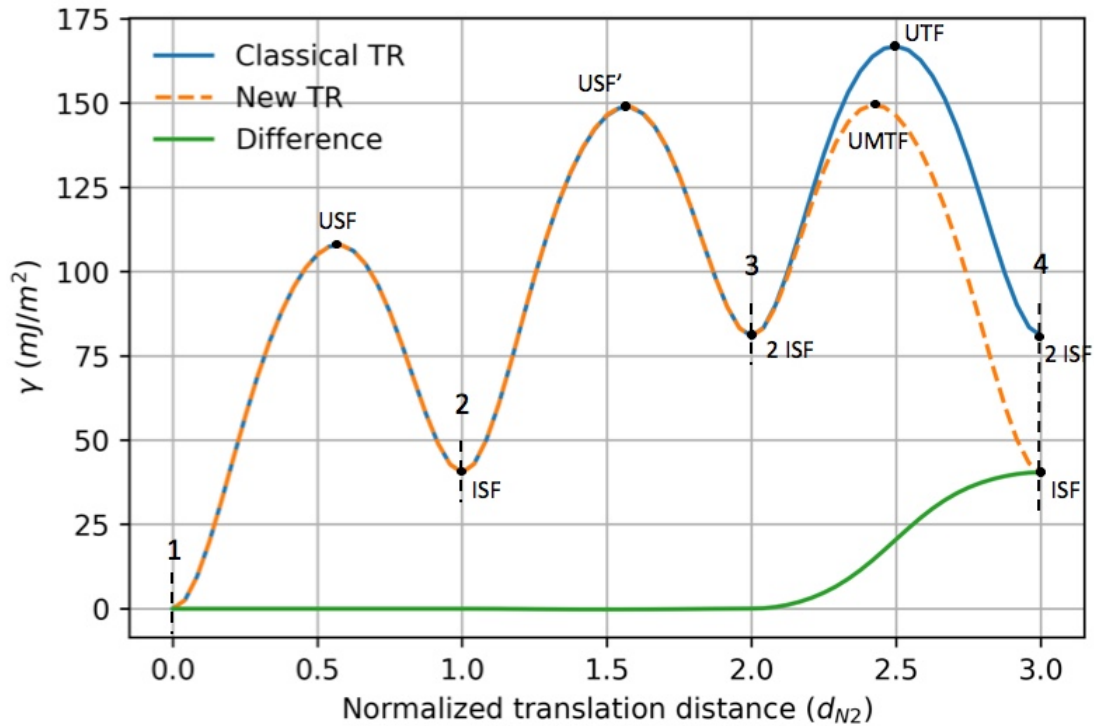


Figure 3.11: The GPFE curve of the classical and new twinning routes.

Wang *et al.*⁴ attributed the source of the new twinning route to be the steps in the grain boundaries of nanocrystalline Pt. Their computation of the twinning energy landscape confirms the new twinning route is energetically more favorable than the classical route. We performed GSFE calculations of the new twinning route starting from an ideal crystal and established relationships between the conventional barriers, USF, ISF and the new barriers USF', UTF and UMTF. Figure 3.11 shows that when a second stacking fault nucleates in the structure, the barriers in general shift upward by the value of the ISF and hence deformation becomes more difficult to proceed along this path since the classical twinning route (GPFE curve in Figure 3.6) would be easier to develop.

3.5 GPFE Curve of β -Oxygen

We construct the geometry in a similar way to FCC Au. β -oxygen has a rhombohedral crystal structure with calculated lattice parameters equal to 4.0735 Å and 48.30°. Figure 3.12 shows an example of the (111) plane supercell of β -oxygen. The relevant crystallographic directions are noted in Figure 3.12 (b). They are the same as those in the (111) of FCC Au owing to the cell symmetry. GSFE and GPFE calculations have been performed as per the procedures described in section 3.2. Supercells of twelve layers in size were used. Translation distances are different than for FCC Au because the lattice vectors in a rhombohedral cell are not aligned along the three Carte-

sian axes and the equilibrium lattice parameters are different. The magnitude of the Burger's vector along the twinning and slipping directions are 1.924 and 3.333 Å, respectively. All the results are summarized in Table 3.2 and Figure 3.13.

The qualitative nature of the energy curves in Figure 3.13 is the same as for the ones reported for

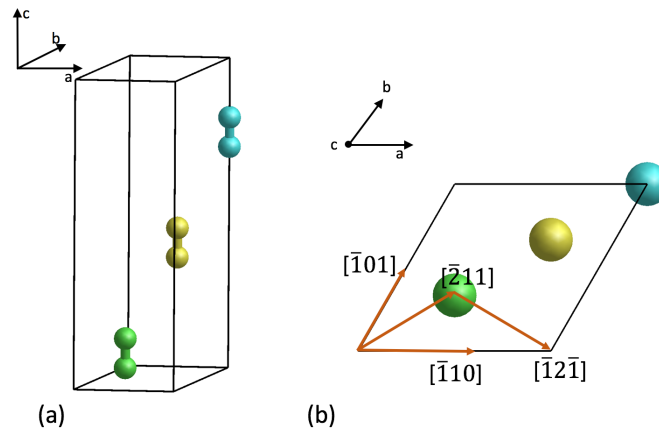


Figure 3.12: (a) 3D view and (b) top view of the (111) β -oxygen supercell. The colors correspond to different ABC stacking sequence.

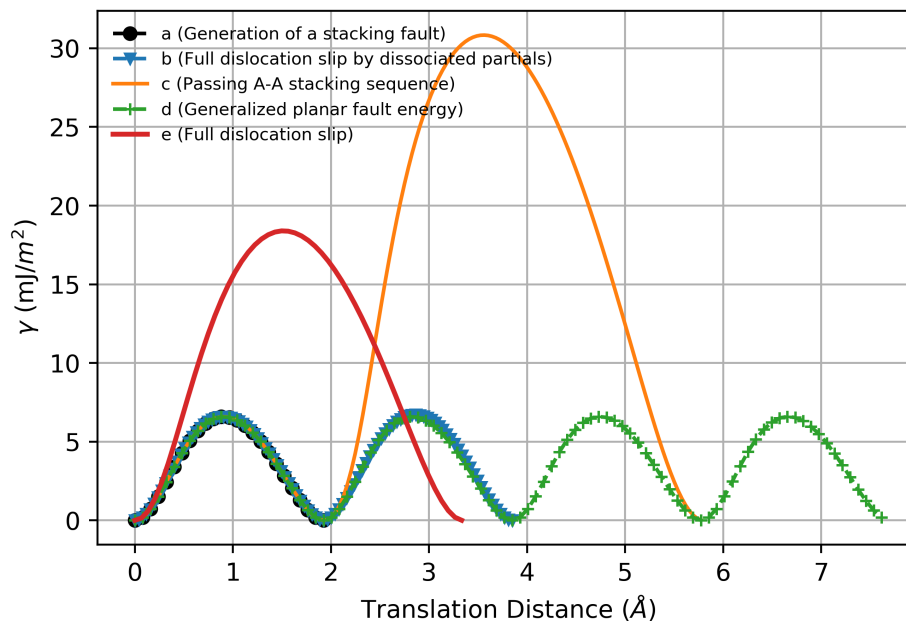


Figure 3.13: The GSFE curves; (a) generation of a stacking fault, (b) full dislocation slip by dissociated partials, (c) passing the A-A stacking sequence, (d) generalized planar fault energy, and full dislocation slip (e) of β -oxygen.

FCC Au. The ranking of the barriers based on the deformation mechanism is consistent, i.e. the UTF is higher than the USF and the TF is larger than the ISF. Compared to FCC Au, the stacking fault energies and the absolute values of the barriers are much less. This is to be expected since intermolecular van der Waals interactions are much weaker than metallic bonds. It is noted the ISF

γ	USF	ISF	UTF	TF	USE	UAA
Value (mJ/m^2)	6.58	0.0069	6.591	0.0087	18.4	30.84

Table 3.2: Summary of the energy barriers and minima from GSFE and GPFE curves of β -oxygen.

value of β -oxygen is $0.0069 mJ/m^2$, three orders of magnitude less than the USF ($6.58 mJ/m^2$, see Table 3.2), while for FCC Au the ratio is only about one order of magnitude different.

Our calculations of the GSFE and GPFE of β -oxygen show qualitative agreement with FCC metals. This indicates a universality of the potential energy hyper-surface between the $\langle 111 \rangle$ planes in FCC Au and oxygen, most importantly, the dissociation of a full dislocation into partial dislocations. This holds at least for β -oxygen, a simple dimer molecule. The calculation of the ISF energy of β -oxygen along the twinning direction gives a very small number, $0.0069 mJ/m^2$. Venables *et al.*¹⁴ calculated the ISF energy of β -oxygen as approximately $0.18 mJ/m^2$. Their value is about two orders of magnitude larger than the one we calculated, presumably due to their more advanced potential, which employs a quadrupole-quadrupole interaction model.¹⁵ However, neither additional computational nor experimental measurements of the ISF of β -oxygen can be found in the literature.

Finally, the different GSFE barriers obtained for β -oxygen will be compared with their counterparts to be obtained via RBSM and TBSM methods.

3.6 Summary

We have performed detailed GSFE energy calculations for the different idealized deformation mechanisms in FCC Au. The GPFE curve describes twinning energetics while the remainder of the methods describe dislocation slip. The most important barriers are the USF and USE linked to the twinning and slip deformation mechanisms. We simulated the new twinning route by Wang *et al.* using the GSFE method and have shown its occurrence in an ideal crystal is more difficult than the occurrence of classical twinning. GSFE calculations were extended to selected FCC metals and β -oxygen. We calculated the barriers and will later compare them against those obtained from our proposed computational methods. The qualitative GSFE curves in (111) are similar between FCC metals and β -oxygen owing to crystallographic symmetry; however, the ratios of the barriers to the local minima (ISF) and their difference is order of magnitudes different due to the different nature of intermolecular interactions. We found Pd exhibits a peculiar GSFE curve and is attributed to the

interactions within a metallic bonds; this peculiar GSFE curve was obtained for different metals using different computational procedures (DFT versus force fields) with different level of accuracy and is thus not an anomaly. This finding supports the motivation to develop the γ -surface method further by considering full relaxation of the atoms, which is a development adopted in RBSM.

Bibliography

- ¹ A. Banerjee, N. Adams, J. Simons, and R. Shepard, “Search for stationary points on surfaces,” *The Journal of Physical Chemistry*, vol. 89, pp. 52–57, 01 1985.
- ² B.-J. Lee, J.-H. Shim, and M. I. Baskes, “Semiempirical atomic potentials for the fcc metals cu, ag, au, ni, pd, pt, al, and pb based on first and second nearest-neighbor modified embedded atom method,” *Phys. Rev. B*, vol. 68, p. 144112, Oct 2003.
- ³ S. Ryu, C. R. Weinberger, M. I. Baskes, and W. Cai, “Improved modified embedded-atom method potentials for gold and silicon,” *Modelling and Simulation in Materials Science and Engineering*, vol. 17, p. 075008, aug 2009.
- ⁴ L. Wang, P. Guan, J. Teng, P. Liu, D. Chen, W. Xie, D. Kong, S. Zhang, T. Zhu, Z. Zhang, E. Ma, M. Chen, and X. Han, “New twinning route in face-centered cubic nanocrystalline metals,” *Nature Communications*, vol. 8, 12 2017.
- ⁵ W. Li, “First-principles description of planar faults in metals and alloys,” *KTH Royal Institute of Technology*, pp. vi, 42, 2014. QC 20141104.
- ⁶ S. Kibey, J. Liu, D. Johnson, and H. Sehitoglu, “Predicting twinning stress in fcc metals: Linking twin-energy pathways to twin nucleation,” *Acta Materialia*, vol. 55, no. 20, pp. 6843 – 6851, 2007.
- ⁷ J. R. Rice, “Dislocation nucleation from a crack tip: An analysis based on the peierls concept,” *Journal of the Mechanics and Physics of Solids*, vol. 40, no. 2, pp. 239 – 271, 1992.
- ⁸ X.-M. Wei, J.-M. Zhang, and K.-W. Xu, “Generalized stacking fault energy in fcc metals with meam,” *Applied Surface Science*, vol. 254, no. 5, pp. 1489 – 1492, 2007.
- ⁹ K. Kang and W. Cai, “Brittle and ductile fracture of semiconductor nanowires - molecular dynamics simulations,” *Philosophical Magazine*, vol. 87, no. 14-15, pp. 2169–2189, 2007.

- ¹⁰ Y. Su, S. Xu, and I. J. Beyerlein, “Density functional theory calculations of generalized stacking fault energy surfaces for eight face-centered cubic transition metals,” *Journal of Applied Physics*, vol. 126, no. 10, p. 105112, 2019.
- ¹¹ S. Hai and E. Tadmor, “Deformation twinning at aluminum crack tips,” *Acta Materialia*, vol. 51, no. 1, pp. 117–131, 2003.
- ¹² D. Farkas, M. Duranduru, W. A. Curtin, and C. Ribbens, “Multiple-dislocation emission from the crack tip in the ductile fracture of al,” *Philosophical Magazine A*, vol. 81, no. 5, pp. 1241–1255, 2001.
- ¹³ D. Farkas, S. Van Petegem, P. Derlet, and H. Van Swygenhoven, “Dislocation activity and nano-void formation near crack tips in nanocrystalline ni,” *Acta Materialia*, vol. 53, no. 11, pp. 3115–3123, 2005.
- ¹⁴ J. Venables, C. English, K. Niebel, and G. Tatlock, “Stacking faults, twins, and the structural stability of van der Waals solids,” *Journal de Physique Colloques*, vol. 35, no. C7, pp. C7–113–C7–119, 1974.
- ¹⁵ C. A. English, J. A. Venables, and C. A. Coulson, “The structure of the diatomic molecular solids,” *Proceedings of the Royal Society of London. A. Mathematical and Physical Sciences*, vol. 340, no. 1620, pp. 57–80, 1974.

Every reasonable effort has been made to acknowledge the owners of copyright material. I would be pleased to hear from any copyright owner who has been omitted or incorrectly acknowledged.

Chapter 4

Rigid Block Shearing Method: Application to FCC Metals

4.1 Introduction

The rigid block shearing method (RBSM) is one of two proposed computational methods to study the deformation of defect-free crystalline material in this thesis. To date, there is a lack of a unified computational framework within which several elementary deformation aspects such as slip barriers, twinning deformation, partial dislocations, ideal shear strength, atomistic strain and stacking faults are described. RBSM is an extension of the generalized stacking fault energy (GSFE) theory¹ through the inclusion of a region of atoms fully relaxed in x , y and z . Unlike the original implementation of GSFE¹ theory, where the computational procedure involves a set of reaction coordinates in a single plane (e.g. the xy plane), the inclusion of the fully-relaxed atom region drastically increases the number of reaction coordinates in the system ($3N_a + 1$, assuming region three relaxes only in z , where N_a is the number of atoms in region one). In order to validate RBSM against experiment data and previous computational findings, it is first applied to Al, Pb, Pd, Au, Ag, Cu, Ni, and Pt FCC metal single crystals because of the extensive previous experimental and theoretical studies on them. FCC Au will be the subject of the main investigation and the deformation barriers and ideal shear strength of the other FCC metals will be provided.

This chapter is divided into five main sections. Section 1 includes the general details of geometry construction for the application of RBSM. Sections 2 and 3 are dedicated to deformation simulations along the slip ($\{111\} \langle 011 \rangle$) and the twinning ($\{111\} \langle 112 \rangle$) systems within which convergence analysis as a function of the system and step sizes will be performed and a variety

of physical phenomena will be uncovered. Section 4 deals mainly with the atomistic definition of strain, compared to other atomic and elastic strain definition as implemented in the Open Visualization Tool (OVITO).² Finally, section 5 provides stress-strain results for FCC Au and a summary of the deformation barriers and ideal shear strengths of the other FCC metals.

4.2 Methodology

RBSM is applied to surface cells constructed from the FCC unit cells (space group $FM\bar{3}M$) of the different metals. GDIS³ is used to generate surface cells of various sizes starting from the energy minimized unit cell. In all our calculations, the rigid blocks, namely regions two and three, consisted of six atoms each where an atom corresponds to a layer in the system. The surface vectors were defined in terms of the Cartesian unit vectors i and j along the x and y axes, respectively, for Au:

$$\vec{a} = 2.88 \hat{i} \text{ (\AA)} \quad (4.1a)$$

$$\vec{b} = 1.44 \hat{i} + 2.49 \hat{j} \text{ (\AA)} \quad (4.1b)$$

The components of the surface vectors in 4.1 are such that \vec{a} and \vec{b} are aligned along equivalent $\langle 011 \rangle$ directions with the twinning direction between them. The $[111]$ direction is aligned with the z axis. Figure 4.1 (a) shows the top view of the (111) plane unit cell containing three stacked atoms, and (b) shows one of the configurations used to study deformation. Surface cells of different

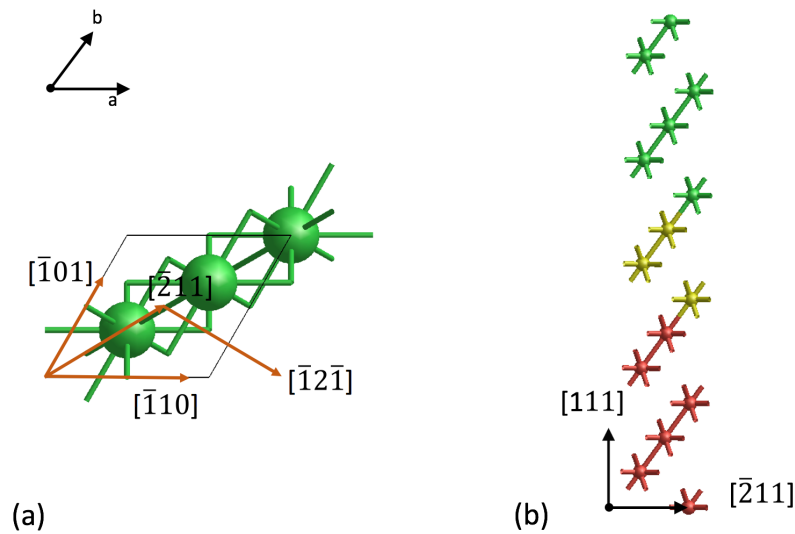


Figure 4.1: (a) Top view of the initial (111) plane unit cell. (b) An example of the geometry of the three layer system to be deformed using RBSM. Region three is colored in green, while region two is in red, and region one is in yellow.

region one sizes are produced to analyze system size effects. The system is subjected to strain by translating region three along a specific direction and optimizing the internal energy. Translation is achieved by specifying two integers corresponding to the translation along \vec{a} and \vec{b} vectors and the number of steps, which determine the strain and step size in the system.

The quasi-static RBSM calculations ultimately result in deformation paths that involve slipped configurations. To explore the topology of the potential energy hyper-surface of the configurations before and after slip, we apply perturbation to selected frames from RBSM via molecular dynamics simulations. We employ the NVT ensemble and solve Newton's equations of motions using the leapfrog Verlet integrator.⁴ A Nosé-Hoover thermostat⁵ of constant 0.1 controls the temperature. Several degrees of perturbation were tested by specifying different MD temperatures. Production simulations lasted 50 ps each. The MD simulations fixed the two rigid blocks (regions two and three) in the frame from RBSM to maintain a constant volume. Following each MD simulation, the last frame is reoptimized by allowing region three to relax in z only, just like the main RBSM simulation, to find any stable local minima.

4.3 Deformation in the $(111)[\bar{1}10]$ System

RBSM was used to study the deformation of FCC Au along the slip system $((111)[\bar{1}10])$. We first summarize the results of the convergence tests for the simulations as a function of the step size and system size. Second, we investigate the slipped configurations in terms of the trajectory and atomistic strain. Third, we analyze the site energies, defined as the potential energy per atom (and consequently layer in these FCC atomic systems), and the differential displacement as a function of strain. Then, the multiplicity of slip is uncovered and studied using the perturbative selective molecular dynamics (MD) procedure. Finally, the occurrence of partial dislocation slip in the simulations will be explained.

4.3.1 Convergence as a Function of System Size

The first set of simulations has the size of region one as a variable. The number of layers in region one was varied from one to eighteen. Because bulk strain in the system is defined according to;

$$\gamma_b = \tan^{-1} \frac{d_{R3}}{h} \approx \frac{d_{R3}}{h} \quad (4.2)$$

where d_{R3} is the translation distance of region three, and h is the height of the system including the interfaces between the rigid blocks and region one, the translation distance per step (d_{R3}) needs to be adjusted such that the strain per step is controlled for all setups. This is achieved by varying the number of steps for each different setup size. Table 4.1 reports the details of the configurations. The definition of normalized strain energy below is useful in calculating the slip barrier;

$$U_{iN} = \frac{\Delta U}{N_a E_c} \quad (4.3)$$

where U_N is the normalized strain energy, i is the index of the barrier, N_a is the number of atoms in region one, and E_c is the lattice energy per atom. In addition, the subscript R (residual) is used in the form U_{iNR} to refer to the frame just after slip of the i^{th} barrier. The results in Table 4.1

N_a	Step Number	d_{R3} /step(Å)	γ /step	U_{1N}	$\gamma_{b,1N}$
1	25800	0.00056	0.00012	0.0194	0.21
3	9000	0.00160	0.00017	0.0088	0.15
6	3600	0.00400	0.00024	0.0072	0.14
7	3000	0.00480	0.00026	0.0071	0.14
8	2580	0.00558	0.00026	0.0070	0.14
9	2280	0.00632	0.00027	0.0069	0.14
12	1650	0.00873	0.00028	0.0067	0.14
18	1080	0.01333	0.00030	0.0066	0.14

Table 4.1: Summary of the simulation parameters and calculated quantities in testing the convergence of RBSM results applied to the slip direction.

demonstrate that U_{1N} and $\gamma_{b,1N}$ converge to about 0.0067 and 0.14, respectively, for system sizes equal to or larger than twelve.

4.3.2 Convergence as a Function of Step Size

A series of step size analyses on the twelve layers system were performed to approach the convergence limit as the step size becomes infinitesimally small, as summarized in Table 4.2. The d_{R3} per step varied from 0.1440 to 0.0144 Å/step. The barriers U_{1N} and the strain before slip $\gamma_{b,1N}$ converge to 0.0067 and 0.14, respectively, at or below 0.00236 strain per step, justifying the step sizes used above in the system size analysis.

The converged barrier has been converted to an energy per unit area per interface, and calculated to be $54.3 \text{ mJ}/\text{m}^2$, which is much smaller than the USE barrier for FCC Au calculated in Chapter

N_a	Step Number	d_{R3} (Å)	γ/step	U_{1N}	$\gamma_{b,1N}$
12	100	0.1440	0.00472	0.0061	0.14
12	200	0.0720	0.00236	0.0067	0.14
12	400	0.0360	0.00118	0.0067	0.14
12	600	0.0240	0.00079	0.0067	0.14
12	1000	0.0144	0.00047	0.0067	0.14

Table 4.2: Convergence as a function of step size for the 12 layer system.

3 ($289 \text{ mJ}/\text{m}^2$). Our results confirm our earlier hypothesis that the barriers from the GSFE method are overestimates of the actual barriers.

4.3.3 Slip Phenomena

After finding the convergence limits from the step and system size analysis, the deformation behavior is investigated. Figure 4.2 shows the evolution of U_N as a function of d_{R3} for the set of simulations in Table 4.1 and shows several unique deformation features:

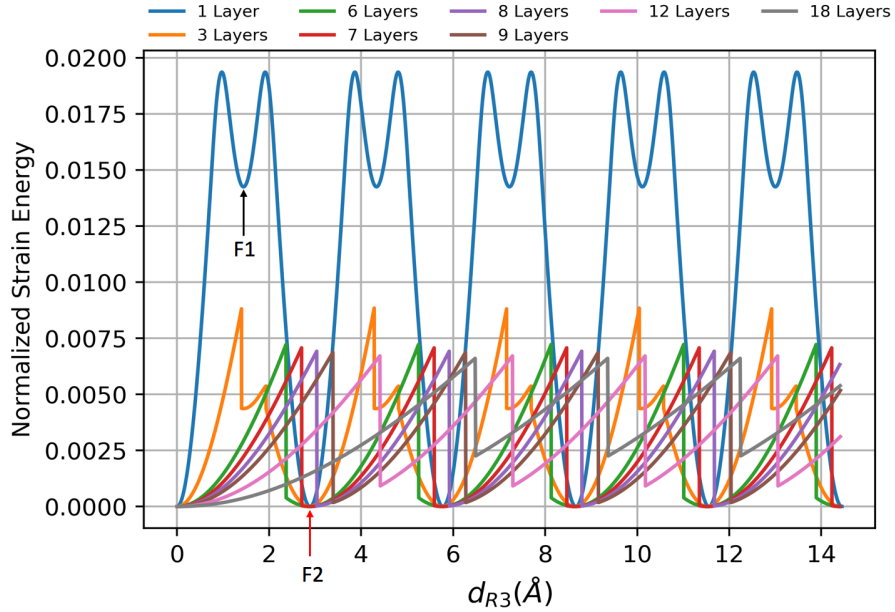


Figure 4.2: Normalized strain energy (U_N) as a function of the translation distance of region three (d_{R3}) for the set of simulations in Table 4.1. The black and red arrows indicate frames that will be analyzed in the main text.

1. In addition to the convergence of the energy barrier, the slip events are periodic for all system sizes.

2. For system sizes equal to or less than seven, the energy curves visit the zero value at $d_{R3} = 2.88 \text{ \AA}$, which equals the lattice vector along this direction, as indicated with the F2 arrow in the figure.
3. The translation distance after which slip happens increases as the size of the system increases. This is because as the number of interfaces between layers in region one increases, and so the overall d_{R3} to trigger slip increases and thus region three needs to be translated further (also can be verified by noting the strain before slip is converged to 0.14, and the height of region one h is higher for larger systems, thus d_{R3} before slip increases according to equation 4.2).

For the case of one layer in region one, the energy curve looks very similar to the one obtained using GSFE by simulating the full dislocation propagation by dissociated partials (see Chapter 3). This is a highly idealized case as the interactions between the rigid blocks is strong. Upon visualizing the trajectory using the visual molecular dynamics program (VMD),⁶ slip does not actually happen but instead the single atom smoothly moves first along the path of a leading partial ($[\bar{2}11]$) and then the trailing partial ($[\bar{1}2\bar{1}]$) dislocations. This is confirmed by considering the displacement vectors of the atom according to;

$$u_{F1} = r_{F1} - r_0 \quad (4.4a)$$

$$u_{F2} = r_{F2} - r_{F1} \quad (4.4b)$$

where u is the displacement vector and r is the position vector. The deformation angles between u_{F1} , u_{F2} and the x axis, which is parallel to the strain direction, are $+30^\circ$ and -30° respectively, which are consistent with the crystallographic angles associated with the leading and trailing partial dislocations.

In the case of three layers in region one, the strain energy increases then the first slip event happens, followed by a second slight increase in the strain energy and a second slip event, after which, the energy smoothly goes back to zero before this cycle is periodically repeated. Visualizing the trajectory shows that slip events happen between layers two and three in region one. Yet, the energy path taken is analogous to the emission of a leading partial dislocation along the $[\bar{2}11]$ (the first slip event) followed by slip along the trailing partial dislocation path, the $[\bar{1}2\bar{1}]$ system. A similar geometric treatment as in the case of a single layer in region one confirmed this result.

For system sizes larger than three, the deformation mechanism involves single slip events where part of the crystal slips in the same strain direction with respect to the other part. Figure 4.3 shows arrow plots of the normalized displacement d_i (normalized with respect to the lattice vector parallel

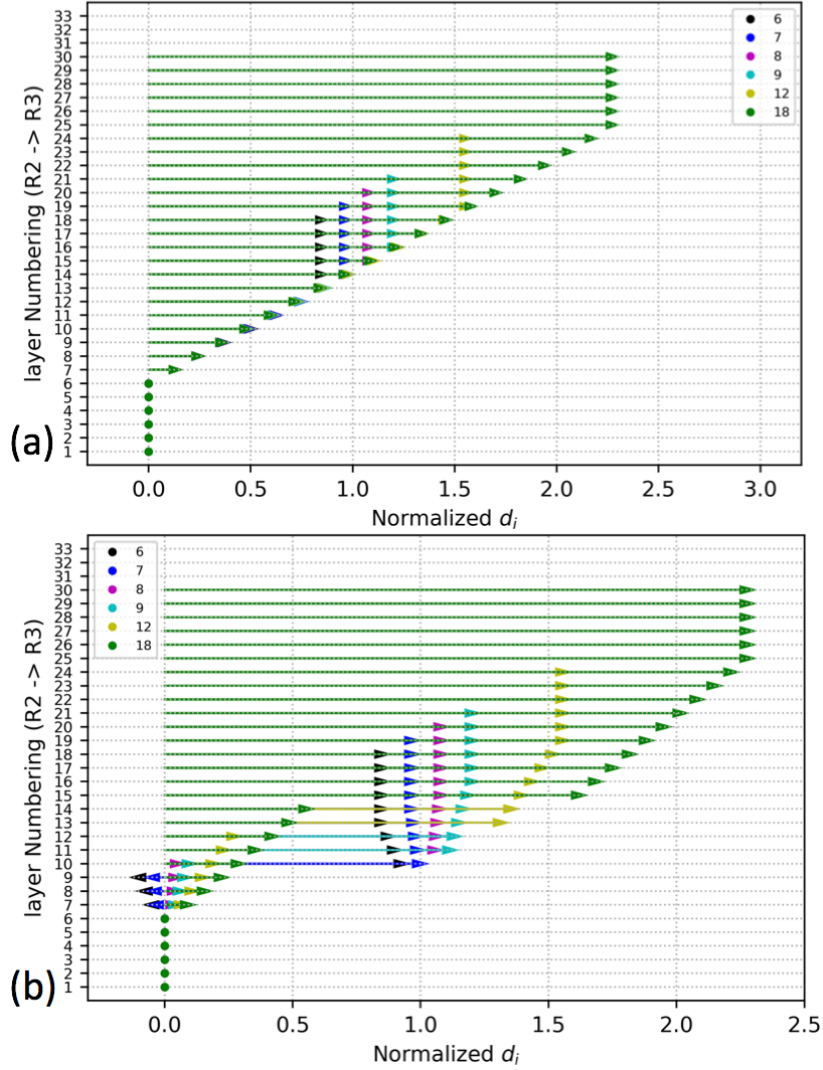


Figure 4.3: Normalized displacement d_i for the layers in the configurations from Table 4.1 for the frames (a) before and (b) after slip.

to the slip direction) of the atoms in the frames before and after slip for system sizes larger than five layers. For the frames before and after slip in Figure 4.3, the atoms in region two are fixed and so have no arrows. For the frame before slip in Figure 4.3 (a), the arrows look homogeneous through region one until the layers of region three where the corresponding d_i values are the same. For the frames after slip in Figure 4.3 (b), the slip interface can be observed as a sudden discontinuity in the homogeneity of the distribution of d_i as a function of layer numbering. For instance, for the eighteen layer system in green, slip happens between layers fourteen and fifteen. In addition, the position of region three after slip is important in determining the normalized displacement d_i profile. For the six and seven layers systems, slip happens when region three translates less than a lattice vector (see Figure 4.3 (a)), i.e. the number of layers is sufficiently small that translating region three less than a lattice vector is required to achieve the required strain energy for the system

to slip. We note for both cases that the d_i values for the layers below the slip interface are negative, as shown in Figure 4.3 (b). This implies the atoms move backward with respect to their original reference positions. Above the slip interface for these two slip systems, the d_i values are the largest and start decreasing as region three is approached, i.e. the atoms are in positions furthest from their commensurate lattice positions. Therefore, based on the results in Figure 4.3, we conclude that the smooth decrease of the energy to zero after a slip event, as observed for the three, six and seven layer results in Figure 4.2, is related to the fact that the first slip happened before reaching a lattice vector in the slip direction. Figure 4.3 (b) also suggests that the slip barrier is independent of the localization of slip, i.e. slip does not always happen in the middle as is the case of the odd layers.

In our first attempts to decipher the atomistic strain and the physical significance of idealized

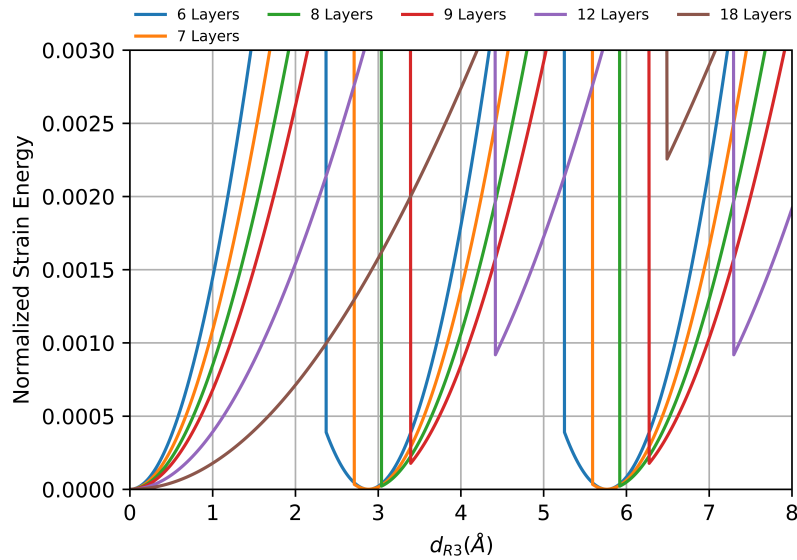


Figure 4.4: Normalized strain energy (U_N) as a function of d_{R3} for a selected set of the simulations in Table 4.1

slip events, we focus on the U_{1NR} frames of selected simulations as shown in Figure 4.4. Energy drops in a non-smooth way when slip happens. After slip, only 6 and 7 layer traces show a smooth decrease on further deformation after slip. We have performed atomistic strain calculations before and after slip (1N and 1NR frames) and also calculated $\gamma_{b,1N}$ values, as listed in Table 4.3. The atomistic strain is calculated according to;

$$\gamma_a = \frac{\sum_{i=1}^{N+1} \Delta d_i}{h} \quad (4.5)$$

where Δd_i is the differential displacement between atoms i and $i-1$. We note that the evaluation of Δd_i for the frame before slip always yields values much less than the lattice vector, as observed in Figure 4.3 (a) if one subtracts one arrow from the adjacent lower arrow, while the Δd_i for the

N	$\gamma_{b,1N}$	$\gamma_{a,1N}$	U_{1NR}	Ranking	$\gamma_{a,1NR}$
6	0.1429	0.1436	0.000389	4	-0.031105
7	0.1429	0.1437	0.000033	2	-0.009186
8	0.1425	0.1432	0.000021	1	0.007384
9	0.1430	0.1437	0.000177	3	0.021487
12	0.1432	0.1439	0.000919	5	0.049961
18	0.1440	0.1447	0.002256	6	0.080575

Table 4.3: Table summarizing the different strain calculations for the frames before and after slip, in addition to the ranking of the energy barriers after slip from lowest to highest.

interface involving slip, as evident in Figure 4.3 (b), is larger than a lattice vector. For this particular interface, a correction is necessary by subtracting a lattice vector from the Δd_i of the slipped interface because atoms after slip fall in the vicinity of commensurate crystallographic positions within periodic boundary conditions. As a general rule, whenever a Δd_i value is larger than half a lattice vector, or $-\Delta d_i$ value is less than minus half a lattice vector, a correction is necessary by subtracting or adding a lattice vector, respectively. The physical interpretation is that the frame of reference becomes the commensurate atomic positions of the ideal crystal.

According to the results in Table 4.3, the calculated $\gamma_{a,1N}$ is very similar to the $\gamma_{b,1N}$. By observing the ranking of the local energy minima U_{1NR} based on the absolute value of the barrier, and by noting that the same ranking is achieved based on the absolute value of the $\gamma_{a,1NR}$, implies that the proposed atomistic strain definition γ_a is able to quantify the residual strain in the structure after slip. One last observation regarding the smooth decrease in energy trend after slip for small size systems is that the $\gamma_{a,1NR}$ is negative for the six- and seven-layer results. This is another powerful feature of the γ_a definition being able to capture such negative internal strains.

To the best of the author's knowledge, our proposed atomistic definition of strain has not been proposed yet in the literature. Vitek⁷ used "displacement maps", similar to differential displacement Δd_i , to study the core of screw dislocations in BCC metals. Vitek later generalized the "displacement maps" concept to dislocation distribution density,⁸ which is the in-plane derivative of differential displacement with respect to coordinates, to describe the displacements near dislocation cores of metallic materials in general. Sempere *et al.*⁹ employed Vitek's dislocation distribution density in their differential displacement analysis to study dislocation cores in HCP Xe. Zimmerman *et al.*¹⁰ proposed the definition of a "slip vector" based on the differential displacement of the near-

est neighbor atoms with respect to an atom, permitting the calculation of the Burger's slip vector which is a useful quantity to quantify the magnitude and direction of slip. Although our atomistic strain definition in equation 4.5 has a very simple form, it calculates the internal strain along the whole deformation path, especially after slip since our definition overcomes the limitation of the bulk strain definition (equation 4.2) tending to infinity since d_{R3} tends to infinity.

4.3.4 Site Energies and Differential Displacement

After introducing the RBSM concept of slip in section 4.3.3 and observing the normalized strain energy profiles as a function of strain, questions arise about the deformation of the structure in the system. Two key parameters are investigated for this purpose, the site energy, defined as the potential energy per atom, which is also the potential energy per layer for FCC metals, and the differential displacement per interface as introduced earlier, as a function of strain. The site energies and differential displacements are reported as a function of d_{R3} for the twelve layer configuration in Table 4.1 in Figures 4.5 and 4.6, respectively.

By inspecting Figure 4.5, we observe a non-linear increase in the site energies as a function of

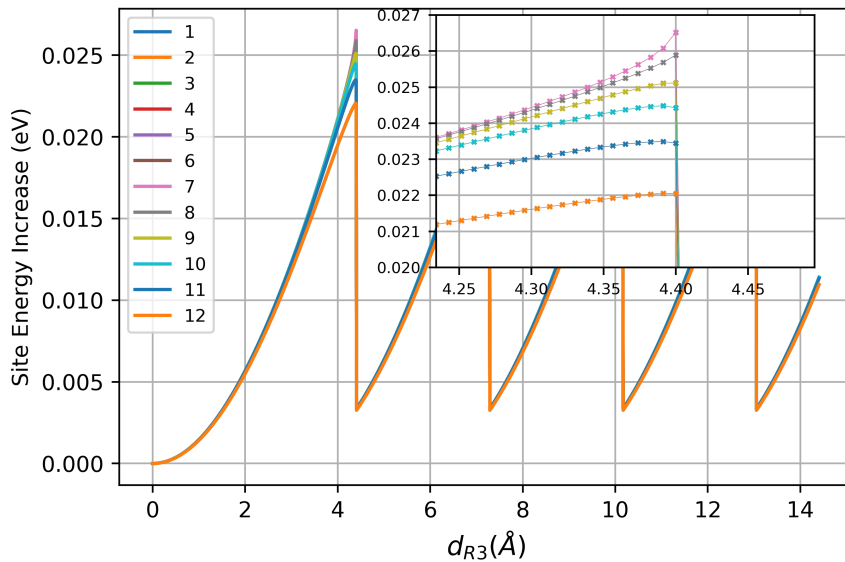


Figure 4.5: The site energy per layer number indicated in the legend as a function of d_{R3} . The inset shows the frames close to slip. The results correspond to the 12 layer case in Table 4.1.

d_{R3} . The evolution is homogeneous up to $d_{R3} \approx 2 \text{ \AA}$ after which a deviation is observed. As d_{R3} approaches the slip frame, the extent of deviation increases. In the frames before slip, the slopes of the site energy curves are very different. The increase in the site energy is the highest for

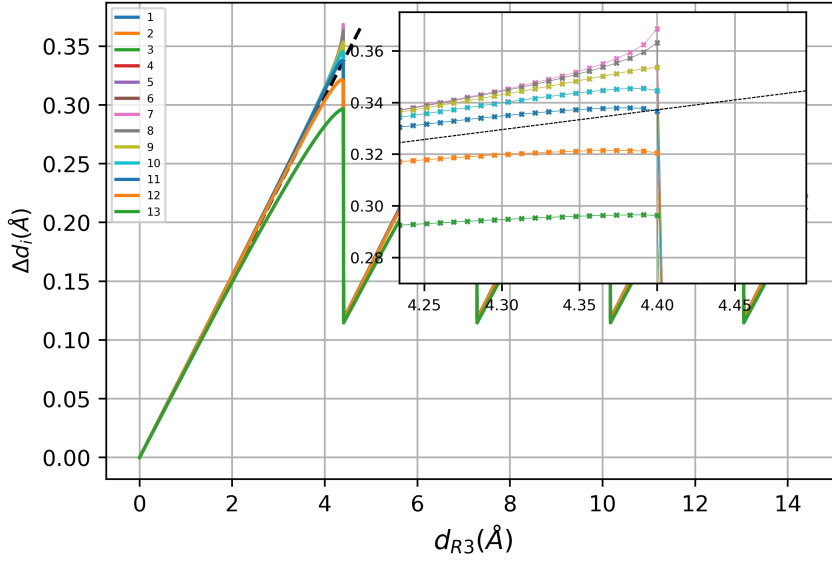


Figure 4.6: The differential displacement per interface indicated in the legend as a function of d_{R3} . The inset shows the zoomed plot of the frames close to slip. The results correspond to the twelve layer case in Table 4.1. The dashed line is based on the linear fit of the data when all the Δd_i s were equal. The legend of the plot represents interfacial indices for Δd_i , e.g. index one between the atom in region three close to region one and the first atom of region one, index two between atoms one and two in region one, etc.

layer number seven, then layers six and eight, whose curves are superimposed on each other, and similarly for five and nine. For the remaining pairs of site energy curves, the curves decrease as a function of d_{R3} . Our findings indicate that slip happens between the layers of the highest difference in the site energy, for this particular case, between layers six and seven.

We now investigate the differential displacement per interface of the same configuration, as shown in Figure 4.6. Since Δd_i is a quantity directly proportional to strain according to equation 4.5, its evolution as a function of d_{R3} is linear, as expected within the framework of linear elasticity theory. However, the same divergence trend is observed beyond a d_{R3} value of $\approx 2 \text{ \AA}$. Deviations from the linear fit (dashed black line in Figure 4.6) are evident and as d_{R3} tends closer to slip the increase in the slope of some Δd_i s and the decrease in others is consistent with the evolution of the site energies.

The observed trends in site energies and Δd_i are common for all converged simulations. Our findings indicate that as the frame of slip is approached, a heterogeneity in the distribution of strain energy occurs throughout the interfaces as a consequence of having rigid blocks in the simulations. Such heterogeneity is interpreted as strain softening in some degrees of freedom, i.e. those atoms and interfaces where the change in energy and Δd_i become abruptly large, and strain hardening in other degrees of freedom, i.e. those where the change in energy and Δd_i is minimal or slightly

negative. In the next subsection, slip phenomena are going to be investigated when modulated by small perturbations.

4.3.5 Multiplicity of Slip

In section 4.3.3, the notion of a single slip deformation mechanism was introduced, which led to metastable energy minima under the constraint of the relative positions of the rigid blocks in regions two and three. Figures 4.5 and 4.6 showed that for the frames after slip, the site energies U_{1NR} and the differential displacement are homogeneously distributed throughout the interfaces. Given the large number of reaction coordinates in the system, are there alternative deformation mechanisms along the slip direction?

To address the above question, perturbative MD simulations were performed on the eighteen-layer case frame U_{1NR} in Table 4.1. The perturbation temperature was varied from 1 to 45 K. At 1 K, the system returns to the same energy minimum found in RBSM, i.e. the single slip energy minimum. For the temperature range 10 to 45 K, the system optimizes to a lower energy minimum characterized by less internal strain in the structure; the differential displacement is homogeneous throughout region one. The finding of a second internal strain energy minimum led us to repeat the MD procedure also at higher temperatures on the U_{1N} frame. The overall results are reported in Table 4.4. The application of the perturbative MD analysis to the configuration of the frame

T (K)	1	10	15	20	25	30	35	40	45	50	70	80	100	150	300
$\gamma_{U_{1NR}}$	356	14.9	14.9	14.9	14.9	14.9	14.9	14.9	14.9						
$\gamma_{U_{1N}}$	353.5	353.5	353.5	353.5	14.4	14.4	14.4	14.4	14.4	14.4	14.4	14.4	135.1	314.4	135

Table 4.4: Summary of the surface energies obtained from the MD perturbation analysis. T is the temperature in Kelvin (K). $\gamma_{U_{1NR}}$ and $\gamma_{U_{1N}}$ are the energy of the local minima converted into a surface energy where the reference is always the unstrained structure. Values of γ are in mJ/m^2 .

before slip U_{1N} (denoted by MD-BS) yields very similar energy minima compared to application of the same to the configuration of the frame after slip U_{1NR} (denoted by MD-AS). For the MD-BS results, the single slip energy minimum is obtained in the temperature range of 1 to 20 K. From 25 to 80 K, the system optimizes to the second internal strain energy minimum identified in the MD-AS analysis. Beyond 80 K, the system optimizes to energy minima that are higher than the second internal strain minimum and lower than the single slip state. The energy minima in Table 4.4 are not exactly equal between MD-AS and MD-BS cases. This is because the translation distance of region three, d_{R3} , is slightly different between the frames. Our results indicate that there are several deformation paths that should be accessible to the system and the barriers to these paths are

separated by very small values. Small changes in the system or the step sizes should enable access to these deformation mechanisms.

Motivated by the findings in Table 4.4, an additional series of RBSM calculations is performed by varying both the step and system sizes. Simulation details, the resulting deformation mechanisms, and U_{1N} barriers are reported in Table 4.5. Our results confirm that small parameter changes in

N_a	Deformation Mechanism	# Steps	d_{R3} /step(Å)	γ /step	U_{1N}
12	Partial Dislocation	560	0.0257	0.00084	0.0067
12	Single Slip	550	0.0262	0.00086	0.0067
14	Single Slip	1380	0.0104	0.00030	0.0067
15	Double Slip	1280	0.0113	0.00030	0.0067
16	Single Slip	1200	0.0120	0.00030	0.0066
17	Single Slip	1120	0.0129	0.00030	0.0066
19	Double Slip	1000	0.0144	0.00031	0.0066
20	Double Slip	940	0.0153	0.00031	0.0066
21	Partial Dislocation	900	0.0160	0.00031	0.0066
22	Double Slip	850	0.0169	0.00033	0.0066
23	Single Slip	810	0.0178	0.00032	0.0066
24	Double Slip	780	0.0185	0.00031	0.0066

Table 4.5: Details of the additional set of RBSM simulations shearing the slip system in FCC Au in addition to deformation mechanisms and the normalized strain energy barriers.

RBSM can push the system along different deformation paths. In addition to single slip, another internal strain deformation mechanism is defined, named “double slip” through which the system slips different distances at two interfaces with respect to the original configuration. Figure 4.7 shows a schematic representation of single and double slip representations for the fourteen and twenty two layer simulations from Table 4.5. The finding of a double slip deformation mechanism further supports our earlier finding that the localization of slip is independent of the barrier.

Seeking additional details related to the deformation mechanisms, a series of perturbative MD simulations has been performed on the pre-slip frames for all the simulations in Table 4.5. Selected results are reported in Table 4.6. γ values are colored according to the type of energy minima; green denotes single slip, blue double slip, pink a third kind of internal strain energy minima, and red stacking fault(s)/twinned regions with or without internal strain. Table 4.5 shows that as the size of the system increases, the number of possible deformation paths increases, as evident with the appearance of the third internal strain set of energy minima for the 24 layer case. This increase in the complexity of the phase-space explains why for system sizes greater than seventeen in Table 4.5, the active deformation mechanisms are most likely not single slip. Finally, even a slight increase in the step size, as in the case of twelve layer configurations in Table 4.5, causes a change in the

potential energy landscape deformation paths.

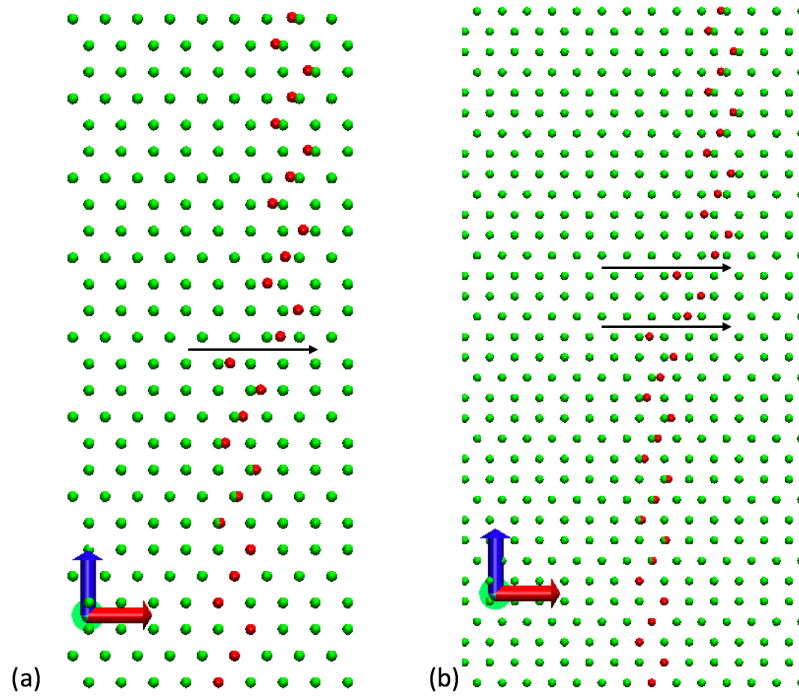


Figure 4.7: Atomic arrangements at the frames after slip for the (a) fourteen layers (singly-slipped) and (b) twenty-two layers (doubly-slipped) simulations in Table 4.5. Atoms in green correspond to the unstrained reference structures and have several images along the x -axis. Atoms in red represent the configurations in the frames just after slip. The Cartesian frame of reference is represented by the red (x) and the blue (z) axes. The y -axis is into the page. Slip direction is aligned along x . The black arrows represent the slip interfaces in both cases.

T (K)	12-FD	12-PD	16 Layers	20 Layers	24 Layers
1	95.6	95.4	261.3	453.6	660.7
5	95.6	95.4	261.3	453.6	169.7
10	95.6	95.4	261.3	51.6	169.7
15	95.6	95.4	261.3	51.6	169.7
20	95.6	95.4	0	51.6	169.7
25	95.6	95.4	0	51.6	169.7
30	95.6	95.4	0	57.6	169.7
35	95.6	67.7	0	51.6	0.1
40	95.6	67.7	0	51.6	0.1
45	67.7	67.7	0	51.6	0.1
50	67.7	95.4	0	57.6	97.0
70	67.7	77.3	0	98.0	178.5
80	109.2	148.7	40.5	175.0	98.5
100	153.6	148.3	40.4	135.3	161.6
150	192.9	171.0	80.8	210.4	264.1
300	232.2	148.8	78.5	138.1	201.7

Table 4.6: Summary of the surface energies obtained from the MD perturbation analysis of selected sizes from Table 4.5; T is the temperature, 12-FD and 12-PD are the twelve layer simulations that yield full dislocation and partial dislocation deformation mechanisms, respectively. All γ values are in mJ/m^2 .

Next, simple mathematical models of slip pathways are sought to assist us in understanding and predicting slip deformation. r_k is defined as the sum of the differential displacement after slip;

$$r_k = \sum_{i=1}^{N+1} \Delta d_{i, \text{ after slip}} \quad (4.6)$$

where index k represents SS, for single slip, DS for double slip, etc. r_k is plotted as a function of the translation distance of region three, d_{R3} , before slip in Figure 4.8 for the single slip minima, where the differential displacement was taken from the MD perturbation analysis (since we have indicated in the previous passages that the single slip energy minima from MD are equivalent to those from RBSM), and double slip whose differential displacement are calculated from RBSM frames, for different system sizes.

The minima were fitted using linear regression and the below models are obtained:

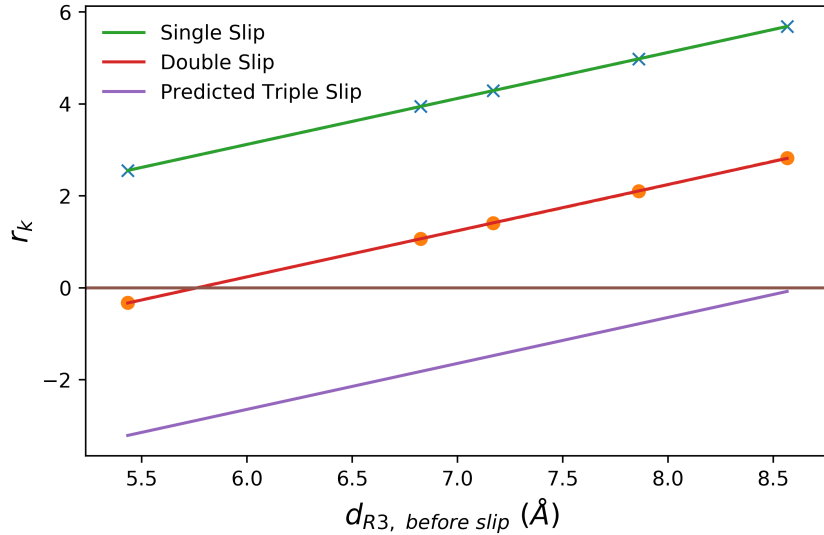


Figure 4.8: The sum of the differential displacement after slip (r_k) as a function of the translation distance of region three (d_{R3}) before slip. x symbols are for single-slip results while solid circles are for double slip. Linear fit models are shown. The system sizes are arranged from the left to the right hand side of the figure as fifteen, nineteen, twenty, twenty two and twenty four layers. Note that if both axes are divided by the height of the system, the plot becomes representative of the strain after slip as a function of the strain before slip.

$$r_{SS} = d_{R3, \text{ before slip}} - 2.879995 \dots (\text{\AA}) \quad (4.7a)$$

$$r_{DS} = d_{R3, \text{ before slip}} - 5.789529 \dots (\text{\AA}) \quad (4.7b)$$

The first finding is that the fitting coefficients in the r_k models are very close to the magnitude of the lattice vector along the slip direction for single slip (2.88 Å), and twice the magnitude for double-slip (5.76 Å). Indeed, the r_{SS} model now explains the negative internal strain after slip for the six and seven layer cases in Table 4.3 as Figure 4.3 (b) clearly shows that slip happened when

d_{R3} was less than a lattice vector, leading to a negative r_{SS} .

According to the observed trend of r_k models, and given that unknown internal strain energy minima have been identified for the 24 layer case in Table 4.6 (and also for the twenty one layer case not reported here), a triple slip pathway is predicted:

$$r_{TS} = d_{R3, \text{ before slip}} - 8.64 \dots (\text{\AA}) \quad (4.8)$$

To verify the model given in equation 4.8, RBSM d_{R3} values before slip for the twenty one and twenty four layer cases (7.5200 and 8.5662 \AA , respectively) are substituted and the predicted r_{TS} are found in excellent agreement with the sum of the differential displacements calculated from the MD perturbation analysis.

Atomistic strain γ_a is defined according to equation 4.5; the displacement d_i is always taken with respect to the original atomic positions. Δd_i is evaluated by taking the difference between consecutive d_i . Another useful way to define the atomistic strain is to determine the d_i terms first, and then to subtract or add depending on the strain direction lattice vector(s) until the d_i falls into the interval: $[-p/2, p/2]$; where p is the repeat vector along the strain direction. The new displacements are defined as d_{ci} ; where c stands for symmetry correction. Afterwards, γ_a calculations can be performed but using d_{ci} rather than d_i . Whether d_{ci} or d_i is used in the γ_a calculation is found to give the same answer.

The success of the d_{ci} definition of strain implies that the commensurate equilibrium lattice positions in 3-dimensional periodic space can be used as a reference structure in calculating strain. Using this notion, a method to calculate the lowest possible differential displacement is described. For instance, Table 4.6 shows that the lowest surface energies for the sixteen and twenty four layer cases, representative of double and triple slip, respectively, are close to zero. The double slip surface energy for the sixteen layer case is lower than the triple slip surface energy for the twenty four layer case because Figure 4.8 shows the following relation: as the size of the system increases, the $d_{R3, \text{ before slip}}$ increases, and thus the order of slip that would lead to the lowest energy after slip changes. Their differential displacements were calculated as 0.024 and -0.074 \AA , respectively. To predict such quantities, $d_{c,R3}$ after slip is calculated which resulted in the predicted differential displacements being in excellent agreement with the MD perturbation analysis. This geometric rule was applied to all the configurations reported in Table 4.5 and resulted in the successful prediction of the lowest Δd_i , i.e. the lowest local energy minimum according to Table 4.6. In other words, if d_{R3} before slip is known, then $d_{c,R3}$ can be evaluated from which the lowest possible Δd_i can be found. This is analogous to plugging d_{R3} before slip into slip models 4.7 and 4.8 and finding the

lowest r_k .

Equation 4.7 (a) can be rearranged into:

$$d_{R3, \text{ before slip}} - r_{SS} = 2.88 \dots (\text{\AA}) \quad (4.9)$$

Equation 4.9 describes the periodicity of single slip events in RBSM along the slip direction such that single slip will be repeated when d_{R3} translates by an additional lattice vector (2.88 \AA). The same applies for double and triple slip. To verify such a prediction, the periodicity of selected simulations representing the variety of deformation mechanisms is shown in Figure 4.9. All the curves were shifted such that the U_{1NR} frame is at the zero point on the x -axis. Figure 4.9 confirms our

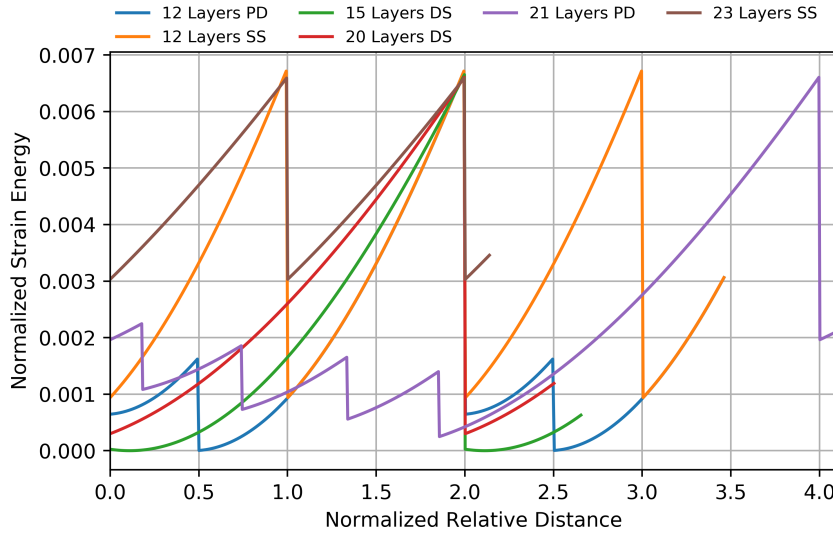


Figure 4.9: Periodicity of slip events for selected configurations from Table 4.5. PD, SS, and DS correspond to partial dislocation, single and, double slip. The translation distance of region three d_{R3} is normalized by the magnitude of the repeat vector along the slip direction. All curves were shifted such that the zero point on the x -axis represents the frame after slip.

prediction that for single slip, the periodicity of the response repeats after a lattice vector, for double slip, two lattice vectors etc. Even for partial dislocation slip for the twelve and twenty one cases, the overall periodicity remains valid for every integer multiple of the lattice vector. This suggests that our multiplicity of slip analysis extends to partial dislocation deformation mechanisms.

Sinha and Kulkarni¹¹ performed NVT MD simulations on about 50,000 atoms by shearing bicrystals of selected FCC metals containing a coherent twin boundary (CTB) using rigid blocks, i.e. the MD version of RBSM where dynamics emerge through simulating temperature and a high strain rate of 10^8 per second. Figure 4.10 shows the stress versus strain results obtained by Sinha and Kulkarni in addition to the representative geometry. The top block (not shown in the figure) is translated with respect to the bottom block (fixed, not shown in the figure) along the twinning di-

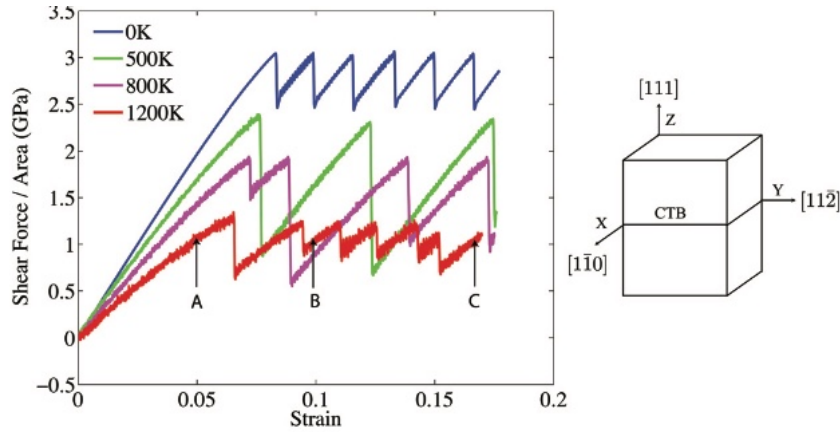


Figure 4.10: Shear stress versus strain plots as a function of temperature resulting from the shear of Cu bicrystals. The crystallographic orientations are shown in the right hand side of the plot. Reproduced from,¹¹ with permission from AIP publishing.

rection and so the bicrystal shears. The authors note for some temperatures, e.g. 500 K in Figure 4.10, there is a large drop in the stress and a change in the periodicity of the response attributed to the migration of the CTB by several lattice sites simultaneously. Sinha and Kulkarni relate such events to thermal fluctuations providing the excess energy to overcome the activation barrier. This result is consistent with our proposed multiplicity of slip and especially the predictions based on the periodicity (Figure 4.9). Sinha and Kulkarni also found twinning deformation being promoted at higher temperatures but stated that they could not provide an explanation of this result. Although our MD perturbative analysis is applied to the slip direction, the prediction of twinning/stacking faults in addition to internal strain being promoted at higher temperatures (see Table 4.6) is consistent with the results by Sinha and Kulkarni in that the high-perturbation regime of FCC metals leads to the emission of twinned portions/stacking fault(s).

The quantized relaxation states of strain after slip emerging from the multiplicity of slip models can also provide an alternative interpretation of the experimentally-observed quantized plastic deformation in gold nanowires.¹²

4.3.6 Partial Dislocation Slip

Two partial dislocation slip mechanisms for twelve and twenty one layer configurations were identified in Table 4.5. Partial dislocations were introduced in Chapter 3 and were considered one of the possible deformation mechanisms according to GSFE analysis. In our RBSM calculations, partial dislocations emerge spontaneously as a response of the system to mechanical deformation. In both the twelve and twenty one layer cases, the partial dislocation is incomplete; region three can not relax in the xy plane while atoms close to the slip interface are characterized by the highest partial-

dislocation properties.

To show that partial dislocation slip occurs, energy re-optimization of all RBSM frames by re-

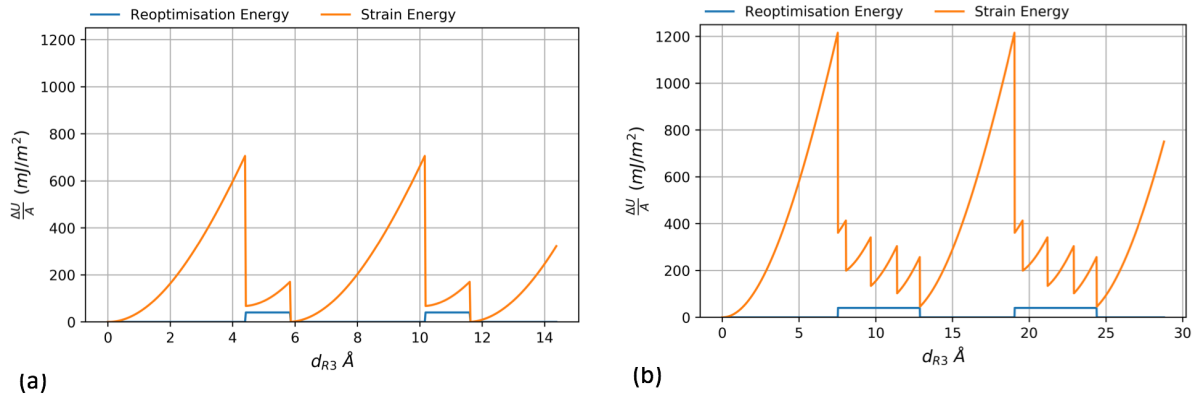


Figure 4.11: Strain and re-optimized surface energy as a function d_{R3} for the twelve and twenty one layer configurations, Table 4.5. The re-optimization energy equals 0 where the curve is not visible.

moving the constraints is performed, i.e. region three can now relax in x , y and z . The results are reported in Figure 4.11. The results indicate that for both cases with a partial dislocation, the re-optimization energy equals the ISF energy of FCC Au ($40 \text{ mJ}/\text{m}^2$). The trajectory was visualized and confirmed that the partial dislocation for the twelve layer case involves the emission and annihilation of a single stacking fault, while for the twenty one layer case involves the emission of a four layer twinned region followed by the annihilation of the twins via trailing partial dislocations, as can be deduced from Figure 4.11 via the micro-slip events in the interval when the surface energy equals to the ISF.

Our previous perturbation analysis, and the occurrence of the idealized full dislocation and partial dislocation slip at the converged U_{1N} barriers, adds valuable insight. For instance, Yamakov *et al.*¹³ used molecular dynamics deformation simulations to propose that the transition from a full dislocation deformation mechanism to partial dislocation depends on the elastic properties of the material and the stacking fault energy (ISF). Swygenhoven *et al.*¹⁴ disputed these findings and instead proposed that the switch in the deformation mechanism has to be analyzed in terms of the ratio ISF/USF and not the ISF alone. Our analysis of the results for FCC Au indicates that both deformation mechanisms can activate during quasi-static deformation at the converged barrier U_{1N} . Small perturbations, likely characteristic of thermal vibrations, control the multiplicity of slip models and the partial dislocations. High perturbations that can be imparted into a test specimen via shock deformation / impulse excitation tend to deform the system along energy paths that involve the emission of partial dislocations (with single/multiple stacking fault(s)/twins as per our findings

or several layer twinned portions as reviewed by¹⁵). This conclusion is further supported by our previous MD perturbation analysis.

We emphasize that our U_{1N} barrier is related to the occurrence of the instability in ideal systems irrespective of the path beyond the instability. Our method to investigate the barriers does not seek to evaluate the activation free energies of surface dislocations, as in references^{16,17}, but rather to gain insights about the zero-temperature barriers of deformation processes under specific idealized constraints along different slip systems. This implies that our methods can not nucleate full dislocations or dislocation loops, except partial dislocations since those are related to stacking sequences.

4.4 Deformation in the $(111)[\bar{2}11]$ System

In this section, RBSM is applied to study twinning deformation in FCC Au in $(111)[\bar{2}11]$, the known twinning system.¹⁸ The geometry of the configurations are generated as per the methodology section. First, convergence analysis is performed in terms of the system and step sizes. Second, twinning deformation mechanisms are introduced and the physical process is explained. Third, twinning is analyzed in detail through differential displacement, re-optimization energy and multiplicity of slip linear models. Finally, alternative twinning deformation pathways are discussed.

4.4.1 Convergence Analysis

RBSM convergence was tested when applied to the twinning direction by varying the system sizes as summarized in Table 4.7. The U_{1N} barrier converges to 0.0046 for system sizes equal to or

Setup	N_a	Step Number	d_{R3} /step (Å)	γ /step	U_{1N}
1	3	9240	0.0016	0.00017	0.0057
2	6	3720	0.0040	0.00024	0.0049
3	9	3900	0.0064	0.00027	0.0047
4	12	3960	0.0088	0.00029	0.0046
5	18	2900	0.0138	0.00031	0.0046
6	24	3760	0.0186	0.00032	0.0046

Table 4.7: Summary of the simulation parameters and results of the setups used in RBSM to test the convergence of the barrier as a function of the system size along the twinning direction. The strain before slip for all cases equals to 0.14.

greater than twelve. The barrier is converged at the very small strain step of 0.00029. Next, step

size analysis simulations were performed on the twelve layer system and are summarized in Table 4.8. U_{1N} and $\gamma_{b,1N}$ converge to 0.0046 and 0.14, respectively, at a strain step equal to or lower than

Setup	Step Number	d_{R3} /step (Å)	γ /step	U_{1N}	$\gamma_{b,1N}$
1	100	0.2972	0.0097	0.0027	0.29
2	200	0.1486	0.0049	0.0043	0.15
3	400	0.0743	0.0024	0.0046	0.14
4	600	0.0495	0.0016	0.0046	0.14
5	1000	0.0297	0.0010	0.0046	0.14

Table 4.8: RBSM convergence of the normalized strain energy as a function of step size when applied to the twinning direction of the 12 layer system.

0.0024. We note that the critical step and system sizes for RBSM convergence are very similar between the slip and twinning simulations.

The converged slip barrier have been calculated along the twinning (0.0046) and slip directions (0.0067) for FCC Au. Our ranking of the slip systems in FCC Au is consistent with the ranking based on GSFE (107 and 289 mJ/m^2 , for the USF and USE from Chapter 3). However, converting our converged U_{1N} barriers to energy per unit area per interface yields 37.6 and 54.3 mJ/m^2 for the equivalents of USF and USE, respectively. This result further confirms our hypothesis that GSFE calculations of the barriers are significant overestimates. Surprisingly, it has been accepted in the scientific community that USF is always greater than the ISF, e.g. see references.^{14, 19–21} Our results provide the first theoretical numerical evidence that USF is actually less than the ISF of FCC Au (40 mJ/m^2). Rice¹⁹ who proposed the definition of USF in developing his dislocation nucleation model from a crack tip, considered a ratio of the USF to ISF in the range of two to four. Our calculations for FCC Au indicate that the ratio of the relaxed barriers is close to unity (0.94 - 1.35; whether evaluating USF/ISF or USE/ISF). This is expected to have a direct impact on dislocation-based models and theories that describe deformation through GSFE barrier calculations.

4.4.2 Twinning Deformation Mechanism

After establishing the convergence parameters, twinning deformation is described. Figure 4.12 shows the normalized strain energy as a function of d_{R3} for the 1000 step configuration in Table 4.8. As the system is strained, the normalized strain energy increases to reach the U_{1N} barrier and then the first slip event happens. This event corresponds to the emission of a stacking fault. Sub-

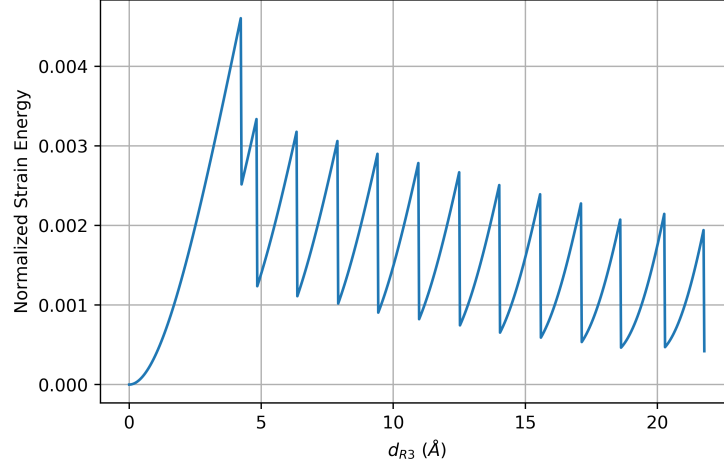


Figure 4.12: Normalized strain energy as a function of the translation distance of region three for shearing along the twinning direction ($\bar{2}11$) using RBSM.

sequent application of strain causes $U_{iN}, i>1$ slip events by which the stacking fault grows into a two layer stacking fault, three layer twinned region, etc. until all the interfaces in region one and between region one and regions two and three twin. We observe the general trend that $U_{(i+1)N} < U_{iN}$; for $i>1$, implying that it should be easier for the twin to grow as a function of strain. The last two twinning events are exceptions to the decreasing barrier. This is where twinning happens at the interfaces between region one and the rigid blocks.

Figure 4.12 can be directly compared to the corresponding figure for the generalized planar fault energy (GPFE), Chapter 3. In Figure 4.12, the first micro-slip event corresponds to the emission of a stacking fault and subsequent micro-slip events lead to the growth of the stacking fault into a twin. This sequence of physical events is consistent with GPFE. However, the subsequent twinning barriers from RBSM follow the relation $U_{(i+1)N} < U_{iN}$, for $i > 1$, and thus contradict the GPFE result of the UTF barrier (calculated in Chapter 3 using GPFE) being higher than the USF.

Tadmor and Hai²² produced an analysis similar to Rice¹⁹ but to describe twinning deformation from a crack tip and thus proposed a new material parameter named the UTF, defined as the resistance of the lattice to nucleate a second stacking fault adjacent to an existing stacking fault in the structure. They also proposed a general formulation of the twinnability parameter. Bernstein and Tadmor²³ developed Tadmor's model further and formulated the twinnability parameter to describe the twinning tendency in polycrystalline FCC metals according to;

$$\tau = \left[1.136 - 0.0151 \right] \frac{\gamma_{isf}}{\gamma_{us}} \sqrt{\frac{\gamma_{us}}{\gamma_{ut}}} \quad (4.10)$$

where τ is the twinnability parameter, the constants in the brackets are the outcome of a normalization procedure across all directions, and γ_{isf} , γ_{us} , and γ_{ut} , are the surface energies of ISF, USF and UTF, respectively. Our RBSM analysis identifies different ratios than those proposed by GPFE and GSFE curves and calls for a re-evaluation of the twinnability parameter.

4.4.3 Twinning Deformation Analysis

Deformation twinning is analyzed in RBSM using two different procedures. The first procedure performs energy re-optimization of all the RBSM frames by removing the constraints, i.e. region three can relax in three-dimensional space, allowing for the detection and energetic measurements of possible local minima including stacking faults, twinned regions, polymorphs or phase transformations. The second procedure relies on the geometric description of the deformation process. The magnitude of Burger's vector along the twinning direction underpins the twinning physical coefficient which is predicted based on dislocation theory,²⁴ e.g. for FCC metals, $\vec{b}_{twinning} = |\frac{1}{6}[\bar{2}11]|$. Our differential displacement Δd_i should be comparable to $|\vec{b}_{twinning}|$. Figure 4.13 shows the re-

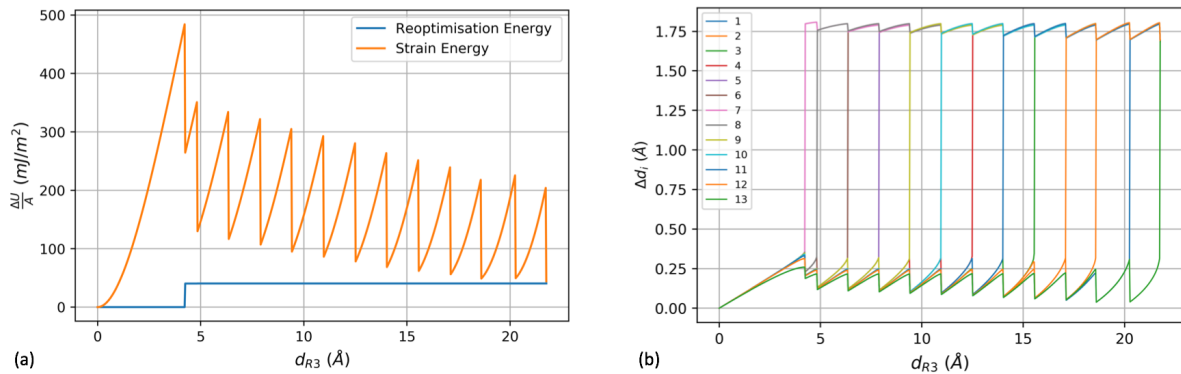


Figure 4.13: Plot of (a) strain and re-optimized strain surface energies and (b) differential displacement Δd_i as a function of the translation distance of region three for 1000 step configuration in Table 4.8. In (b), index one (i.e. Δd_1) refers to the interface between region three and the first atom in region one, index two (i.e. Δd_2) refers to the interface between atoms one and two in region one, etc.

sults for the application of the two investigative procedures to analyze twinning deformation for the 1000 step configuration in Table 4.8. The re-optimized strain surface energy in Figure 4.13 (a) equals the intrinsic stacking fault (ISF) energy of FCC Au for the frame after slip U_{INR} . As the stacking fault grows into twins, the re-optimized energy still equals the FCC Au ISF energy to within $0.2 \text{ mJ}/\text{m}^2$. This slight difference is due to the interaction of the twin boundaries with the remainder of the neighboring atoms. On the other hand, the differential displacement, as shown in Figure 4.13 (b), starts increasing linearly and homogeneously until the frames before the first slip event happens, where a slight divergence is observed similar to that along the slip direction.

Following the first twinning event, an overall relative displacement Δd_7 of 1.8 Å occurs between layers six and seven, second twinning Δd_8 event between layers seven and eight, etc. Following the last twinning event, all Δd_i s have a value of 1.7 Å, very close to the theoretical $|\vec{b}_{twinning}|$ of 1.66 Å. The order of twinning is readily inferred from Figure 4.13 (b). These findings based on the re-optimization and differential displacement procedures are generally consistent for all the twinning results when the deformation mechanism involves the emission of a single stacking fault.

Based on the analysis of the system size convergence simulations in Table 4.7, deformation mechanisms are classified based on the number of stacking faults emitted in the configuration of the U_{1NR} frame. The single-stacking fault (SSF) emission mechanism activates for system sizes between three and twelve layers, and the double-stacking fault (DSF) emission mechanism for the eighteen and twenty four layer configurations. The three layer simulation showed that at the configuration of U_{1NR} frame and beyond, the energy smoothly decreases to a minimum before it increases again, consistent with similar observations when RBSM was applied to the slip direction. The proposed slip models in equation 4.7 linked this energy behavior to the multiplicity of slip and d_{R3} when slip happened. Motivated by the same reasoning, we have plotted the sum of the differential displacement before slip, r_{SSF} , as a function of the translation distance of region three for selected configurations from Table 4.7 in Figure 4.14. The variation of r_{SSF} as a function of $d_{R3, before slip}$ is linear:

$$r_{SSF} = d_{R3, before slip} - 1.66 \dots (\text{Å}) \quad (4.11)$$

This relationship shows that for the SSF deformation mechanism, r_{SSF} is linearly related to d_{R3} and the magnitude of the Burger's vector along the twinning direction $|\vec{b}_{twinning}|$, rather than the lattice vector (which in the twinning of FCC metals corresponds to three times $|\vec{b}_{twinning}|$). Hence, our results show that the multiplicity of slip extends beyond slip deformation to cover also the twinning deformation. Small parameter changes in RBSM simulations should enable the activation of different twinning deformation mechanisms.

4.4.4 Alternative Twinning Deformation Mechanisms

One of the recent findings by Wang *et al.*²⁵ is the proposed new twinning route which was extensively reviewed in Chapter 3. Briefly summarized, the new twinning route involves the emission of two stacking faults into the crystal separated by an interface of the ideal structure with the grain boundaries being the source of the stacking faults. Then, a third stacking fault is emitted between the previous two stacking faults and a three layer twin forms. The authors found that this is an

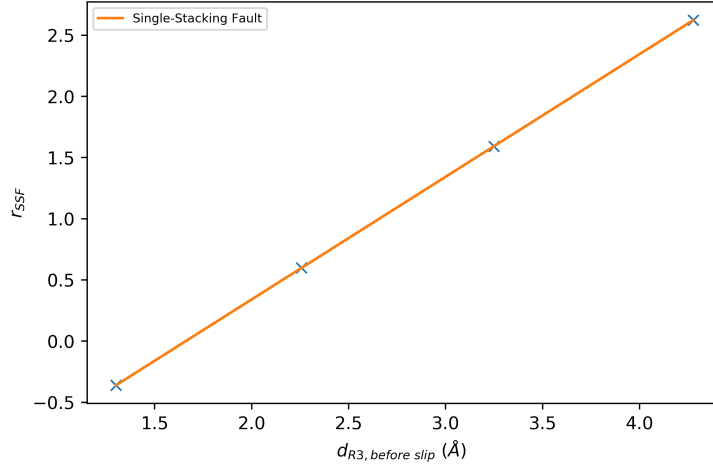


Figure 4.14: Plot of the sum of the differential displacement before slip, r_{SSF} , for the single-stacking fault deformation mechanism as a function of the translation distance of region three after slip. The data points from the left to the right mark the r_{SSF} values for the three, six, nine and twelve layer configurations in Table 4.7. Dividing both axes by the height of region one, gives the strain on each axis.

easier route to twinning compared to the classical route.

Several simulations have been attempted to find a deformation path similar to the proposed new twinning route by Wang *et al.*. RBSM was applied to the eighteen layer setup in Table 4.7 and the step size was slightly changed. Instead of having region three translated by eight lattice vectors along a and b over the course of 2900 steps, same translation have been achieved but in 2915 steps resulting in an almost negligible change in the strain and step size. The new U_{1N} barrier is found equal 0.0046, the same as the converged barrier. Figure 4.15 shows that this new deformation mechanism is very similar to the one proposed by Wang *et al.* As the crystal is sheared, the strain energy increases toward the U_{1N} barrier and then a twinning event happens corresponding to the emission of two stacking faults. This is supported by the re-optimized strain energy in Figure 4.15 (a) which equals 81 mJ/m^2 , almost exactly twice the ISF of FCC Au (40 mJ/m^2). Figure 4.15 (b) indicates that two stacking faults are emitted, the first between layers eight and nine (index 9, the plot with + symbol) and the second between layers ten and eleven (index 11, the cyan plot). More deformation is applied to the system and a second twinning event happens characterized by the barrier U_{2N} which is significantly lower than both U_{1N} and U_{3N} . The re-optimized energy is now 40 mJ/m^2 , the ISF of FCC Au. The twinning interface of the second twinning event in Figure 4.15 (b) is traced and it's index was found equal ten, between layers nine and ten, further confirming the merger of the two stacking faults into a three layer twinned region. Twinning evolution then proceeds as recorded earlier for the SSF case.

RBSM shows several new insights regarding twinning deformation mechanisms. First, multiple

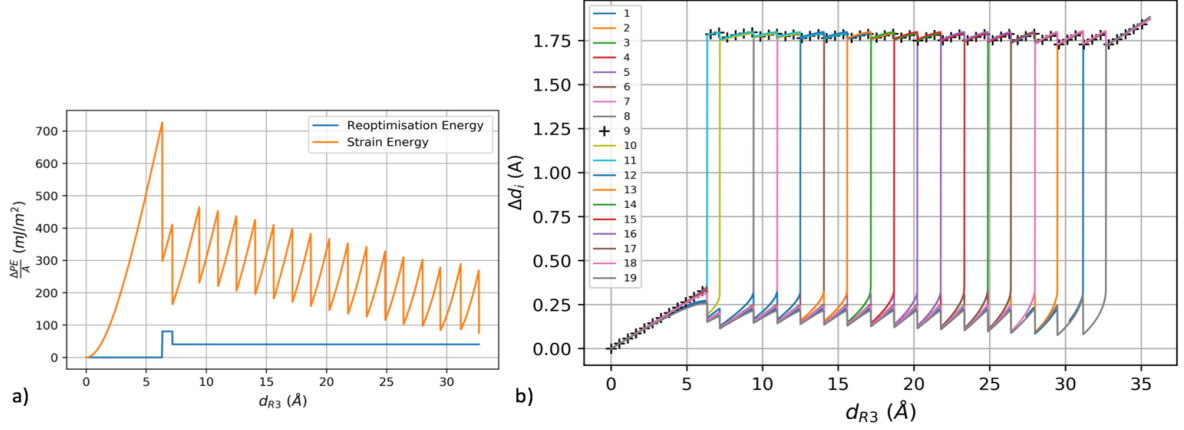


Figure 4.15: (a) Strain and re-optimized surface energies, (b) and the differential displacement, as a function of the translation distance of region three d_{R3} for the eighteen layer simulation. Index one refers to the interface between region three and the first atom in region one, two for the interface between atoms one and two, etc.

deformation paths exist at the same normalized strain energy barrier. While Wang *et al.*²⁵ found the origin of the two stacking faults to be from steps in the grain boundaries, our finding is that this kind of deformation mechanism can occur inside an ideal crystal in the absence of defects at a converged U_{1N} barrier. Our results are consistent with Wang *et al.* in that the merger of two stacking faults into a three layer twinned region is energetically more favorable than the growth of a twinned region by a single layer.

Indeed, the double-stacking fault deformation mechanisms of the eighteen layer and twenty four layer simulations from Table 4.7 are slightly different. For the eighteen layer case, the U_{1NR} frame corresponds to two stacking faults separated by two ideally-stacked layers, the U_{2N} barrier leads to the emission of two stacking faults in between forming a four layer twinned portion. There is no remarkable change in the sequence of barriers (unlike the new twinning route where the second barrier is lower than the adjacent ones), but the spatial periodicity of the response is largely consistent with the change in the periodicity of the response between single and double slip deformation mechanisms along the slip direction. For the twenty layer case, the U_{1NR} corresponds to the emission of two adjacent stacking faults and subsequent U_{iN} barriers correspond to the layer-by-layer growth of the twinned portion.

Our twinning deformation mechanism analysis indicates that there are several deformation paths that could lead to twinning in ideal defect-free FCC metals and the proposed new twinning route by Wang *et al.*²⁵ is but one.

4.5 Atomistic Definition of Strain

In our analysis, an atomistic definition of strain (equation 4.5) based on the differential displacement throughout the interfaces has been proposed. Section 4.3 has shown that the bulk and atomistic definitions of strain for the frames before slip U_{1N} are consistent. Beyond the point of slip, continuum mechanics breaks down due to the sudden jump of atoms over others along the slip plane. Atomically, the internal strain is relieved via slip deformation mechanisms and their behavior is explained in terms of the multiplicity of slip models (see section 4.3.5). The bulk strain, on the other hand, measures an ever-increasing value of strain as d_{R3} tends to infinity (see equation 4.2). Therefore, the internal strain in the frame after slip, the configuration of the U_{1NR} , is an important quantity that requires additional investigation.

The open visualization tool (OVITO)² program includes features to calculate and visualize the elastic and atomistic strain of molecular simulations. OVITO performs strain calculations by decomposing the system into smaller subsystems. Each subsystem is modeled by a central atom and the surrounding volume of the closest neighbor atoms. Continuum mechanics formulations are applied²⁶ and the strain based on atomic contributions is calculated in a least-squares sense such that it captures the overall average deformations of the neighbors of a specific atom.

The difference between the elastic and atomic strain definitions in OVITO is that the elastic definition takes into account the symmetry of the crystal, i.e. if an atom slips over another, its relative displacement is with respect to the commensurate equilibrium lattice sites. On the other hand, the atomic strain keeps incrementing the relative displacement and thus ignores the symmetry of the system. Because of this, we limit our analysis to the elastic strain.

Figure 4.16 shows the elastic strain found using OVITO for several configurations. In the frame just before slip, the heterogeneity in the elastic strain is highlighted by the gradient from the yellow color in the middle (about 0.07 strain) to the cyan color at the first atoms in the rigid blocks. Just after slip, the internal strain is homogeneous (the green color). We note that because OVITO calculates the elastic strain even for the atoms of the rigid blocks, it assigns to them a strain value because some of the neighboring atoms in region one undergo deformation. This analysis using OVITO confirms earlier findings regarding the heterogeneity of the strain distribution in RBSM after slip.

Table 4.9 compares the strains before and after slip calculated using our proposed atomistic definition γ_a and the elastic strain in OVITO. For brevity, only system sizes of seven and twenty-three layers in region one are considered. We note that our atomistic definition of strain ε_a is consistent

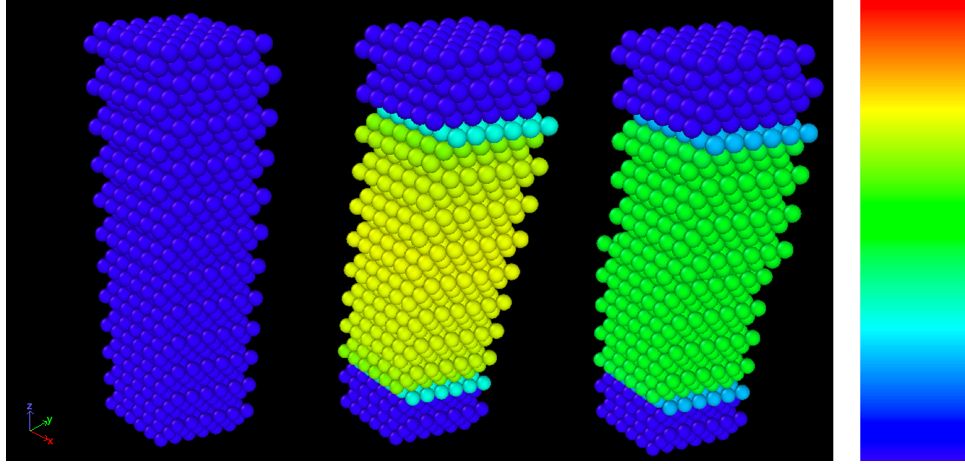


Figure 4.16: Several snapshots of configurations for the twenty three layer system as a function of strain along the slip direction. From left to right are frames corresponding to the initial geometry, before slip and just after slip. The limits of the color bar representing the strain are 0 to 0.1.

Slip System	Layer Number	Frame Number	OVITO	ε_a
(111)[$\bar{1}10$]	7	1N	0.072	0.072
(111)[$\bar{1}10$]	7	1NR	-0.005	-0.005
(111)[$\bar{1}10$]	23	1N	0.072	0.073
(111)[$\bar{1}10$]	23	1NR	0.047	0.047
(111)[$\bar{2}11$]	6	1N	0.070	0.069
(111)[$\bar{2}11$]	6	1NR	0.012	0.018
(111)[$\bar{2}11$]	18	1N	0.071	0.071
(111)[$\bar{2}11$]	18	1NR	0.027	0.034

Table 4.9: OVITO elastic strain and our proposed atomistic strain ε_a average values for several systems along the slip and twinning directions, for the frames before and after slip (frame number 1N denotes the frame before slip, and 1NR denotes the frame after slip).

with OVITO for the frames before and after slip along the slip direction. Furthermore, the negative internal strain described in earlier chapters is also measured in OVITO for the seven layer system. For the twinning direction, both strain definitions are consistent for the frame before slip. However, for the frame after slip, the one obtained from OVITO is always lower than our definition for two reasons. First, our measure of atomistic strain does not include a least-squares consideration. Heterogeneous differential displacement Δd_i values are allowed and equally considered in the summation, see equation 4.5. Second, for the twinning direction, we correct the relative displacement by subtracting the Burger's vector along the twinning direction from the Δd_i at the stacking fault interface. On the other hand, OVITO treats stacking faults in a special way²⁷ that assigns zero strain to the first stacking fault in the structure.

Our proposed atomistic strain definition γ_a provides consistent results with those obtained from the continuum mechanics formulation resolved atom-wise via OVITO. This further supports our findings of the multiplicity of strain being based on an accurate description of strain in the structure and makes it possible to calculate the ideal shear strength.

4.6 Ideal Shear Strength and Application to FCC Metals

4.6.1 Shear Stress Versus Strain in FCC Au

Shear stresses are calculated according to:

$$\sigma = \frac{1}{V_0} \frac{dU}{d\gamma_a} \quad (4.12)$$

where V_0 is the original volume of region one within the surface cell. Equation 4.12 is solved using the finite difference approximation. Figure 4.17 shows the shear stress versus strain for the twelve layer simulations along the slip and twinning directions. The evolution of both stress curves is con-

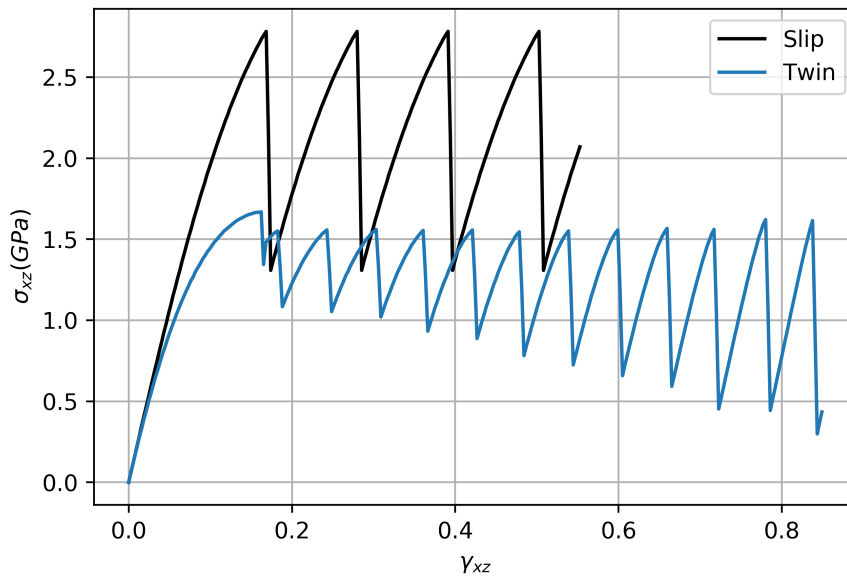


Figure 4.17: Stress as a function of strain plot for the twelve layer case sheared by RBSM along the slip and the twinning directions.

sistent with the evolution of normalized strain energy as a function of strain. The stresses increase up to the ideal shear stress value before slip happens. The early phase of deformation ($\gamma_b < 0.05$) shows both curves follow the same linear trend which becomes different at later stages of the elastic deformation. The ideal shear stress along the twinning direction (1.7 GPa) is lower than that along

the slip direction (2.8 GPa), consistent with the U_{1N} barrier being lower in the twinning direction compared to the slip direction. The ideal shear stresses were computed for several converged system size simulations and confirmed that this value is a converged intrinsic material property. Generation of the graphs is impossible using the bulk definition of strain (equation 4.2) but only with the atomistic definition (equation 4.5) because the latter accounts for the correction of the differential displacement through the slip interface by the lattice/Burger's vector.

Shang *et al.* published an article²⁸ reporting several stacking fault quantities and ideal shear strength in Ni₃Al using the alias shear deformation method, which involves shearing a rigid block with respect to a fixed one but in a three dimensional periodic supercell. Shang *et al.* cites unpublished work stating that the ideal shear strength is inversely proportional to the number of layers in the supercell. We note that our RBSM ideal shear strength calculations on FCC Au showed that the ideal shear strength is a converged property as a function of the size of the system.

4.6.2 Slip Barriers and Ideal Shear Strength of FCC Metals

Throughout Chapter 4, RBSM was applied to study the deformation of FCC Au. RBSM led to two integral physical quantities characteristic of each material's slip system, namely the slip barrier and the ideal shear strength. To confirm the generality of our findings for FCC Au, RBSM was applied to the slip and twinning directions in Pb, Pt, Pd, Al, Cu, Ag and Ni. For all the simulations, the geometry was constructed as per the same procedure used for FCC Au. The size of each system was twelve layers in region one. A 0.001 strain per step is chosen for all the simulations because this value falls below the threshold for convergence established in FCC Au (0.0024). Table 4.10 shows that the barrier and the ideal shear strengths along the twinning direction are always lower than these along the slip direction. The consistency in the ranking of the slip systems can be derived from either the energetics or the stress data. This is expected based on elasticity theory.

4.7 Summary

In this chapter, RBSM was been applied to study the idealized deformation of FCC Au in detail and the converged slip barriers and ideal shear strengths of FCC Al, Pd, Pt, Pb, Cu, Ag, and Ni are obtained. For all the tested FCC metals, the barrier to twinning deformation was found always

Material	$U_{1N, SLIP}$	$U_{1N, TWIN}$	σ_{SLIP}	σ_{TWIN}
Pb	0.0117	0.0083	1.3	0.9
Ag	0.0245	0.0173	5.5	3.7
Al	0.0131	0.0107	3.6	3.2
Cu	0.0236	0.0167	8.5	5.8
Ni	0.0253	0.0185	12.6	9.3
Pd	0.0219	0.0157	10.2	7.2
Pt	0.0179	0.0122	10.5	6.6

Table 4.10: Summary of the slip barriers (U_{1N}) and ideal shear strengths for selected FCC metals along the twinning and slip directions. Normalized strain energy barriers are dimensionless while all stresses (σ) are in GPa.

lower than that for slip. This is consistent with the qualitative nature of GSFE curves of FCC metals. However, an in-depth analysis of FCC Au indicated that the actual relaxed barriers are much smaller than those from GSFE. These findings call for the re-evaluation of dislocation-based models that use GSFE energy quantities in their calculations.

Shearing FCC Au along the slip direction resulted in a variety of deformation mechanisms such as the multiple slip, partial and full dislocation slip. The difference in the barrier to activate these deformation mechanisms is small, of the order of a few degrees Kelvin (which converts to less than 0.0001 on the normalized strain energy scale used here) and as the size of the system increases, the density of the phase-space increases. We predict these results are important in establishing multi-scale models of plasticity, and give deeper insight into the quantized nature of plasticity events.¹² RBSM describes twinning deformation mechanisms with an unprecedented level of detail. Our RBSM twinning curve contradicts the GPFE curve in that subsequent growth of the twin is relatively easier, however, GPFE predicts the growth to be harder than the nucleation. The new twinning route proposed in reference²⁵ was reproduced as a consequence of the existence of a variety of deformation mechanisms on the potential energy hyper-surface of the system. Indeed, Pattamatta *et al.*²⁹ proposed a branch-following and bifurcation (BFB) computational method to construct equilibrium maps; potential energy hypersurface equilibria and associated paths. Their method was applied to nanocrystalline nickel in compression and revealed a large number of stable structures and possible deformation paths. It would be of interest to apply the BFB method to study an RBSM analogue (where the structure is sheared instead of compressed) and compare the results of the stable structures and deformation paths to those directly obtained from RBSM.

A simple definition of atomistic strain based on the infinitesimal strain approximation has been proposed and tested. Our strain definition was shown to match the bulk definition of strain before slip and the elastic atomic strain as defined in OVITO.² Even the strains after slip were tested and both OVITO and our definition gave consistent answers including the negative internal strain after slip in some of our simulations. Since OVITO uses a different continuum-based least-squares strain definition, it is further suggesting that our simple proposed definition is accurate and can be used to calculate the full stress versus strain history of the deformed defect-free material.

The ideal shear strength has been calculated for all the tested FCC metals in this chapter. An additional feature is that our calculations are based on physically stable frames throughout the calculations since the RFO ensures the Hessian is positive definite, unlike the case of DFT alias shear deformation simulations^{28,30} where neither convergence nor phonon analysis have been checked. Since we have established that both the ideal shear strength and normalized strain energy barriers converge, we found that the localization of deformation (single-, double-, multiple-) slip is independent of both. This has an implication that homogeneously strained ideal defect-free material could exhibit non-localized deformation.

During our analysis, a heterogeneity in the strain distribution throughout the interfaces and especially in the frames before slip was identified. This heterogeneity is attributed to the use of rigid blocks as our boundary conditions. This motivated the development of the second proposed method in this research, the tensor-based shearing method (TBSM) to be explored in the next chapter.

RBSM is able to model several plastic deformation aspects such as slip barriers, ideal shear strengths, full and partial dislocation slip, twinning and stacking faults within the single formalism. Defect materials with heterogeneities and plastic deformation based on the interaction of such defects remain elusive. For instance, it is not possible to simulate the formation of dislocation cores and loops using RBSM due to the use of rigid surfaces. In principle, RBSM is also applicable to other classes of crystalline material, such as BCC and HCP metals, alloys, ionic crystals and organic molecular crystals.

Bibliography

- ¹ V. Vitek, “Intrinsic stacking faults in body-centred cubic crystals,” *The Philosophical Magazine: A Journal of Theoretical Experimental and Applied Physics*, vol. 18, no. 154, pp. 773–786, 1968.
- ² A. Stukowski, “Visualization and analysis of atomistic simulation data with OVITO—the open visualization tool,” *Modelling and Simulation in Materials Science and Engineering*, vol. 18, p. 015012, dec 2009.
- ³ S. Fleming and A. Rohl, “Gdis: A visualization program for molecular and periodic systems,” *Zeitschrift Fur Kristallographie - Z KRISTALLOGR*, vol. 220, pp. 580–584, 01 2005.
- ⁴ R. Hockney, S. Goel, and J. Eastwood, “Quiet high-resolution computer models of a plasma,” *Journal of Computational Physics*, vol. 14, no. 2, pp. 148 – 158, 1974.
- ⁵ W. G. Hoover, “Canonical dynamics: Equilibrium phase-space distributions,” *Phys. Rev. A*, vol. 31, pp. 1695–1697, Mar 1985.
- ⁶ W. Humphrey, A. Dalke, and K. Schulten, “Vmd: Visual molecular dynamics,” *Journal of Molecular Graphics*, vol. 14, no. 1, pp. 33 – 38, 1996.
- ⁷ V. Vitek, R. C. Perrin, and D. K. Bowen, “The core structure of $\frac{1}{2}(111)$ screw dislocations in b.c.c. crystals,” *The Philosophical Magazine: A Journal of Theoretical Experimental and Applied Physics*, vol. 21, no. 173, pp. 1049–1073, 1970.
- ⁸ V. Vitek, “Structure of dislocation cores in metallic materials and its impact on their plastic behaviour,” *Progress in Materials Science*, vol. 36, pp. 1 – 27, 1992.
- ⁹ S. Sempere, A. Serra, J. Boronat, and C. Cazorla, “Dislocation structure and mobility in hcp rare-gas solids: Quantum versus classical,” *Crystals*, vol. 8, no. 2, 2018.
- ¹⁰ J. A. Zimmerman, C. L. Kelchner, P. A. Klein, J. C. Hamilton, and S. M. Foiles, “Surface step effects on nanoindentation,” *Phys. Rev. Lett.*, vol. 87, p. 165507, Oct 2001.

- ¹¹ T. Sinha and Y. Kulkarni, “Anomalous deformation twinning in fcc metals at high temperatures,” *Journal of Applied Physics*, vol. 109, no. 11, p. 114315, 2011.
- ¹² P. E. Marszalek, W. J. Greenleaf, H. Li, A. F. Oberhauser, and J. M. Fernandez, “Atomic force microscopy captures quantized plastic deformation in gold nanowires,” *Proceedings of the National Academy of Sciences*, vol. 97, no. 12, pp. 6282–6286, 2000.
- ¹³ V. Yamakov, D. Wolf, S. R. Phillpot, A. K. Mukherjee, and H. Gleiter, “Deformation-mechanism map for nanocrystalline metals by molecular-dynamics simulation,” *Nature Materials*, vol. 3, no. 1, pp. 43–47, 2004.
- ¹⁴ H. Van Swygenhoven, P. M. Derlet, and A. G. Frøseth, “Stacking fault energies and slip in nanocrystalline metals,” *Nature Materials*, vol. 3, no. 6, pp. 399–403, 2004.
- ¹⁵ Y. Zhu, X. Liao, and X. Wu, “Deformation twinning in nanocrystalline materials,” *Progress in Materials Science*, vol. 57, no. 1, pp. 1 – 62, 2012.
- ¹⁶ L. Y. Chen, M.-r. He, J. Shin, G. Richter, and D. S. Gianola, “Measuring surface dislocation nucleation in defect-scarce nanostructures,” *Nature Materials*, vol. 14, no. 7, pp. 707–713, 2015.
- ¹⁷ T. Zhu, J. Li, A. Samanta, A. Leach, and K. Gall, “Temperature and strain-rate dependence of surface dislocation nucleation,” *Phys. Rev. Lett.*, vol. 100, p. 025502, Jan 2008.
- ¹⁸ J. A. Venables, “Deformation twinning in face-centred cubic metals,” *The Philosophical Magazine: A Journal of Theoretical Experimental and Applied Physics*, vol. 6, no. 63, pp. 379–396, 1961.
- ¹⁹ J. R. Rice, “Dislocation nucleation from a crack tip: An analysis based on the peierls concept,” *Journal of the Mechanics and Physics of Solids*, vol. 40, no. 2, pp. 239 – 271, 1992.
- ²⁰ S. Ogata, J. Li, and S. Yip, “Energy landscape of deformation twinning in bcc and fcc metals,” *Phys. Rev. B*, vol. 71, p. 224102, Jun 2005.
- ²¹ S. Kibey, J. Liu, D. Johnson, and H. Sehitoglu, “Predicting twinning stress in fcc metals: Linking twin-energy pathways to twin nucleation,” *Acta Materialia*, vol. 55, no. 20, pp. 6843 – 6851, 2007.
- ²² E. Tadmor and S. Hai, “A peierls criterion for the onset of deformation twinning at a crack tip,” *Journal of the Mechanics and Physics of Solids*, vol. 51, no. 5, pp. 765 – 793, 2003.

- ²³ N. Bernstein and E. B. Tadmor, “Tight-binding calculations of stacking energies and twinnability in fcc metals,” *Phys. Rev. B*, vol. 69, p. 094116, Mar 2004.
- ²⁴ J. P. Hirth and J. Lothe, *Theory of Dislocations (2nd ed.)*. New York: Wiley, 1982.
- ²⁵ L. Wang, P. Guan, J. Teng, P. Liu, D. Chen, W. Xie, D. Kong, S. Zhang, T. Zhu, Z. Zhang, E. Ma, M. Chen, and X. Han, “New twinning route in face-centered cubic nanocrystalline metals,” *Nature Communications*, vol. 8, 12 2017.
- ²⁶ F. Shimizu, S. Ogata, and J. Li, “Theory of shear banding in metallic glasses and molecular dynamics calculations,” *MATERIALS TRANSACTIONS*, vol. 48, no. 11, pp. 2923–2927, 2007.
- ²⁷ A. Stukowski and A. Arsenlis, “On the elastic-plastic decomposition of crystal deformation at the atomic scale,” *Modelling and Simulation in Materials Science and Engineering*, vol. 20, p. 035012, mar 2012.
- ²⁸ S.-L. Shang, J. Shimanek, S. Qin, Y. Wang, A. M. Beese, and Z.-K. Liu, “Unveiling dislocation characteristics in Ni₃Al from stacking fault energy and ideal strength: A first-principles study via pure alias shear deformation,” *Phys. Rev. B*, vol. 101, p. 024102, Jan 2020.
- ²⁹ S. Pattamatta, R. S. Elliott, and E. B. Tadmor, “Mapping the stochastic response of nanostructures,” *Proceedings of the National Academy of Sciences*, vol. 111, no. 17, pp. E1678–E1686, 2014.
- ³⁰ M. Jahnátek, J. Hafner, and M. Krajčí, “Shear deformation, ideal strength, and stacking fault formation of fcc metals: A density-functional study of al and cu,” *Phys. Rev. B*, vol. 79, p. 224103, Jun 2009.

Every reasonable effort has been made to acknowledge the owners of copyright material. I would be pleased to hear from any copyright owner who has been omitted or incorrectly acknowledged.

Chapter 5

Tensor-Based Shearing Method: Application to FCC metals

5.1 Introduction

The Tensor-Based Shearing Method (TBSM) belongs to the broad category of affine shear deformation methods, used by Roundy *et al.*¹ and then Ogata *et al.*,² under full relaxation conditions. Affine shear deformation methods, also known as pure shear³ deformation methods, were extensively reviewed in the introduction of this thesis. Briefly summarized, these methods are based on constrained quasi-static energy minimization simulations with the application of a deformation tensor to a reference structure. One component of strain is fixed while the other components are relaxed along with the internal energy of the system. TBSM is an extended version of affine shear deformation methods with the improvements of the application of analytic finite strain derivatives to a reference structure at all frames, and the use of the rational function optimizer (RFO).⁴

In this chapter, TBSM will be applied to study the deformation of FCC Au and ultimately calculate the slip barriers and ideal shear strengths of Al, Pd, Pb, Cu, Ni, Pt, and Ag. The second section deals with the general methodology. The third section tests the influence of the energy minimization algorithm on the deformation. The fourth and fifth sections apply TBSM to the twinning and slip directions, respectively. Section six compares the strain definition in TBSM to the Green-Lagrange finite strain. Section seven applies TBSM to find the slip barriers and ideal shear strength for a series of FCC metals. Section eight describes a geometrical tool to determine the easiest slip direction in a slip system. Throughout this chapter, discussions will involve comparison of the results against RBSM and other experimental and computational findings.

5.2 Methodology

Deformation will be simulated in the (111) plane along the slip ($[\bar{1}10]$) and the twinning ($[\bar{2}11]$) directions. Thus, a rhombohedral unit cell is constructed with the (111) planes along c having a single atom. The lattice vectors are:

$$\vec{a} = 2.88 \hat{i} \text{ \AA} \quad (5.1a)$$

$$\vec{b} = 1.44 \hat{i} + 2.49 \hat{j} \text{ \AA} \quad (5.1b)$$

$$\vec{c} = c_x \hat{i} + c_y \hat{j} + c_z \hat{k} \text{ \AA} \quad (5.1c)$$

where \hat{i} , \hat{j} , and \hat{k} are the Cartesian unit vectors along x , y , and z , respectively. Similar to the surface vectors generated in earlier sections, the alignment of the lattice vectors a and b takes the form given in equation 5.1. The slip direction coincides with lattice vector a and the twinning direction is at 30° to both a and b . Lattice vector c has three Cartesian components and is a function of the

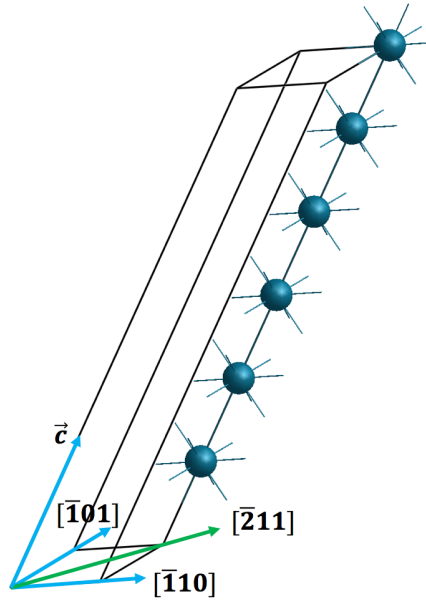


Figure 5.1: Representative supercell of the six layer system to be sheared using RBSM. The crystallographic cell vectors are plotted as blue arrows while the twinning direction is plotted as a green arrow.

system size. For a single layer, c_x , c_y and c_z are 1.44, 0.83 and 2.34 \AA , respectively. The choice of a rhombohedral representation of the (111) plane primitive unit cell is favored because it enables the construction of configurations with both an odd and even number of layers. Figure 5.1 shows an example of a supercell with six atoms (or layers, since we have a single atom per layer in TBSM supercells used here) with the crystallographic directions of interest indicated.

Throughout TBSM calculations, a single component of strain (γ_{xz}) is always fixed and other components are relaxed. For slip deformation simulations, the generated cell is used in its original form. For the twinning deformation configurations, an orthogonal rotation tensor about the z axis is applied to the lattice vectors and atomic coordinates to rotate the system 30° clock-wise such that the twinning direction lies in the xz plane.

The force field and the molecular dynamics (MD) parameters used are the same as in the case of RBSM simulations in Chapter three.

5.3 Influence of the Energy Minimization Algorithm

In this section, the impact of the energy minimization algorithm on TBSM is examined as this work is the first time that RFO has been used in affine shear simulations. A twelve layer supercell with the twinning direction in the xz plane was constructed. An overall γ_{xz} of 0.7 was applied over the course of 700 steps. The normalized strain energy is defined as;

$$U_{iN} = \frac{\Delta U}{N_a E_c} \quad (5.2)$$

where ΔU is the change in internal energy, N_a is the number of atoms in the supercell and E_c is the cohesive lattice energy per atom. Shear stress σ_{xz} is analytically calculated in TBSM as the first

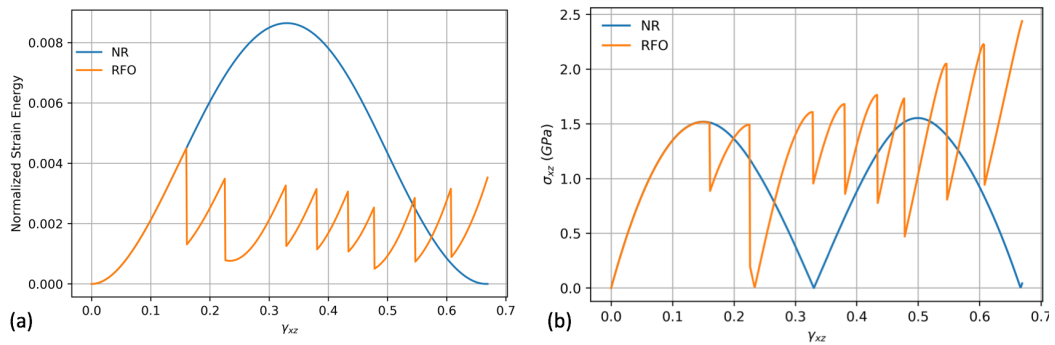


Figure 5.2: (a) Normalized strain energy and, (b) shear stress σ_{xz} , along the twinning direction as a function of strain for simulations employing Newton-Raphson and RFO energy minimizers.

derivative of energy with respect to strain divided by the volume of the reference supercell.

According to Figures 5.2 (a) and (b), our NR results replicate the trends reported by Roundy *et al.* and Ogata *et al.* in that the energy increases to a maximum at a strain about 0.33, which coincides with σ_{xz} being equal to zero. In contrast, our RFO results show a different evolution of the normalized strain energy U_N with a sharp drop in both energy and stress as a function of strain

marking the first slip event. Similar events were observed using a branch-following and bifurcation (BFB) technique applied to an FCC nano-slab in compression⁵, therefore would of interest to compare this BFB method to an FCC system under shear deformation. Clatterbuck *et al.*⁶ have performed phonon instability analysis as a function of strain for the affine shear deformation method¹ on FCC Al along several crystallographic and deformation modes and found that the phonon instability occurs before the maximum stress is reached. Throughout our TBSM calculations, phonon frequencies were calculated for every frame where the NR simulation led to multiple imaginary phonons per frame in the strain interval $0.16 \leq \gamma_{xz} \leq 0.48$, unlike the RFO simulation where all frames were physically stable structures.

Figure 5.2 (b) shows that the ideal shear strengths from the RFO and NR simulations are very similar. Our results agree with the findings of Clatterbuck *et al.*⁶ in that both the highest stress and the stress at the point of instability are very similar for the twinning system in FCC metals. However, the results of Clatterbuck *et al.* (Table 2 reference⁶) show that the instability stress and the highest stress difference becomes large (several GPa) when simulating tensile deformation along different crystallographic directions, presumably, because these tensile deformations are not the easiest in FCC Au. RBSM showed that the twinning barrier is lower than the slip barrier in FCC metals. Combined with our findings in Figure 5.2 and the results of Clatterbuck *et al.*, the phonon instability occurs near the highest stress only for the easiest slip system.

Our minimization algorithm comparative analysis confirms the importance of the phonon instability findings of Clatterbuck *et al.* Our use of RFO combined with TBSM yielded a slip profile along the lowest energy path where slip events are marked by the sudden decrease in both energy and stress as a function of strain. Our results call for additional care to be taken when using NR and trying to go beyond the ideal shear strength estimation to infer conclusions about structural parameters^{7,8} or deformation.⁹

5.4 Shearing the (111)[$\bar{2}11$] System in FCC Au

Careful examination of the literature looking for deformation twinning simulations using affine shear deformation methods yielded no papers on this topic. However, Roundy *et al.*¹ and Ogata *et al.*² both simulated affine shear deformation of FCC metals along the twinning directions but did not find twinning deformation, perhaps because their objective was to only find the ideal shear strength. This section applies TBSM to the twinning system in FCC Au. Convergence analysis

as a function of the system and step sizes is performed. The deformation and alignment of the lattice vectors, twinning deformation mechanisms including the twinning route proposed by Wang *et al.*,¹⁰ site energies, relative displacement, and finally the multiplicity of slip analysis via MD analysis followed by minimization, are all described.

5.4.1 Convergence: System and Step Size Variables

The convergence of TBSM as a function of the size of the system was first tested. An overall 0.8 γ_{xz} was applied over the course of 2285 steps resulting in 0.00035 of strain per step. The simulation parameters and the results for the U_{1N} and γ_{1N} are reported in Table 5.1. These results indicate that

N_a	$\gamma_{xz,1N}$	U_{1N}
3	0.165	0.0047
6	0.162	0.0046
7	0.161	0.0046
8	0.161	0.0045
9	0.161	0.0045
12	0.160	0.0045
14	0.160	0.0045
15	0.160	0.0045
20	0.160	0.0045
24	0.160	0.0045

Table 5.1: The normalized strain energy U_{1N} and shear strain $\gamma_{xz,1N}$ before slip as a function of the size of the system when TBSM is used to shear in the twinning direction in FCC Au. N_a corresponds to the number of atoms (layers) in each system.

the U_{1N} and $\gamma_{xz,1N}$ converge to 0.0045 and 0.16 for system sizes equal to or greater than twelve layers.

The next step is to test the step size convergence of the results. The twelve layer structure was chosen and the strain varied per step from 0.08 to 0.0005, as listed in Table 5.2. Step size analysis results indicate that the U_{1N} and $\gamma_{xz,1N}$ converge to 0.0045 and 0.16 at a strain per step equal to or less than 0.008.

The converged TBSM U_{1N} and $\gamma_{xz,1N}$ (0.0045 and 0.16, respectively) are very similar to those obtained from RBSM (0.0046 and 0.14, respectively) in Chapter 4. Converting the TBSM U_{1N} to an interfacial surface energy yields 39.5 mJ/m^2 , slightly higher than that from RBSM (37.6

Strain / Step	$\gamma_{xz,1N}$	U_{1N}
0.08	0.08	0.0014
0.016	0.144	0.0038
0.008	0.16	0.0045
0.004	0.16	0.0045
0.0016	0.16	0.0045
0.0008	0.16	0.0045
0.0005	0.16	0.0045

Table 5.2: The normalized strain energy U_{1N} and shear strain $\gamma_{xz,1N}$ before slip as a function of the strain per step for the twelve layer configuration when TBSM is used to shear in the twinning direction in FCC Au.

mJ/m^2) but still much lower than that of the USF ($107 mJ/m^2$). TBSM and RBSM interfacial surface energies are both slightly lower than the ISF ($40 mJ/m^2$) of FCC Au. Although U_{1N} from TBSM is slightly lower than that from RBSM, the interfacial energy calculated using TBSM is higher than that from RBSM. This is because RBSM has two rigid blocks that interact with the system and provide two additional interfaces in the system, while TBSM provides only an additional interlayer boundary through the periodic boundary condition connecting the bottom-most and top-most atoms in the system, i.e. the different boundary conditions in each method leads to the different measures of the interfacial surface energies.

In summary, the same discussion made based on the RBSM converged twinning barrier is equally applicable for TBSM. TBSM findings support the re-evaluation of dislocation-based models that rely on the unstable stacking fault energy (USF), defined by Rice¹¹ as the resistance of the lattice to dislocation nucleation from a crack tip. Having found the convergence limits in terms of system and step sizes, the next section proceeds by describing the effects of this deformation on the lattice vectors.

5.4.2 Deformation of the Lattice Vectors

Owing to the relaxation of all the strain components bar one in TBSM, the lattice vectors deform as a function of strain. Figure 5.3 shows the evolution of the components of the lattice vectors as a function of strain for the twelve layer configuration in Table 5.1. This has consequences for the crystallographic directions. The energy is invariant to the rotation of the cell vectors and atomic coordinates. However, concepts such as differential displacement, Δd_i , the difference in the dis-

placement of atoms i and $i+1$ for $i \geq 1$, used to analyze the structural evolution of twinning in RBSM are variant. Before calculating Δd_i , we need to understand and properly align the lattice vectors such that the crystallographic directions in the deformed configuration point in the same Cartesian sense as the reference structure.

The twinning direction lies along the vector $(\vec{a} + \vec{b})$. At γ_{xz} equal to 0, the unit vector for the

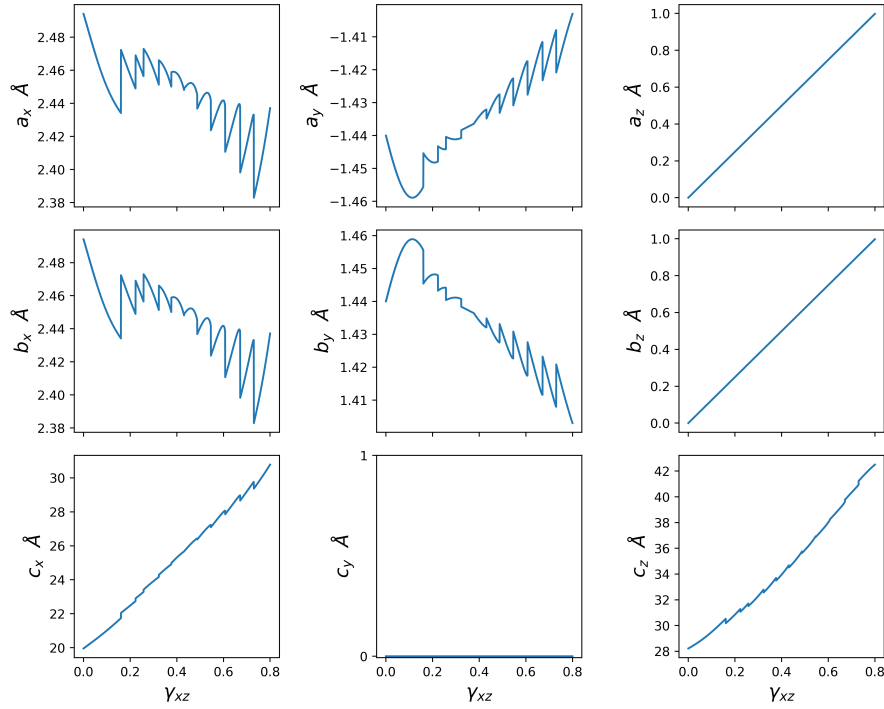


Figure 5.3: The change in the Cartesian components of the lattice vectors as a function of strain for twelve layer configuration in Table 5.1.

twinning direction is aligned along x . For $\gamma_{xz} > 0$, both vectors a and b develop z components and thus the twinning direction is no longer aligned along x . Chapter 2 detailed the procedure to find the rotation tensor necessary to align the lattice vectors along the original directions by using the lattice parameters of a supercell sheared along the slip direction. The procedure needs to be amended for twinning deformation since the shape of the lattice vectors is different, i.e. the twinning direction is aligned along the x -axis. To this end, the transformation of the deformed lattice vectors R' is recast, $R'_c = TR'$ into:

$$\begin{bmatrix} a'_{xc} & b'_{xc} & c'_{xc} \\ a'_{yc} & b'_{yc} & 0 \\ 0 & 0 & c'_{zc} \end{bmatrix} = \mathbf{T} \begin{bmatrix} a'_x & b'_x & c'_x \\ a'_y & b'_y & c'_y \\ a'_z & b'_z & c'_z \end{bmatrix} \quad (5.3)$$

where a , b , and c represent the lattice vectors and the $'$ symbol denotes after deformation, $\mathbf{T} = T_z(\eta)T_y(\theta)T_x(\phi)$ is a three-dimensional rotation tensor, and subscript c for the lattice vectors after rotation. The two equations in Chapter 2, $a'_{zc} = 0$ and $b'_{zc} = 0$, are still valid. The third equation,

that was originally $a'_{yc} = 0$ in Chapter 2, needs to be amended for this case such that, $c'_{yc} = 0$;

$$(\sin \eta \cos \theta)c'_x + (\sin \eta \sin \theta \sin \phi + \cos \eta \cos \phi)c'_y + (\sin \eta \sin \theta \cos \phi - \cos \eta \sin \phi)c'_z = 0 \quad (5.4)$$

The non-linear system of the three equations ($a'_{zc} = 0, b'_{zc} = 0, c'_{yc} = 0$) were solved using, the SPyder¹² scientific environment in the Anaconda data science toolkit, for the configurations with different number of layers in Table 5.1. The results are summarized in Table 5.3. Interestingly,

N_a	3	6	7	8	9	12	14	15	20	24
θ	4.8	4.8	4.7	4.7	4.7	4.7	4.7	4.7	4.7	4.7

Table 5.3: Summary of the solution of the transformation angles to align the deformed lattice vectors and atomic coordinates along the same original orientations. Only θ values are reported, in degrees, as η and ϕ values were zero for all the cases.

the alignment procedure resulted in a counter-clock-wise rotation about the y-axis by a converged value of 4.7° .

5.4.3 Twinning Deformation Mechanism

Our objective is to analyze the twinning deformation simulated in TBSM and thus the results of selected systems sizes are reported. Figure 5.4 shows the typical evolution of the normalized strain energy U_N as a function of strain γ_{xz} .

Several TBSM twinning deformation features can be compared to the same in RBSM. First, the

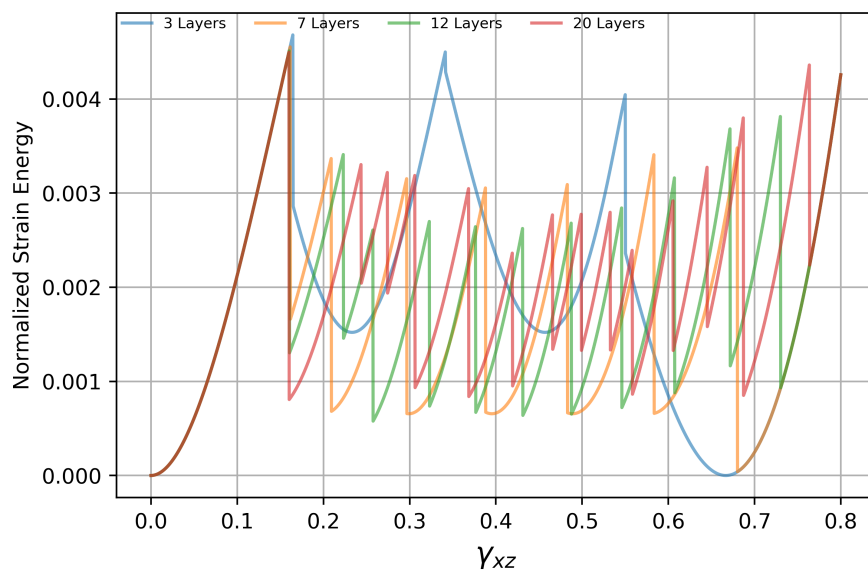


Figure 5.4: Normalized strain energy U_N as a function of strain γ_{xz} for selected system sizes obtained from TBSM simulations of the twinning system in FCC Au.

U_{1N} barrier is always greater than the first few subsequent barriers. This first slip event corresponds to the emission of stacking fault(s) in the system followed by micro-slip events representing the growth of the stacking fault(s) into twins. Second, for the three layer system, and following each micro-slip event, the energy smoothly goes to a minimum before it starts increasing again. This suggests the presence of negative internal strain in the structure and that possibly the multiplicity of slip can be generalized to TBSM.

An important distinction between TBSM and RBSM is the number of interfaces in the system. RBSM surface cells have $N_a + 1$ interfaces owing to the additional two interfaces due to the rigid blocks, while noting that these interfaces are generally different since each represents an interaction between one rigid block and the atoms in region one. TBSM has N_a interfaces because the top-most and bottom-most atoms interact with each other via the periodic boundary condition. This affects the indices i of Δd_i and implies a unique boundary condition where the top and bottom edges of the system interact with each other.

Unlike RBSM where for all the twinning deformation paths, the inequality $U_{(i+1)N} < U_{iN}$ for $i \geq 1$ holds, except for the last two twinning events which involve rigid blocks, TBSM shows that for an approximate condition $\gamma_{xz} > 0.4$, $U_{(i+1)N} > U_{iN}$. This is explained because TBSM is constructed such that the strain tensor and finite strain derivatives are always applied and calculated with respect to the original reference configuration. However, for large-enough strain e.g. $\gamma_{xz} > 0.4$, the deformation of the lattice vectors implies that the intended direction of shear deviates from the actual direction and thereby leads to the non-linear shift in the energy barriers.

5.4.4 Twinning Deformation Analysis

Further investigation of twinning deformation via energetic and structural approaches is sought, and thus the focus is on the three and the twenty layer case from Table 5.1. Differential displacement Δd_i and re-optimization energy analysis were performed and reported in Figure 5.5. For both cases, the Δd_i increases linearly as a function of strain until the first micro-slip event happens. This shows that the strain is homogeneously distributed throughout the interfaces.

For the three layer case, the first micro-slip event corresponds to the emission of a stacking fault between layers one and two (Δd_2 in Figure 5.5 (a)), then through the periodic boundary condition (Δd_1), at last between layers two and three (Δd_3). The re-optimization energy equals the ISF of FCC Au (40 mJ/m^2) throughout the deformation path that involves the presence of stacking fault(s)/twins in the structure until all the structure twins after which the re-optimization energy re-

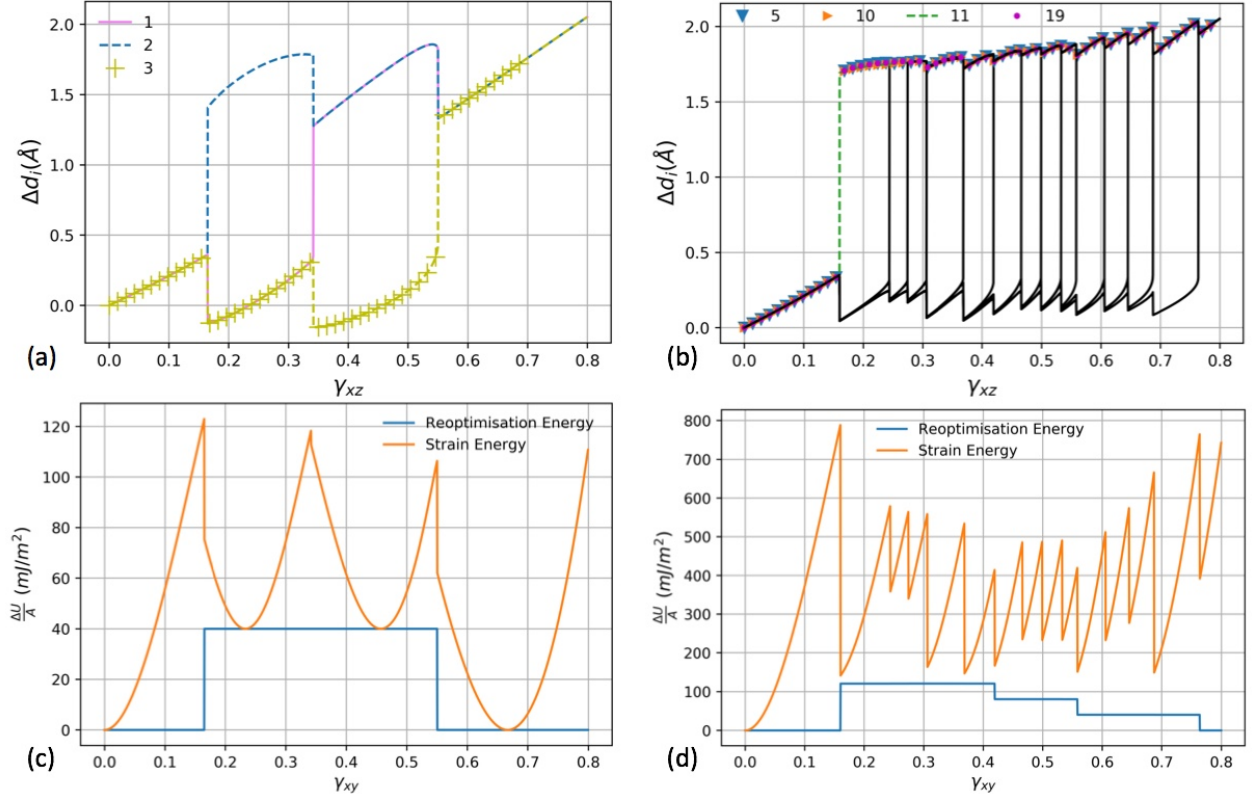


Figure 5.5: Differential displacement Δd_i and strain and re-optimization surface energies for the three layer, (a) and (c), and twenty layer, (b) and (d) systems. Δd_1 represents the differential displacement between the top-most atom one and bottom-most atom N_a in the system, Δd_2 between atoms one and two, etc.

turns to zero. Some negative Δd_i values are noted, which is again attributed to the smooth decrease of energy to a minimum in simulations with a few layers.

For the twenty layer case, the twinning deformation mechanism is different. Tracing the differential displacement plot in Figure 5.5 (b) shows that the first micro-slip event corresponds to the emission of four stacking faults, Δd_5 , Δd_{10} , Δd_{11} , and Δd_{19} , between layers four and five, nine and ten, ten and eleven, and eighteen and nineteen, respectively. The surface energies plot in Figure 5.5 (d) shows that the structure contains about three times ($121 \text{ mJ}/\text{m}^2$) the ISF of FCC Au ($40 \text{ mJ}/\text{m}^2$). This is because Δd_{10} and Δd_{11} produce two adjacent stacking faults. Subsequent growth of the stacking faults proceeds by either single- or double-emission of stacking faults. For the cases where the drop of energy is relatively gradual, e.g. U_{2N} and U_{3N} , growth happens by single stacking fault emission. On the other hand, if the energy drop is sharp, e.g. U_{4N} , U_{5N} and U_{13N} , then double stacking fault emission occurs. The strain and re-optimization surface energies show another important finding. In Figure 5.5 (b) the barrier U_{6N} is less than U_{5N} and U_{7N} , however the re-optimized surface energy profiles show that the energy decreases from three times the ISF to two times the ISF. This indicates that two twinned portions of the crystal have merged into

a single twin.

Wang *et al.*¹⁰ showed that the barrier for twin formation according to their new twinning route is lower than that of the classical route. Our analysis identifies physical situations where the barrier is lower, especially when two twinned portions of a crystal merge into one. This indicates that Wang *et al.*'s discovery of the new twinning route is actually a special case of a more general structure-energy relationship such that whenever twinned portions/stacking faults merge, their mergers occur with a relatively lower barrier compared to generating a single stacking fault in either portion/side of the crystal.

TBSM has been shown as the first affine shear deformation method to produce twinning deformation in FCC Au with such a level of detail to the best of our knowledge. Earlier works of Roundy *et al.*¹ and Ogata *et al.*² yielded approximations of the ideal shear strength, but no twinning evolution was observed although affine shear deformation was applied to FCC metals along the twinning system. This is understandable in light of our earlier result on the influence of the energy minimization algorithm.

5.4.5 Multiplicity of Slip: Alternative Twinning Routes

The occurrence of different multiplicities of slip has been observed in RBSM deformation simulations. Does TBSM also find that a variety of multiplicities of slip can occur? TBSM system size analysis found that the deformation mechanism evolves as a function of the size of the system. For system sizes ranging between three to seven layers, the frame after slip U_{1NR} emitted a single stacking fault, between eight and fourteen layers led to double stacking faults, fifteen layers emitted three stacking faults, and twenty and twenty four layers emitted four stacking faults. Sufficient points are available for single stacking fault (SSF) and double stacking fault (DSF) occurrence to perform linear regression. The below quantities are defined;

$$r_{k_{as}} = \sum_{i=1}^N \Delta d_{i, \text{ after slip}} \quad (5.5a)$$

$$r_{k_{bs}} = \sum_{i=1}^N \Delta d_{i, \text{ before slip}} \quad (5.5b)$$

where $r_{k_{as}}$ and $r_{k_{bs}}$ represent the sum of differential displacements after or before slip, respectively. Indices k take the value of SSF or DSF, as previously defined. $r_{k_{as}}$ versus $r_{k_{bs}}$ were plotted for the SSF and DSF simulations in Figure 5.6. Excellent linear regression models were found for both cases;

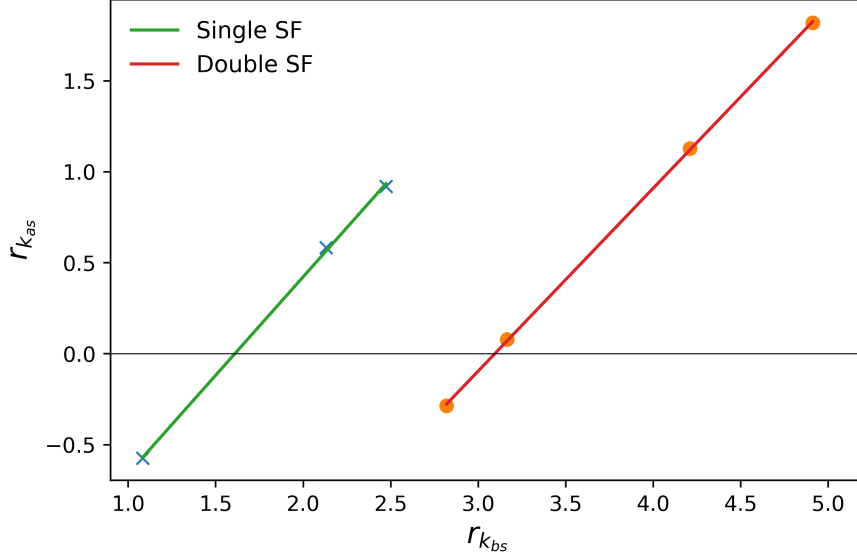


Figure 5.6: Plot of the differential displacement after slip $r_{k_{as}}$ as a function of $r_{k_{bs}}$ for the single stacking fault (SSF) deformation mechanisms denoted by crosses and double stacking fault (DSF) by filled circles. The green and red lines are the linear regression of the data for single and double stacking faults, respectively. From the left hand side to the right, the system sizes are three, six, seven, eight, nine, twelve, and fourteen layers. Units are in Å.

$$r_{SSF_{as}} = 1.08 r_{SSF_{bs}} - 1.74 \dots (\text{Å}) \quad (5.6a)$$

$$r_{DSF_{as}} = 1 r_{DSF_{bs}} - 3.11 \dots (\text{Å}) \quad (5.6b)$$

The equations 5.6a and 5.6b show that TBSM yields similar models for the multiplicity of slip as RBSM. A distinctive feature is that the fitting constant in the linear regression model does not compare to the lattice vector along the twinning direction, but to the magnitude of the Burger's twinning vector (1.66 Å for FCC Au). Interestingly, Figure 5.6 shows that for the three layer case, slip happens when the sum of the differential displacement before slip $r_{k_{bs}}$ was lower than 1.66 Å and thus the energy smoothly goes to a minimum before the next micro-slip happens, as can be confirmed from Figure 5.4.

Additional insight is sought about the topology of the potential energy hyper-surface via MD analysis as described in the methodology section. The twenty layer simulation from Table 5.1 is chosen and the perturbation temperature varies from 1 to 150 K, as reported in Table 5.4. The last MD frame is taken and constant pressure energy minimization is performed. Our results indicate the

T (K)	1	5	10	15	20	25	30	35	40	45	50	70	80	100	150
γ (mJ/m ²)	81	121	121	121	161	121	161	161	161	161	81	0	121	121	200

Table 5.4: Surface energy, γ , after re-optimization following short molecular dynamics annealing runs at the specified temperatures.

system re-optimizes to a structure having stacking fault(s)/twins in the final configuration. This

can be verified by observing that the surface energies γ after re-optimization are approximately equal to integer multiples of the ISF of FCC Au (40 mJ/m^2). Upon the visual inspection of the output structures using the GDIS software,¹³ and for all perturbations at temperatures below 50 K, the structure contained only separated multiples of stacking faults. However, starting from 50 K, twinned portions were observed in the final configuration.

Our MD perturbation analysis agrees with that from RBSM. For small perturbations, multiple-slip minima are uncovered, e.g. single, double and triple, etc. stacking fault emissions. For relatively large perturbations, twinned portions / stacking faults in the final structure are obtained. This implies that there are several deformation paths in TBSM that should be accessible by changing the simulation parameters. It is not possible to obtain internal strain after TBSM re-optimization (e.g. single, double, triple, etc. slip energy minima as in the case of RBSM) because the method is based on constrained strain optimization and accordingly the re-optimization calculations are performed using constant pressure settings which removes any residual internal strain in the structure.

While performing tests on TBSM shearing of the twinning direction in FCC Au, the deformation path is found sensitive to numerical noise, i.e. if the number of CPUs to run the simulation changes, or if the same run is repeated multiple times in parallel. This was confirmed with simulations performed using the twenty layer system at a step size of 0.008, performed in parallel using twenty four CPUs which gave three possible deformation mechanisms in six trial runs. This shows that even without changing the simulation parameters, the system is able to access different deformation mechanisms in TBSM. This is rationalized because TBSM applies homogeneous strain throughout the interfaces and thus any factor that would help break the symmetry, such as numerical noise obtained through summing energy contributions in a different order, would affect the active deformation mechanism.

The twinning deformation section would be incomplete unless the new twinning route proposed by Wang *et al.* is examined. To this end, TBSM shear simulation along the twinning direction for the twenty layer configuration in Table 5.1 was repeated multiple times using twenty CPUs in parallel and found that there are two accessible deformation mechanisms, of which one is similar to the new twinning route. Figure 5.7 (a) shows that the strain surface energy increases as the system shears, until the first micro-slip event happens, after which three stacking faults are emitted in the system, as deduced by observing the re-optimized surface energy for the U_{1NR} frame being equal to three times the ISF of FCC Au (40 mJ/m^2). Differential displacements Δd_i change linearly

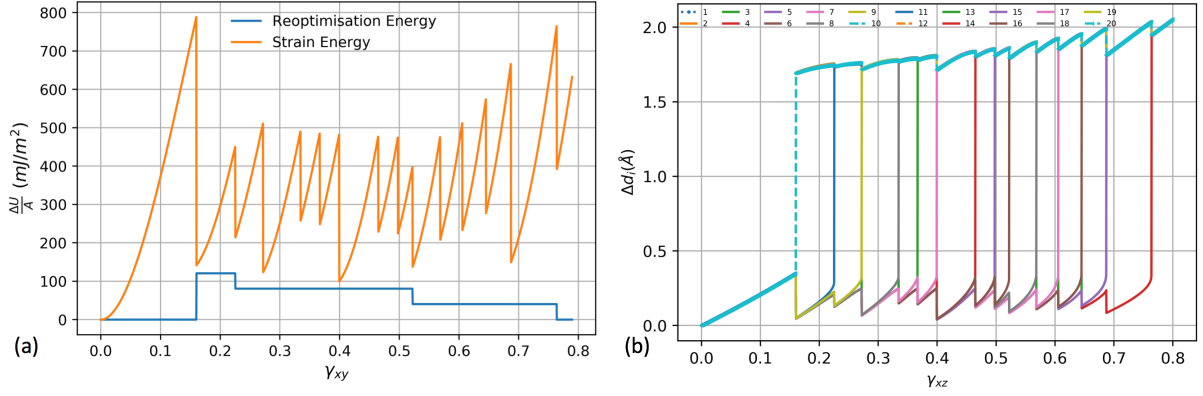


Figure 5.7: (a) Re-optimization and strain surface energies, and (b) the differential displacements Δd_i , as a function of strain describing the new twinning route proposed by Wang *et al.* found for the twenty layer simulation. The index i in Δd_i is one for the interface between the bottom-most and top-most atoms in the system, two for the interface between atoms one and two, etc.

as a function of strain until the first micro-slip event happens. Three stacking faults are emitted in the structure, where one has double-layers corresponding to the interface between the top-most and bottom-most atoms in the system (Δd_1) and the interface between atoms number nineteen and twenty (Δd_{20}). The two other stacking faults belong to the category of the new twinning route proposed by Wang *et al.* involving the interfaces between layers nine and ten (Δd_{10}) and layers eleven and twelve (Δd_{12}). Subsequent straining of the structure increases the strain energy to the U_{2N} barrier which is lower than the previous and subsequent barriers, consistent with the proposed new twinning route. The re-optimization surface energy becomes $80 \text{ mJ}/\text{m}^2$ as a stacking fault is emitted between layers ten and eleven (Δd_{11}), as observed by the blue line in Figure 5.7 (b) leading to a three layer twinned-region. Subsequent steps cause the twin to grow via emission of single/multiple stacking faults. Observing that the U_{9N} barrier in Figure 5.7 (a) is lower than U_{8N} and U_{10N} , and noting that the re-optimized surface energy equals to the ISF of FCC Au ($40 \text{ mJ}/\text{m}^2$) implies that two twinned portions of the crystal have merged into one. The discussion regarding the new twinning route proposed in reference¹⁰ being a special case of a more general scheme of the merger of stacking fault(s)/twinned regions happening at relatively lower barriers is equally applicable as discussed in section 5.4.4.

TBSM yields twinning deformation results similar to RBSM. The discussion in Chapter 4 regarding twinning deformation observed in RBSM is therefore equally applicable. Twinning deformation mechanisms naturally emerge from our simulations as a consequence of RFO calculating the twinning pathways for a given set of system parameters. The linear regression models for the prediction of the deformation mechanisms suggest a similar evolution of the potential energy hyper-surface as a function of the size of the system and predicts an increasing order of slip as a function of the

size of the system.

5.5 Shearing the (111)[$\bar{1}10$] System in FCC Au

TBSM was applied to study the shear deformation in FCC Au along the slip direction (111)[$\bar{1}10$]. The first part of this section deals with the convergence of the results as a function of the system and step sizes. Then, the deformation and alignment of the lattice vectors are investigated and compared to those obtained for the twinning deformation. Next, the strain energy versus strain for several sizes beyond the point of slip is described and the dominance of partial dislocation slip is highlighted. For one case, a detailed analysis is undertaken to clarify the different aspects of the complex deformation observed.

5.5.1 Convergence Analysis: System and Step Sizes

First, system size convergence analysis is performed by varying the number of layers in the system from two to twenty four. For all the simulations, $0.7 \gamma_{xz}$ is applied over the course of 2000 steps. The results of the normalized strain energy U_{1N} and shear strain before slip γ_{xz} are reported in Table 5.5. U_{1N} and γ_{xz} before slip converge to 0.0047 and 0.15, respectively, for system sizes greater

N_a	$\gamma_{xz,1N}$	U_{1N}
2	0.176	0.0055
3	0.155	0.0050
6	0.152	0.0048
7	0.152	0.0048
8	0.151	0.0048
9	0.151	0.0048
12	0.151	0.0048
14	0.150	0.0047
15	0.150	0.0047
20	0.150	0.0047
24	0.150	0.0047

Table 5.5: Summary of the system size dependent simulations when TBSM is applied to shear the slip direction in FCC Au.

than twelve. Next, a step size analysis is performed on the twelve layer simulation by varying the

strain per step from 0.07 to 0.007. The results are reported in Table 5.6. The normalized strain

Strain / Step	$\gamma_{xz,1N}$	U_{1N}
0.07	0.140	0.0043
0.014	0.140	0.0043
0.007	0.147	0.0046
0.0035	0.151	0.0048
0.0014	0.150	0.0047
0.0007	0.151	0.0048

Table 5.6: Summary of the step size convergence tests when TBSM is applied to shear the slip direction in FCC Au.

energy barrier U_{1N} and the strain γ_{xz} before slip converge to 0.0048 and 0.151, respectively, for strain sizes lower than 0.007.

The converged TBSM slip barrier U_{1N} and strain γ_{xz} (0.0047 and 0.15, respectively) are different to the RBSM results (0.0067 and 0.14, respectively), while noting γ_{xz} values are very close to each other. Converting the TBSM barrier to per interface per unit area yields 41.7 mJ/m^2 , which is lower than that obtained via RBSM, 54.3 mJ/m^2 , but both barriers remain much lower than the unstable slipping energy barrier (USE) of FCC Au (289 mJ/m^2) and slightly higher than the ISF of FCC Au (40 mJ/m^2). Our TBSM results imply that shearing the slip direction in FCC Au yields a much lower barrier than that calculated from γ surface theory.

The slip barriers U_{1N} are different between RBSM and TBSM because of the different simulated experimental conditions. RBSM emulates shearing part of the material whilst fixing its base, while TBSM emulates homogeneous strain of the structure. The twinning direction was shown as the easiest slip system in FCC metals based on RBSM in Chapter 3. It is interesting to note that both methods gave very similar barriers for twinning deformation but different barriers for slip. This is because TBSM in this case causes an exaggerated distortion of the lattice vectors and thus deviates from the RBSM situation. More information will be provided on this in the next section.

5.5.2 Deformation of the Lattice Vectors

Deformation of the lattice vectors as a consequence of the application of TBSM to the slip direction in FCC Au is addressed. Figure 5.8 reports the deformation of the components of the lattice vectors as a function of strain for the twelve layer simulation. Initially, lattice vector a was aligned along x , lattice vector b in the xy -plane, and lattice vector c had three Cartesian components. As

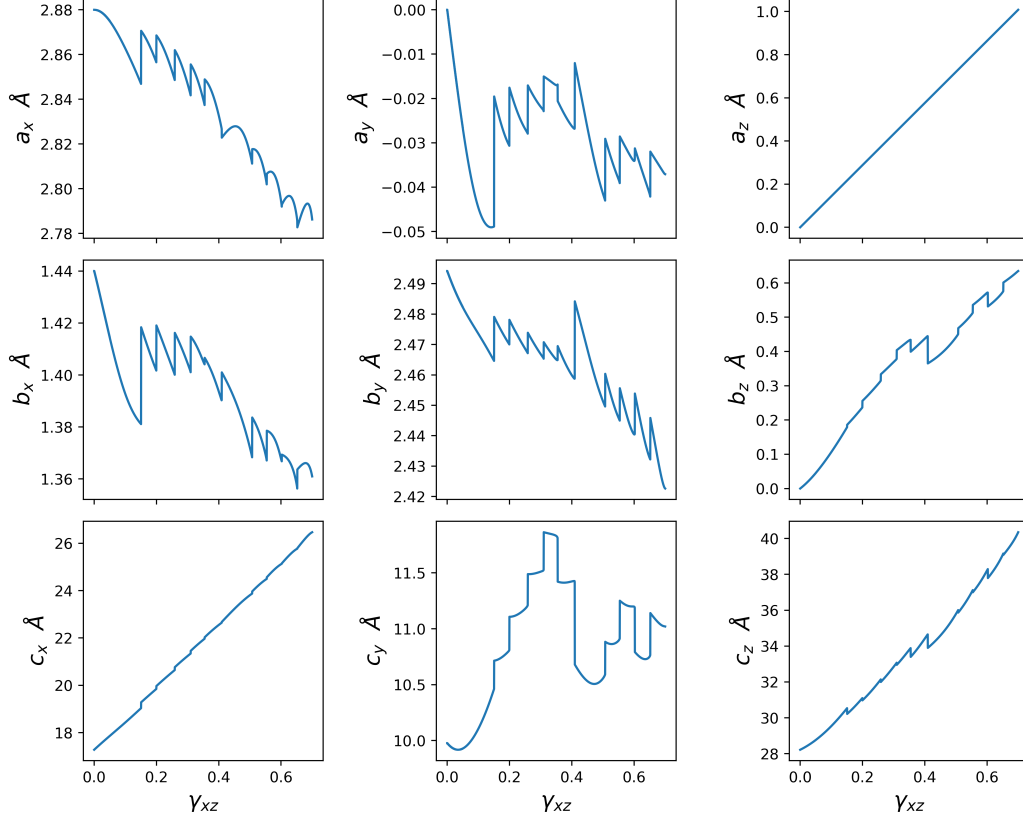


Figure 5.8: Change in the components of the lattice vectors as a function of TBSM strain, for the twelve layer configuration in Table 5.5.

the system shears by γ_{xz} , lattice vectors a and b start developing components in the other Cartesian directions. This necessitates the proper alignment of the crystallographic directions prior to any differential displacement Δd_i analysis. To this end, the formalism proposed in Chapter 2 to achieve the alignment is adopted and the three rotational angles are summarized in Table 5.7. Our

N_a	η	θ	ϕ
2	0.4	5.1	-2.9
3	0.8	4.5	-1.8
6	0.9	4.4	-1.7
7	0.9	4.4	-1.7

Table 5.7: The three angles η , θ , and ϕ for rotations about around z -, y -, and x -axis calculated for the frame before slip as a function of the size of the system. Note that the angles do not change for sizes greater than seven and so the remainder of the results are omitted. All units are in degrees.

results indicate that to achieve the desired alignment, rotations around all the three Cartesian axes are required. Interestingly, the θ value obtained (4.4°) is very similar to that along the twinning direction (4.7°). This is reasonable since even shearing the slip direction using TBSM leads to partial dislocation slip which involves the twinning direction. In contrast to the twinning direction,

the other two angles η and ϕ are not zero, 0.9° and -1.7° , respectively. This is consistent with the twinning direction being the easiest slip direction, as shearing other directions, such as the slip direction, causes a more severe distortion of the lattice vectors as manifested by the requirement of a more complicated three-dimensional rotation to achieve the alignment of the lattice vectors.

5.5.3 Slip Deformation Mechanisms

For TBSM shear of the slip system, the deformation of the lattice vectors and internal coordinates as a function of strain complicates the geometric propagation and description of slip. Figure 5.9 reports the normalized strain energy profiles as a function of strain for selected TBSM slip simulations.

For the two layer system, the evolution of the normalized strain energy is very similar to that

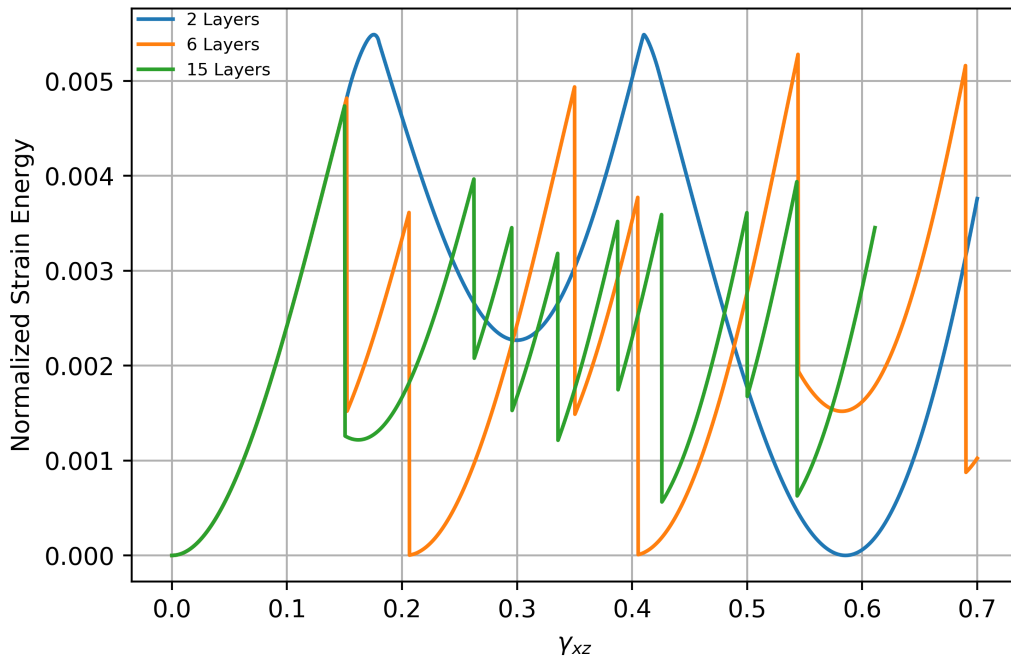


Figure 5.9: Normalized strain energy U_N profile as a function of strain for the two, six, and fifteen layer simulations when TBSM is used to shear in the slip direction in FCC Au.

obtained via RBSM and GSFE simulation of a full dislocation via dissociated partials. As the size of the system changes, the deformation mechanism becomes different. For instance, for the six layer simulation, U_{1N} and U_{2N} describe similar strain energy evolution as those of U_{3N} and U_{4N} . However, the U_{5N} barrier leads to an energy curve that is different from the previously periodic one. For the fifteen layer simulation, there are sharp drops in the energy for some slipping events (i.e. U_{1N} and U_{6N}) compared to shallow drops for other events (i.e. U_{2N} , U_{3N}). The trajectories

were visualized using VMD¹⁴ showing that as the size of the system changes, the system always activates full dislocation propagation by a partial dislocation mechanism. However, unlike RBSM, where the system is trapped in the same deformation mechanism beyond the U_{1N} barrier, e.g. if the system double slips, then it will always double slip in a periodic response to external strain, TBSM shear activates more than a single deformation mechanism along the same deformation path. For instance, the deformation may start with the emission of a partial dislocation involving two adjacent stacking faults, and would proceed, instead of annihilating these stacking faults as in RBSM, by producing other partial dislocations at different interfaces before the annihilation process starts. This can further be validated by observing that the periodicity of the slip events in Figure 5.9 is not fixed along the same deformation path.

RBSM and TBSM are found to give different deformation mechanisms. This is because the boundary conditions (or analogously, the emulated experiments of simple and pure shear by RBSM and TBSM, respectively) in each method are different. This is why when the slip direction shears in FCC Au, TBSM favors the activation of partial dislocation slip by dissociated partials, while RBSM allows for different multiplicities of slip and partial dislocation slip. From the perspective of continuum mechanics, the problems of simple shear and pure shear have been studied using different methods, models, assumptions, and constitutive descriptions.^{15–18} The common consensus is that simple shear and pure shear describe different strain energy density functions in the finite strain limit. Our atomistic simulations support this conclusion in that the detail of the deformations simulated are different between RBSM and TBSM.

Finally, the partial dislocations emitted in RBSM were characterized by incompleteness due to the rigid blocks. However, these dislocations are complete in the case of TBSM as there are no constraints apart from the homogeneous shear strain which does not affect the shape of the partial dislocation. In the next subsection, a detailed analysis of a full dislocation slip by partial dislocations in TBSM is provided and the complexity of the slip pattern obtained is highlighted.

5.5.4 Dislocation Slip By Partial Dislocations

The example of the twelve layer TBSM slip deformation is considered. The simulation details are found in section 5.5.1. Lattice vectors have been aligned as per previous sections in order to calculate the differential displacement Δd_i . Figure 5.10 summarizes the strain and re-optimization surface energies, and the differential displacement Δd_i as a function of TBSM strain γ_{xz} . For the Δd_i plots in Figure 5.10 (b), five atoms deform plastically in the xy plane and their traces are

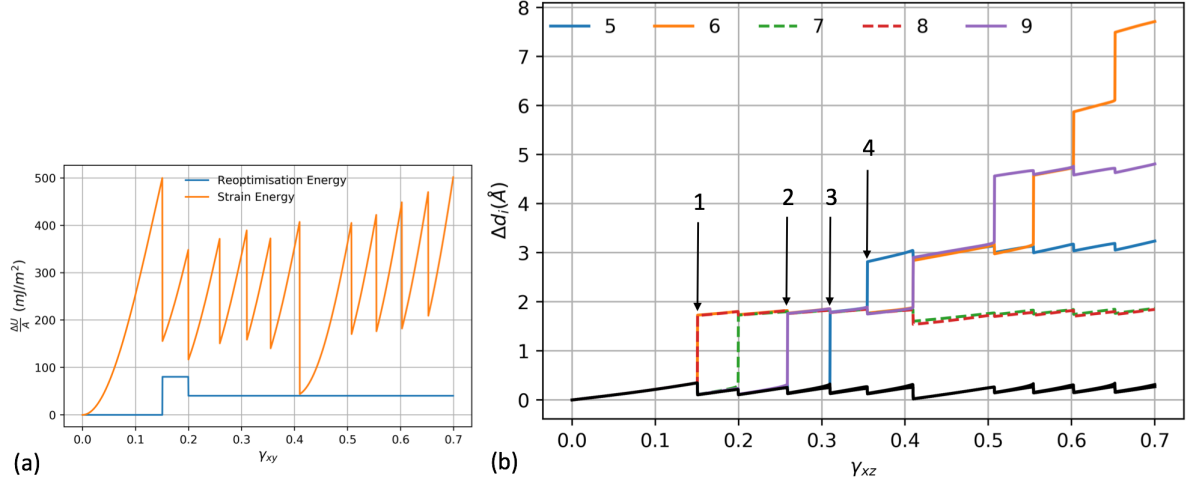


Figure 5.10: (a) Strain and re-optimized surface energies, (b) and differential displacement Δd_i as a function of TBSM γ_{xz} shearing the slip system in FCC Au. Index i of Δd_i takes the value of one for the differential displacement between the top-most atom and bottom-most atom in the system, two for layers one and two, etc. Arrows indicate specific frames to be elaborated on in the main text.

colored, while the remainder of the atoms deform elastically in the same plane and their traces are all colored in black. As the system shears, the strain surface energy increases until the first slip event happens (see arrow 1 in Figure 5.10 (b)). The re-optimization surface energy shows the system slips into a state having twice ($80 \text{ mJ}/m^2$) the ISF of FCC Au. The differential displacement Δd_i in Figure 5.10 (b) show large increases in Δd_6 and Δd_8 , i.e. between layers five and six, and seven and eight, respectively, analogous to the new twinning route.¹⁰ Additional shearing of the system leads to the U_{2N} barrier for which a large increase in Δd_7 is observed, i.e. between layers six and seven, leading to the formation of a three layered twinned region. Thus, the re-optimization energy in Figure 5.10 (a) equals to the ISF of FCC Au. The subsequent slip events indicated by arrows 2 and 3 in Figure 5.10 (b) show that the twinned region grows by one layer per frame. The slip event indicated by arrow 4 shows another distinct increase in Δd_5 . Inspection using VMD¹⁴ showed that this event corresponded to the emission of a trailing partial dislocation. Because in this particular supercell, lattice vector a is aligned along the x -axis and the twinning direction is aligned along $\vec{a} + \vec{b}$, Δd_i is calculated based on the travelled distance, and thus provides no sense of the direction of the increase in Δd_5 . Subsequent slip events correspond to additional large increase in different Δd_i and thus we deduce that it is not a single deformation mechanism that is activated along the deformation, but several mechanisms.

Based on the above analysis, slip deformation becomes complicated as TBSM shears the slipping system in FCC Au and especially with the activation of more than one deformation mechanism in the same run. This feature of TBSM, that was not observed in RBSM, is attributed to the difference

in the boundary conditions of each method.

5.6 TBSM Strain Versus Green-Lagrange

TBSM adopts a finite strain derivative formalism and therefore can evaluate these derivatives far from equilibrium. TBSM calculates the Voigt strain tensor according;

$$\boldsymbol{\epsilon} = R.R_0^{-1} \quad (5.7)$$

where $\boldsymbol{\epsilon}$ is the TBSM strain tensor, R and R_0^{-1} are the column-wise deformed and inverse reference lattice vectors. The aim of this section is to verify the validity of such a strain definition compared to the Green-Lagrange finite strain tensor, at least for the frames before slip where the barrier is determined. Green-Lagrange strain is found by evaluating;

$$\boldsymbol{E} = \frac{1}{2}(\boldsymbol{C} - \boldsymbol{I}) \quad (5.8)$$

where \boldsymbol{E} is the Green-Lagrange strain tensor, \boldsymbol{C} is the Cauchy-Green deformation tensor and \boldsymbol{I} is the identity tensor. In principle, \boldsymbol{E} describes deformation which involves not only the constituent material in the system, but also the frame of reference. To compare both strain tensors, the shear strain invariant formalism¹⁹ is used;

$$s = \sqrt{s_{yz}^2 + s_{xz}^2 + s_{xy}^2 + \frac{(s_{yy} - s_{zz})^2 + (s_{xx} - s_{zz})^2 + (s_{xx} - s_{yy})^2}{6}} \quad (5.9)$$

where s represents the shear invariant, and s_{ij} represent the components of either the \boldsymbol{E} or $\boldsymbol{\epsilon}$ strain tensors.

For brevity, the results of the different strain tensors and their invariants only for the seven and fifteen layer systems are collected in Table 5.8 for both the slip and twin deformation simulations at the frame U_{1N} before slip. The shear invariants are equal between $\boldsymbol{\epsilon}$ and \boldsymbol{E} . This demonstrates that the normalized strain energy barriers U_{1N} happen at frames where both definitions of strain are consistent and so justifies the current formalism of TBSM in applying the strain tensor $\boldsymbol{\epsilon}$ to simulate deformation.

The degree of distortion in the system when strain is applied to the easy (twin, (111)[$\bar{2}11$]) or a relatively difficult (slip, (111)[$\bar{1}10$]) slip system, is highlighted. For the twinning system, the yz and xy components of strain are zero, and so four components of strain describe the current state of strain. On the other hand, the slip system has five components of strain describing the current strain state in the system - that is if we neglect the yy component since it has a very small strain

Deformation	Size	Strain Tensor	xx	yy	zz	yz	xz	xy	s
Slip	7	ϵ	-0.012	-0.002	0.026	0.029	0.076	-0.017	0.085
Slip	7	E	-0.009	-0.002	0.03	0.028	0.076	-0.016	0.085
Slip	15	ϵ	-0.011	-0.002	0.026	0.028	0.075	-0.017	0.084
Slip	15	E	-0.008	-0.001	0.029	0.028	0.075	-0.016	0.084
Twin	7	ϵ	-0.024	0.011	0.026	0.000	0.081	0.000	0.085
Twin	7	E	-0.021	0.011	0.029	0.000	0.081	0.000	0.085
Twin	15	ϵ	-0.024	0.011	0.025	0.000	0.080	0.000	0.084
Twin	15	E	-0.021	0.011	0.029	0.000	0.080	0.000	0.084

Table 5.8: Summary of the TBSM strain tensor ϵ and Green-Lagrange finite strain tensor E and the shear invariant s for the frame before slip U_{1N} in the seven and fifteen layer simulations sheared along the slip and twinning directions.

value. This shows that there exists a correlation between the number of non-zero strain components before slip and the relative “ease” of slip/twin along a particular slip system.

5.7 Ideal Shear Strengths and Slip Barriers of FCC Metals

This section first elaborates on the calculation of the ideal shear stress based on TBSM calculations. Then, TBSM is applied to FCC Ag, Pd, Pt, Pb Cu, Ni, and Al to find the slip barriers and ideal shear strengths.

5.7.1 Stress Tensor in TBSM: Ideal Shear Strength of FCC Au

TBSM calculates the stress tensor by the analytic evaluation of the first derivative of energy with respect to strain, divided by the volume of the supercell;

$$\sigma_{ij} = \frac{1}{V_0} \frac{dU}{d\epsilon_{ij}} \quad (5.10)$$

where V_0 is the volume of the supercell, U is the energy of the supercell, σ and ϵ are stress and strain tensors, respectively, i and j indices refer to the x , y and z Cartesian components. Supplemented with RFO calculations to ensure the positive-definiteness of the Hessian, calculations of the stress tensor becomes relatively accurate compared to affine shear deformation methods in general.⁶

Figure 5.11 shows typical stress-versus-strain curves for FCC Au along the slip and twinning directions. The observed general trend of the stress versus strain curves is common for all the converged

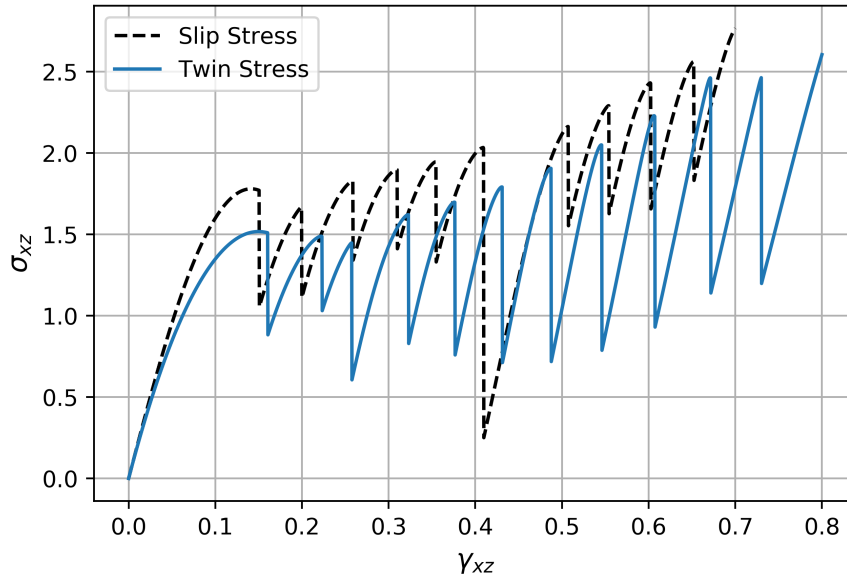


Figure 5.11: Shear stress σ_{xz} versus strain for the twelve layer simulation of FCC Au for the twinning and slip directions.

simulations. As TBSM shears the system within the limit $\gamma_{xz} < 0.025$, both stress curves follow the same linear curve as they are superimposed on each other. As the system approaches the strain at which slip occurs, the slopes of the curves become different. Based on the system size analysis, the ideal shear stresses converged to 1.51 and 1.77 GPa for the twinning and slip directions, respectively. In the next subsection, the slip barriers and ideal shear strengths for FCC Au and all other FCC metals are discussed and compared to RBSM.

The stress curves obtained from TBSM are different compared to those of RBSM, where the periodic stress versus strain curve showed equal stress after slip for the slip and twinning curves. However, TBSM shows that for both slip systems, the stress peaks after slip exhibit a non-linear trend. The deformation of the lattice vectors caused a similar non-linear trend in the energy profiles discussed in earlier sections. Thus, a similar non-linear trend also affects the stress peaks in TBSM calculations.

5.7.2 Slip barriers and Ideal Shear Strength for FCC Metals

TBSM is used to calculate the slip barriers and ideal shear strengths for FCC Ag, Pd, Pt, Pb, Cu, Ni, and Al. Each simulation used the twelve layer supercell at a strain per step of 0.00035. The results are summarized in Tables 5.9 and 5.10.

According to the slip barriers in Table 5.9, TBSM yields slip barriers that are consistent with

Material	Slip		Twin	
	RBSM	TBSM	RBSM	TBSM
Pb	0.0117	0.0100	0.0083	0.0090
Ag	0.0245	0.0177	0.0173	0.0164
Au	0.0067	0.0047	0.0046	0.0045
Al	0.0131	0.0114	0.0107	0.0101
Cu	0.0236	0.0167	0.0167	0.0152
Ni	0.0253	0.0198	0.0185	0.0176
Pd	0.0219	0.0186	0.0157	0.0163
Pt	0.0179	0.0125	0.0122	0.0115

Table 5.9: Normalized strain energy barriers before slip for the slip and twinning directions for FCC metals obtained from RBSM and TBSM.

Material	Slip		Twin	
	RBSM	TBSM	RBSM	TBSM
Pb	1.25	1.04	0.88	0.88
Ag	5.51	4.13	3.67	3.44
Au	2.78	1.77	1.70	1.51
Al	3.55	3.26	3.16	2.97
Cu	8.53	6.56	5.78	5.46
Ni	12.61	11.42	9.30	9.75
Pd	10.20	8.25	7.15	6.83
Pt	10.49	7.87	6.60	6.71

Table 5.10: Ideal shear strength along the slip and twinning directions calculated from RBSM and TBSM for several FCC metals. Experimental values are included for comparison, where available. All units are in GPa.

RBSM for the purpose of ranking the slip systems, e.g. the twinning deformation barrier is always lower than the slip barrier. However, the difference between the two barriers is not the same. Taking the example of FCC Au, TBSM predicts the slip and twinning barriers are very close to each other (0.0047 and 0.0045, respectively) while RBSM predicts there is a larger difference (0.0067 and 0.0046, respectively). This difference in the barriers is attributed to the unique boundary conditions modeled by each method, as discussed earlier. Since each method simulates a different

physical experiment with different constraints, we expect that this difference in the barriers is realistic. However, both methods consistently rank the slip barriers in FCC metals.

Next, the ideal shear strength results in Table 5.10 are considered. Interestingly, regardless of whether TBSM or RBSM is used to deform the FCC metal single crystal, the ideal shear strength along the easiest slip system (e.g. the twinning system) is relatively close, with a maximum difference of 0.45 GPa which occurs for Ni. This implies that the influence of constraints in RBSM has little impact on the results when the easiest slip system is sheared. On the other hand, the ideal shear strength results based on the slip deformation are similar in some cases (i.e. FCC Al and Pb) and very different in other cases (FCC Cu and Pd) with an approximate maximum difference of 2 GPa. Such a difference is reasonable as it implies shearing a slip system that is not the easiest would strongly depend on the constraints and the relaxations in the system; RBSM maintains the rigid block constraint in the xy plane while TBSM deforms the lattice vectors while relaxing the constraints other than the fixed component of strain to find the slipped state.

5.8 Finding the Easiest Slip Direction

A procedure was devised to identify the easiest slip system based on geometric treatment of the deformed configuration before slip. The Green-Lagrange finite strain, found by equation 5.8, defines the finite strain with respect to the reference configuration. Let us assume we apply TBSM by fixing γ_{xz} to a specific slip system in an FCC metal along the (111) plane. Subjecting the Green-Lagrange finite strain (\mathbf{E}) and Cauchy-Green (\mathbf{C}) tensors to a three-dimensional rotation tensor $\mathbf{T} = T_z(\eta)T_y(\theta)T_x(\phi)$ such that;

$$\mathbf{E}'_f = \mathbf{T}^T \mathbf{E} \mathbf{T} = \frac{1}{2}(\mathbf{T}^T \mathbf{C} \mathbf{T} - \mathbf{I}) \quad (5.11)$$

where \mathbf{E}'_f is the transformed Green-Lagrange strain, provides the unique orientation of easy slip. In principle, because TBSM relaxes all other strain components except the fixed one, we would potentially obtain several components of the strain tensor in the frame before slip. Thus, we reformulate the strain tensor via the application of rotation \mathbf{T} such that components E_{xx} , E_{xy} , and E_{yz} vanish. This can be achieved by solving the non-linear system of three equations in A.1 ($E_{xx} = 0$, $E_{xy} = 0$, and $E_{yz} = 0$) to find η , θ , and ϕ .

Physically, the above procedure eliminates all other shear strain components and finds a maximized

$E'_{f,xz}$ that is greater than E_{xz} . Such a procedure combines the instability point, as atomistically calculated via TBSM (e.g. the last deformed configuration before slip), with the geometric description from continuum mechanics by reformulating the Green-Lagrange strain in a transformed frame of reference, to find the unique orientation which presumably should be pointing toward the easiest slip system. The detailed system of equations can be found in Appendix A.

SPyder¹² scientific environment in the Anaconda data science toolkit has been used to solve the non-linear system of equations for all the system sizes along the slip and twinning directions. The resulting angles converge much faster than the normalized strain energy barrier and thus the converged results are reported for the twelve layer simulations in Table 5.11. For the twinning de-

	η	θ	ϕ	ε_{yy}	ε_{zz}	ε_{xz}
Twin	0.0	-7.1	0.0	0.011	0.008	0.084
Slip	21.3	-6.3	6.4	0.008	0.011	0.084

Table 5.11: Summary of the three principal rotation angles, η , θ , and ϕ , about the z , y , and x axes, respectively, to align the system along the easiest slip direction for the twelve layer simulations. ε_{ij} are the components of the transformed Green-Lagrange finite strain tensor.

formation, a clock-wise rotation about the y -axis by 7.1° aligns the reference structure along the direction of easiest shear. The other rotations by angles η and ϕ are zero. This highlights that the twinning direction is the easiest slip system in FCC Au and that the role of the clock-wise rotation is to nullify the ε_{xx} component of strain. This result also agrees with those obtained for the alignment of the lattice vectors along the reference crystallographic direction, as can be seen in section 5.4.2, which only required a single rotation.

On the other hand, the easiest direction of shear when TBSM is applied to the slip direction requires three-dimensional orthogonal rotations, 21.3° η counter clock-wise rotation about z , 6.3° θ clock-wise rotation about y , and 6.4° ϕ counter clock-wise rotation about x . The most significant angle is η since it involves a rotation of the plane of shear xz about the z axis. Ideally, the resulting η should be close to the ideal angle between the slip and twinning directions (30°) compared to the calculated 21.3° . This difference between the ideal and calculated values is due to the distortion of the lattice vectors as a function of strain, and implies this geometric tool is approximate and not exact. Similar to previous observations, when the shear direction is away from the easiest slip, three-dimensional orthogonal rotations are necessary to approach the direction of easiest slip, similar to the results we obtained for the alignment of the lattice vectors in section 5.5.2.

Another powerful feature of this geometric tool is the ability to analyze the strain tensor for two

different configurations with respect to the same strain state (space). For instance, the transformed strain tensors in Table 5.11 are very similar, and in fact the shear stresses ε_{xz} are equal.

5.9 Summary

Tensor-Based Shearing Method (TBSM) was utilized to study the deformation of FCC Au and other FCC metals. By varying the energy minimization algorithm, it was shown that the Rational Function Optimizer (RFO) is best suited to simulate deformation in affine shear deformation methods. Previous versions of affine shear deformation methods used Newton-Raphson (NR) and did not succeed in describing deformation aspects owing to the presence of phonon instabilities and the system traversing a higher energy path.

TBSM is therefore the first affine shear deformation method to describe twinning deformation mechanisms in this level of detail. The classical and new twinning routes are revealed and investigated using energetic and structural techniques. Our post-processing showed that the lower barrier characteristic of the new twinning route is a special case of a more general structural-energy phenomena when twins/stacking faults merge.

Our TBSM analysis identified the multiplicity of slip models along the twinning direction, consistent with similar findings in RBSM. These models should be useful in developing multi-scale computational theories of metallic crystal deformation. Owing to the boundary conditions, TBSM favored full dislocation slip by dissociated partial dislocations when shearing along the slipping direction in FCC Au. This calls for further experimental investigation on the influence of the boundary conditions on the deformation mechanisms when deforming metallic single crystals.

TBSM was used to shear several FCC metals along the slip and twinning directions. The ranking of the slip systems is consistent, in that it is always easier for the FCC crystal to twin rather than slip, consistent with RBSM findings. Ideal shear strengths calculations agreed with RBSM values, except for the slip direction because of the interaction of the boundary conditions with the deformation pathways. Such differences were anticipated and are rooted in the theoretical and experimental investigation of simple and pure shear deformation.^{15–18}

Like RBSM, TBSM is not able to simulate all aspects of plastic deformation. In particular, materials with heterogeneities and defects cannot be simulated, as well as the nucleation of dislocation loops and dislocation cores and their interactions. However, TBSM should, in principle, apply for all classes of crystalline materials.

Finally, the TBSM strain tensor was compared to the Green-Lagrange finite strain tensor. Both tensors reasonably agree with each other. A geometric tool has been introduced to find the easiest slip system when TBSM is applied to shear a material with an unknown slip system ranking. The geometric tool was shown to yield approximate results due to the deformation of the lattice vectors. However, a consequence of the geometric tool is the comparison of two different strain tensors under the same enforced strain state conditions. This showed that indeed the transformed fixed strain components in TBSM between the slipping and twinning directions are equal. This geometric tool may find applications beyond approaching the easiest slip system, especially in deformation experiments where specific strain states are sought with respect to the original reference structure.

Bibliography

- ¹ D. Roundy, C. R. Krenn, M. L. Cohen, and J. W. Morris, “Ideal shear strengths of fcc aluminum and copper,” *Phys. Rev. Lett.*, vol. 82, pp. 2713–2716, Mar 1999.
- ² S. Ogata, J. Li, and S. Yip, “Ideal pure shear strength of aluminum and copper,” *Science*, vol. 298, no. 5594, pp. 807–811, 2002.
- ³ V. Segal, “Severe plastic deformation: simple shear versus pure shear,” *Materials Science and Engineering: A*, vol. 338, no. 1, pp. 331–344, 2002.
- ⁴ A. Banerjee, N. Adams, J. Simons, and R. Shepard, “Search for stationary points on surfaces,” *The Journal of Physical Chemistry*, vol. 89, pp. 52–57, 01 1985.
- ⁵ S. Pattamatta, R. S. Elliott, and E. B. Tadmor, “Mapping the stochastic response of nanostructures,” *Proceedings of the National Academy of Sciences*, vol. 111, no. 17, pp. E1678–E1686, 2014.
- ⁶ D. M. Clatterbuck, C. R. Krenn, M. L. Cohen, and J. W. Morris, “Phonon instabilities and the ideal strength of aluminum,” *Phys. Rev. Lett.*, vol. 91, p. 135501, Sep 2003.
- ⁷ M. Jahnátek, J. Hafner, and M. Krajčí, “Shear deformation, ideal strength, and stacking fault formation of fcc metals: A density-functional study of al and cu,” *Phys. Rev. B*, vol. 79, p. 224103, Jun 2009.
- ⁸ S.-L. Shang, J. Shimanek, S. Qin, Y. Wang, A. M. Beese, and Z.-K. Liu, “Unveiling dislocation characteristics in Ni₃Al from stacking fault energy and ideal strength: A first-principles study via pure alias shear deformation,” *Phys. Rev. B*, vol. 101, p. 024102, Jan 2020.
- ⁹ G. Li, Q. An, U. Aydemir, S. I. Morozov, B. Duan, P. Zhai, Q. Zhang, and W. A. Goddard, “Intrinsic mechanical behavior of mgagsb thermoelectric material: An ab initio study,” *Journal of Materiomics*, vol. 6, no. 1, pp. 24–32, 2020.

- ¹⁰ L. Wang, P. Guan, J. Teng, P. Liu, D. Chen, W. Xie, D. Kong, S. Zhang, T. Zhu, Z. Zhang, E. Ma, M. Chen, and X. Han, “New twinning route in face-centered cubic nanocrystalline metals,” *Nature Communications*, vol. 8, 12 2017.
- ¹¹ J. R. Rice, “Dislocation nucleation from a crack tip: An analysis based on the peierls concept,” *Journal of the Mechanics and Physics of Solids*, vol. 40, no. 2, pp. 239 – 271, 1992.
- ¹² “<https://www.spyder-ide.org/>.”
- ¹³ S. Fleming and A. Rohl, “Gdis: A visualization program for molecular and periodic systems,” *Zeitschrift Fur Kristallographie - Z KRISTALLOGR*, vol. 220, pp. 580–584, 01 2005.
- ¹⁴ W. Humphrey, A. Dalke, and K. Schulten, “Vmd: Visual molecular dynamics,” *Journal of Molecular Graphics*, vol. 14, no. 1, pp. 33 – 38, 1996.
- ¹⁵ C. Thiel, J. Voss, R. J. Martin, and P. Neff, “Shear, pure and simple,” *International Journal of Non-Linear Mechanics*, vol. 112, pp. 57–72, 2019.
- ¹⁶ D. Moreira and L. Nunes, “Comparison of simple and pure shear for an incompressible isotropic hyperelastic material under large deformation,” *Polymer Testing*, vol. 32, no. 2, pp. 240–248, 2013.
- ¹⁷ M. Destrade, J. Murphy, and G. Saccomandi, “Simple shear is not so simple,” *International Journal of Non-Linear Mechanics*, vol. 47, no. 2, pp. 210–214, 2012. Nonlinear Continuum Theories.
- ¹⁸ M. B. Rubin, “Pure shearing and pure distortional deformations are not equivalent,” *Journal of Elasticity*, vol. 142, no. 2, pp. 383–393, 2020.
- ¹⁹ F. Shimizu, S. Ogata, and J. Li, “Theory of shear banding in metallic glasses and molecular dynamics calculations,” *MATERIALS TRANSACTIONS*, vol. 48, no. 11, pp. 2923–2927, 2007.

Every reasonable effort has been made to acknowledge the owners of copyright material. I would be pleased to hear from any copyright owner who has been omitted or incorrectly acknowledged.

Chapter 6

Deformation in MgO

6.1 Introduction

Having tested our methods on several FCC metals, we turn our attention to ionic crystals, because ionic interactions can also be present in organic molecular crystals. Accordingly, this chapter applies RBSM and TBSM to study the deformation of MgO, an ubiquitous ionic crystal whose slip systems are experimentally known. Deformation in ionic crystals and especially MgO was reviewed in Chapter One. The active slip systems in MgO are the $\{110\}\langle 110\rangle$ and $\{001\}\langle 110\rangle$ systems.¹ The presence of charges in ionic crystals adds an additional complexity to determining the active slip systems, as suggested by Amodeo *et al.*,¹ because it is impossible to force ions of the same charge against each other.

In Chapter One, the experimental evidence for the presence of electrical effects associated with the plastic deformation of ionic crystals, as reviewed by Urusovskaya,² was presented. Can such effects emerge in the course of quasi-static deformation of ionic crystals? In anticipation of such an emergence, Coulomb's law and two variants of the Ewald Sum to calculate the electrostatic interactions in periodic systems are discussed below. The electrostatic interaction energy is calculated using Coulomb's law;³

$$U^{Coulomb} = \frac{1}{2} \sum_{i=1}^N \sum_{\substack{j=2 \\ i \neq j}}^N \frac{q_i q_j e^2}{4\pi\epsilon_0 r_{ij}} \quad (6.1)$$

where q_i and q_j are the elementary charges of atoms i and j , e is the magnitude of the charge of an electron in Coulomb C , ϵ_0 is the vacuum permittivity, and r_{ij} is the distance between atoms i and j . Because of the inverse proportionality of the electrostatic interaction to the distance r_{ij} , and bearing in mind that the number of terms in equation 6.1 (which is a mathematical series) is

directly proportional to r^2 (surface area of a sphere), the evaluation of 6.1 in periodic simulations, is conditionally convergent.³ The solution to this conditional convergence involves dividing the sum into two absolutely convergent series while imposing the two conditions on the sum; the sum of charges must be zero and the dipole moment must have a defined value. This is known as the Ewald sum^{4,5} and can be expressed in atomic units as;

$$U^{real} = \frac{1}{2} \sum_{i=1}^N \sum_{j=1}^N \frac{q_i q_j}{r_{ij}} \operatorname{erfc}(\eta^{\frac{1}{2}} r_{ij}) \quad (6.2a)$$

$$U^{recip} = \frac{1}{2} \sum_{i=1}^N \sum_{j=1}^N \sum_{\mathbf{G}} \frac{4\pi}{V} q_i q_j e^{i\mathbf{G} \cdot \mathbf{r}_{ij}} \frac{e^{-\frac{G^2}{4\eta}}}{G^2} \quad (6.2b)$$

$$U^{self} = - \sum_{i=1}^N q_i^2 \left(\frac{\eta}{\pi} \right)^{\frac{1}{2}} \quad (6.2c)$$

$$U^{electrostatic} = U^{real} + U^{recip} + U^{self} \quad (6.2d)$$

where V is the unit cell volume, G is the reciprocal lattice vector, η is a parameter dividing the contributions between the reciprocal and real space calculations. Equation 6.2 shows that electrostatic interactions in a periodic system are found by calculating the contributions from real space which is short-range, reciprocal space which is long-range, and the subtraction of the self-charge energy which corrects for the introduction of Gaussian distributions on atomic sites. There are certain conditions to use equation 6.2. By construction, the system cannot be charged and a special procedure needs to be followed (a modified version of 6.2) if charged systems are to be considered. In addition, equations 6.2 assume tin-foil boundary conditions, i.e. an infinite dielectric constant surrounds the system. The physical consequence of tin-foil boundary conditions is that no dipole/macroscopic polarization is allowed and so any arising are assumed to be screened by a compensating opposite dipole even though this dipole in reality must either interact with the surfaces or cause a flow of current.

To replace the tin-foil boundary conditions in 6.2 (i.e. the other form of Ewald sum), it is possible to add a dipolar term that accounts for an excited dipole in the system. This is termed the dipole correction and adopts the form of the last term in equation (2) reference;⁶

$$U^{corr} = \frac{2\pi}{(2\epsilon_S + 1)V} \left| \sum_{i=1}^N q_i r_i \right|^2 \quad (6.3)$$

where ϵ_S is the dielectric constant of the surrounding medium, and V is the volume of the unit cell. It is readily observed that equation 6.3 vanishes under tin-foil boundary condition since ϵ_S tends to

$+\infty$. On the other hand, if we assume the system is surrounded by vacuum, i.e. ϵ_S equals to 1, then the coefficient of the squared sum of the dipole moment ($|\sum_{i=1}^N q_i r_i|^2$) becomes $2\pi/3V$. The dipole correction term for the case of having vacuum as the surrounding medium is implemented in GULP³ and hence will be used in simulations. We note that an excited dipole⁷ in a 3D periodic system is ambiguous and ill-defined, thus our focus will be on the change of the dipole, i.e. the relative polarization of the system.

The aim behind this chapter is to confirm our proposed methods provide a consistent ranking of the slip systems in MgO, thus we will not treat deformation aspects in as much detail as for FCC Au. The first part of this chapter gives an overview of the system geometry and setup preparation. The second part addresses the application of RBSM to MgO slip systems, with a focus on slip barriers and ideal shear strengths. The third part applies TBSM to investigate slip systems in MgO with two sets of calculations; with and without the dipole correction term.

6.2 Geometry and Setup Details

All MgO deformation simulations use the breathing shell model³ introduced in Chapter Two. MgO adopts a rock-salt structure, with a face-centered cubic distribution of ions in the cell. GDIS⁸ was

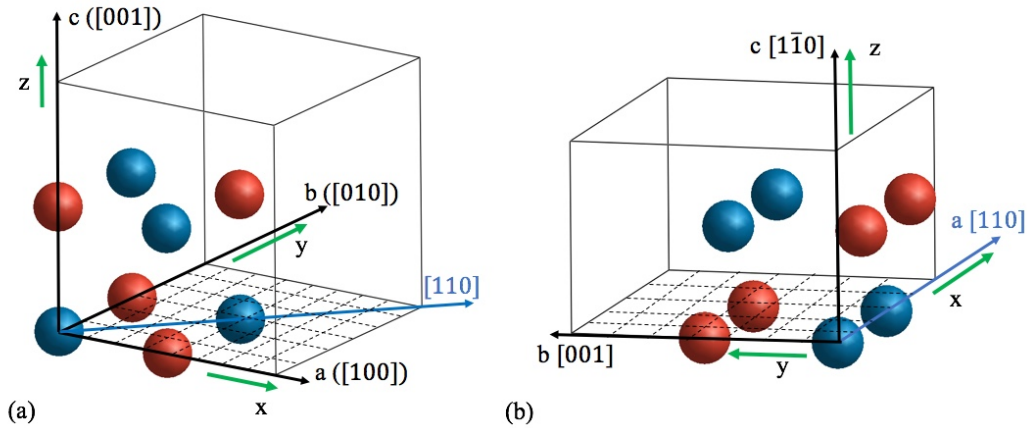


Figure 6.1: Different cell representations of MgO. (a) face-centered cubic cell used in (001) plane simulations, and (b) cell representation used in $(\bar{1}10)$ plane simulations. Spheres in blue and red represent Mg and O ions, respectively. Cartesian axes are indicated by the green arrows, while crystallographic directions (w.r.t. the face-centered cubic cell) and the lattice vectors are indicated by black arrows. The dashed lines represent the slip plane. The slip direction $[110]$ is indicated by the blue arrow.

used to construct surface cells. We note that shearing the crystal along the $[110]$ direction in the (001) plane forces ions of different signs closer together, yet shearing the same direction in the $(\bar{1}10)$ plane brings ions of the same sign closer together.

For the convergence analysis, step and system analysis for both systems have been performed and the results are detailed in Appendix B. All the technical details of the system's size and step size used in the below analysis falls within the convergence limit. For RBSM calculations, the size of the rigid blocks are set to four layers each. As a rule of thumb, the size of the rigid blocks must be larger than the highest potential cut-off, which in our case, corresponds to 10 Å (Buckingham potentials) and is slightly lower than a rigid block having 10 layers in the $(\bar{1}10)$ plane. Whether our choice of the size of the rigid blocks converge the energy or not will be visited in the results section. The size of region one is twelve layers and 0.0009 strain per step was used to shear both slip systems. The ideal shear strength for both slip systems was calculated following the same procedure in Chapter Two.

For TBSM, the geometry based on the cells reported in Figure 6.1 was generated. The system sizes for both slip systems contained twelve layers in total, with four ions per layer. A strain size of 0.0013 per step was used to shear both slip systems. A rotation tensor mapped the (001) supercell into another via a 45° counter-clockwise rotation about the z -axis so that the [110] direction aligned along the x -axis allowing TBSM to shear the (001)[110] by fixing the γ_{xz} component. The $(\bar{1}10)$ supercell already has the [110] direction aligned along the x -axis. All TBSM simulations incrementally fixed the γ_{xz} component while the other components of strain were relaxed.

6.3 Application of RBSM to MgO Slip Systems

This section describes the results from the application of RBSM to MgO slip systems. Figure 6.2, illustrating the normalized strain energy as a function of strain, clearly shows that the barrier to activate the $(\bar{1}10)[110]$ slip system (0.0044) is much lower than for the (001)[110] slip system (0.0163). In addition, the slip strain for the $(\bar{1}10)[110]$ system equals 0.17 ($\gamma_{b,xz}$), lower than that for the (001)[110] system (0.27). Our results are consistent with the experimental ranking of the slip systems in MgO based on the shear stress.¹ We also repeated the twenty layer simulation but with the rigid blocks having 10 layers each for both slip systems and found that the U_{1N} are exactly equal for each slip system, which implies our choice of the size of the rigid blocks is converged. By visualizing the trajectory, we observed that slip in the $(\bar{1}10)[110]$ system occurred at the mid-section of region one, i.e. between layers 6 and 7, while slip in the (001)[110] system occurred very close to region three (between layers one and two in region one).

In order to calculate the stress versus strain curve and estimate the ideal shear stress of MgO ac-

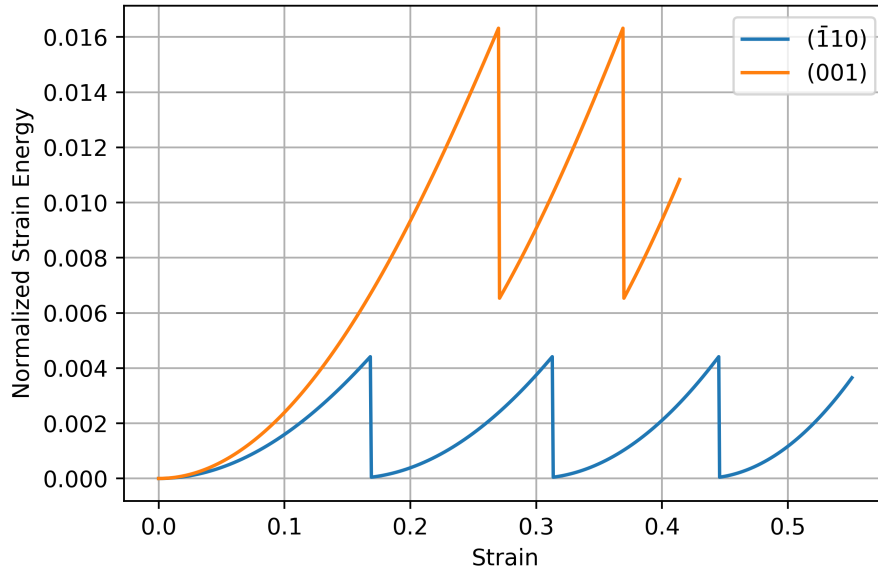


Figure 6.2: Normalized strain energy as a function of strain, resulting from the application of RBSM to shear MgO (001) and $(\bar{1}10)$ slip systems.

According to equation 2.13, it is necessary to evaluate the differential displacement (Δd_i). This was computed for both slip systems. Since the shear direction is aligned along x for the $(\bar{1}10)$ plane, only the d_{xi} (where d denotes the displacement vector of atom i , and x is the Cartesian component) increments greater than zero are considered, while for the (001) plane, the magnitude of the x and y components of d_i were evaluated because the shear direction is at 45° with respect to the [100] direction. For both cases, it was found that only inter-planar components are greater than zero.

Differential displacement as a function of strain increased linearly initially for both slip systems.

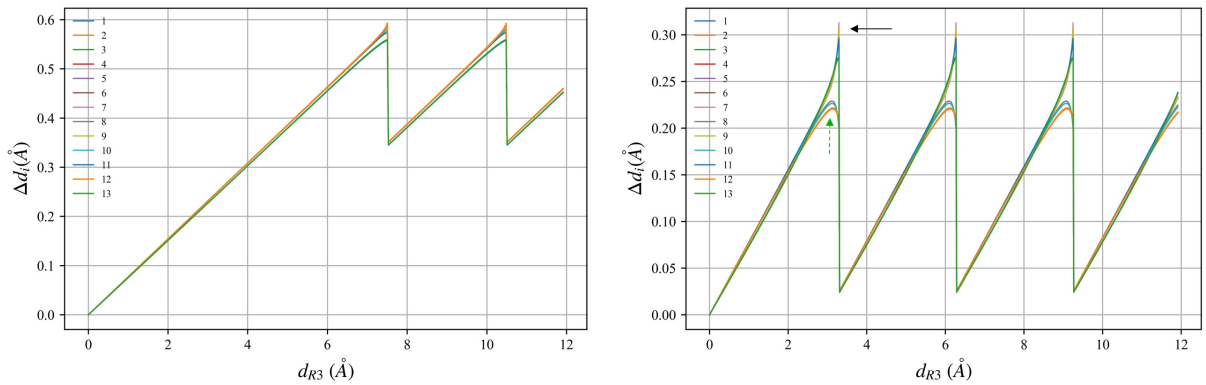


Figure 6.3: Differential displacement Δd_i plot as a function of the translation distance of region three d_{R3} for; (a) (001)[110], and (b) $(\bar{1}10)$ [110] slip systems. Green and black arrows in (b) indicate regimes of Δd_i divergence from linear trend.

For the (001)[110] slip system, there is a slight divergence in Δd_i in the frames before slip. This is very similar to Δd_i results reported for FCC Au where a higher increase in some Δd_i with respect

to the rest were labelled as strain softening, and the opposite effect as strain hardening. However, the $(\bar{1}10)[110]$ system shows a different Δd_i response to that observed in FCC Au. For some (Δd_i) in Figure 6.3 (b), as indicated by the solid black arrow, strain softening is very similar to FCC Au. In contrast, some Δd_i , indicated by the green dashed arrow, show evident inflection points followed by a decrease in Δd_i before slip happens. Upon examining which Δd_i show hardening and softening, we found that every alternate interface shows hardening, while the rest show softening (i.e. $\Delta d_1, \Delta d_3, \Delta d_5$, etc. show hardening and other Δd_i where i is even show softening).

Referring to Figure 6.1 (b), we observe that a $(\bar{1}10)$ cell is composed of alternating layers in the z direction where there is mirror-image symmetry and a translation along the xz plane, i.e. the Mg and O positions are exchanged. The presence of rigid blocks might also strongly affect the system response. Hence, we anticipate TBSM will assist in uncovering MgO's response in both slip systems.

The ideal shear strengths of MgO in the $(001)[110]$ and $(\bar{1}10)[110]$ slip systems was calculated to be 32 and 15 GPa, respectively.

6.4 Application of TBSM to MgO Slip Systems

Four TBSM simulations to shear the $(001)[110]$ and $(\bar{1}10)[110]$ slip systems in MgO were undertaken; for each slip system, two simulations were performed with and without the dipole correction term to the Ewald sum. For the $(001)[110]$ slip system, the result was the same whether or not

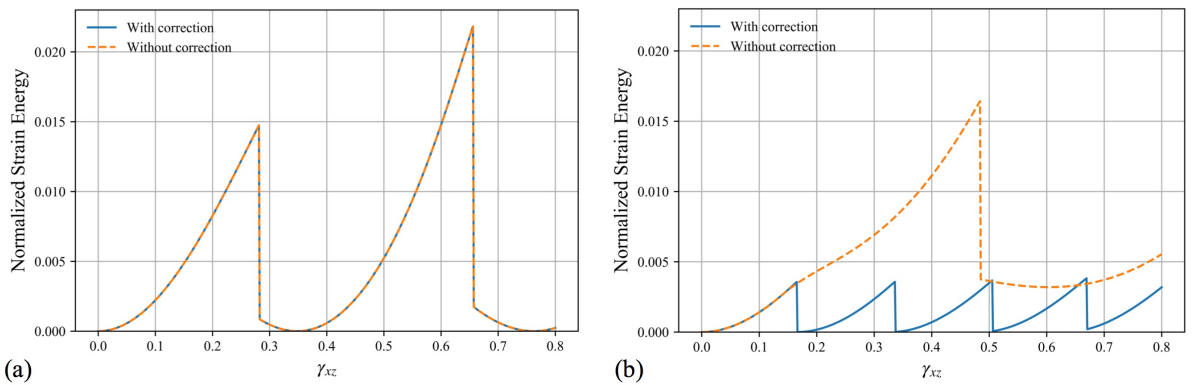


Figure 6.4: Normalized strain energy as a function of strain resulting from the application of TBSM to MgO in the (a) $(001)[110]$ and (b) $(\bar{1}10)[110]$ slip systems. Two curves are shown corresponding to with and without the correction to simulate a system surrounded by vacuum or using tinfoil boundary conditions, respectively.

the dipole correction was applied, as shown in Figure 6.4 (a). The U_{1N} barrier is equal to 0.0147, similar to the RBSM U_{1N} result (0.0163). In contrast, the response of the $(\bar{1}10)[110]$ slip system

strongly depends on whether or not the dipole correction is used, as shown in Figure 6.4 (b), with the blue curve (with correction) showing a regular slip profile while the dashed-orange curve (without dipole correction) shows an inflection point on the curve where a delayed structural change happens at about $0.49 \gamma_{xz}$. We measured the dipole moment in both simulations and found that no dipole is excited for the case with correction, i.e. the system slips, while we found that for the case without correction, a dipole moment develops very close to the frame of slip of the simulation with the correction, and starts growing until the structural change occurs. This raises the question as to whether this polarization changes as a function of system size. To examine this, an additional TBSM shear simulation for a twenty layer system was performed with the same strain step. The macroscopic polarization was calculated by;

$$P_{\alpha} = \frac{\sum_{i=1}^N \mu_{\alpha,i}}{V} \quad (6.4)$$

where α specifies a Cartesian component, $\mu_{\alpha,i}$ is the dipole moment of atom i along the α Cartesian direction, and V is the volume of the supercell. For the twelve layer simulation at the frame before the structural change, the induced macroscopic polarization P_x equals P_z (-0.67262 C/m^2) with P_y equal to zero. Note that the xz plane coincides with the shear plane (i.e. γ_{xz}). The same quantities were evaluated for the twenty layer simulation and found the same result, except the signs of P_x and P_z are reversed, i.e. $+0.67262 \text{ C/m}^2$ - the sign reversal is due to alternate layer deformation, i.e. the twelve layer deformation interfaces 1, 3, etc. correspond to the black arrow in Figure 6.3 and vice versa for the twenty layer simulation. The twenty layer simulation shows that the magnitude of the macroscopic polarization before the structural change is independent of the size of the system, which implies this calculated P_{α} must be material-specific rather than an arbitrary outcome.

There are several features of the TBSM results for shearing the $(\bar{1}10)[110]$ of MgO in Figure 6.4 (b) that require further examination. Firstly, the energy for the simulation without dipole correction is greater than that with dipole correction. From equation 6.3, the opposite is expected since an additional positive term in the electrostatic energy (equation 6.2). To interpret this finding, we highlight that the dipole correction term (equation 6.3) has a quadratic term in the displacement (the square of the sum of the dipole moments). Thus, there must exist first and second order energy derivatives of equation 6.3 with respect to coordinates, which further contributes to the calculations of the Hessian and RFO slip state, e.g. when RFO encounters one or more negative eigenvalues and keeps pushing the system until all the eigenvalues are positive. In other words, the RFO $(\bar{1}10)[110]$ slip calculation while considering the dipole correction involves a dipole moment excited along a direction that coincides with the slip direction, hence, leading the system to slip into a new state that

has no excited dipole. In contrast, the RFO slip calculation of the same system in the absence of the dipole correction term does not have the capability to push the system along that particular direction, since the induced macroscopic polarization contribution is absent from the Hessian, leading to the development of an excited dipole that ends with a structural change and vanishing of the dipole.

We mentioned that near $0.49 \gamma_{xz}$, a structural change happens in MgO for the case without the dipole correction, as shown by the sudden drop of energy in Figure 6.4 (b) and subsequent shallow energy profile. To examine the structural change, we performed re-optimizations of all TBSM frames by removing the constraint and found that before the sudden drop of energy, the system optimizes to that of the rock-salt structure. Yet, for the frames beyond the sudden drop of energy, the system optimizes to the hexagonal MgO (h-MgO) structure with a relative energy of +12.35 kJ/mol with respect to the rock-salt structure. The calculated E_{rs-h} is higher than that predicted in reference¹⁰ (7.72 kJ/mol, obtained via GGA DFT with PW91 functional) and lower than that predicted in reference¹¹ (36.66 kJ/mol/f.u., obtained via LDA DFT). The reported different values of E_{rs-h} by different groups may be rationalized based on the work of Peng *et al.*,¹² who found, using random phase approximation adiabatic connection fluctuation-dissipation theorem (RPA-ACFDT) calculations, that standard DFT (GGA with PBE+U and HSE06 functionals) only qualitatively finds the relative stabilities of non-transition metal compounds such as MgO. Regarding lattice parameters of h-MgO, our calculated a_h and c_h are equal to 3.470 and 4.193 Å, respectively, in good agreement with those reported in reference¹⁰ (3.552 and 4.236 Å, respectively) and reference¹³ (3.486 and 4.199 Å, respectively, obtained via PBE-GGA dispersion correction DFT).

Recently, shear-induced phase transformation has attracted the attention of several groups. In related research, McCulloch *et al.*¹⁴ have successfully transformed glassy carbon (made of randomly stacked and oriented graphene layers) into nanocarbon lonsdaleite and diamond phases (12% and 3%, respectively). Their experiments involved compressing carbon precursors at a pressure of about 80 GPa in a diamond anvil cell at room temperature. Lonsdaleite and diamond phases formed inside the shear bands, convincing the authors that such a phase transformation is shear-induced. Hexagonal boron nitride (hBN) was successfully transformed into a wurtzite structure at room temperature via the application of shear deformation starting from highly disorder nanocrystalline¹⁵ and high purity crystallite¹⁶ precursors. The results in references¹⁴⁻¹⁶ are encouraging since they provide preliminary experimental methods to obtain high energy phases at room temperature. However, the authors were unable to provide information about which crystallographic slip system

activates prior to the phase transformation, and whether it involves a single or multiple slip systems. Our TBSM simulations with MgO provide a possible solid-solid phase transformation route from the rock-salt structure to h-MgO. The only concern is regarding the excited dipole and the incompatibility of tinfoil boundary condition with macroscopic polarization, since surface effects are ignored in our calculations. Therefore, our results show that how polarization is treated couples with shear deformation leading to either slip or phase transition.

The calculated TBSM ideal shear strengths of MgO for the $(\bar{1}10)[110]$ and $(001)[110]$ slip systems are 12 and 28 GPa, respectively. These values are comparable to those obtained via RBSM (15 and 32 GPa, respectively).

6.5 Summary

RBSM and TBSM were applied to study the deformation of MgO and rank its slip systems. Both methods yielded a consistent ranking of slip systems compared to experiment, as well as a consistent ideal shear stress estimation.

The differential displacement analysis, within the RBSM framework, revealed that the $(\bar{1}10)[110]$ system responds differently to shear deformation compared to $(001)[110]$. The unique strain hardening and softening in the $(\bar{1}10)[110]$ slip system indicated that this system promises additional deformation features not seen with FCC metals.

TBSM simulations of MgO slip coupled with two different ways of handling macroscopic polarization also displayed the RBSM differential displacement signature of the $(\bar{1}10)[110]$ slip system. In the absence of the dipole correction term (i.e. tinfoil boundary conditions), a dipole moment is induced in the system and leads to a structural change from rock-salt MgO to h-MgO. Conversely, if the vacuum-surrounded Ewald sum is applied, the system slips in a similar manner as seen in FCC Au. Our results show that shear deformation combined with different polarization treatment leads either to slip deformation or phase transition for the $(\bar{1}10)[110]$ but not the $(001)[110]$. Finally, this phase transformation emerged in TBSM, but not RBSM, because of the boundary conditions in each method; RBSM can never has apply tinfoil boundary conditions in the z direction, while TBSM can.

Although RBSM and TBSM can not simulate full dislocation nucleation and dislocation cores, they provide a consistent ranking of the slip systems with experiment. This is a remarkable for ionic crystals since our methods provide the ranking of the slip systems without recourse to dislocation

theory metrics such as Burger's vector or interplanar spacing distance.

Bibliography

- ¹ J. Amodeo, S. Merkel, C. Tromas, P. Carrez, S. Korte-Kerzel, P. Cordier, and J. Chevalier, “Dislocations and plastic deformation in mgo crystals: A review,” *Crystals (Basel)*, vol. 8, no. 6, pp. 240–53, 2018.
- ² A. A. Urusovskaya, “Electric effects associated with plastic deformation of ionic crystals,” *Soviet Physics Uspekhi*, vol. 11, pp. 631–643, may 1969.
- ³ J. D. Gale and A. L. Rohl, “The general utility lattice program (gulp),” *Molecular Simulation*, vol. 29, no. 5, pp. 291–341, 2003.
- ⁴ P. P. Ewald, “Die berechnung optischer und elektrostatischer gitterpotentiale,” *Annalen der Physik*, vol. 369, no. 3, pp. 253–287, 1921.
- ⁵ N. J. K. Withey, “Computer simulations of dipolar fluids using ewald summations,” 2012.
- ⁶ C. J. Fennell and J. D. Gezelter, “Is the ewald summation still necessary? pairwise alternatives to the accepted standard for long-range electrostatics,” *The Journal of Chemical Physics*, vol. 124, no. 23, p. 234104, 2006.
- ⁷ N. A. Spaldin, “A beginner’s guide to the modern theory of polarization,” *Journal of Solid State Chemistry*, vol. 195, pp. 2–10, 2012. Polar Inorganic Materials: Design Strategies and Functional Properties.
- ⁸ S. Fleming and A. Rohl, “Gdis: A visualization program for molecular and periodic systems,” *Zeitschrift Fur Kristallographie - Z KRISTALLOGR*, vol. 220, pp. 580–584, 01 2005.
- ⁹ T.-C. Lin, C.-C. Yen, S.-Y. Lin, Y.-C. Huang, C.-H. Tung, Y.-T. Hsiao, and S.-Y. Chang, “Small-size-induced plasticity and dislocation activities on non-charge-balanced slip system of ionic mgo pillars,” *Nano Letters*, vol. 18, pp. 4993–5000, 08 2018.

- ¹⁰ M. A. Zwijnenburg and S. T. Bromley, “Structural richness of ionic binary materials: An exploration of the energy landscape of magnesium oxide,” *Phys. Rev. B*, vol. 83, p. 024104, Jan 2011.
- ¹¹ S. Limpijumnong and W. R. L. Lambrecht, “Theoretical study of the relative stability of wurtzite and rocksalt phases in mgo and gan,” *Phys. Rev. B*, vol. 63, p. 104103, Feb 2001.
- ¹² H. Peng and S. Lany, “Polymorphic energy ordering of mgo, zno, gan, and mno within the random phase approximation,” *Phys. Rev. B*, vol. 87, p. 174113, May 2013.
- ¹³ A.-A. Sun, S.-P. Gao, and G. Gu, “Peculiar bond characters of fivefold coordinated octet compound crystals,” *Chem. Sci.*, vol. 11, pp. 4340–4350, 2020.
- ¹⁴ D. G. McCulloch, S. Wong, T. B. Shiell, B. Haberl, B. A. Cook, X. Huang, R. Boehler, D. R. McKenzie, and J. E. Bradby, “Investigation of room temperature formation of the ultra-hard nanocarbons diamond and lonsdaleite,” *Small*, vol. 16, no. 50, p. 2004695, 2020.
- ¹⁵ C. Ji, V. I. Levitas, H. Zhu, J. Chaudhuri, A. Marathe, and Y. Ma, “Shear-induced phase transition of nanocrystalline hexagonal boron nitride to wurtzitic structure at room temperature and lower pressure,” *Proceedings of the National Academy of Sciences*, 2012.
- ¹⁶ V. I. Levitas, Y. Ma, J. Hashemi, M. Holtz, and N. Guven, “Strain-induced disorder, phase transformations, and transformation-induced plasticity in hexagonal boron nitride under compression and shear in a rotational diamond anvil cell: In situ x-ray diffraction study and modeling,” *The Journal of Chemical Physics*, vol. 125, no. 4, p. 044507, 2006.

Every reasonable effort has been made to acknowledge the owners of copyright material. I would be pleased to hear from any copyright owner who has been omitted or incorrectly acknowledged.

Chapter 7

Deformation of Simple Molecular Solids: the Case of Diatomic Oxygen

7.1 Introduction

Oxygen in solid, liquid, or gas phase, is the only elemental magnet in nature¹ and enjoys a very rich phase diagram with nine distinct solid phases.¹ Of the nine, the α and β phases are dominant at low temperatures and pressures, with the α phase characterized by long range magnetic order and the β phase by short range magnetic order.¹ We are interested in applying our methods to study the deformation of oxygen because a crystal consisting of diatomic molecules is the simplest possible molecular crystal. The second motivation is because the (111) planes in FCC metals and β -oxygen are very similar with the same hexagonal packing resulting in similar crystallographic features for slip and twinning deformation along $\{111\}\langle 011\rangle$ and $\{111\}\langle 112\rangle$, respectively (see Chapter Three). To the best of our knowledge there are no publications on the active slip systems in O_2 . However, Venables *et al.*² studied defects in van der Waals solids and reported some stacking fault energies of β - O_2 , along with some experimental evidence of annealing-induced twinning in the higher index planes. Consequently, we explored the same slip systems as in FCC metals, as well as other slip systems including the higher index planes.

The first section of this chapter briefly describes the methodology, in terms of the crystal structure, force field, configurations, slip systems, and crystallographic versus shorthand notations. The second section briefly describes convergence analysis as a function of system and step sizes. The third section studies some (111) deformation results and includes a summary of the normalized

strain energy barriers of O₂ deformation obtained by RBSM and TBSM. Finally, a twinning mechanism discovered in this work for oxygen that is absent in metals is introduced.

7.2 Methodology

7.2.1 Force Field and Crystal Structure

In 1979, Kobashi *et al.*³ reviewed several force fields to simulate the lattice dynamics of the α and β phases of oxygen.⁴⁻⁶ According to the librational frequency results at the γ point in Table 2 reference,³ the force field model developed by Cheung⁴ best approximates the experimental librational frequencies, and thus we used this force field in simulating the deformation of β oxygen with all the technical details as reported in Chapter Two.

β -O₂ adopts a rhombohedral structure with lattice parameter of 4.074 Å and cell angle of 48.3°, as depicted in Figure 7.1 (a). The vectors connecting oxygen molecules are parallel to the [111]. This leads to the hexagonal (111) supercell representation shown in Figure 7.1 (b). The different colors of the molecules indicate the stacking sequence (ABC stacking), and the supercell vectors are indicated such that $[10\bar{1}]$ and $[01\bar{1}]$ are slip directions, and $[11\bar{2}]$ the twinning direction.

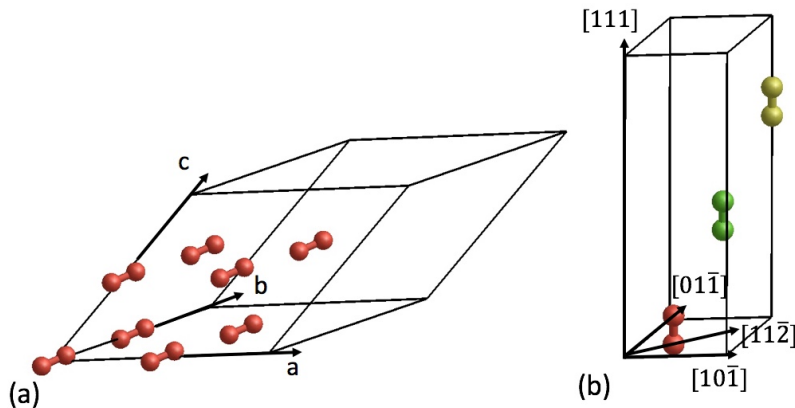


Figure 7.1: Images showing different supercells of oxygen; (a) shows a rhombohedral supercell (lattice vectors are shown with arrows). (b) shows a hexagonal (111) supercell of oxygen with the main lattice directions indicated.

7.2.2 Slip Systems and Geometry

In order to simulate higher index planes in O₂, it is necessary to generate supercells containing these planes. The General Purpose Trajectory Analyser (GPTA) program, developed by A/Prof.

Paolo Raiteri⁷ was used. GPTA takes the energy minimized unit cell from GULP and produces an output file with a list of supercells along a user-specified plane. These supercell structures are fed into GDIS⁸ and produce supercells for TBSM calculations. For RBSM surface cells, GDIS⁸ was used to produce all configurations.

In order to apply RBSM and TBSM, the relevant crystallographic directions needs to be determined. For the (111) supercells, this task is relatively straightforward since both the $\langle 011 \rangle$ and $\langle 112 \rangle$ directions can be determined by visualizing the structure. Figure 7.2 shows an example of a

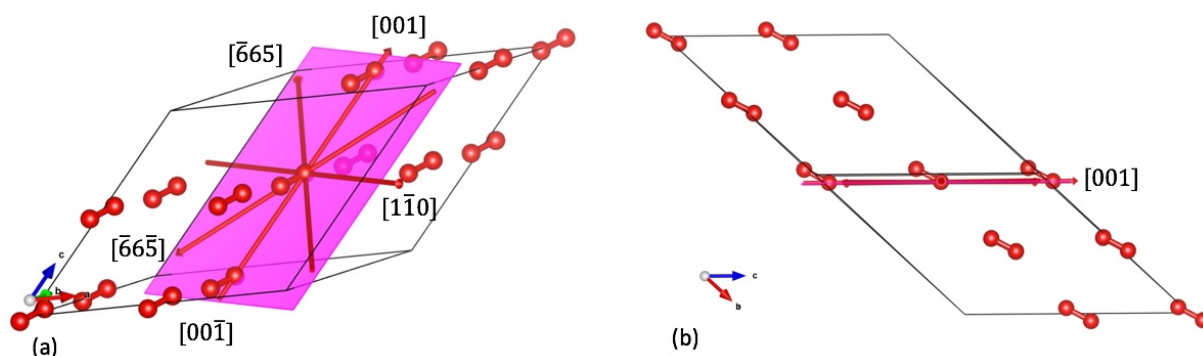


Figure 7.2: Images of the (110) plane (in pink) for a rhombohedral cell of oxygen and the important crystallographic directions (indicated by red arrows) in two different views.

(110) plane (in pink) with the important crystallographic directions for our shear simulations also displayed.

Because of the experimental observation of annealing-induced twins in the higher index planes of β -oxygen,² RBSM and TBSM will be used to shear a few higher index planes requiring the development of a tool to find higher index crystallographic directions with respect to an oxygen rhombohedral unit cell. The Weiss Zone law⁹ (valid for all types of unit cells) is used which states that if a crystallographic direction $[uvw]$ lies in plane (hkl) , then the following equation must hold:

$$hu + kv + lw = 0 \quad (7.1)$$

The starting point following the generation of the required higher index plane supercell is to find a reference direction; this direction is chosen to be anti-parallel to the projection of the molecular vector (the vector connecting two oxygen atoms to form a molecule, with the reference oxygen atom lying in the plane) along the plane, e.g. this is the $[001]$ direction in Figure 7.2 (a). Next, all the $[uvw]$ directions in that plane are found and their angles calculated with respect to the ref-

reference directions. The number of possible directions is limited by setting limits on the high index directions, i.e. u , v , and w , can vary from -15 to 15. Then, the required directions are chosen by their angle. For a surface cell, all the directions in terms of u and v components of surface vectors a and b are found, and then the angles are compared to the angles from the previous procedure to find the exact crystallographic direction with respect to the reference unit cell.

Deformation in the following higher index planes: (112), (113), (114), (115), and (116), as shown Figure 7.3 (a), was investigated. For each slip plane, five different shear systems were

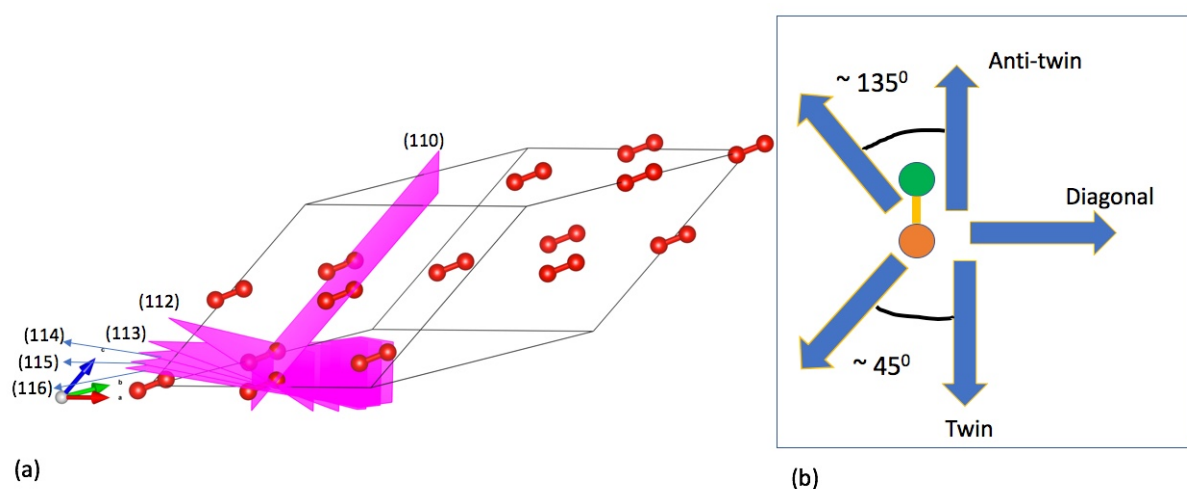


Figure 7.3: Schematics showing the: (a) higher index planes and the (110) in rhombohedral oxygen, and (b) the notation of the directions to be used throughout this chapter. The green atom always lies in the higher index crystallographic plane while the orange one does not.

tested. These directions are denoted as shown in Figure 7.3 (b) with the twin direction as our reference.

The table below summarizes all the slip systems studied (except the (111) plane) and their corresponding notations. Table 7.1 also shows the angle ϕ , which is the angle between the projection of the molecular vector on the plane and the molecular vector (see Figure 7.4), and it is highest for the (112) plane and decreases gradually as the (116) plane is approached.

Compared to atomic solids, such as metals, O_2 molecules can rotate as the crystal is deformed. To quantify these rotations, two angles are defined; the azimuth θ and the inclination δ , according to Figure 7.5. Because of the procedure used to generate surfaces and supercells, the molecular vectors always lie in (or are parallel to) the yz plane. The azimuth angle θ is 90° in all reference configurations, and is calculated between the projection of the molecular vector onto the y axis and

Plane	(110)	(112)	(113)	(114)	(115)	(116)
Twin	[001]	$[\bar{1}\bar{1}1]$	$[\bar{3}\bar{3}2]$	$[\bar{2}\bar{2}1]$	$[\bar{5}\bar{5}2]$	$[\bar{3}\bar{3}1]$
Anti-Twin	$[00\bar{1}]$	$[11\bar{1}]$	$[33\bar{2}]$	$[22\bar{1}]$	$[55\bar{2}]$	$[33\bar{1}]$
Diagonal	$[1\bar{1}0]$	$[1\bar{1}0]$	$[1\bar{1}0]$	$[1\bar{1}0]$	$[1\bar{1}0]$	$[1\bar{1}0]$
135°	$[\bar{6}\bar{6}5]$	$[13\bar{3}5]$	$[8\bar{2}2]$	$[6\bar{2}1]$	$[7\bar{2}1]$	$[\bar{3}9\bar{1}]$
45°	$[\bar{6}\bar{6}5]$	$[3\bar{1}3\bar{5}]$	$[2\bar{8}2]$	$[2\bar{6}1]$	$[2\bar{7}1]$	$[\bar{9}3\bar{1}]$
ϕ	28.18°	47°	33.82°	28.18°	25.12°	23.21°

Table 7.1: List of all the slip systems studied in this chapter and their corresponding notation. Angle ϕ is the angle between the projection of the molecular vector on the slip plane, and the molecular vector; see Figure 7.4 for more details.

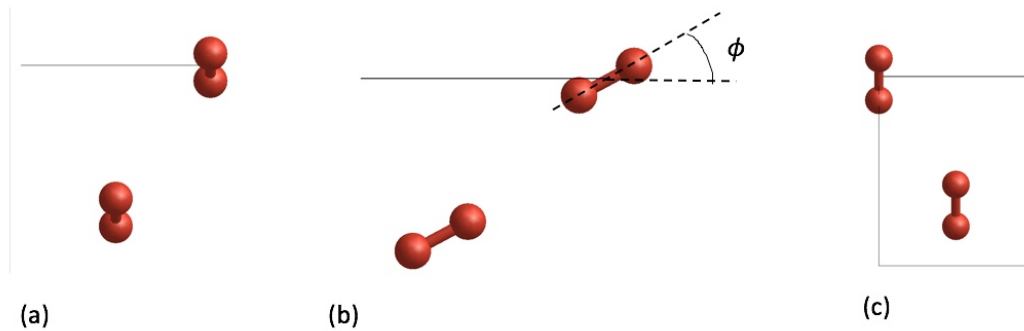


Figure 7.4: The (a) view 1, (b) view 2, (c) and the top view of an oxygen surface cell generated in the (110). Angle ϕ is indicated in (b) and this layout is common for all higher index planes such that angle ϕ is always defined.

the x axis as a function of deformation, while the inclination angle δ is different in the reference configuration of different planes, and is calculated between the molecular vector and the z axis.

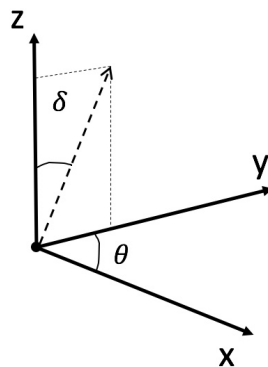


Figure 7.5: The angles θ and δ and the molecular vector (dashed arrow). The Cartesian axes correspond to a surface/supercell in any of the sheared crystallographic planes. It is possible to define such a construction because in the (111), the molecular vector is aligned along the z axis and so δ is zero and θ is 90°. For all the other sheared slip planes, the molecular vector always lies in or is parallel to the yz plane implying that θ is 90° and δ is different from one crystallographic plane to another.

7.3 Convergence Analysis

7.3.1 RBSM Convergence

System and step size analysis were conducted for several slip systems in O_2 . Figure 7.6 reports the normalized strain energy barriers as a function of the number of layers in region one for four different slip systems, where the strain per step was equal to or less than 0.0008. The results in-

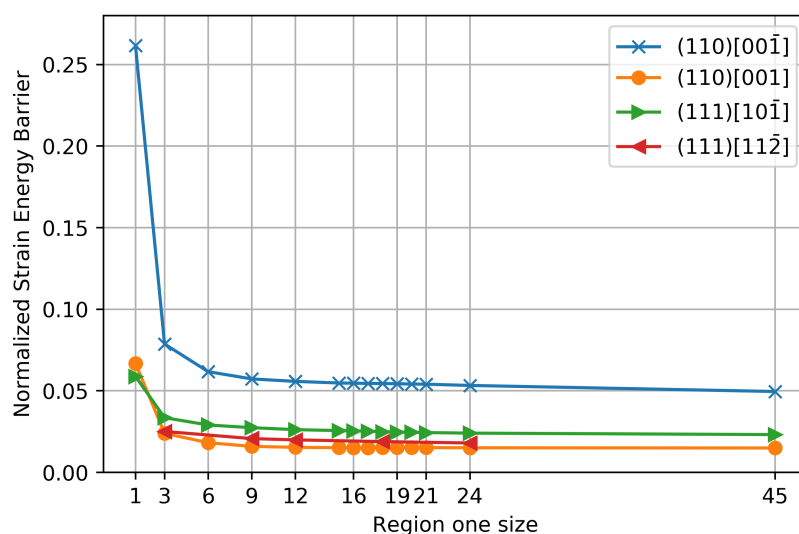


Figure 7.6: Normalized strain energy barrier as a function of the system region one size for several systems, obtained via RBSM for shear of O_2 . Lines are guides to the eye only.

dicates that the normalized strain energy barriers converge at a system size equal to or greater than twelve layers for the four slip systems. Next, step size analysis was conducted on the twelve layer configuration along the four slip systems, as reported in Figure 7.7. The results indicate that a strain per step equal to or less than 0.0008 converges the normalized strain energy barriers.

7.3.2 TBSM Convergence

Convergence analysis was conducted for the same systems of O_2 , and for the system size analysis at a strain per step equal 0.0008. Figure 7.8 shows that the normalized strain energy converges for system sizes equal to or greater than twelve layers for the (110)[001], and is converged for the others irrespective of the system size. Figure 7.9 shows that the normalized strain energy converges with a strain step size less than 0.005.

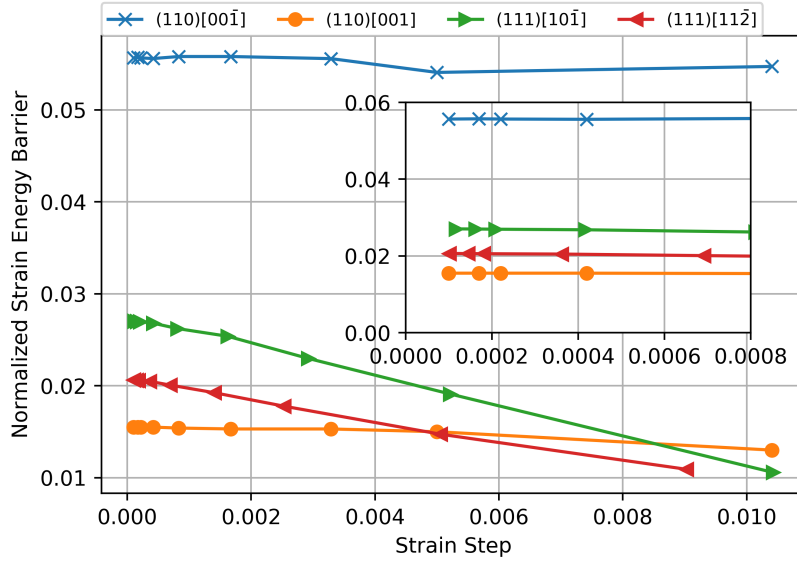


Figure 7.7: Normalized strain energy barrier as a function of the strain step size for the twelve layer configuration sheared along four slip systems, obtained via RBSM. The inset plot is a magnification of the main plot where the x limits are now confined to the range of convergence indicated in the main text. Lines are guides to the eye only.

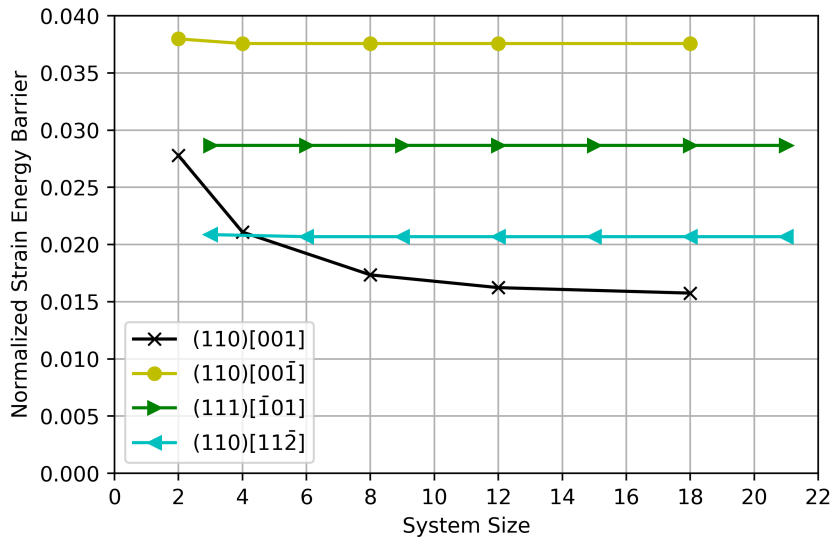


Figure 7.8: Normalized strain energy as a function of the system size, obtained via TBSM shear. Lines are guides to the eye only.

7.4 Deformation Results

7.4.1 Slip in (111)

RBSM was used to shear the (111)[101̄] and the (111)[112̄] slip systems. Figure 7.10 reports their normalized strain energy as a function of strain. The results are similar to those obtained in FCC Au. Slip events (blue curve) are periodic and have the same barrier for successive events. Twinning

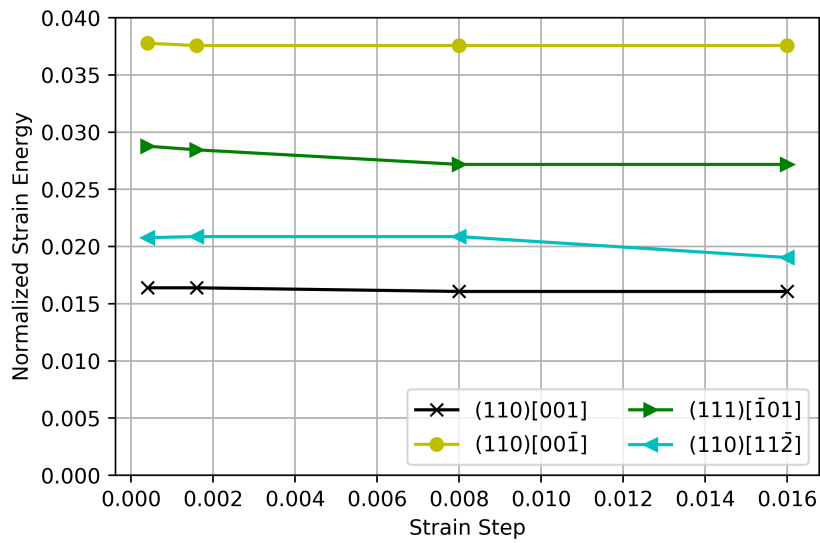


Figure 7.9: Normalized strain energy as a function of the strain step size for several system systems, obtained via TBSM shear. Lines are guides to the eye only.

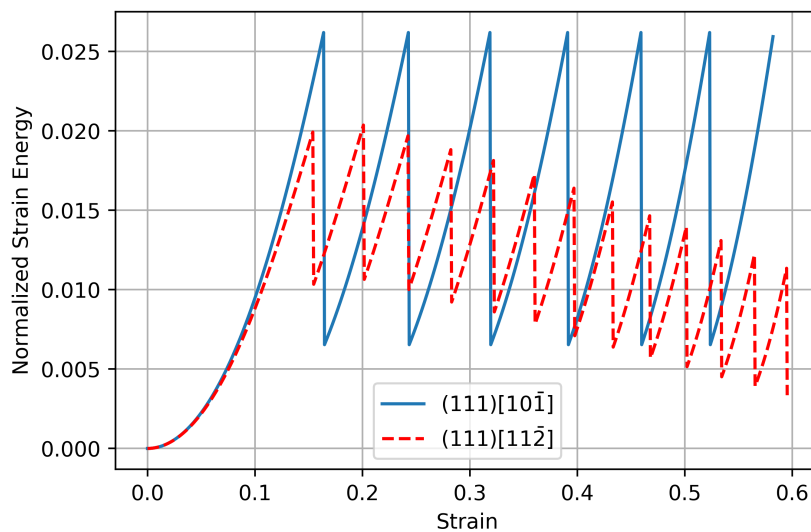


Figure 7.10: Normalized strain energy as a function of the strain for the twelve layer system sheared via RBSM along $(111)[10\bar{1}]$ and $(111)[11\bar{2}]$.

(red curve) starts with the nucleation of a stacking fault. Interestingly, the second twinning barrier is higher than the first. This is because stacking faults can interact over a longer range than in FCC metals.¹⁰ The barrier for twinning deformation is lower than that of slip, as was the case with FCC metals.

Analysis of the molecular orientation as a function of strain indicates that shearing in this direction causes rotation of the molecules. Figure 7.11 shows that shear in the $(111)[11\bar{2}]$ causes a

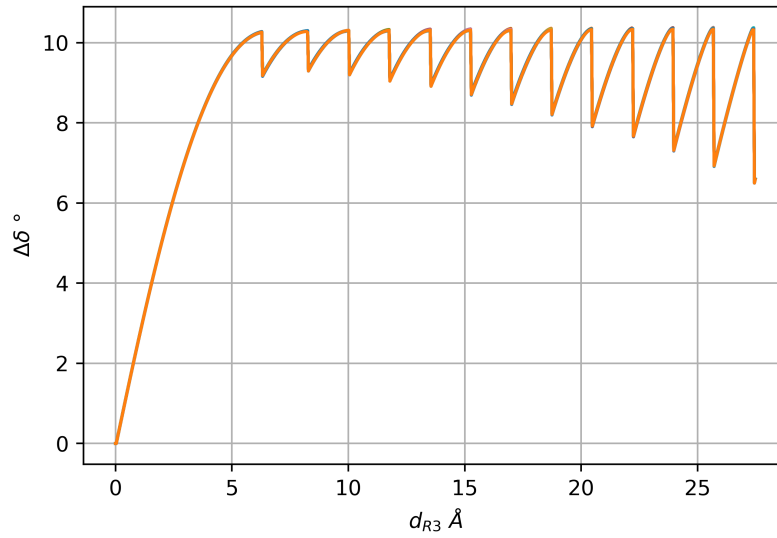


Figure 7.11: Change in inclination angle δ as a function of the translation distance of region three d_{R3} , for the twelve layer simulation sheared along the $(111)[11\bar{2}]$. Curves for all the molecules are displayed, showing that they are all superimposed.

change in the inclination angle δ , which increases up to about 10.2° before the first twinning event happens. This twinning causes a slight relief in the angular strain and so delta drops to about 9.2° . The discontinuities in the slope of the curve of δ occur at the same d_{R3} as that of the normalized strain energy in Figure 7.10. Angular distortion happens uniformly in (111) as the trends of the twelve molecules are almost superimposed on top of each other in Figure 7.11. Zero change for the azimuth angle was found.

In contrast to the above, Figure 7.12 shows that shear in $(111)[10\bar{1}]$ is accompanied by rotation of the molecules via the change of both δ and θ . Similar to the twinning case, the curves of the angles are consistent with the normalized strain energy profile in Figure 7.10. The molecule tilts side-ways (i.e. change in θ) because there is a twinning direction to one side of the molecule, i.e. the partial dislocation deformation path.

TBSM was then used to shear in the same directions as reported above for RBSM. Figure 7.13 reports the normalized strain energy versus strain result. For shearing in $(111)[10\bar{1}]$, the system emits partial dislocations following the first peak. However, as the system is sheared further, it changes its cell representation and now shear acts in a completely different slip system. Shearing the $(111)[11\bar{2}]$ system emits stacking faults following the first and second twinning events, but during the third event changes its cell representation and shear now acts in a different slip system.

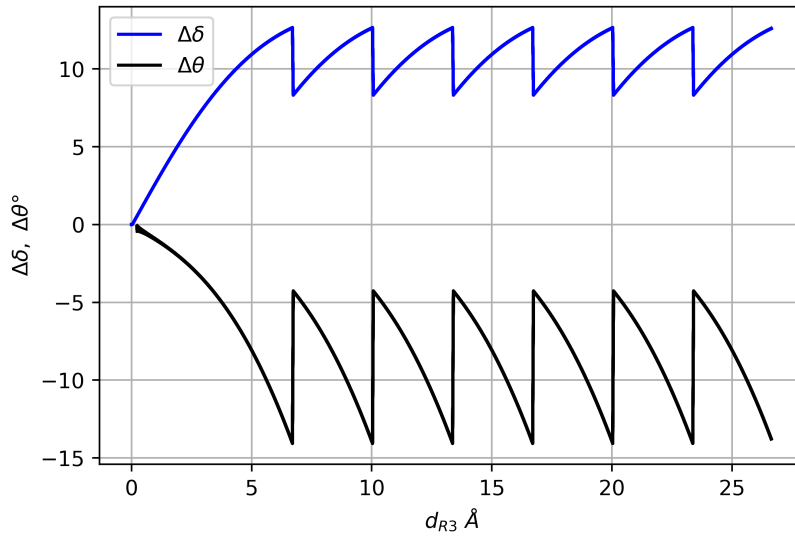


Figure 7.12: Change in inclination δ and azimuth θ as a function of the translation distance of region three d_{R3} , for the twelve layer simulation sheared along $(111)[10\bar{1}]$. The curves correspond to the angular deformation of all the molecules in the configuration which are superimposed on each other.

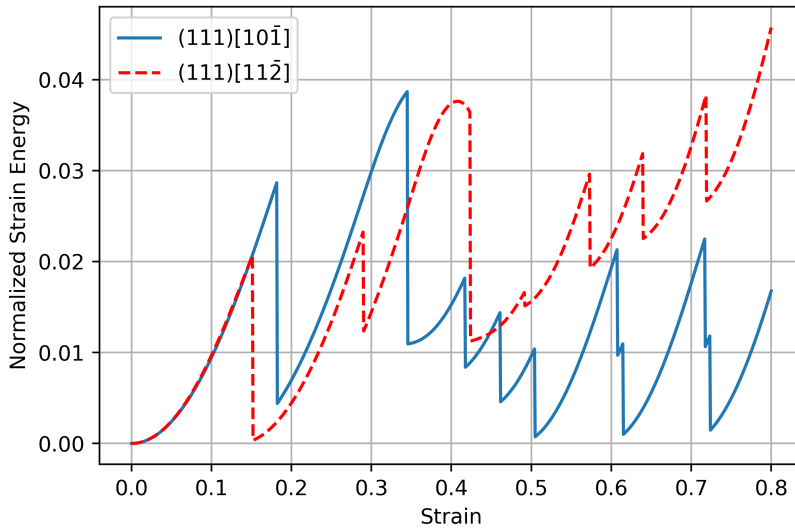


Figure 7.13: Normalized strain energy as a function of the strain for the twelve layer system sheared via TBSM along $(111)[10\bar{1}]$ and $(111)[11\bar{2}]$.

These TBSM results show that the method of homogeneous shear leads to a more complicated material response where the supercell is able to change its representation due to the relaxation of the other components of strain (deformation of lattice vectors).

The rotation of molecules for the frames before the change in cell representation were inspected and indeed TBSM gives similar results to RBSM. For the twinning direction, there is no change

in θ while the change in δ is positive and reaches a maximum value of 10.7° . For the slip system, both angles change in the same fashion as RBSM with δ and θ reaching about 17.2° and -16.4° , respectively.

Below, the normalized strain energy barriers are converted to barriers per interface with units mJ/m^2 so they can be compared to the barriers obtained from the GSFE method in Chapter Three. The results show that the barriers obtained via GSFE are overestimates of the barriers calculated

Method	USE	USF
GSFE	18.4	6.58
RBSM	3.90	2.97
TBSM	4.63	3.34

Table 7.2: List of the USE and USF barriers (along $(111)[10\bar{1}]$ and $(111)[11\bar{2}]$, respectively) obtained via the GSFE method (Chapter two), RBSM and TBSM. All values are in mJ/m^2 .

by RBSM and TBSM, which agrees with our earlier results for FCC metals.

7.4.2 Slip in Higher Index Planes

A series of RBSM and TBSM shear simulations of oxygen along the higher index planes were performed and the normalized strain energy barriers are summarized in Figure 7.14. Systems and simulation parameters were chosen to fall within the convergence limit of the (111) and (110) system analysis, and assuming convergence limits hold for the higher index planes, RBSM sheared configurations have 18 layers in region one at ~ 0.0004 strain per step while TBSM sheared configurations have 20 layers at 0.0008 strain per step.

Several insights can be drawn based on the RBSM results in Figure 7.14 (a). First, the “Twin” system is the easiest for all the deformed slip systems. This is followed by the “ 45° ” slip system, then the “Anti-Twin” slip system, the “Diagonal” slip system, and finally the “ 135° ” slip system. The only exception to this ranking is the (113) slip system where the ranking is switched between the “Diagonal” and the “Anti-Twin” slip system. The other observation is that the barriers appear to converge as the index of the crystallographic plane increases.

For the TBSM results in Figure 7.14 (b), the “Twin” and the “ 45° ” slip system barriers are the

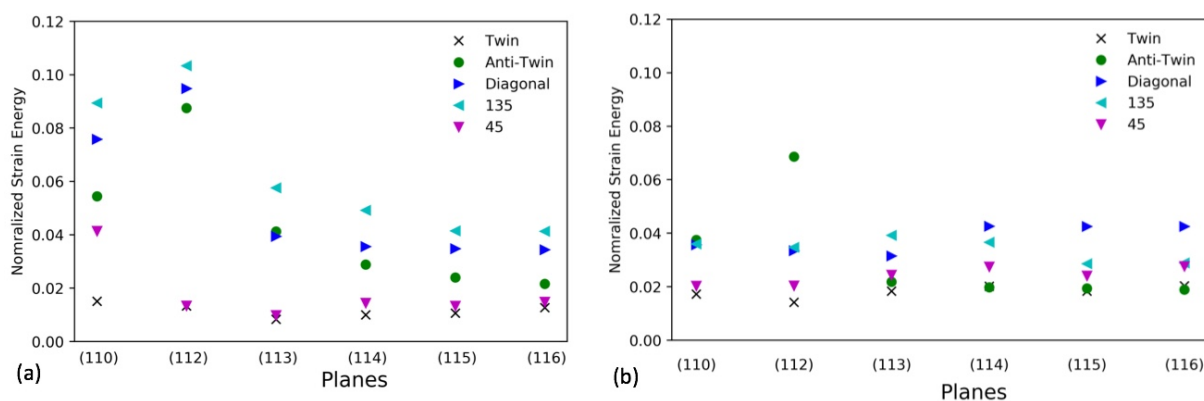


Figure 7.14: Normalized strain energy barriers for several slip systems obtained using (a) RBSM, and (b) TBSM.

lowest for the (110), (112), (113), and (115) slip systems. This result is consistent with the RBSM. The ranking of the other slip systems is different and not fixed for the same slip plane. The “Anti-Twin” slip system changes its rank from the most difficult in the (112) plane to the easiest in the (116) plane. TBSM predicts the easiest slip system lies in the (112) plane, while RBSM predicts the same in (113). Overall, there are some differences between RBSM and TBSM results, but considering the angle between the (113) and (112) planes is just 13° , both methods predict very similar ranking of the slip systems.

7.4.3 Twinning Deformation in the (110) Plane: Rotational Twinning

Molecular crystals have particular modes of deformation twinning, absent from other materials that have a single atom/ion per lattice site. Chapter One provided one example of the work of Takamizawa and Takasaki.¹¹ Twinning deformation has also been computationally studied in calcite by tensile molecular dynamics simulations of a conventional orthorhombic cell along the (001) while observing the formation and growth of {104} twin boundaries.¹² In this context, twinning deformation corresponded to the rotation of carbonate, and hence we name it rotational twinning. We note that the twins form in a higher index plane in calcite, which shows reflection twinning does not necessarily need to occur in low index planes (e.g. the {111} in FCC metals).

RBSM and TBSM simulations have uncovered rotational twinning in oxygen. In both methods, twinning occurred in (110)[001]. Figure 7.15 shows the twinning results for twelve layer configurations. These results are similar to the ones obtained for FCC metals. The normalized strain energy increases until a first twinning event happens, which correspond, in this case, to the

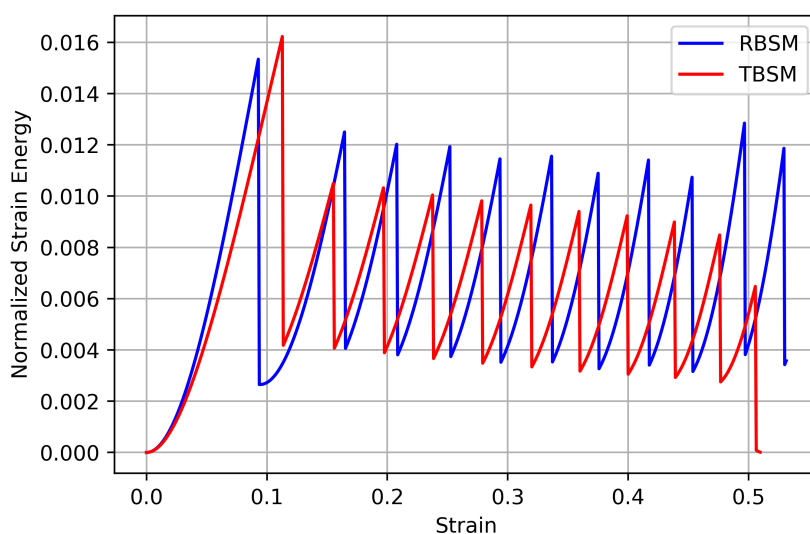


Figure 7.15: Normalized strain energy as a function of strain for shearing the (110)[001] system using RBSM and TBSM.

simultaneous rotation of two molecules, as depicted in Figure 7.16. Subsequent twinning events

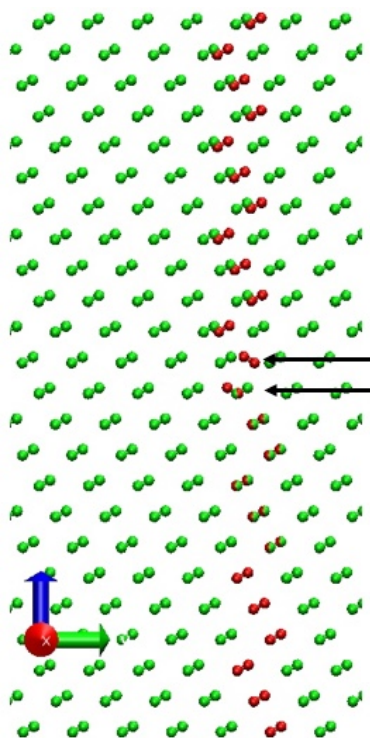


Figure 7.16: An example showing a (110)[001] twin obtained via RBSM. Reference lattice molecules are colored in green with multiple images in the xy plane, while sheared lattice molecules are colored in red. Twinning by rotation happens for two red molecules across the planes indicated by the arrows.

in Figure 7.15 correspond to the growth of the twinned region until all region one molecules are twinned in RBSM, or all the molecules are twinned in TBSM and thus the energy goes to zero as a result. In RBSM, the last two twinning events have barriers remarkably higher than the previous

barriers, which occurs because twinning occurs at the boundary molecules between region one and regions two and three.

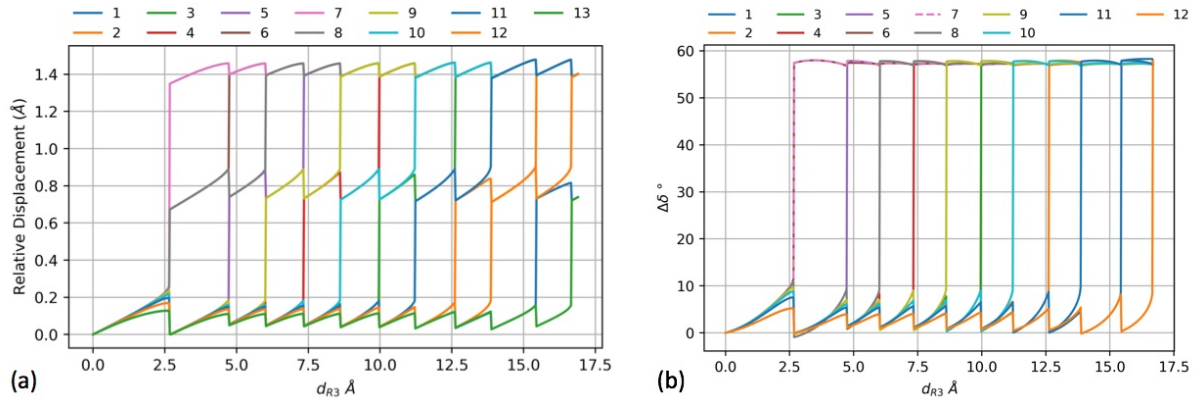


Figure 7.17: RBSM twinning deformation details in the (110)[001] plane analyzed via (a) differential displacement, and (b) change in inclination angle, as a function of the translation distance of region three d_{R3} . The indices in the legend of (a) correspond to interfaces i in Δd_i where i equals 1 for the interface between region three and the center of mass of molecule one, index 2 for the interface between the centers of mass of molecules 1 and 2, etc. The indices in the legend of (b) correspond to molecule identities where index 1 is the first molecule at the boundary with region three and index 12 is the molecule at the boundary with region two.

Rotational twinning has been analyzed in detail for the RBSM twelve layer configuration. Figure 7.17 shows the differential displacement Δd_i and the change in inclination angle δ as a function of the translation distance of region three. Figure 7.17 (b) shows that the first twinning event corresponds to a change in the inclination of molecules six and seven by about 58° , suggesting a multiplicity of slip model, which is reflected in the Δd_i plot in (a) through the jump in Δd_6 and Δd_8 by about 0.68 \AA and Δd_7 by about 1.37 \AA . The change in δ of one molecule will be reflected by the change of two Δd_i s because a single molecule contributes to two interfaces (above and below). In this case, the two adjacent molecules (6 and 7) rotated and thus three Δd_i s changed with Δd_7 receiving twice the other two since it is in the middle. The second twinning event corresponds to the rotation of molecule 5, which is evident in the differential displacement plot by the increase in Δd_5 and Δd_6 .

We have studied twinning deformation in FCC Au and in the (111) of O_2 and were able to link the differential displacement to the magnitude of the Burger's twinning vector. When rotational twinning occurs in the (110)[001] of O_2 , the relation to crystallography becomes dependent on the

lattice vector and the symmetry operation. The lattice vectors below represent a (110) unit cell:

$$\vec{a} = 3.3332 \hat{j} \text{ (\AA)} \quad (7.2a)$$

$$\vec{b} = -4.0735 \hat{i} \text{ (\AA)} \quad (7.2b)$$

$$\vec{c} = 1.3461 \hat{i} + 5.0884 \hat{k} \text{ (\AA)} \quad (7.2c)$$

Rotational twinning involves the x component of the lattice vector c in equation 7.2, i.e. c_x . Since the rotation and displacement of a single molecule contributes to two interfaces (i.e. above and below the molecule), it implies that a single such event contributes only half of the twinning differential displacement value. Rotation of a single molecule can be considered as a defect. Rotation of two adjacent molecules produces a structure having the minimum size of a rotational twin. Thus two adjacent molecules rotating would produce a differential displacement equal to the c_x at the interface between them, and to half c_x at the other two interfaces. This becomes rather evident when observing the differential displacements following the last twinning event in Figure 7.17 (a); the differential displacement of all interfaces except 1 and 13 equals 1.4 \AA , which almost equals c_x . For the excepted interfaces, their differential displacement equals 0.72 \AA , almost half c_x , because the atoms in the rigid blocks are unable to rotate.

Energy re-optimization calculations of all the RBSM frames of the rotational twinning simulation were performed and the calculated the twinning interfacial energy is 3.64 mJ/m^2 , which is much larger than the calculated ISF of O_2 (0.0068 mJ/m^2).

The TBSM differential displacement, angular distortion, and re-optimization calculations were similar to the results of RBSM.

We have shown that RBSM and TBSM are not only able to simulate deformation twinning in the (111) of FCC Au and O_2 , but also rotational twinning in molecular oxygen. The combined differential displacement and change in δ analysis provides in-depth detail of the physical process. We have also shown that twinning of this type is related to the crystallographic component of the unit cell which appears in the differential displacement, not the Burger's vector, though the twinning energetics look very similar to that in (111).

7.5 Summary

RBSM and TBSM have been used to study the deformation of solid O₂. The ranking of the (111) slip systems in O₂ was found to be the same as for FCC metals. The deformation of an O₂ crystal involves molecular rotations, quantified in terms of inclination and azimuth angles, with their variation consistent with the trends for the normalized strain energy, indicating that angular rotations contribute to both the strain before slip and strain relief after slip. Shear deformation in (110)[001] was found to occur via a rotational twinning mechanism for both RBSM and TBSM. Its molecular rotations, interfacial energy, and differential displacement were calculated with a clear link to the crystallographic lattice vector c_x in the (110) instead of the Burger's vector. These collective findings for molecular oxygen constitute some of the major complex deformation features absent from atomic solids, such as FCC metals, due to the coupling of rotations with shear deformation.

Shearing the higher index planes in oxygen provided a map in terms of the barriers. Both methods, RBSM and TBSM, showed that it is the easiest to deform the "Twin" direction even in the (110) plane, which is a low index plane. The next easiest slip system is the "45°". Beyond these slip systems, RBSM and TBSM give different rankings, presumably because of the different constraints enforced by each method.

The shear deformation results of O₂ compelled us to explore the shear deformation of a more complicated molecular crystal and thus we choose to apply RBSM and TBSM to anthracene, a planar organic molecular crystals, in Chapter Eight.

Bibliography

- ¹ Y. Freiman, H. Jodl, and Y. Crespo, “Solid oxygen revisited,” *Physics Reports*, vol. 743, pp. 1–55, 2018. Solid oxygen revisited.
- ² J. Venables, C. English, K. Niebel, and G. Tatlock, “Stacking faults, twins, and the structural stability of van der Waals solids,” *Journal de Physique Colloques*, vol. 35, no. C7, pp. C7–113–C7–119, 1974.
- ³ K. Kobashi, M. L. Klein, and V. Chandrasekharan, “Lattice dynamics in solid oxygen,” *The Journal of Chemical Physics*, vol. 71, no. 2, pp. 843–849, 1979.
- ⁴ J. Powles and K. Gubbins, “The intermolecular potential for nitrogen,” *Chemical Physics Letters*, vol. 38, no. 3, pp. 405–406, 1976.
- ⁵ J. C. Laufer and G. E. Leroi, “Calculation of the zero wave vector lattice frequencies of alpha- and beta-oxygen,” *The Journal of Chemical Physics*, vol. 55, no. 3, pp. 993–1003, 1971.
- ⁶ G. Jelinek, L. Slutsky, and A. Karo, “Model for the lattice vibrations of a crystal of diatomic molecules—i. frequency distributions, debye-waller factors, and infrared spectra,” *Journal of Physics and Chemistry of Solids*, vol. 33, no. 6, pp. 1279–1290, 1972.
- ⁷ P. Raiteri, “General purpose trajectory analyzer,” <https://github.com/praiteri/GPTA>, 2021.
- ⁸ S. Fleming and A. Rohl, “Gdis: A visualization program for molecular and periodic systems,” *Zeitschrift Fur Kristallographie - Z KRISTALLOGR*, vol. 220, pp. 580–584, 01 2005.
- ⁹ A. Kelly and K. M. Knowles, “Lattice geometry,” in *Crystallography and Crystal Defects*, ch. 1, pp. 1–41, John Wiley & Sons, Ltd, 2012.
- ¹⁰ B.-J. Lee, J.-H. Shim, and M. I. Baskes, “Semiempirical atomic potentials for the fcc metals cu, ag, au, ni, pd, pt, al, and pb based on first and second nearest-neighbor modified embedded atom method,” *Phys. Rev. B*, vol. 68, p. 144112, Oct 2003.

- ¹¹ S. Takamizawa and Y. Takasaki, “Superelastic shape recovery of mechanically twinned 3,5-difluorobenzoic acid crystals,” *Angewandte Chemie International Edition*, vol. 54, no. 16, pp. 4815–4817, 2015.
- ¹² A. S. Côté, R. Darkins, and D. M. Duffy, “Deformation twinning and the role of amino acids and magnesium in calcite hardness from molecular simulation,” *Phys. Chem. Chem. Phys.*, vol. 17, pp. 20178–20184, 2015.

Every reasonable effort has been made to acknowledge the owners of copyright material. I would be pleased to hear from any copyright owner who has been omitted or incorrectly acknowledged.

Chapter 8

Slip Barriers in Anthracene

8.1 Introduction

Anthracene ($C_{14}H_{10}$), is an aromatic hydrocarbon and is considered an archetypical molecular crystal since its properties are amongst the best known for such a material.¹ Anthracene has three polymorphs,^{2,3} and possesses photoplastic effects.⁴ The slip barriers in anthracene were studied here because it is a flat molecule with no conformational degrees of freedom, and thus should in principle exhibit less complicated slip behavior than molecular systems containing one or more torsion angles. Furthermore, anthracene (space group P21/a) is experimentally known to have two active slip systems: (001)[110] and (001)[010].⁵

This chapter discusses the computational determination of the slip barriers in anthracene using RBSM and TBSM. The first section introduces the crystal structure and the methodology. The second section summarizes the convergence analysis results. The third section discusses the slip barriers obtained from deforming anthracene along eight slip systems.

8.2 Methodology

At ambient conditions, anthracene crystallizes in a monoclinic unit cell (space group P21/a) with two molecules per unit cell.⁶ We have used the General Amber Force Field (GAFF)⁷ to model the interactions in anthracene. The maximum cut-off in GAFF force field is set to 10 Å. To find the partial charges of the carbon and hydrogen atoms in anthracene, A/Prof. Paolo Raiteri used

Gaussian⁸ employing the HF/6-311G(1d,1p) method to find the ESP derived charges and provided the output file (private communication). The charges for anthracene are summarized in Figure 8.1. Table 8.1 shows that the calculated lattice parameters following optimization with the present force field are in good agreement with those reported from experiment⁶ being within 1 %.

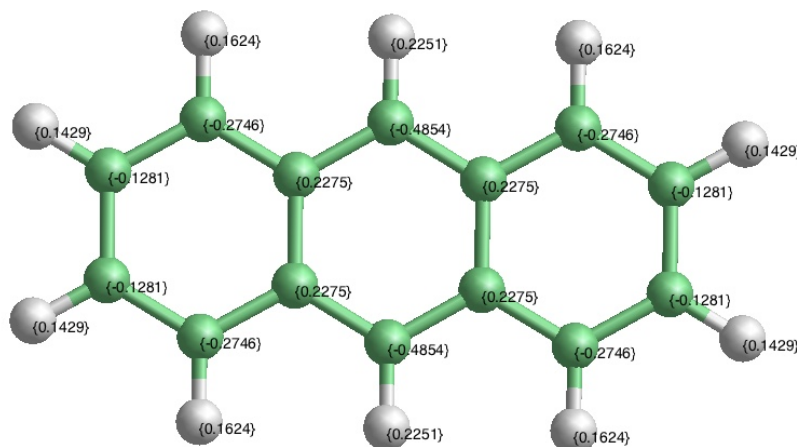


Figure 8.1: View of a single anthracene molecule with all the partial charges (a.u.) indicated for carbon (green) and hydrogen (white) atoms.

Lattice Parameters	a (Å)	b (Å)	c (Å)	α°	β°	γ°
GAFF	8.257	5.929	10.914	90.00	124.48	90.00
Exp. ⁶	8.561	6.036	11.163	90.00	124.42	90.00

Table 8.1: Comparison of the lattice parameters calculated using the General Amber Force Field (GAFF) and from experiment.

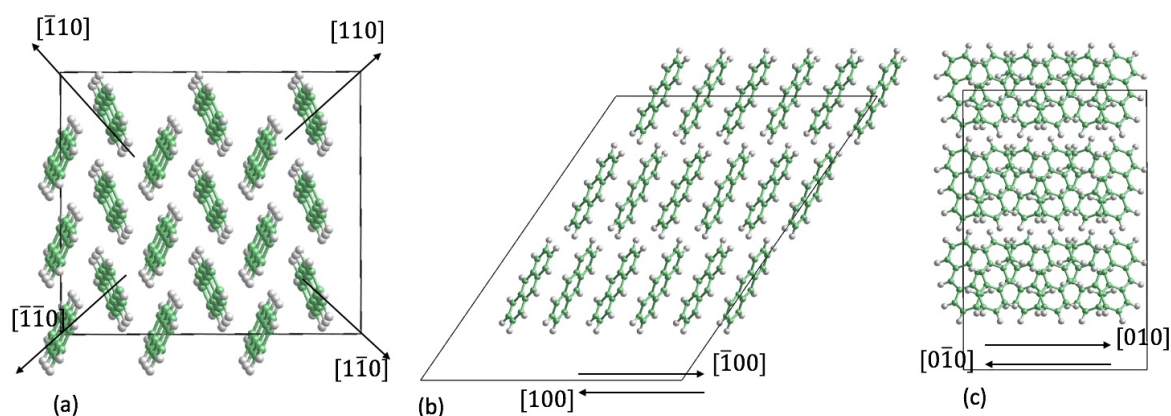


Figure 8.2: Several views of an anthracene monoclinic supercell: (a) ab , (b) ac , and (c) bc plane views. Crystallographic directions are indicated by arrows.

Figure 8.2 shows several views of an anthracene monoclinic supercell illustrating the $[110]$ and the $[\bar{1}\bar{1}0]$ directions are symmetric, as are the $[\bar{1}\bar{1}0]$ and $[\bar{1}10]$ directions. However, the $[110]$ and

$[\bar{1}\bar{1}0]$ directions are not symmetric because the cell is monoclinic with lattice vector c at 124.24° to lattice vector a . Figure 8.2 (b) shows that the $[100]$ and $[\bar{1}00]$ directions are asymmetric, in contrast to the $[010]$ and $[0\bar{1}0]$ as evident in Figure 8.2 (c).

Configurations for RBSM and TBSM simulations were prepared as per the previous procedure in Chapter Two. The size of the rigid blocks for RBSM was two layers (with a height of about 17.62 \AA), where two molecules are present per layer.

8.3 Convergence Analysis

RBSM convergence analysis on anthracene was conducted by testing the $(001)[100]$ slip system. The system size analysis varied the size of region one from one to sixteen layers at 0.0004 strain per step, and the results are reported in Figure 8.3 (a). The normalized strain energy converges for

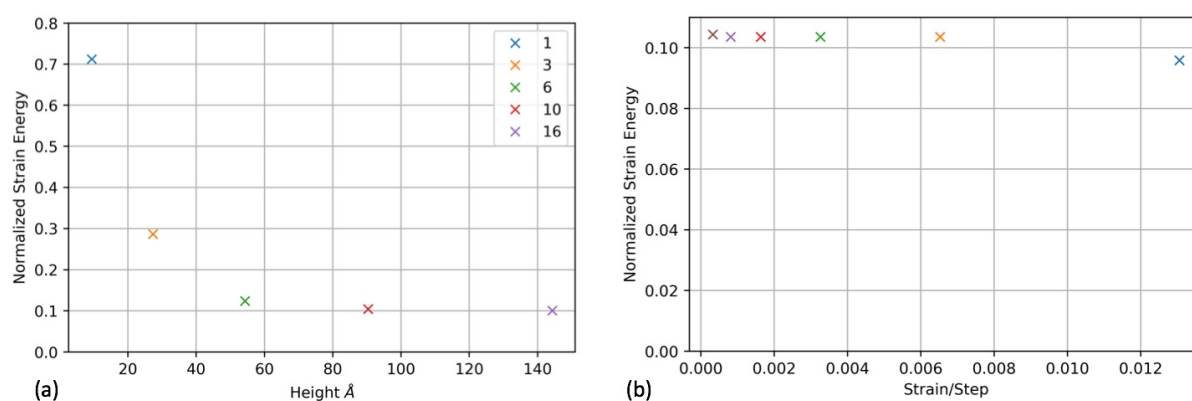


Figure 8.3: RBSM convergence analysis applied to the $(001)[100]$ in anthracene; (a) the normalized strain energy as a function of the height (size) of the system where the numbers in the legend correspond to the layer numbers in region one, and (b) the same quantity as a function of the step size for the ten layer configuration.

system sizes equal to or greater than ten. Hence the step size analysis was performed on the ten layer configuration by varying the strain per step as per Figure 8.3 (b). Convergence of the barriers is achieved at a strain per step less than 0.0065 .

A similar convergence analysis using TBSM was conducted by shearing the same $(001)[100]$ system. System size was varied from two to ten layers at 0.0004 strain per step. The normalized strain energy was converged even for the two layer simulation. Then, the six layer configuration was used to perform step size analysis by varying the strain. The results indicated that the normal-

ized strain energy is converged for strain steps lower than 0.0033.

8.4 Slip Barriers

RBSM and TBSM were used to shear the following slip systems in anthracene: $(001)[010]$, $(001)[0\bar{1}0]$, $(001)[100]$, $(001)[\bar{1}00]$, $(001)[110]$, $(001)[\bar{1}\bar{1}0]$, $(001)[\bar{1}10]$, and $(001)[1\bar{1}0]$. System sizes equal ten layers and ~ 0.0004 strain per step were used with the results summarized in Figure 8.4.

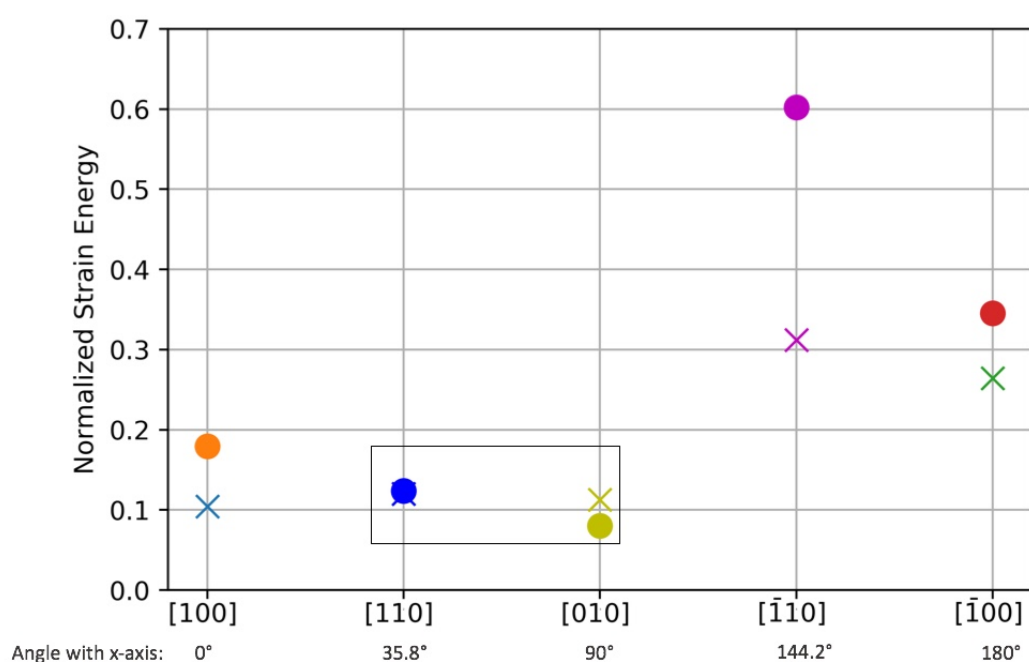


Figure 8.4: Normalized strain energy barriers obtained from RBSM (crosses) and TBSM (solid circles) for the slip systems indicated on the x axis. The box indicates slip systems that are observed experimentally. The angle of the directions with respect to the x axis are indicated at the bottom of the figure.

The barriers to slip shown in Figure 8.4 appear to fall into two groups; the first group are the set of barriers that are less than 0.2 normalized strain energy and predicted to be the easy slip directions, and the second group has barriers that are higher, and represent slip systems that are more difficult to activate. The ranking of the first group of barriers obtained from each method is different, but the normalized strain energies are all very close from both methods, with the exception of TBSM for the $(001)[100]$ slip system. Both methods predict the same ranking of the higher barriers. The experimentally observed slip systems fall within the rectangle in Figure 8.4 and are the easiest slip systems, according to TBSM while RBSM predicts a slightly easier slip system, the $(001)[100]$.

Using the angles in Figure 8.4 and by taking into account the symmetry, we can sketch a 2D map of the slip barriers in anthracene in (001), as per Figure 8.5. The arrows are plotted along

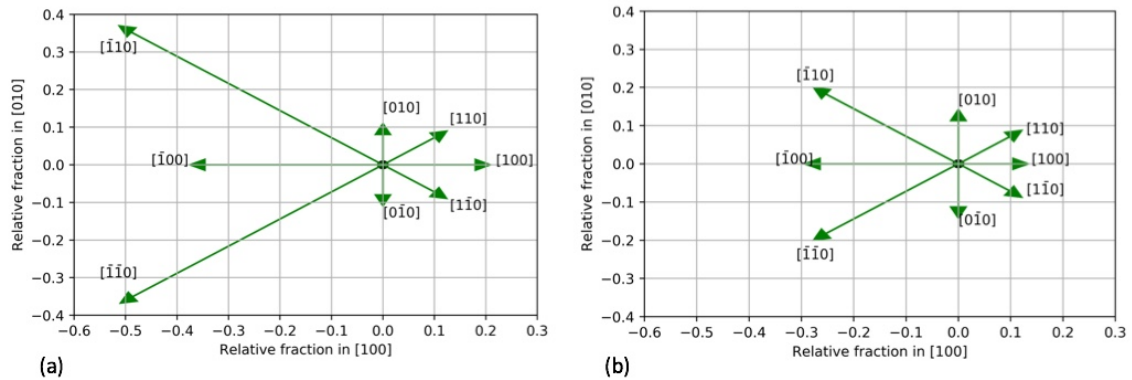


Figure 8.5: 2D barrier map showing the region of easy and difficult slip for anthracene deformation in (001) where the arrow length represents the magnitude of the barrier, for the results obtained from (a) TBSM and (b) RBSM. The crystallographic directions were constructed according to their angles reported in Figure 8.4.

the relevant crystallographic directions with their actual angles taken into account. The length of the arrow represents the barrier. TBSM and RBSM results in Figures 8.5 (a) and (b), respectively, indicate that it is relatively easy to shear in [100], [110], [010], [010̄], [110̄] and thus all the bounded directions (i.e. [120], [210̄], etc.) compared to the [110], [100], [110̄] and the bounded directions (i.e. [210], [210]).

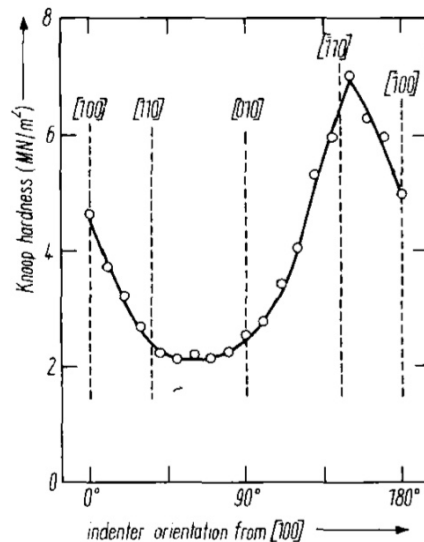


Figure 8.6: Knoop hardness results found for different orientations with respect to (001)[100] in anthracene. Reproduced from reference⁹ with permission from Wiley and Sons.

Our results for the barriers and the 2D barrier map are consistent with those reported by Sasaki and Iwata⁹ for hardness measurements, as reported in Figure 8.6. Sasaki and Iwata used Knoop's

hardness test to measure the hardness of anthracene along different crystallographic orientations in the (001) plane. As the authors cautioned,⁹ this is a hardness measurement, not a slip line analysis, and thus it is expected several deformation mechanisms may activate in the indented region. It is interesting to note that the hardness of [100] is higher than that for [110] and [010]. This supports the TBSM result in Figure 8.4 rather than that of RBSM.

Robinson and Scott^{10,11} performed extensive analysis of the tensile, compressive, and shear deformation of anthracene along several orientations and used slip line analysis to deduce the active slip systems. Their results indicated that basal slip occurred in anthracene along (001)[110] and (001)[010] for a wide variety of deformation orientations, though, we could not find comments or indications of (001)[100] system slip. Thus, there is currently insufficient experimental evidence to support the low RBSM [100] barrier. However, some indirect evidence can be inferred from the another work by Robinson and Scott¹² where the authors deformed an anthracene crystal by bending around the [100] direction. They observed tilt boundaries, which are dark fringes appearing on the specimen that can be easily recognized as compared to slip lines (see Figures 6, 7, and 8 in reference¹²) and slip lines indicating the presence of dislocations with Burger's vector components in the [010] and [100] directions, hypothesizing that the most probable dislocation offering both components is the one with Burger's vector $1/2\langle 110 \rangle$. We note that this proposed partial dislocation is expected to emerge from the $\langle 110 \rangle$ dislocation, but we could not find experimental or numerical evidence providing deeper insight into its occurrence and structure. Hence, Robinson and Scott¹² proposed that tilt boundaries are composed of mobile dislocations having the $1/2\langle 110 \rangle$ and [010] components. Our RBSM results for the plastic deformation revealed that deformation mechanisms in the [110] and [100] systems were very similar, while even TBSM gave the same deformation mechanism for these systems (but one that is different from RBSM). This finding suggests that it may not be trivial to experimentally find the difference in the deformation mechanisms between [110] and [100] and thus the RBSM lower [100] barrier may be of relevance.

8.5 Summary

RBSM and TBSM were used to study the slip barriers in anthracene. The results show that there exist two groups of barriers: the first corresponds to easy slip and the second corresponds to more difficult slip. RBSM and TBSM predict the experimentally observed slip systems to fall within the

first group range, as well as having similar ranges for group one and group two barriers, although the ranking for each method slightly differs in group one, but not in group two barriers.

The proposed 2D barrier map for the (001) plane in anthracene is consistent with the hardness experimental results, with the exception of the RBSM [100] barrier. Our literature review of the deformation features in the (001)[100] showed that there is the possibility of the formation of tilt boundaries which have components of a Burger's vector in [100], with their origin proposed to be the partial dislocations $1/2\langle 110 \rangle$ in anthracene.¹² In addition, Robinson and Scott¹³ observed growth twinning in anthracene grown from solution or vapor, but not from melt. They deduced that the fault energy for the twin formation must be low, in agreement with their previous postulate that partial dislocations $1/2\langle 110 \rangle$ in the (001) occur in anthracene. With this set of observations, and given that RBSM and TBSM produce very similar deformation mechanisms in (001)[110] and (001)[100], there is a need for a more thorough elaboration on our computational results in terms of deformation mechanisms, in addition to more specialized experiments probing the deformation in the (001)[100] direction and its relation to tilt boundaries and twins, as well as the experimental and computational verification of the existence of $1/2\langle 110 \rangle$ partial dislocations in anthracene.

Bibliography

- ¹ B. Marciniak and V. Pavlyuk, “Crystal structure of a metastable anthracene modification, grown from the vapor phase,” *Molecular Crystals and Liquid Crystals*, vol. 373, no. 1, pp. 237–250, 2002.
- ² A. J. Cruz-Cabeza, N. Feeder, and R. J. Davey, “Open questions in organic crystal polymorphism,” *Communications Chemistry*, vol. 3, no. 1, p. 142, 2020.
- ³ D. P. Craig, J. F. Ogilvie, and P. A. Reynolds, “Calculated molecular orientational disorder in anthracene crystals,” *J. Chem. Soc., Faraday Trans. 2*, vol. 72, pp. 1603–1612, 1976.
- ⁴ K. Kojima, “Crystal growth and defect control in organic crystals,” *Progress in Crystal Growth and Characterization of Materials*, vol. 23, pp. 369 – 420, 1992.
- ⁵ K. Kojima, “Slip systems in deformed anthracene crystals,” *physica status solidi (a)*, vol. 51, no. 1, pp. 71–78, 1979.
- ⁶ R. Mason, “The crystallography of anthracene at 95 °k and 290 °k,” *Acta Crystallographica*, vol. 17, no. 5, pp. 547–555, 1964.
- ⁷ J. Wang, R. M. Wolf, J. W. Caldwell, P. A. Kollman, and D. A. Case, “Development and testing of a general amber force field,” *Journal of Computational Chemistry*, vol. 25, no. 9, pp. 1157–1174, 2004.
- ⁸ M. J. Frisch, G. W. Trucks, H. B. Schlegel, G. E. Scuseria, M. A. Robb, J. R. Cheeseman, G. Scalmani, V. Barone, G. A. Petersson, H. Nakatsuji, X. Li, M. Caricato, A. V. Marenich, J. Bloino, B. G. Janesko, R. Gomperts, B. Mennucci, H. P. Hratchian, J. V. Ortiz, A. F. Izmaylov, J. L. Sonnenberg, Williams, F. Ding, F. Lipparini, F. Egidi, J. Goings, B. Peng, A. Petrone, T. Henderson, D. Ranasinghe, V. G. Zakrzewski, J. Gao, N. Rega, G. Zheng, W. Liang, M. Hada, M. Ehara, K. Toyota, R. Fukuda, J. Hasegawa, M. Ishida, T. Nakajima, Y. Honda, O. Kitao, H. Nakai,

T. Vreven, K. Throssell, J. A. Montgomery Jr., J. E. Peralta, F. Ogliaro, M. J. Bearpark, J. J. Heyd, E. N. Brothers, K. N. Kudin, V. N. Staroverov, T. A. Keith, R. Kobayashi, J. Normand, K. Raghavachari, A. P. Rendell, J. C. Burant, S. S. Iyengar, J. Tomasi, M. Cossi, J. M. Millam, M. Klene, C. Adamo, R. Cammi, J. W. Ochterski, R. L. Martin, K. Morokuma, O. Farkas, J. B. Foresman, and D. J. Fox, "Gaussian 16 rev. c.01," 2016.

⁹ A. Sasaki and M. Iwata, "Anisotropy of microhardness in anthracene single crystals," *physica status solidi (a)*, vol. 85, no. 2, pp. K105–K107, 1984.

¹⁰ P. Robinson and H. Scott, "Plastic deformation of anthracene single crystals," *Acta Metallurgica*, vol. 15, no. 10, pp. 1581–1590, 1967.

¹¹ P. M. Robinson and H. G. Scott, "Basal and non-basal slip in anthracene single crystals," *Molecular Crystals and Liquid Crystals*, vol. 11, no. 1, pp. 13–23, 1970.

¹² P. M. Robinson and H. G. Scott, "Tilt boundaries in deformed anthracene single crystals," *physica status solidi (b)*, vol. 20, no. 2, pp. 461–471, 1967.

¹³ P. Robinson and H. Scott, "The morphology of anthracene crystals," *Journal of Crystal Growth*, vol. 1, no. 4, pp. 187–194, 1967.

Every reasonable effort has been made to acknowledge the owners of copyright material. I would be pleased to hear from any copyright owner who has been omitted or incorrectly acknowledged.

Chapter 9

Conclusions and Future Outlook

This thesis has introduced two new computational methods to study the deformation of ideal defect-free crystalline materials, the rigid block shearing method (RBSM) and the tensor based shearing method (TBSM). RBSM is a generalization of the well-known γ surface calculation method¹ and consists of a rigid block which is sheared with respect to another while having a region of fully relaxed atoms in between. TBSM is an advanced version of affine shear deformation methods^{2,3} where finite strain derivatives permit the energy minimization of a deformed configuration far from equilibrium with respect to a reference configuration. Both methods use the Rational Function Optimizer⁴ in energy minimization calculations, which ensures the deformed configuration is physically stable, and to the best of our knowledge, has not been used in deformation simulations before.

Before applying our methods to different classes of materials, we first needed to calculate the generalized stacking fault (GSFE)¹ and the generalized planar fault energy curves (GPFE)⁵ so that we can compare the calculated energy barriers from our new methods to those from GSFE and GPFE. This was addressed in Chapter Three where several GSFE and GPFE barriers for FCC metals and O₂ were calculated. We also performed GSFE calculations of the new twinning route⁶ and showed that its occurrence in ideal crystals is more difficult (i.e. has a higher barrier) than the classical twinning route.

Having calculated GSFE and GPFE barriers, in Chapter Four RBSM was applied to FCC Au in detail and to FCC Pb, Pd, Pt, Al, Cu, Ni, and Ag, in general, to study the deformation in the slip system (111)[$\bar{1}10$] and twinning system (111)[$\bar{2}11$]. RBSM provided a ranking of slip systems in FCC metals via the normalized strain energy barriers and the twinning deformation barrier was found

to be always lower than that for slip deformation. Our results for FCC Au showed that the RBSM surface energy barriers are much less than those calculated from GSFE and GPFE curves. This result is expected to affect the variety of dislocation-based models⁷⁻⁹ which are extensively based on GSFE energetic quantities, such as the unstable stacking fault energy.¹⁰ Using molecular dynamics perturbation analysis, we have shown that there are several deformation paths which are separated by very small barriers. Further examination of these barriers and the resulting meta-stable energy minima led us to propose a multiplicity of slip models, where we predict single, double, triple, etc. slip as a function of the size of the system, in addition to twinning/stacking fault(s) in the higher perturbation regime representative of shock-loading conditions in experiment. It would be of interest to apply the branch-following and bifurcation method¹¹ to shear deformation problems and compare against our results. We believe our multiplicity of slip models are pre-requisite for successful multi-scale continuum models that are able to describe the microstructure during plastic deformation, and add valuable insight regarding the quantized plastic deformation of FCC Au nanowires using atomic force microscopy.¹² RBSM also described deformation twinning in FCC Au and, for the first time, confirmed the possibility of the activation of the new twinning route proposed by Wang *et al.* in ideal defect-free crystals. RBSM also predicts several twinning deformation pathways. We proposed an atomistic definition of strain, based on the differential displacement of the atoms throughout the deformation path, which provided consistent strain measures with those calculated using OVITO.¹³ Our atomistic definition of strain permitted the calculation of the shear stress versus strain profile, including the ideal shear strength. RBSM is a powerful method able to simulate full dislocation slip, partial dislocation slip, twinning deformation, stacking fault emission, atomistic strain, and ideal shear strength of materials, within a single computational framework. However, RBSM is unable to simulate dislocation nucleation, dislocation cores, or plastic deformation resulting from the interactions of pre-existing defects.

Next, we applied TBSM to FCC Au and FCC Pb, Pd, Pt, Al, Cu, Ni, and Ag, along the slip system (111)[$\bar{1}10$] and twinning system (111)[$\bar{2}11$] in Chapter Five. By testing the influence of the energy minimizer on the simulation results, we showed that RFO is better suited to simulate deformation compared to standard Newton-Raphson. The RFO-simulated strain energy showed a sudden drop as a function of strain, as did the stress, which was absent from the original implementation of affine shear deformation methods,^{2,3} and is consistent with experimental results.¹⁴⁻¹⁶ TBSM provides consistent results with RBSM in terms of the barriers; the twinning deformation

barrier is always lower than slip deformation barrier. Twinning deformation mechanisms simulated in TBSM are very similar to those in RBSM, including the new twinning route of Wang *et al.* TBSM is the first affine shear deformation method to simulate twinning deformation. On the other hand, slip deformation in TBSM always favored partial dislocation slip, in contrast to slip deformation mechanisms in RBSM. We reasoned that this difference in the deformation mechanism along the slipping direction is due to the different boundary conditions employed by each method (simple shear against pure shear). The same conclusions derived from RBSM results are generally applicable to TBSM results, so are the limitations in terms of dislocation nucleation. We calculated the shear invariant¹³ of the strain in TBSM¹⁷ and compared it to that of Green-Lagrange finite strain finding that both are equal for the frame before slip, justifying the accuracy of our results in determining the slip barriers. In addition, we proposed a geometric tool that uses rotation tensors on the frame before slip to find the approximate easiest slip direction in the material in terms of the three Eulerian angles, though this tool is approximate due to the deformation of the lattice vectors.

Next, we applied RBSM and TBSM to find the slip barriers in MgO, as reported in Chapter Six. Our ranking of the slip systems is consistent with experiment.¹⁸ In anticipation of electric effects associated with the plastic deformation of MgO,¹⁹ we tested TBSM with two different computational procedures for calculating the electrostatic interactions; one with dipole correction and the other without. Our results show that the plastic deformation in $(\bar{1}10)[110]$ strongly depends on the computational procedure. Using the method without dipole correction induces a change in the macroscopic polarization in the system before rock-salt MgO transforms to h-MgO. In contrast, TBSM shearing of $(\bar{1}10)[110]$ using the method with dipole correction gives periodic slip without a change in the macroscopic polarization. We reasoned that the case with correction leads to slip because of the existence of the second derivatives of the correction term changing the curvature in the RFO calculations of the slip state, i.e. as the polarization tries to change its value in the system, it activates some line search directions and contributes to RFO yielding a slipped state without a change in the net polarization. This is not the case without the dipole correction. We predict there may exist a solid-solid phase transformation path in MgO when shearing $(\bar{1}10)[110]$, especially since recent research²⁰⁻²² suggests that phase transition is shear-induced in several materials. In contrast to dislocation theory metrics, our proposed methods are able to successfully rank the slip systems of MgO, although our methods do not explicitly simulate dislocation core effects. It would be of interest to extend our methods to other ionic crystals.

O_2 is one of the simplest possible molecular crystals. In Chapter Seven, RBSM and TBSM were used to shear $\beta - O_2$ on several slip systems: two slip systems in (111), five slip systems in (110), and five slip systems in each of (112), (113), (114), (115), and (116). We computed the deformation barriers and found that the results for (111) are consistent with the case of FCC metals. Shearing the (110) plane and other higher index directions yielded a ranking of the barriers where the “Twin” direction and the directions at “45°” and “135°” are the easiest to shear. There are no publications reporting the microstructure of the deformation of O_2 . However, annealing-induced twins have been experimentally observed in the higher index planes of $\beta - O_2$.²³ RBSM and TBSM found rotational twinning in (110)[001]. This kind of twinning is due to the rotation of molecules, and has been observed, for instance, in the molecular dynamics deformation simulations of calcite.²⁴ Our post-processing of the results established the difference between a defect (one molecular rotation) and a twin (two or more molecules rotating), as well as the link between this twinning mechanism and the crystallographic lattice vector component, c_x .

Anthracene, a flat aromatic molecule consisting of three benzene rings, was sheared using TBSM and RBSM in Chapter Eight. We deformed the system in eight different directions in the (001) plane. Our results identified two groups of barriers: a group where RBSM and TBSM predicts the easiest slip systems (the (001)[010] and (001)[110]) consistent with experimental slip system ranking,²⁵ however RBSM also predicts (001)[100] to be slightly lower than the other two barriers, while TBSM predicts (001)[100] is similar to the experimental ones. Another group of barriers are predicted by both methods to be significantly (at least 1.93 times) larger than the group one barriers. Both methods predict similar deformation mechanisms for the (001)[100] and (001)[110], implying that it may be non-trivial to experimentally distinguish the deformation morphology of these two slip systems.

RBSM and TBSM show novel insights related to the deformation of crystalline materials in general. They are able to probe deformation of materials that have not been tested with these kinds of methods, e.g. O_2 and anthracene. The results are promising and perhaps can be extended to several other materials. For instance, FCC metals sheared with RBSM and TBSM consistently showed a twinning barrier that is lower than the slip barrier. Slip in BCC and HCP metals is more complicated since there is no consistent ranking of slip systems for all the metals.^{26, 27} Therefore, a

question for future investigation is would applying RBSM and TBSM to BCC and HCP metals give the same ranking of slip barriers across several slip systems or different ones? Our electrostatic analysis in MgO simulations implies that care has to be taken when simulating organic molecular crystals with large charges/dipole moments. We expect our methods to provide the slip barriers and deformation mechanisms for organic molecular crystals in general where the change in macroscopic polarization has been correctly accounted for. Perhaps the reversible twinning deformation of 3,5-difluorobenzoic acid,²⁸ which is surprisingly found for an organic molecular crystal instead of brittleness, warrants additional theoretical investigation of the underlying mechanisms, where we believe that RBSM and TBSM can provide atomistic insight into this kind of deformation.

Finally, we anticipate that RBSM and TBSM will be able to provide insight into the coupling between the deformation of organic molecular crystals and their torsional degrees of freedom. This is expected to be a critical component in the successful ranking of the slip systems in pharmaceutical crystals.

Bibliography

- ¹ V. Vitek, “Intrinsic stacking faults in body-centred cubic crystals,” *The Philosophical Magazine: A Journal of Theoretical Experimental and Applied Physics*, vol. 18, no. 154, pp. 773–786, 1968.
- ² D. Roundy, C. R. Krenn, M. L. Cohen, and J. W. Morris, “Ideal shear strengths of fcc aluminum and copper,” *Phys. Rev. Lett.*, vol. 82, pp. 2713–2716, Mar 1999.
- ³ S. Ogata, J. Li, and S. Yip, “Ideal pure shear strength of aluminum and copper,” *Science*, vol. 298, no. 5594, pp. 807–811, 2002.
- ⁴ A. Banerjee, N. Adams, J. Simons, and R. Shepard, “Search for stationary points on surfaces,” *The Journal of Physical Chemistry*, vol. 89, pp. 52–57, 01 1985.
- ⁵ E. Tadmor and S. Hai, “A peierls criterion for the onset of deformation twinning at a crack tip,” *Journal of the Mechanics and Physics of Solids*, vol. 51, no. 5, pp. 765 – 793, 2003.
- ⁶ L. Wang, P. Guan, J. Teng, P. Liu, D. Chen, W. Xie, D. Kong, S. Zhang, T. Zhu, Z. Zhang, E. Ma, M. Chen, and X. Han, “New twinning route in face-centered cubic nanocrystalline metals,” *Nature Communications*, vol. 8, 12 2017.
- ⁷ S. Kibey, J. Liu, D. Johnson, and H. Sehitoglu, “Predicting twinning stress in fcc metals: Linking twin-energy pathways to twin nucleation,” *Acta Materialia*, vol. 55, no. 20, pp. 6843 – 6851, 2007.
- ⁸ H. Huang, X. Li, Z. Dong, W. Li, S. Huang, D. Meng, X. Lai, T. Liu, S. Zhu, and L. Vitos, “Critical stress for twinning nucleation in crconi-based medium and high entropy alloys,” *Acta Materialia*, vol. 149, pp. 388 – 396, 2018.
- ⁹ S.-H. Kim, H.-K. Kim, J.-H. Seo, D.-M. Whang, J.-P. Ahn, and J.-C. Lee, “Deformation twinning of ultrahigh strength aluminum nanowire,” *Acta Materialia*, vol. 160, pp. 14–21, 2018.

- ¹⁰ J. R. Rice, “Dislocation nucleation from a crack tip: An analysis based on the peierls concept,” *Journal of the Mechanics and Physics of Solids*, vol. 40, no. 2, pp. 239 – 271, 1992.
- ¹¹ S. Pattamatta, R. S. Elliott, and E. B. Tadmor, “Mapping the stochastic response of nanostructures,” *Proceedings of the National Academy of Sciences*, vol. 111, no. 17, pp. E1678–E1686, 2014.
- ¹² P. E. Marszalek, W. J. Greenleaf, H. Li, A. F. Oberhauser, and J. M. Fernandez, “Atomic force microscopy captures quantized plastic deformation in gold nanowires,” *Proceedings of the National Academy of Sciences*, vol. 97, no. 12, pp. 6282–6286, 2000.
- ¹³ F. Shimizu, S. Ogata, and J. Li, “Theory of shear banding in metallic glasses and molecular dynamics calculations,” *MATERIALS TRANSACTIONS*, vol. 48, no. 11, pp. 2923–2927, 2007.
- ¹⁴ A. Gouldstone, H.-J. Koh, K.-Y. Zeng, A. Giannakopoulos, and S. Suresh, “Discrete and continuous deformation during nanoindentation of thin films,” *Acta Materialia*, vol. 48, no. 9, pp. 2277 – 2295, 2000.
- ¹⁵ J. Li, K. J. Van Vliet, T. Zhu, S. Yip, and S. Suresh, “Atomistic mechanisms governing elastic limit and incipient plasticity in crystals,” *Nature*, vol. 418, no. 6895, pp. 307–310, 2002.
- ¹⁶ C. L. Kelchner, S. J. Plimpton, and J. C. Hamilton, “Dislocation nucleation and defect structure during surface indentation,” *Phys. Rev. B*, vol. 58, pp. 11085–11088, Nov 1998.
- ¹⁷ J. D. Gale and A. L. Rohl, “The general utility lattice program (gulp),” *Molecular Simulation*, vol. 29, no. 5, pp. 291–341, 2003.
- ¹⁸ J. Amodeo, S. Merkel, C. Tromas, P. Carrez, S. Korte-Kerzel, P. Cordier, and J. Chevalier, “Dislocations and plastic deformation in mgo crystals: A review,” *Crystals (Basel)*, vol. 8, no. 6, pp. 240–53, 2018.
- ¹⁹ A. A. Urusovskaya, “Electric effects associated with plastic deformation of ionic crystals,” *Soviet Physics Uspekhi*, vol. 11, pp. 631–643, may 1969.
- ²⁰ D. G. McCulloch, S. Wong, T. B. Shiell, B. Haberl, B. A. Cook, X. Huang, R. Boehler, D. R. McKenzie, and J. E. Bradby, “Investigation of room temperature formation of the ultra-hard nanocarbons diamond and lonsdaleite,” *Small*, vol. 16, no. 50, p. 2004695, 2020.

- ²¹ C. Ji, V. I. Levitas, H. Zhu, J. Chaudhuri, A. Marathe, and Y. Ma, “Shear-induced phase transition of nanocrystalline hexagonal boron nitride to wurtzitic structure at room temperature and lower pressure,” *Proceedings of the National Academy of Sciences*, 2012.
- ²² V. I. Levitas, Y. Ma, J. Hashemi, M. Holtz, and N. Guven, “Strain-induced disorder, phase transformations, and transformation-induced plasticity in hexagonal boron nitride under compression and shear in a rotational diamond anvil cell: In situ x-ray diffraction study and modeling,” *The Journal of Chemical Physics*, vol. 125, no. 4, p. 044507, 2006.
- ²³ J. Venables, C. English, K. Niebel, and G. Tatlock, “Stacking faults, twins, and the structural stability of van der Waals solids,” *Journal de Physique Colloques*, vol. 35, no. C7, pp. C7–113–C7–119, 1974.
- ²⁴ A. S. Côté, R. Darkins, and D. M. Duffy, “Deformation twinning and the role of amino acids and magnesium in calcite hardness from molecular simulation,” *Phys. Chem. Chem. Phys.*, vol. 17, pp. 20178–20184, 2015.
- ²⁵ K. Kojima, “Slip systems in deformed anthracene crystals,” *physica status solidi (a)*, vol. 51, no. 1, pp. 71–78, 1979.
- ²⁶ C. R. Weinberger, B. L. Boyce, and C. C. Battaile, “Slip planes in bcc transition metals,” *International Materials Reviews*, vol. 58, no. 5, pp. 296–314, 2013.
- ²⁷ T. B. Britton, F. P. E. Dunne, and A. J. Wilkinson, “On the mechanistic basis of deformation at the microscale in hexagonal close-packed metals,” *Proceedings of the Royal Society A: Mathematical, Physical and Engineering Sciences*, vol. 471, no. 2178, p. 20140881, 2015.
- ²⁸ S. Takamizawa and Y. Takasaki, “Superelastic shape recovery of mechanically twinned 3,5-difluorobenzoic acid crystals,” *Angewandte Chemie International Edition*, vol. 54, no. 16, pp. 4815–4817, 2015.

Every reasonable effort has been made to acknowledge the owners of copyright material. I would be pleased to hear from any copyright owner who has been omitted or incorrectly acknowledged.

Appendix A

Finding The Easiest Slip Direction

Chapter 5 introduced a geometric tool that uses information from both atomistic and continuum mechanics to find the easiest slip system. We recall the set of equations;

$$E'_f = T^T E T = \frac{1}{2}(T^T C T - I) \quad (\text{A.1})$$

where we indicated that solving the three equations ($E'_{11} = 0$, $E'_{12} = 0$, and $E'_{23} = 0$) in terms of the three angles η , θ , and ϕ would provide the orientation with respect to the original frame of reference along which slip is the easiest. We note indices 1, 2, and 3 correspond to the Cartesian components x , y , and z . Writing the three equations in one-go is useless as each has too many terms.

First, we write the rotation matrix T as:

$$T = \begin{bmatrix} \cos \eta \cos \theta & \cos \eta \sin \theta \sin \phi - \sin \eta \cos \phi & \cos \eta \sin \theta \cos \phi + \sin \eta \sin \phi \\ \sin \eta \cos \theta & \sin \eta \sin \theta \sin \phi + \cos \eta \cos \phi & \sin \eta \sin \theta \cos \phi - \cos \eta \sin \phi \\ -\sin \theta & \cos \theta \sin \phi & \cos \theta \cos \phi \end{bmatrix} \quad (\text{A.2})$$

where T_{ij} represents the elements of A.2 for $i, j = 1, 2$, and 3 .

Equation $E'_{11} = 0$ reads:

$$T_{11}T_{11}C_{11} + T_{21}T_{21}C_{22} + T_{31}T_{31}C_{33} + 2T_{11}T_{21}C_{12} + 2T_{11}T_{31}C_{13} + 2T_{21}T_{31}C_{23} - 1 = 0 \quad (\text{A.3})$$

Equation $E'_{12} = 0$:

$$T_{11}T_{12}C_{11} + T_{21}T_{22}C_{22} + T_{31}T_{32}C_{33} + (T_{12}T_{31} + T_{11}T_{32})C_{13} + (T_{11}T_{22} + T_{21}T_{12})C_{12} \\ + (T_{31}T_{22} + T_{21}T_{32})C_{23} = 0 \quad (\text{A.4})$$

Equation $E'_{23} = 0$:

$$T_{12}T_{13}C_{11} + T_{22}T_{23}C_{22} + T_{32}T_{33}C_{33} + (T_{13}T_{22} + T_{12}T_{23})C_{12} + (T_{32}T_{13} + T_{12}T_{33})C_{13} \\ + (T_{22}T_{33} + T_{32}T_{23})C_{23} = 0 \quad (\text{A.5})$$

The above three equations can't be solved by hand and need to be typed into a script that can solve them using non-linear optimizers.

Appendix B

MgO Convergence Analysis

Chapter Six described the deformation of MgO. Since the objective of the chapter was not to examine the plastic deformation in detail, all the convergence analysis for RBSM and TBSM are included here.

B.1 RBSM Convergence Results

We performed several system and step size convergence simulations in the (001) and the $(\bar{1}10)$ slip systems. Figure B.1 shows the convergence simulation results for the (001)[110] slip system. In

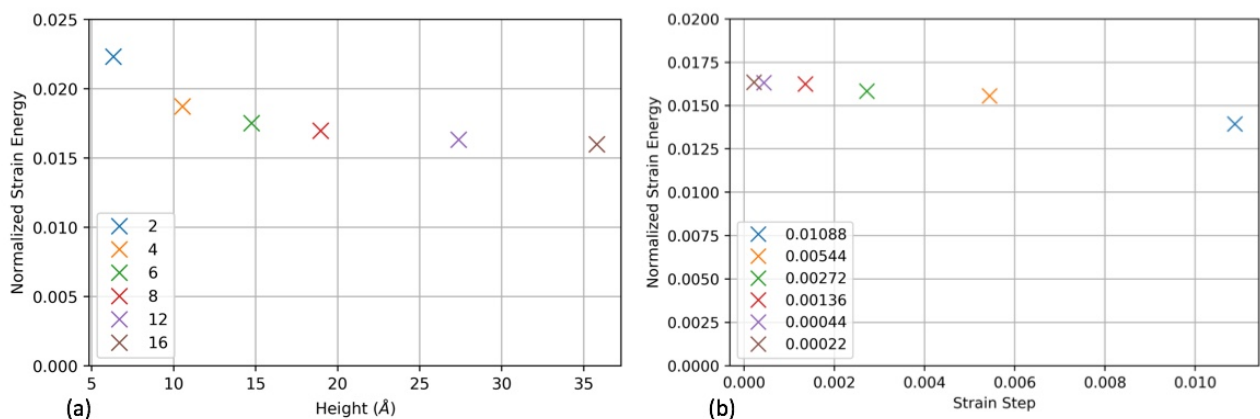


Figure B.1: Convergence analysis simulations of the normalized strain energy by varying the (a) system size at a strain per step equal to or less than 0.00095, and (b) the step size for the twelve-layer configuration, for the (001)[110] slip system.

Figure B.1 (a), we observe that the size of the system changes from two to sixteen. The strain per step was the highest for the sixteen layer simulation (0.00095) and decreased to 0.00033 for the two layer simulation. Figure B.1 (a) indicates that the normalized strain energy converges for system

sizes equal to or greater than twelve layers.

Having identified the system size convergence limit, we performed a series of step size simulations by varying the strain per step from 0.01088 to 0.00022 in the twelve layer configuration. Figure B.1 (b) indicates that the convergence limit is reached when the strain per step equals to or less than 0.003.

We also performed convergence analysis for the $(\bar{1}10)(110)$ slip system in MgO. We varied the system size and step size parameters in the same manner as for the $(001)(110)$ slip system. The results are shown in Figure B.2. The results show that the normalized strain energy converges at a

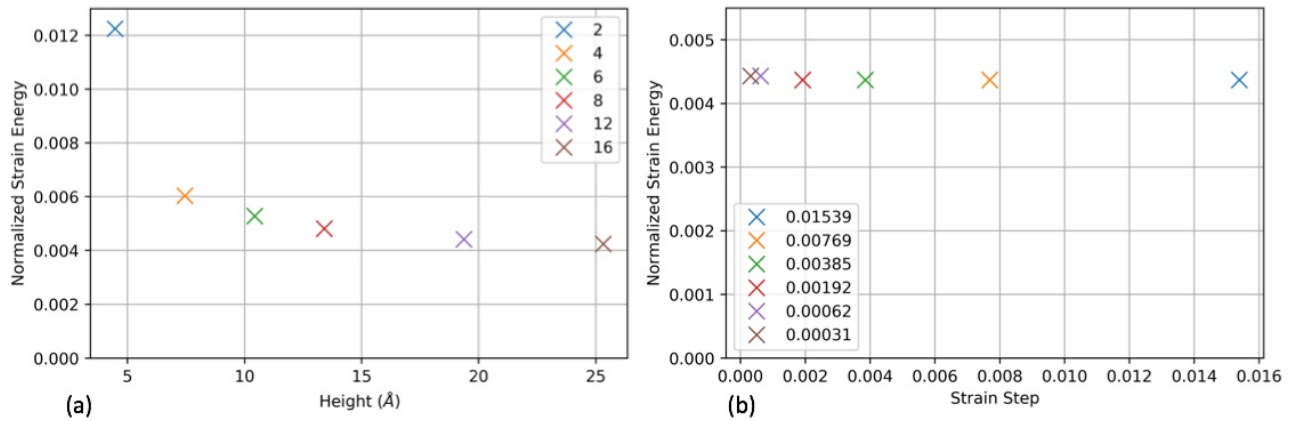


Figure B.2: Convergence analysis simulations of the normalized strain energy by varying the (a) system size at a strain per step equal to or less than 0.00095, and (b) the step size for the twelve-layer configuration, for the $(\bar{1}10)(110)$ slip system.

system size equals to or larger than twelve layers. For the step size analysis shown in Figure B.2 (b), the normalized strain energy is weakly affected by the strain per step.

B.2 TBSM Convergence Results

We performed TBSM convergence analysis on the two slip systems of MgO. Figure B.3 shows the normalized strain energy convergence results as a function of the system and step sizes, for the $(001)[110]$ slip system. For system size simulations, we chose a 0.00066 strain per step. Figure B.3 (a) shows that the normalized strain energy is not very sensitive to the system size in the $(001)[110]$ slip system. The same applies to the strain step analysis in Figure B.3 (b).

We turn our attention to the $(\bar{1}10)[110]$ slip system results shown in Figure B.4. In contrast to the previous slip system, the $(\bar{1}10)[110]$ shows a convergence trend. The normalized strain energy

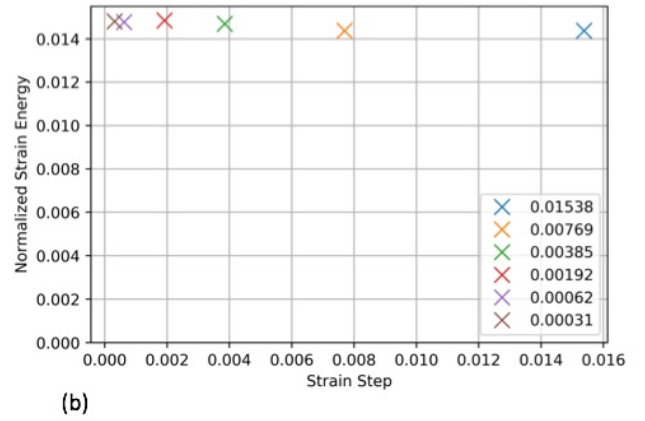
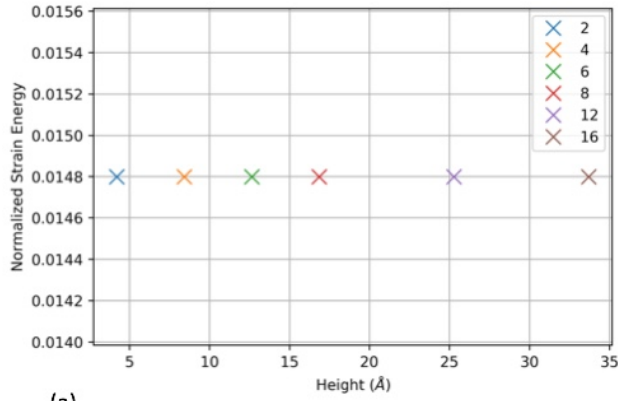


Figure B.3: Convergence analysis simulations of the normalized strain energy by varying the (a) system size at a strain per step equal to or less than 0.00095, and (b) the step size for the twelve-layer configuration, for the $(\bar{1}10)(110)$ slip system.

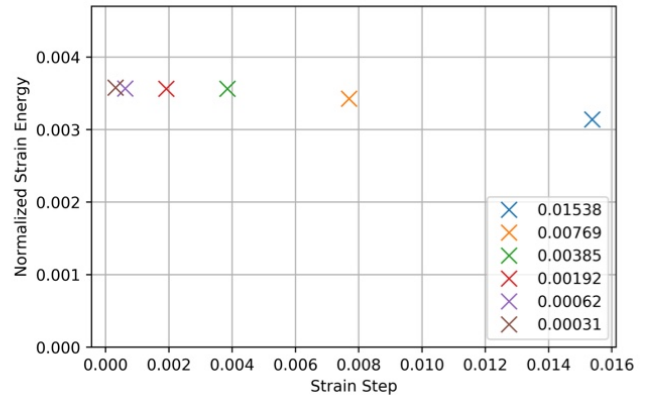
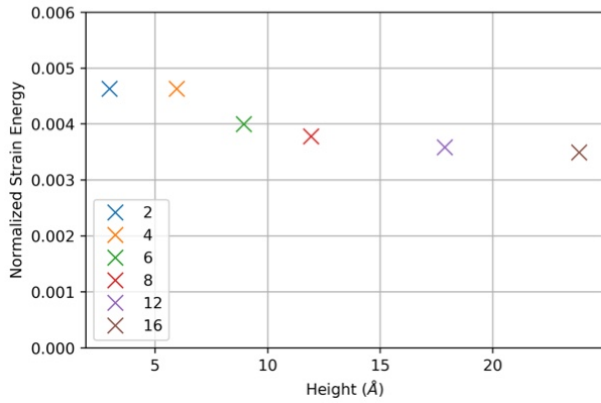


Figure B.4: Convergence analysis simulations of the normalized strain energy by varying the (a) system size at a strain per step equal to or less than 0.00095, and (b) the step size for the twelve-layer configuration, for the $(\bar{1}10)(110)$ slip system.

converges for system sizes equal to or larger than twelve layers (Figure B.4 (a)), while the same converges at a strain per step less than 0.004.

Appendix C

Copyrights and Permission

This appendix contains all the copyright permissions obtained for the figures and tables excerpted from third parties and used in this thesis. For every attached license, the thesis Figure number and Chapter are added to the header.

Figure 1.2; Chapter 1

11/06/2021

<https://marketplace.copyright.com/rs-ui-web/mp/license/8fe12f87-40cf-4339-a27e-ec1dbcf6fd4e/4ffb603f-860c-4a74-b246-e800f1532496>



Marketplace™

Taylor & Francis Group LLC - Books - License Terms and Conditions

This is a License Agreement between Mustafa Hamad / Curtin University ("You") and Taylor & Francis Group LLC - Books ("Publisher") provided by Copyright Clearance Center ("CCC"). The license consists of your order details, the terms and conditions provided by Taylor & Francis Group LLC - Books, and the CCC terms and conditions.

All payments must be made in full to CCC.

Order Date	11-Jun-2021	Type of Use	Republish in a thesis/dissertation
Order License ID	1125229-1	Publisher	TAYLOR & FRANCIS
ISBN-13	9780849390142	Portion	Chart/graph/table/figure

LICENSED CONTENT

Publication Title	Pharmaceutical dosage forms : Unit Operations and Mechanical Properties. Tablets	Country	United States of America
Author/Editor	Augsburger, Larry L., Hoag, Stephen W.	Rightsholder	Taylor & Francis Group LLC - Books
Date	06/03/2008	Publication Type	Book
Language	English		

REQUEST DETAILS

Portion Type	Chart/graph/table/figure	Distribution	Worldwide
Number of charts / graphs / tables / figures requested	1	Translation	Original language of publication
Format (select all that apply)	Print, Electronic	Copies for the disabled?	No
Who will republish the content?	Academic institution	Minor editing privileges?	No
Duration of Use	Life of current edition	Incidental promotional use?	No
Lifetime Unit Quantity	Up to 499	Currency	USD
Rights Requested	Main product		

NEW WORK DETAILS

Title	In-Silico Prediction of the Physical Performance of Pharmaceutical Crystals	Institution name	Curtin University
Instructor name	Professor Andrew Rohl	Expected presentation date	2021-07-16

ADDITIONAL DETAILS

Order reference number	N/A	The requesting person / organization to appear on the license	Mustafa Hamad / Curtin University
------------------------	-----	---	-----------------------------------

REUSE CONTENT DETAILS

<https://marketplace.copyright.com/rs-ui-web/mp/license/8fe12f87-40cf-4339-a27e-ec1dbcf6fd4e/4ffb603f-860c-4a74-b246-e800f1532496>

1/4

Figure 1.2; Chapter 1

11/06/2021 <https://marketplace.copyright.com/rs-ui-web/mp/license/8fe12f87-40cf-4339-a27e-ec1dbcf6fd4e/4ffb603f-860c-4a74-b246-e800f1532496>

Title, description or numeric reference of the portion(s)	Figure 33	Title of the article/chapter the portion is from	Compression and Compaction
Editor of portion(s)	N/A	Author of portion(s)	Augsburger, Larry L.; Hoag, Stephen W.
Volume of serial or monograph	N/A	Issue, if republishing an article from a serial	N/A
Page or page range of portion	616	Publication date of portion	2008-06-03

PUBLISHER TERMS AND CONDITIONS

Taylor and Francis Group and Informa healthcare are division of Informa plc. Permission will be void if material exceeds 10% of all the total pages in your publication and over 20% of the original publication. This includes permission granted by Informa plc and all of its subsidiaries.

CCC Replication Terms and Conditions

1. Description of Service; Defined Terms. This Replication License enables the User to obtain licenses for republication of one or more copyrighted works as described in detail on the relevant Order Confirmation (the "Work(s)"). Copyright Clearance Center, Inc. ("CCC") grants licenses through the Service on behalf of the rightsholder identified on the Order Confirmation (the "Rightsholder"). "Replication", as used herein, generally means the inclusion of a Work, in whole or in part, in a new work or works, also as described on the Order Confirmation. "User", as used herein, means the person or entity making such republication.
2. The terms set forth in the relevant Order Confirmation, and any terms set by the Rightsholder with respect to a particular Work, govern the terms of use of Works in connection with the Service. By using the Service, the person transacting for a republication license on behalf of the User represents and warrants that he/she/it (a) has been duly authorized by the User to accept, and hereby does accept, all such terms and conditions on behalf of User, and (b) shall inform User of all such terms and conditions. In the event such person is a "freelancer" or other third party independent of User and CCC, such party shall be deemed jointly a "User" for purposes of these terms and conditions. In any event, User shall be deemed to have accepted and agreed to all such terms and conditions if User republishes the Work in any fashion.
3. Scope of License; Limitations and Obligations.
 - 3.1. All Works and all rights therein, including copyright rights, remain the sole and exclusive property of the Rightsholder. The license created by the exchange of an Order Confirmation (and/or any invoice) and payment by User of the full amount set forth on that document includes only those rights expressly set forth in the Order Confirmation and in these terms and conditions, and conveys no other rights in the Work(s) to User. All rights not expressly granted are hereby reserved.
 - 3.2. General Payment Terms: You may pay by credit card or through an account with us payable at the end of the month. If you and we agree that you may establish a standing account with CCC, then the following terms apply: Remit Payment to: Copyright Clearance Center, 29118 Network Place, Chicago, IL 60673-1291. Payments Due: Invoices are payable upon their delivery to you (or upon our notice to you that they are available to you for downloading). After 30 days, outstanding amounts will be subject to a service charge of 1-1/2% per month or, if less, the maximum rate allowed by applicable law. Unless otherwise specifically set forth in the Order Confirmation or in a separate written agreement signed by CCC, invoices are due and payable on "net 30" terms. While User may exercise the rights licensed immediately upon issuance of the Order Confirmation, the license is automatically revoked and is null and void, as if it had never been issued, if complete payment for the license is not received on a timely basis either from User directly or through a payment agent, such as a credit card company.
 - 3.3. Unless otherwise provided in the Order Confirmation, any grant of rights to User (i) is "one-time" (including the editions and product family specified in the license), (ii) is non-exclusive and non-transferable and (iii) is subject to any and all limitations and restrictions (such as, but not limited to, limitations on duration of use or circulation) included in the Order Confirmation or invoice and/or in these terms and conditions. Upon completion of the licensed use, User shall either secure a new permission for further use of the Work(s) or immediately cease any new use of the Work(s) and shall render inaccessible (such as by deleting or by removing or severing links or other locators) any further copies of the Work (except for copies printed on paper in accordance with this license and still in User's stock at the end of such period).

<https://marketplace.copyright.com/rs-ui-web/mp/license/8fe12f87-40cf-4339-a27e-ec1dbcf6fd4e/4ffb603f-860c-4a74-b246-e800f1532496>

2/4

Figure 1.2; Chapter 1

11/06/2021

<https://marketplace.copyright.com/rs-ui-web/mp/license/8fe12f87-40cf-4339-a27e-ec1dbcf6fd4e/4ffb603f-860c-4a74-b246-e800f1532496>

- 3.4. In the event that the material for which a republication license is sought includes third party materials (such as photographs, illustrations, graphs, inserts and similar materials) which are identified in such material as having been used by permission, User is responsible for identifying, and seeking separate licenses (under this Service or otherwise) for, any of such third party materials; without a separate license, such third party materials may not be used.
- 3.5. Use of proper copyright notice for a Work is required as a condition of any license granted under the Service. Unless otherwise provided in the Order Confirmation, a proper copyright notice will read substantially as follows: "Republished with permission of [Rightsholder's name], from [Work's title, author, volume, edition number and year of copyright]; permission conveyed through Copyright Clearance Center, Inc. " Such notice must be provided in a reasonably legible font size and must be placed either immediately adjacent to the Work as used (for example, as part of a by-line or footnote but not as a separate electronic link) or in the place where substantially all other credits or notices for the new work containing the republished Work are located. Failure to include the required notice results in loss to the Rightsholder and CCC, and the User shall be liable to pay liquidated damages for each such failure equal to twice the use fee specified in the Order Confirmation, in addition to the use fee itself and any other fees and charges specified.
- 3.6. User may only make alterations to the Work if and as expressly set forth in the Order Confirmation. No Work may be used in any way that is defamatory, violates the rights of third parties (including such third parties' rights of copyright, privacy, publicity, or other tangible or intangible property), or is otherwise illegal, sexually explicit or obscene. In addition, User may not conjoin a Work with any other material that may result in damage to the reputation of the Rightsholder. User agrees to inform CCC if it becomes aware of any infringement of any rights in a Work and to cooperate with any reasonable request of CCC or the Rightsholder in connection therewith.
4. Indemnity. User hereby indemnifies and agrees to defend the Rightsholder and CCC, and their respective employees and directors, against all claims, liability, damages, costs and expenses, including legal fees and expenses, arising out of any use of a Work beyond the scope of the rights granted herein, or any use of a Work which has been altered in any unauthorized way by User, including claims of defamation or infringement of rights of copyright, publicity, privacy or other tangible or intangible property.
5. Limitation of Liability. UNDER NO CIRCUMSTANCES WILL CCC OR THE RIGHTSHOLDER BE LIABLE FOR ANY DIRECT, INDIRECT, CONSEQUENTIAL OR INCIDENTAL DAMAGES (INCLUDING WITHOUT LIMITATION DAMAGES FOR LOSS OF BUSINESS PROFITS OR INFORMATION, OR FOR BUSINESS INTERRUPTION) ARISING OUT OF THE USE OR INABILITY TO USE A WORK, EVEN IF ONE OF THEM HAS BEEN ADVISED OF THE POSSIBILITY OF SUCH DAMAGES. In any event, the total liability of the Rightsholder and CCC (including their respective employees and directors) shall not exceed the total amount actually paid by User for this license. User assumes full liability for the actions and omissions of its principals, employees, agents, affiliates, successors and assigns.
6. Limited Warranties. THE WORK(S) AND RIGHT(S) ARE PROVIDED "AS IS". CCC HAS THE RIGHT TO GRANT TO USER THE RIGHTS GRANTED IN THE ORDER CONFIRMATION DOCUMENT. CCC AND THE RIGHTSHOLDER DISCLAIM ALL OTHER WARRANTIES RELATING TO THE WORK(S) AND RIGHT(S), EITHER EXPRESS OR IMPLIED, INCLUDING WITHOUT LIMITATION IMPLIED WARRANTIES OF MERCHANTABILITY OR FITNESS FOR A PARTICULAR PURPOSE. ADDITIONAL RIGHTS MAY BE REQUIRED TO USE ILLUSTRATIONS, GRAPHS, PHOTOGRAPHS, ABSTRACTS, INSERTS OR OTHER PORTIONS OF THE WORK (AS OPPOSED TO THE ENTIRE WORK) IN A MANNER CONTEMPLATED BY USER; USER UNDERSTANDS AND AGREES THAT NEITHER CCC NOR THE RIGHTSHOLDER MAY HAVE SUCH ADDITIONAL RIGHTS TO GRANT.
7. Effect of Breach. Any failure by User to pay any amount when due, or any use by User of a Work beyond the scope of the license set forth in the Order Confirmation and/or these terms and conditions, shall be a material breach of the license created by the Order Confirmation and these terms and conditions. Any breach not cured within 30 days of written notice thereof shall result in immediate termination of such license without further notice. Any unauthorized (but licensable) use of a Work that is terminated immediately upon notice thereof may be liquidated by payment of the Rightsholder's ordinary license price therefor; any unauthorized (and unlicensable) use that is not terminated immediately for any reason (including, for example, because materials containing the Work cannot reasonably be recalled) will be subject to all remedies available at law or in equity, but in no event to a payment of less than three times the Rightsholder's ordinary license price for the most closely analogous licensable use plus Rightsholder's and/or CCC's costs and expenses incurred in collecting such payment.

<https://marketplace.copyright.com/rs-ui-web/mp/license/8fe12f87-40cf-4339-a27e-ec1dbcf6fd4e/4ffb603f-860c-4a74-b246-e800f1532496>

3/4

Figure 1.2; Chapter 1

11/06/2021 <https://marketplace.copyright.com/rs-ui-web/mp/license/8fe12f87-40cf-4339-a27e-ec1dbcf6fd4e/4ffb603f-860c-4a74-b246-e800f1532496>

8. Miscellaneous.

- 8.1. User acknowledges that CCC may, from time to time, make changes or additions to the Service or to these terms and conditions, and CCC reserves the right to send notice to the User by electronic mail or otherwise for the purposes of notifying User of such changes or additions; provided that any such changes or additions shall not apply to permissions already secured and paid for.
- 8.2. Use of User-related information collected through the Service is governed by CCC's privacy policy, available online here:<https://marketplace.copyright.com/rs-ui-web/mp/privacy-policy>
- 8.3. The licensing transaction described in the Order Confirmation is personal to User. Therefore, User may not assign or transfer to any other person (whether a natural person or an organization of any kind) the license created by the Order Confirmation and these terms and conditions or any rights granted hereunder; provided, however, that User may assign such license in its entirety on written notice to CCC in the event of a transfer of all or substantially all of User's rights in the new material which includes the Work(s) licensed under this Service.
- 8.4. No amendment or waiver of any terms is binding unless set forth in writing and signed by the parties. The Rightsholder and CCC hereby object to any terms contained in any writing prepared by the User or its principals, employees, agents or affiliates and purporting to govern or otherwise relate to the licensing transaction described in the Order Confirmation, which terms are in any way inconsistent with any terms set forth in the Order Confirmation and/or in these terms and conditions or CCC's standard operating procedures, whether such writing is prepared prior to, simultaneously with or subsequent to the Order Confirmation, and whether such writing appears on a copy of the Order Confirmation or in a separate instrument.
- 8.5. The licensing transaction described in the Order Confirmation document shall be governed by and construed under the law of the State of New York, USA, without regard to the principles thereof of conflicts of law. Any case, controversy, suit, action, or proceeding arising out of, in connection with, or related to such licensing transaction shall be brought, at CCC's sole discretion, in any federal or state court located in the County of New York, State of New York, USA, or in any federal or state court whose geographical jurisdiction covers the location of the Rightsholder set forth in the Order Confirmation. The parties expressly submit to the personal jurisdiction and venue of each such federal or state court. If you have any comments or questions about the Service or Copyright Clearance Center, please contact us at 978-750-8400 or send an e-mail to support@copyright.com.

v 1.1

Figure 1.6; Chapter 1

03/06/2021

<https://marketplace.copyright.com/rs-ui-web/mp/license/2bfa0514-6fa2-442f-a0b8-a58af2d58c06/fe20a894-8e21-4aa5-a3a6-359e427a5875>



Marketplace™

John Wiley & Sons - Books - License Terms and Conditions

This is a License Agreement between Mustafa Hamad / Curtin University ("You") and John Wiley & Sons - Books ("Publisher") provided by Copyright Clearance Center ("CCC"). The license consists of your order details, the terms and conditions provided by John Wiley & Sons - Books, and the CCC terms and conditions.

All payments must be made in full to CCC.

Order Date	03-Jun-2021	Type of Use	Republish in a thesis/dissertation
Order license ID	1123454-1	Publisher	JOHN WILEY & SONS
ISBN-13	978-0-471-73696-7	Portion	Chart/graph/table/figure

LICENSED CONTENT

Publication Title	Materials science and engineering : an introduction	Country	United States of America
Author/Editor	CALLISTER, WILLIAM D.	Rightsholder	John Wiley & Sons - Books
Date	01/01/2007	Publication Type	Book
Language	English		

REQUEST DETAILS

Portion Type	Chart/graph/table/figure	Distribution	Worldwide
Number of charts / graphs / tables / figures requested	1	Translation	Original language of publication
Format (select all that apply)	Print, Electronic	Copies for the disabled?	No
Who will republish the content?	Academic institution	Minor editing privileges?	No
Duration of Use	Life of current and all future editions	Incidental promotional use?	No
Lifetime Unit Quantity	Up to 499	Currency	AUD
Rights Requested	Main product		

NEW WORK DETAILS

Title	In-Silico Prediction of the Physical Performance of Pharmaceutical Crystals	Institution name	Curtin University
Instructor name	Professor Andrew Rohl	Expected presentation date	2021-07-15

ADDITIONAL DETAILS

The requesting person / organization to appear on the license	Mustafa Hamad / Curtin University
---	-----------------------------------

REUSE CONTENT DETAILS

<https://marketplace.copyright.com/rs-ui-web/mp/license/2bfa0514-6fa2-442f-a0b8-a58af2d58c06/fe20a894-8e21-4aa5-a3a6-359e427a5875>

1/4

Figure 1.6; Chapter 1

03/06/2021 <https://marketplace.copyright.com/rs-ui-web/mp/license/2bfa0514-6fa2-442f-a0b8-a58af2d58c06/fe20a894-8e21-4aa5-a3a6-359e427a5875>

Title, description or numeric reference of the portion(s)	Table 6.5	Title of the article/chapter the portion is from	Mechanical Properties of Metals
Editor of portion(s)	N/A	Author of portion(s)	CALLISTER, WILLIAM D.
Volume of serial or monograph	N/A	Publication date of portion	2007-01-01
Page or page range of portion	156		

PUBLISHER TERMS AND CONDITIONS

No right, license or interest to any trademark, trade name, service mark or other branding ("Marks") of WILEY or its licensors is granted hereunder, and you agree that you shall not assert any such right, license or interest with respect thereto. You may not alter, remove or suppress in any manner any copyright, trademark or other notices displayed by the Wiley material. This Agreement will be void if the Type of Use, Format, Circulation, or Requestor Type was misrepresented during the licensing process. In no instance may the total amount of Wiley Materials used in any Main Product, Compilation or Collective work comprise more than 5% (if figures/tables) or 15% (if full articles/chapters) of the (entirety of the) Main Product, Compilation or Collective Work. Some titles may be available under an Open Access license. It is the Licensors' responsibility to identify the type of Open Access license on which the requested material was published, and comply fully with the terms of that license for the type of use specified Further details can be found on Wiley Online Library <http://olabout.wiley.com/WileyCDA/Section/id-410895.html>.

CCC Republication Terms and Conditions

1. Description of Service; Defined Terms. This Republication License enables the User to obtain licenses for republication of one or more copyrighted works as described in detail on the relevant Order Confirmation (the "Work(s)"). Copyright Clearance Center, Inc. ("CCC") grants licenses through the Service on behalf of the rightsholder identified on the Order Confirmation (the "Rightsholder"). "Republication", as used herein, generally means the inclusion of a Work, in whole or in part, in a new work or works, also as described on the Order Confirmation. "User", as used herein, means the person or entity making such republication.
2. The terms set forth in the relevant Order Confirmation, and any terms set by the Rightsholder with respect to a particular Work, govern the terms of use of Works in connection with the Service. By using the Service, the person transacting for a republication license on behalf of the User represents and warrants that he/she/it (a) has been duly authorized by the User to accept, and hereby does accept, all such terms and conditions on behalf of User, and (b) shall inform User of all such terms and conditions. In the event such person is a "freelancer" or other third party independent of User and CCC, such party shall be deemed jointly a "User" for purposes of these terms and conditions. In any event, User shall be deemed to have accepted and agreed to all such terms and conditions if User republishes the Work in any fashion.
3. Scope of License; Limitations and Obligations.
 - 3.1. All Works and all rights therein, including copyright rights, remain the sole and exclusive property of the Rightsholder. The license created by the exchange of an Order Confirmation (and/or any invoice) and payment by User of the full amount set forth on that document includes only those rights expressly set forth in the Order Confirmation and in these terms and conditions, and conveys no other rights in the Work(s) to User. All rights not expressly granted are hereby reserved.
 - 3.2. General Payment Terms: You may pay by credit card or through an account with us payable at the end of the month. If you and we agree that you may establish a standing account with CCC, then the following terms apply: Remit Payment to: Copyright Clearance Center, 29118 Network Place, Chicago, IL 60673-1291. Payments Due: Invoices are payable upon their delivery to you (or upon our notice to you that they are available to you for downloading). After 30 days, outstanding amounts will be subject to a service charge of 1-1/2% per month or, if less, the maximum rate allowed by applicable law. Unless otherwise specifically set forth in the Order Confirmation or in a separate written agreement signed by CCC, invoices are due and payable on "net 30" terms. While User may exercise the rights licensed immediately upon issuance of the Order Confirmation, the license is automatically revoked and is null and void, as if it had never been issued, if complete payment for the license is not received on a timely basis either from User directly or through a payment agent, such as a credit card company.
 - 3.3. Unless otherwise provided in the Order Confirmation, any grant of rights to User (i) is "one-time" (including the editions and product family specified in the license), (ii) is non-exclusive and non-transferable and (iii)

<https://marketplace.copyright.com/rs-ui-web/mp/license/2bfa0514-6fa2-442f-a0b8-a58af2d58c06/fe20a894-8e21-4aa5-a3a6-359e427a5875>

2/4

Figure 1.6; Chapter 1

03/06/2021

<https://marketplace.copyright.com/rs-ui-web/mp/license/2bfa0514-6fa2-442f-a0b8-a58af2d58c06/fe20a894-8e21-4aa5-a3a6-359e427a5875>

is subject to any and all limitations and restrictions (such as, but not limited to, limitations on duration of use or circulation) included in the Order Confirmation or invoice and/or in these terms and conditions. Upon completion of the licensed use, User shall either secure a new permission for further use of the Work(s) or immediately cease any new use of the Work(s) and shall render inaccessible (such as by deleting or by removing or severing links or other locators) any further copies of the Work (except for copies printed on paper in accordance with this license and still in User's stock at the end of such period).

- 3.4. In the event that the material for which a republication license is sought includes third party materials (such as photographs, illustrations, graphs, inserts and similar materials) which are identified in such material as having been used by permission, User is responsible for identifying, and seeking separate licenses (under this Service or otherwise) for, any of such third party materials; without a separate license, such third party materials may not be used.
- 3.5. Use of proper copyright notice for a Work is required as a condition of any license granted under the Service. Unless otherwise provided in the Order Confirmation, a proper copyright notice will read substantially as follows: "Republished with permission of [Rightsholder's name], from [Work's title, author, volume, edition number and year of copyright]; permission conveyed through Copyright Clearance Center, Inc. " Such notice must be provided in a reasonably legible font size and must be placed either immediately adjacent to the Work as used (for example, as part of a by-line or footnote but not as a separate electronic link) or in the place where substantially all other credits or notices for the new work containing the republished Work are located. Failure to include the required notice results in loss to the Rightsholder and CCC, and the User shall be liable to pay liquidated damages for each such failure equal to twice the use fee specified in the Order Confirmation, in addition to the use fee itself and any other fees and charges specified.
- 3.6. User may only make alterations to the Work if and as expressly set forth in the Order Confirmation. No Work may be used in any way that is defamatory, violates the rights of third parties (including such third parties' rights of copyright, privacy, publicity, or other tangible or intangible property), or is otherwise illegal, sexually explicit or obscene. In addition, User may not conjoin a Work with any other material that may result in damage to the reputation of the Rightsholder. User agrees to inform CCC if it becomes aware of any infringement of any rights in a Work and to cooperate with any reasonable request of CCC or the Rightsholder in connection therewith.
4. Indemnity. User hereby indemnifies and agrees to defend the Rightsholder and CCC, and their respective employees and directors, against all claims, liability, damages, costs and expenses, including legal fees and expenses, arising out of any use of a Work beyond the scope of the rights granted herein, or any use of a Work which has been altered in any unauthorized way by User, including claims of defamation or infringement of rights of copyright, publicity, privacy or other tangible or intangible property.
5. Limitation of Liability. UNDER NO CIRCUMSTANCES WILL CCC OR THE RIGHTSHOLDER BE LIABLE FOR ANY DIRECT, INDIRECT, CONSEQUENTIAL OR INCIDENTAL DAMAGES (INCLUDING WITHOUT LIMITATION DAMAGES FOR LOSS OF BUSINESS PROFITS OR INFORMATION, OR FOR BUSINESS INTERRUPTION) ARISING OUT OF THE USE OR INABILITY TO USE A WORK, EVEN IF ONE OF THEM HAS BEEN ADVISED OF THE POSSIBILITY OF SUCH DAMAGES. In any event, the total liability of the Rightsholder and CCC (including their respective employees and directors) shall not exceed the total amount actually paid by User for this license. User assumes full liability for the actions and omissions of its principals, employees, agents, affiliates, successors and assigns.
6. Limited Warranties. THE WORK(S) AND RIGHT(S) ARE PROVIDED "AS IS". CCC HAS THE RIGHT TO GRANT TO USER THE RIGHTS GRANTED IN THE ORDER CONFIRMATION DOCUMENT. CCC AND THE RIGHTSHOLDER DISCLAIM ALL OTHER WARRANTIES RELATING TO THE WORK(S) AND RIGHT(S), EITHER EXPRESS OR IMPLIED, INCLUDING WITHOUT LIMITATION IMPLIED WARRANTIES OF MERCHANTABILITY OR FITNESS FOR A PARTICULAR PURPOSE. ADDITIONAL RIGHTS MAY BE REQUIRED TO USE ILLUSTRATIONS, GRAPHS, PHOTOGRAPHS, ABSTRACTS, INSERTS OR OTHER PORTIONS OF THE WORK (AS OPPOSED TO THE ENTIRE WORK) IN A MANNER CONTEMPLATED BY USER; USER UNDERSTANDS AND AGREES THAT NEITHER CCC NOR THE RIGHTSHOLDER MAY HAVE SUCH ADDITIONAL RIGHTS TO GRANT.
7. Effect of Breach. Any failure by User to pay any amount when due, or any use by User of a Work beyond the scope of the license set forth in the Order Confirmation and/or these terms and conditions, shall be a material breach of the license created by the Order Confirmation and these terms and conditions. Any breach not cured within 30 days of written notice thereof shall result in immediate termination of such license without further notice. Any unauthorized (but licensable) use of a Work that is terminated immediately upon notice thereof may be liquidated

<https://marketplace.copyright.com/rs-ui-web/mp/license/2bfa0514-6fa2-442f-a0b8-a58af2d58c06/fe20a894-8e21-4aa5-a3a6-359e427a5875>

3/4

Figure 1.6; Chapter 1

03/06/2021 <https://marketplace.copyright.com/rs-ui-web/mp/license/2bfa0514-6fa2-442f-a0b8-a58af2d58c06/fe20a894-8e21-4aa5-a3a6-359e427a5875>

by payment of the Rightsholder's ordinary license price therefor; any unauthorized (and unlicensable) use that is not terminated immediately for any reason (including, for example, because materials containing the Work cannot reasonably be recalled) will be subject to all remedies available at law or in equity, but in no event to a payment of less than three times the Rightsholder's ordinary license price for the most closely analogous licensable use plus Rightsholder's and/or CCC's costs and expenses incurred in collecting such payment.

8. Miscellaneous.

- 8.1. User acknowledges that CCC may, from time to time, make changes or additions to the Service or to these terms and conditions, and CCC reserves the right to send notice to the User by electronic mail or otherwise for the purposes of notifying User of such changes or additions; provided that any such changes or additions shall not apply to permissions already secured and paid for.
- 8.2. Use of User-related information collected through the Service is governed by CCC's privacy policy, available online here:<https://marketplace.copyright.com/rs-ui-web/mp/privacy-policy>
- 8.3. The licensing transaction described in the Order Confirmation is personal to User. Therefore, User may not assign or transfer to any other person (whether a natural person or an organization of any kind) the license created by the Order Confirmation and these terms and conditions or any rights granted hereunder; provided, however, that User may assign such license in its entirety on written notice to CCC in the event of a transfer of all or substantially all of User's rights in the new material which includes the Work(s) licensed under this Service.
- 8.4. No amendment or waiver of any terms is binding unless set forth in writing and signed by the parties. The Rightsholder and CCC hereby object to any terms contained in any writing prepared by the User or its principals, employees, agents or affiliates and purporting to govern or otherwise relate to the licensing transaction described in the Order Confirmation, which terms are in any way inconsistent with any terms set forth in the Order Confirmation and/or in these terms and conditions or CCC's standard operating procedures, whether such writing is prepared prior to, simultaneously with or subsequent to the Order Confirmation, and whether such writing appears on a copy of the Order Confirmation or in a separate instrument.
- 8.5. The licensing transaction described in the Order Confirmation document shall be governed by and construed under the law of the State of New York, USA, without regard to the principles thereof of conflicts of law. Any case, controversy, suit, action, or proceeding arising out of, in connection with, or related to such licensing transaction shall be brought, at CCC's sole discretion, in any federal or state court located in the County of New York, State of New York, USA, or in any federal or state court whose geographical jurisdiction covers the location of the Rightsholder set forth in the Order Confirmation. The parties expressly submit to the personal jurisdiction and venue of each such federal or state court. If you have any comments or questions about the Service or Copyright Clearance Center, please contact us at 978-750-8400 or send an e-mail to support@copyright.com.

v 1.1

Figure 1.8; Chapter 1

11/06/2021

RightsLink Printable License

ELSEVIER LICENSE TERMS AND CONDITIONS

Jun 11, 2021

This Agreement between Mustafa Hamad ("You") and Elsevier ("Elsevier") consists of your license details and the terms and conditions provided by Elsevier and Copyright Clearance Center.

License Number	5085720310094
License date	Jun 11, 2021
Licensed Content Publisher	Elsevier
Licensed Content Publication	International Journal of Pharmaceutics
Licensed Content Title	Evaluating particle hardness of pharmaceutical solids using AFM nanoindentation
Licensed Content Author	Victoria M. Masterson,Xiaoping Cao
Licensed Content Date	Oct 1, 2008
Licensed Content Volume	362
Licensed Content Issue	1-2
Licensed Content Pages	9
Start Page	163
End Page	171
Type of Use	reuse in a thesis/dissertation
Portion	figures/tables/illustrations

Figure 1.8; Chapter 1

11/06/2021

RightsLink Printable License

Number of figures/tables/illustrations	1
Format	both print and electronic
Are you the author of this Elsevier article?	No
Will you be translating?	No
Title	In silico prediction of the physical performance of pharmaceutical crystals
Institution name	Curtin University
Expected presentation date	Jul 2021
Portions	Figure 2 / page 164
Requestor Location	Mustafa Hamad Kent Street Bentley Perth, WA 6102 Australia Attn: Mustafa Hamad
Publisher Tax ID	GB 494 6272 12
Total	0.00 USD

Terms and Conditions

INTRODUCTION

1. The publisher for this copyrighted material is Elsevier. By clicking "accept" in connection with completing this licensing transaction, you agree that the following terms and conditions apply to this transaction (along with the Billing and Payment terms and conditions established by Copyright Clearance Center, Inc. ("CCC"), at the time that you opened your Rightslink account and that are available at any time at <http://myaccount.copyright.com>).

GENERAL TERMS

2. Elsevier hereby grants you permission to reproduce the aforementioned material subject to the terms and conditions indicated.

Figure 1.8; Chapter 1

11/06/2021

RightsLink Printable License

3. Acknowledgement: If any part of the material to be used (for example, figures) has appeared in our publication with credit or acknowledgement to another source, permission must also be sought from that source. If such permission is not obtained then that material may not be included in your publication/copies. Suitable acknowledgement to the source must be made, either as a footnote or in a reference list at the end of your publication, as follows:

"Reprinted from Publication title, Vol /edition number, Author(s), Title of article / title of chapter, Pages No., Copyright (Year), with permission from Elsevier [OR APPLICABLE SOCIETY COPYRIGHT OWNER]." Also Lancet special credit - "Reprinted from The Lancet, Vol. number, Author(s), Title of article, Pages No., Copyright (Year), with permission from Elsevier."

4. Reproduction of this material is confined to the purpose and/or media for which permission is hereby given.

5. Altering/Modifying Material: Not Permitted. However figures and illustrations may be altered/adapted minimally to serve your work. Any other abbreviations, additions, deletions and/or any other alterations shall be made only with prior written authorization of Elsevier Ltd. (Please contact Elsevier's permissions helpdesk [here](#)). No modifications can be made to any Lancet figures/tables and they must be reproduced in full.

6. If the permission fee for the requested use of our material is waived in this instance, please be advised that your future requests for Elsevier materials may attract a fee.

7. Reservation of Rights: Publisher reserves all rights not specifically granted in the combination of (i) the license details provided by you and accepted in the course of this licensing transaction, (ii) these terms and conditions and (iii) CCC's Billing and Payment terms and conditions.

8. License Contingent Upon Payment: While you may exercise the rights licensed immediately upon issuance of the license at the end of the licensing process for the transaction, provided that you have disclosed complete and accurate details of your proposed use, no license is finally effective unless and until full payment is received from you (either by publisher or by CCC) as provided in CCC's Billing and Payment terms and conditions. If full payment is not received on a timely basis, then any license preliminarily granted shall be deemed automatically revoked and shall be void as if never granted. Further, in the event that you breach any of these terms and conditions or any of CCC's Billing and Payment terms and conditions, the license is automatically revoked and shall be void as if never granted. Use of materials as described in a revoked license, as well as any use of the materials beyond the scope of an unrevoked license, may constitute copyright infringement and publisher reserves the right to take any and all action to protect its copyright in the materials.

9. Warranties: Publisher makes no representations or warranties with respect to the licensed material.

10. Indemnity: You hereby indemnify and agree to hold harmless publisher and CCC, and their respective officers, directors, employees and agents, from and against any and all claims arising out of your use of the licensed material other than as specifically authorized pursuant to this license.

11. No Transfer of License: This license is personal to you and may not be sublicensed, assigned, or transferred by you to any other person without publisher's written permission.

12. No Amendment Except in Writing: This license may not be amended except in a writing signed by both parties (or, in the case of publisher, by CCC on publisher's behalf).

Figure 1.8; Chapter 1

11/06/2021

RightsLink Printable License

13. **Objection to Contrary Terms:** Publisher hereby objects to any terms contained in any purchase order, acknowledgment, check endorsement or other writing prepared by you, which terms are inconsistent with these terms and conditions or CCC's Billing and Payment terms and conditions. These terms and conditions, together with CCC's Billing and Payment terms and conditions (which are incorporated herein), comprise the entire agreement between you and publisher (and CCC) concerning this licensing transaction. In the event of any conflict between your obligations established by these terms and conditions and those established by CCC's Billing and Payment terms and conditions, these terms and conditions shall control.

14. **Revocation:** Elsevier or Copyright Clearance Center may deny the permissions described in this License at their sole discretion, for any reason or no reason, with a full refund payable to you. Notice of such denial will be made using the contact information provided by you. Failure to receive such notice will not alter or invalidate the denial. In no event will Elsevier or Copyright Clearance Center be responsible or liable for any costs, expenses or damage incurred by you as a result of a denial of your permission request, other than a refund of the amount(s) paid by you to Elsevier and/or Copyright Clearance Center for denied permissions.

LIMITED LICENSE

The following terms and conditions apply only to specific license types:

15. **Translation:** This permission is granted for non-exclusive world **English** rights only unless your license was granted for translation rights. If you licensed translation rights you may only translate this content into the languages you requested. A professional translator must perform all translations and reproduce the content word for word preserving the integrity of the article.

16. **Posting licensed content on any Website:** The following terms and conditions apply as follows: Licensing material from an Elsevier journal: All content posted to the web site must maintain the copyright information line on the bottom of each image; A hyper-text must be included to the Homepage of the journal from which you are licensing at <http://www.sciencedirect.com/science/journal/xxxxx> or the Elsevier homepage for books at <http://www.elsevier.com>; Central Storage: This license does not include permission for a scanned version of the material to be stored in a central repository such as that provided by Heron/XanEdu.

Licensing material from an Elsevier book: A hyper-text link must be included to the Elsevier homepage at <http://www.elsevier.com>. All content posted to the web site must maintain the copyright information line on the bottom of each image.

Posting licensed content on Electronic reserve: In addition to the above the following clauses are applicable: The web site must be password-protected and made available only to bona fide students registered on a relevant course. This permission is granted for 1 year only. You may obtain a new license for future website posting.

17. **For journal authors:** the following clauses are applicable in addition to the above:

Preprints:

A preprint is an author's own write-up of research results and analysis, it has not been peer-reviewed, nor has it had any other value added to it by a publisher (such as formatting, copyright, technical enhancement etc.).

Authors can share their preprints anywhere at any time. Preprints should not be added to or enhanced in any way in order to appear more like, or to substitute for, the final versions of

Figure 1.8; Chapter 1

11/06/2021

RightsLink Printable License

articles however authors can update their preprints on arXiv or RePEc with their Accepted Author Manuscript (see below).

If accepted for publication, we encourage authors to link from the preprint to their formal publication via its DOI. Millions of researchers have access to the formal publications on ScienceDirect, and so links will help users to find, access, cite and use the best available version. Please note that Cell Press, The Lancet and some society-owned have different preprint policies. Information on these policies is available on the journal homepage.

Accepted Author Manuscripts: An accepted author manuscript is the manuscript of an article that has been accepted for publication and which typically includes author-incorporated changes suggested during submission, peer review and editor-author communications.

Authors can share their accepted author manuscript:

- immediately
 - via their non-commercial person homepage or blog
 - by updating a preprint in arXiv or RePEc with the accepted manuscript
 - via their research institute or institutional repository for internal institutional uses or as part of an invitation-only research collaboration work-group
 - directly by providing copies to their students or to research collaborators for their personal use
 - for private scholarly sharing as part of an invitation-only work group on commercial sites with which Elsevier has an agreement
- After the embargo period
 - via non-commercial hosting platforms such as their institutional repository
 - via commercial sites with which Elsevier has an agreement

In all cases accepted manuscripts should:

- link to the formal publication via its DOI
- bear a CC-BY-NC-ND license - this is easy to do
- if aggregated with other manuscripts, for example in a repository or other site, be shared in alignment with our hosting policy not be added to or enhanced in any way to appear more like, or to substitute for, the published journal article.

Published journal article (JPA): A published journal article (PJA) is the definitive final record of published research that appears or will appear in the journal and embodies all value-adding publishing activities including peer review co-ordination, copy-editing, formatting, (if relevant) pagination and online enrichment.

Policies for sharing publishing journal articles differ for subscription and gold open access articles:

Subscription Articles: If you are an author, please share a link to your article rather than the full-text. Millions of researchers have access to the formal publications on ScienceDirect, and so links will help your users to find, access, cite, and use the best available version.

Theses and dissertations which contain embedded PJAs as part of the formal submission can be posted publicly by the awarding institution with DOI links back to the formal publications on ScienceDirect.

If you are affiliated with a library that subscribes to ScienceDirect you have additional private sharing rights for others' research accessed under that agreement. This includes use for classroom teaching and internal training at the institution (including use in course packs and courseware programs), and inclusion of the article for grant funding purposes.

Figure 1.8; Chapter 1

11/06/2021

RightsLink Printable License

Gold Open Access Articles: May be shared according to the author-selected end-user license and should contain a [CrossMark logo](#), the end user license, and a DOI link to the formal publication on ScienceDirect.

Please refer to Elsevier's [posting policy](#) for further information.

18. **For book authors** the following clauses are applicable in addition to the above: Authors are permitted to place a brief summary of their work online only. You are not allowed to download and post the published electronic version of your chapter, nor may you scan the printed edition to create an electronic version. **Posting to a repository:** Authors are permitted to post a summary of their chapter only in their institution's repository.

19. **Thesis/Dissertation:** If your license is for use in a thesis/dissertation your thesis may be submitted to your institution in either print or electronic form. Should your thesis be published commercially, please reapply for permission. These requirements include permission for the Library and Archives of Canada to supply single copies, on demand, of the complete thesis and include permission for Proquest/UMI to supply single copies, on demand, of the complete thesis. Should your thesis be published commercially, please reapply for permission. Theses and dissertations which contain embedded PJAs as part of the formal submission can be posted publicly by the awarding institution with DOI links back to the formal publications on ScienceDirect.

Elsevier Open Access Terms and Conditions

You can publish open access with Elsevier in hundreds of open access journals or in nearly 2000 established subscription journals that support open access publishing. Permitted third party re-use of these open access articles is defined by the author's choice of Creative Commons user license. See our [open access license policy](#) for more information.

Terms & Conditions applicable to all Open Access articles published with Elsevier:

Any reuse of the article must not represent the author as endorsing the adaptation of the article nor should the article be modified in such a way as to damage the author's honour or reputation. If any changes have been made, such changes must be clearly indicated.

The author(s) must be appropriately credited and we ask that you include the end user license and a DOI link to the formal publication on ScienceDirect.

If any part of the material to be used (for example, figures) has appeared in our publication with credit or acknowledgement to another source it is the responsibility of the user to ensure their reuse complies with the terms and conditions determined by the rights holder.

Additional Terms & Conditions applicable to each Creative Commons user license:

CC BY: The CC-BY license allows users to copy, to create extracts, abstracts and new works from the Article, to alter and revise the Article and to make commercial use of the Article (including reuse and/or resale of the Article by commercial entities), provided the user gives appropriate credit (with a link to the formal publication through the relevant DOI), provides a link to the license, indicates if changes were made and the licensor is not represented as endorsing the use made of the work. The full details of the license are available at <http://creativecommons.org/licenses/by/4.0>.

CC BY NC SA: The CC BY-NC-SA license allows users to copy, to create extracts, abstracts and new works from the Article, to alter and revise the Article, provided this is not done for commercial purposes, and that the user gives appropriate credit (with a link to the formal publication through the relevant DOI), provides a link to the license, indicates if changes were made and the licensor is not represented as endorsing the use made of the

Figure 1.8; Chapter 1

11/06/2021

RightsLink Printable License

work. Further, any new works must be made available on the same conditions. The full details of the license are available at <http://creativecommons.org/licenses/by-nc-sa/4.0>.

CC BY NC ND: The CC BY-NC-ND license allows users to copy and distribute the Article, provided this is not done for commercial purposes and further does not permit distribution of the Article if it is changed or edited in any way, and provided the user gives appropriate credit (with a link to the formal publication through the relevant DOI), provides a link to the license, and that the licensor is not represented as endorsing the use made of the work. The full details of the license are available at <http://creativecommons.org/licenses/by-nc-nd/4.0>. Any commercial reuse of Open Access articles published with a CC BY NC SA or CC BY NC ND license requires permission from Elsevier and will be subject to a fee.

Commercial reuse includes:

- Associating advertising with the full text of the Article
- Charging fees for document delivery or access
- Article aggregation
- Systematic distribution via e-mail lists or share buttons

Posting or linking by commercial companies for use by customers of those companies.

20. Other Conditions:

v1.10

Questions? customercare@copyright.com or +1-855-239-3415 (toll free in the US) or +1-978-646-2777.

Figure 1.9; Chapter 1

11/06/2021

RightsLink Printable License

ELSEVIER LICENSE TERMS AND CONDITIONS

Jun 11, 2021

This Agreement between Mustafa Hamad ("You") and Elsevier ("Elsevier") consists of your license details and the terms and conditions provided by Elsevier and Copyright Clearance Center.

License Number	5085750719442
License date	Jun 11, 2021
Licensed Content Publisher	Elsevier
Licensed Content Publication	Acta Metallurgica
Licensed Content Title	A first report on deformation-mechanism maps
Licensed Content Author	M.F Ashby
Licensed Content Date	Jul 1, 1972
Licensed Content Volume	20
Licensed Content Issue	7
Licensed Content Pages	11
Start Page	887
End Page	897
Type of Use	reuse in a thesis/dissertation
Portion	figures/tables/illustrations

Figure 1.9; Chapter 1

11/06/2021

RightsLink Printable License

Number of figures/tables/illustrations	1
Format	both print and electronic
Are you the author of this Elsevier article?	No
Will you be translating?	No
Title	In silico prediction of the physical performance of pharmaceutical crystals
Institution name	Curtin University
Expected presentation date	Jul 2021
Portions	Figure 1 / Page 888
Requestor Location	Mustafa Hamad Kent Street Bentley Perth, WA 6102 Australia Attn: Mustafa Hamad
Publisher Tax ID	GB 494 6272 12
Total	0.00 USD
Terms and Conditions	

INTRODUCTION

1. The publisher for this copyrighted material is Elsevier. By clicking "accept" in connection with completing this licensing transaction, you agree that the following terms and conditions apply to this transaction (along with the Billing and Payment terms and conditions established by Copyright Clearance Center, Inc. ("CCC"), at the time that you opened your Rightslink account and that are available at any time at <http://myaccount.copyright.com>).

GENERAL TERMS

2. Elsevier hereby grants you permission to reproduce the aforementioned material subject to the terms and conditions indicated.

Figure 1.9; Chapter 1

11/06/2021

RightsLink Printable License

3. Acknowledgement: If any part of the material to be used (for example, figures) has appeared in our publication with credit or acknowledgement to another source, permission must also be sought from that source. If such permission is not obtained then that material may not be included in your publication/copies. Suitable acknowledgement to the source must be made, either as a footnote or in a reference list at the end of your publication, as follows:

"Reprinted from Publication title, Vol /edition number, Author(s), Title of article / title of chapter, Pages No., Copyright (Year), with permission from Elsevier [OR APPLICABLE SOCIETY COPYRIGHT OWNER]." Also Lancet special credit - "Reprinted from The Lancet, Vol. number, Author(s), Title of article, Pages No., Copyright (Year), with permission from Elsevier."

4. Reproduction of this material is confined to the purpose and/or media for which permission is hereby given.

5. Altering/Modifying Material: Not Permitted. However figures and illustrations may be altered/adapted minimally to serve your work. Any other abbreviations, additions, deletions and/or any other alterations shall be made only with prior written authorization of Elsevier Ltd. (Please contact Elsevier's permissions helpdesk [here](#)). No modifications can be made to any Lancet figures/tables and they must be reproduced in full.

6. If the permission fee for the requested use of our material is waived in this instance, please be advised that your future requests for Elsevier materials may attract a fee.

7. Reservation of Rights: Publisher reserves all rights not specifically granted in the combination of (i) the license details provided by you and accepted in the course of this licensing transaction, (ii) these terms and conditions and (iii) CCC's Billing and Payment terms and conditions.

8. License Contingent Upon Payment: While you may exercise the rights licensed immediately upon issuance of the license at the end of the licensing process for the transaction, provided that you have disclosed complete and accurate details of your proposed use, no license is finally effective unless and until full payment is received from you (either by publisher or by CCC) as provided in CCC's Billing and Payment terms and conditions. If full payment is not received on a timely basis, then any license preliminarily granted shall be deemed automatically revoked and shall be void as if never granted. Further, in the event that you breach any of these terms and conditions or any of CCC's Billing and Payment terms and conditions, the license is automatically revoked and shall be void as if never granted. Use of materials as described in a revoked license, as well as any use of the materials beyond the scope of an unrevoked license, may constitute copyright infringement and publisher reserves the right to take any and all action to protect its copyright in the materials.

9. Warranties: Publisher makes no representations or warranties with respect to the licensed material.

10. Indemnity: You hereby indemnify and agree to hold harmless publisher and CCC, and their respective officers, directors, employees and agents, from and against any and all claims arising out of your use of the licensed material other than as specifically authorized pursuant to this license.

11. No Transfer of License: This license is personal to you and may not be sublicensed, assigned, or transferred by you to any other person without publisher's written permission.

12. No Amendment Except in Writing: This license may not be amended except in a writing signed by both parties (or, in the case of publisher, by CCC on publisher's behalf).

Figure 1.9; Chapter 1

11/06/2021

RightsLink Printable License

13. **Objection to Contrary Terms:** Publisher hereby objects to any terms contained in any purchase order, acknowledgment, check endorsement or other writing prepared by you, which terms are inconsistent with these terms and conditions or CCC's Billing and Payment terms and conditions. These terms and conditions, together with CCC's Billing and Payment terms and conditions (which are incorporated herein), comprise the entire agreement between you and publisher (and CCC) concerning this licensing transaction. In the event of any conflict between your obligations established by these terms and conditions and those established by CCC's Billing and Payment terms and conditions, these terms and conditions shall control.

14. **Revocation:** Elsevier or Copyright Clearance Center may deny the permissions described in this License at their sole discretion, for any reason or no reason, with a full refund payable to you. Notice of such denial will be made using the contact information provided by you. Failure to receive such notice will not alter or invalidate the denial. In no event will Elsevier or Copyright Clearance Center be responsible or liable for any costs, expenses or damage incurred by you as a result of a denial of your permission request, other than a refund of the amount(s) paid by you to Elsevier and/or Copyright Clearance Center for denied permissions.

LIMITED LICENSE

The following terms and conditions apply only to specific license types:

15. **Translation:** This permission is granted for non-exclusive world **English** rights only unless your license was granted for translation rights. If you licensed translation rights you may only translate this content into the languages you requested. A professional translator must perform all translations and reproduce the content word for word preserving the integrity of the article.

16. **Posting licensed content on any Website:** The following terms and conditions apply as follows: Licensing material from an Elsevier journal: All content posted to the web site must maintain the copyright information line on the bottom of each image; A hyper-text must be included to the Homepage of the journal from which you are licensing at <http://www.sciencedirect.com/science/journal/xxxxx> or the Elsevier homepage for books at <http://www.elsevier.com>; Central Storage: This license does not include permission for a scanned version of the material to be stored in a central repository such as that provided by Heron/XanEdu.

Licensing material from an Elsevier book: A hyper-text link must be included to the Elsevier homepage at <http://www.elsevier.com>. All content posted to the web site must maintain the copyright information line on the bottom of each image.

Posting licensed content on Electronic reserve: In addition to the above the following clauses are applicable: The web site must be password-protected and made available only to bona fide students registered on a relevant course. This permission is granted for 1 year only. You may obtain a new license for future website posting.

17. **For journal authors:** the following clauses are applicable in addition to the above:

Preprints:

A preprint is an author's own write-up of research results and analysis, it has not been peer-reviewed, nor has it had any other value added to it by a publisher (such as formatting, copyright, technical enhancement etc.).

Authors can share their preprints anywhere at any time. Preprints should not be added to or enhanced in any way in order to appear more like, or to substitute for, the final versions of

Figure 1.9; Chapter 1

11/06/2021

RightsLink Printable License

articles however authors can update their preprints on arXiv or RePEc with their Accepted Author Manuscript (see below).

If accepted for publication, we encourage authors to link from the preprint to their formal publication via its DOI. Millions of researchers have access to the formal publications on ScienceDirect, and so links will help users to find, access, cite and use the best available version. Please note that Cell Press, The Lancet and some society-owned have different preprint policies. Information on these policies is available on the journal homepage.

Accepted Author Manuscripts: An accepted author manuscript is the manuscript of an article that has been accepted for publication and which typically includes author-incorporated changes suggested during submission, peer review and editor-author communications.

Authors can share their accepted author manuscript:

- immediately
 - via their non-commercial person homepage or blog
 - by updating a preprint in arXiv or RePEc with the accepted manuscript
 - via their research institute or institutional repository for internal institutional uses or as part of an invitation-only research collaboration work-group
 - directly by providing copies to their students or to research collaborators for their personal use
 - for private scholarly sharing as part of an invitation-only work group on commercial sites with which Elsevier has an agreement
- After the embargo period
 - via non-commercial hosting platforms such as their institutional repository
 - via commercial sites with which Elsevier has an agreement

In all cases accepted manuscripts should:

- link to the formal publication via its DOI
- bear a CC-BY-NC-ND license - this is easy to do
- if aggregated with other manuscripts, for example in a repository or other site, be shared in alignment with our hosting policy not be added to or enhanced in any way to appear more like, or to substitute for, the published journal article.

Published journal article (JPA): A published journal article (PJA) is the definitive final record of published research that appears or will appear in the journal and embodies all value-adding publishing activities including peer review co-ordination, copy-editing, formatting, (if relevant) pagination and online enrichment.

Policies for sharing publishing journal articles differ for subscription and gold open access articles:

Subscription Articles: If you are an author, please share a link to your article rather than the full-text. Millions of researchers have access to the formal publications on ScienceDirect, and so links will help your users to find, access, cite, and use the best available version.

Theses and dissertations which contain embedded PJAs as part of the formal submission can be posted publicly by the awarding institution with DOI links back to the formal publications on ScienceDirect.

If you are affiliated with a library that subscribes to ScienceDirect you have additional private sharing rights for others' research accessed under that agreement. This includes use for classroom teaching and internal training at the institution (including use in course packs and courseware programs), and inclusion of the article for grant funding purposes.

Figure 1.9; Chapter 1

11/06/2021

RightsLink Printable License

Gold Open Access Articles: May be shared according to the author-selected end-user license and should contain a [CrossMark logo](#), the end user license, and a DOI link to the formal publication on ScienceDirect.

Please refer to Elsevier's [posting policy](#) for further information.

18. For book authors the following clauses are applicable in addition to the above: Authors are permitted to place a brief summary of their work online only. You are not allowed to download and post the published electronic version of your chapter, nor may you scan the printed edition to create an electronic version. **Posting to a repository:** Authors are permitted to post a summary of their chapter only in their institution's repository.

19. Thesis/Dissertation: If your license is for use in a thesis/dissertation your thesis may be submitted to your institution in either print or electronic form. Should your thesis be published commercially, please reapply for permission. These requirements include permission for the Library and Archives of Canada to supply single copies, on demand, of the complete thesis and include permission for Proquest/UMI to supply single copies, on demand, of the complete thesis. Should your thesis be published commercially, please reapply for permission. Theses and dissertations which contain embedded PJAs as part of the formal submission can be posted publicly by the awarding institution with DOI links back to the formal publications on ScienceDirect.

Elsevier Open Access Terms and Conditions

You can publish open access with Elsevier in hundreds of open access journals or in nearly 2000 established subscription journals that support open access publishing. Permitted third party re-use of these open access articles is defined by the author's choice of Creative Commons user license. See our [open access license policy](#) for more information.

Terms & Conditions applicable to all Open Access articles published with Elsevier:

Any reuse of the article must not represent the author as endorsing the adaptation of the article nor should the article be modified in such a way as to damage the author's honour or reputation. If any changes have been made, such changes must be clearly indicated.

The author(s) must be appropriately credited and we ask that you include the end user license and a DOI link to the formal publication on ScienceDirect.

If any part of the material to be used (for example, figures) has appeared in our publication with credit or acknowledgement to another source it is the responsibility of the user to ensure their reuse complies with the terms and conditions determined by the rights holder.

Additional Terms & Conditions applicable to each Creative Commons user license:

CC BY: The CC-BY license allows users to copy, to create extracts, abstracts and new works from the Article, to alter and revise the Article and to make commercial use of the Article (including reuse and/or resale of the Article by commercial entities), provided the user gives appropriate credit (with a link to the formal publication through the relevant DOI), provides a link to the license, indicates if changes were made and the licensor is not represented as endorsing the use made of the work. The full details of the license are available at <http://creativecommons.org/licenses/by/4.0>.

CC BY NC SA: The CC BY-NC-SA license allows users to copy, to create extracts, abstracts and new works from the Article, to alter and revise the Article, provided this is not done for commercial purposes, and that the user gives appropriate credit (with a link to the formal publication through the relevant DOI), provides a link to the license, indicates if changes were made and the licensor is not represented as endorsing the use made of the

Figure 1.9; Chapter 1

11/06/2021

RightsLink Printable License

work. Further, any new works must be made available on the same conditions. The full details of the license are available at <http://creativecommons.org/licenses/by-nc-sa/4.0>.

CC BY NC ND: The CC BY-NC-ND license allows users to copy and distribute the Article, provided this is not done for commercial purposes and further does not permit distribution of the Article if it is changed or edited in any way, and provided the user gives appropriate credit (with a link to the formal publication through the relevant DOI), provides a link to the license, and that the licensor is not represented as endorsing the use made of the work. The full details of the license are available at <http://creativecommons.org/licenses/by-nc-nd/4.0>. Any commercial reuse of Open Access articles published with a CC BY NC SA or CC BY NC ND license requires permission from Elsevier and will be subject to a fee.

Commercial reuse includes:

- Associating advertising with the full text of the Article
- Charging fees for document delivery or access
- Article aggregation
- Systematic distribution via e-mail lists or share buttons

Posting or linking by commercial companies for use by customers of those companies.

20. Other Conditions:

v1.10

Questions? customercare@copyright.com or +1-855-239-3415 (toll free in the US) or +1-978-646-2777.

Figures 1.11 and 1.12; Chapter 1

06/06/2021

RightsLink Printable License

ELSEVIER LICENSE TERMS AND CONDITIONS

Jun 06, 2021

This Agreement between Mustafa Hamad ("You") and Elsevier ("Elsevier") consists of your license details and the terms and conditions provided by Elsevier and Copyright Clearance Center.

License Number	5082860967893
License date	Jun 06, 2021
Licensed Content Publisher	Elsevier
Licensed Content Publication	Elsevier Books
Licensed Content Title	Introduction to Dislocations
Licensed Content Author	D. Hull,D.J. Bacon
Licensed Content Date	Jan 1, 2011
Licensed Content Pages	20
Start Page	43
End Page	62
Type of Use	reuse in a thesis/dissertation
Portion	figures/tables/illustrations
Number of figures/tables/illustrations	2
Format	both print and electronic

<https://s100.copyright.com/CustomAdmin/PLF.jsp?ref=0357dbd7-92c2-49b8-b80a-61e9d4ae6ed8>

1/7

Figures 1.11 and 1.12; Chapter 1

06/06/2021

RightsLink Printable License

Are you the author of this Elsevier chapter? No

Will you be translating? No

Title In silico prediction of the physical performance of pharmaceutical crystals

Institution name Curtin University

Expected presentation date Jul 2021

Portions Figure 3.4 / page 46 Figure 3.5 / page 47

Requestor Location
Mustafa Hamad
Kent street
Bentley
Perth, WA 6102
Australia
Attn: Mustafa Hamad

Publisher Tax ID GB 494 6272 12

Total 0.00 USD

Terms and Conditions

INTRODUCTION

1. The publisher for this copyrighted material is Elsevier. By clicking "accept" in connection with completing this licensing transaction, you agree that the following terms and conditions apply to this transaction (along with the Billing and Payment terms and conditions established by Copyright Clearance Center, Inc. ("CCC"), at the time that you opened your Rightslink account and that are available at any time at <http://myaccount.copyright.com>).

GENERAL TERMS

2. Elsevier hereby grants you permission to reproduce the aforementioned material subject to the terms and conditions indicated.

3. Acknowledgement: If any part of the material to be used (for example, figures) has appeared in our publication with credit or acknowledgement to another source, permission must also be sought from that source. If such permission is not obtained then that material may not be included in your publication/copies. Suitable acknowledgement to the source must be made, either as a footnote or in a reference list at the end of your publication, as follows:

Figures 1.11 and 1.12; Chapter 1

06/06/2021

RightsLink Printable License

"Reprinted from Publication title, Vol /edition number, Author(s), Title of article / title of chapter, Pages No., Copyright (Year), with permission from Elsevier [OR APPLICABLE SOCIETY COPYRIGHT OWNER]." Also Lancet special credit - "Reprinted from The Lancet, Vol. number, Author(s), Title of article, Pages No., Copyright (Year), with permission from Elsevier."

4. Reproduction of this material is confined to the purpose and/or media for which permission is hereby given.

5. Altering/Modifying Material: Not Permitted. However figures and illustrations may be altered/adapted minimally to serve your work. Any other abbreviations, additions, deletions and/or any other alterations shall be made only with prior written authorization of Elsevier Ltd. (Please contact Elsevier's permissions helpdesk [here](#)). No modifications can be made to any Lancet figures/tables and they must be reproduced in full.

6. If the permission fee for the requested use of our material is waived in this instance, please be advised that your future requests for Elsevier materials may attract a fee.

7. Reservation of Rights: Publisher reserves all rights not specifically granted in the combination of (i) the license details provided by you and accepted in the course of this licensing transaction, (ii) these terms and conditions and (iii) CCC's Billing and Payment terms and conditions.

8. License Contingent Upon Payment: While you may exercise the rights licensed immediately upon issuance of the license at the end of the licensing process for the transaction, provided that you have disclosed complete and accurate details of your proposed use, no license is finally effective unless and until full payment is received from you (either by publisher or by CCC) as provided in CCC's Billing and Payment terms and conditions. If full payment is not received on a timely basis, then any license preliminarily granted shall be deemed automatically revoked and shall be void as if never granted. Further, in the event that you breach any of these terms and conditions or any of CCC's Billing and Payment terms and conditions, the license is automatically revoked and shall be void as if never granted. Use of materials as described in a revoked license, as well as any use of the materials beyond the scope of an unrevoked license, may constitute copyright infringement and publisher reserves the right to take any and all action to protect its copyright in the materials.

9. Warranties: Publisher makes no representations or warranties with respect to the licensed material.

10. Indemnity: You hereby indemnify and agree to hold harmless publisher and CCC, and their respective officers, directors, employees and agents, from and against any and all claims arising out of your use of the licensed material other than as specifically authorized pursuant to this license.

11. No Transfer of License: This license is personal to you and may not be sublicensed, assigned, or transferred by you to any other person without publisher's written permission.

12. No Amendment Except in Writing: This license may not be amended except in a writing signed by both parties (or, in the case of publisher, by CCC on publisher's behalf).

13. Objection to Contrary Terms: Publisher hereby objects to any terms contained in any purchase order, acknowledgment, check endorsement or other writing prepared by you, which terms are inconsistent with these terms and conditions or CCC's Billing and Payment terms and conditions. These terms and conditions, together with CCC's Billing and Payment terms and conditions (which are incorporated herein), comprise the entire agreement between you and publisher (and CCC) concerning this licensing transaction. In the event of any conflict between your obligations established by these terms and conditions and those

Figures 1.11 and 1.12; Chapter 1

06/06/2021

RightsLink Printable License

established by CCC's Billing and Payment terms and conditions, these terms and conditions shall control.

14. **Revocation:** Elsevier or Copyright Clearance Center may deny the permissions described in this License at their sole discretion, for any reason or no reason, with a full refund payable to you. Notice of such denial will be made using the contact information provided by you. Failure to receive such notice will not alter or invalidate the denial. In no event will Elsevier or Copyright Clearance Center be responsible or liable for any costs, expenses or damage incurred by you as a result of a denial of your permission request, other than a refund of the amount(s) paid by you to Elsevier and/or Copyright Clearance Center for denied permissions.

LIMITED LICENSE

The following terms and conditions apply only to specific license types:

15. **Translation:** This permission is granted for non-exclusive world **English** rights only unless your license was granted for translation rights. If you licensed translation rights you may only translate this content into the languages you requested. A professional translator must perform all translations and reproduce the content word for word preserving the integrity of the article.

16. **Posting licensed content on any Website:** The following terms and conditions apply as follows: Licensing material from an Elsevier journal: All content posted to the web site must maintain the copyright information line on the bottom of each image; A hyper-text must be included to the Homepage of the journal from which you are licensing at <http://www.sciencedirect.com/science/journal/xxxxx> or the Elsevier homepage for books at <http://www.elsevier.com>; Central Storage: This license does not include permission for a scanned version of the material to be stored in a central repository such as that provided by Heron/XanEdu.

Licensing material from an Elsevier book: A hyper-text link must be included to the Elsevier homepage at <http://www.elsevier.com>. All content posted to the web site must maintain the copyright information line on the bottom of each image.

Posting licensed content on Electronic reserve: In addition to the above the following clauses are applicable: The web site must be password-protected and made available only to bona fide students registered on a relevant course. This permission is granted for 1 year only. You may obtain a new license for future website posting.

17. **For journal authors:** the following clauses are applicable in addition to the above:

Preprints:

A preprint is an author's own write-up of research results and analysis, it has not been peer-reviewed, nor has it had any other value added to it by a publisher (such as formatting, copyright, technical enhancement etc.).

Authors can share their preprints anywhere at any time. Preprints should not be added to or enhanced in any way in order to appear more like, or to substitute for, the final versions of articles however authors can update their preprints on arXiv or RePEc with their Accepted Author Manuscript (see below).

If accepted for publication, we encourage authors to link from the preprint to their formal publication via its DOI. Millions of researchers have access to the formal publications on ScienceDirect, and so links will help users to find, access, cite and use the best available version. Please note that Cell Press, The Lancet and some society-owned have different preprint policies. Information on these policies is available on the journal homepage.

Figures 1.11 and 1.12; Chapter 1

06/06/2021

RightsLink Printable License

Accepted Author Manuscripts: An accepted author manuscript is the manuscript of an article that has been accepted for publication and which typically includes author-incorporated changes suggested during submission, peer review and editor-author communications.

Authors can share their accepted author manuscript:

- immediately
 - via their non-commercial person homepage or blog
 - by updating a preprint in arXiv or RePEc with the accepted manuscript
 - via their research institute or institutional repository for internal institutional uses or as part of an invitation-only research collaboration work-group
 - directly by providing copies to their students or to research collaborators for their personal use
 - for private scholarly sharing as part of an invitation-only work group on commercial sites with which Elsevier has an agreement
- After the embargo period
 - via non-commercial hosting platforms such as their institutional repository
 - via commercial sites with which Elsevier has an agreement

In all cases accepted manuscripts should:

- link to the formal publication via its DOI
- bear a CC-BY-NC-ND license - this is easy to do
- if aggregated with other manuscripts, for example in a repository or other site, be shared in alignment with our hosting policy not be added to or enhanced in any way to appear more like, or to substitute for, the published journal article.

Published journal article (JPA): A published journal article (PJA) is the definitive final record of published research that appears or will appear in the journal and embodies all value-adding publishing activities including peer review co-ordination, copy-editing, formatting, (if relevant) pagination and online enrichment.

Policies for sharing publishing journal articles differ for subscription and gold open access articles:

Subscription Articles: If you are an author, please share a link to your article rather than the full-text. Millions of researchers have access to the formal publications on ScienceDirect, and so links will help your users to find, access, cite, and use the best available version.

Theses and dissertations which contain embedded PJAs as part of the formal submission can be posted publicly by the awarding institution with DOI links back to the formal publications on ScienceDirect.

If you are affiliated with a library that subscribes to ScienceDirect you have additional private sharing rights for others' research accessed under that agreement. This includes use for classroom teaching and internal training at the institution (including use in course packs and courseware programs), and inclusion of the article for grant funding purposes.

Gold Open Access Articles: May be shared according to the author-selected end-user license and should contain a [CrossMark logo](#), the end user license, and a DOI link to the formal publication on ScienceDirect.

Please refer to Elsevier's [posting policy](#) for further information.

18. **For book authors** the following clauses are applicable in addition to the above: Authors are permitted to place a brief summary of their work online only. You are not allowed to download and post the published electronic version of your chapter, nor may you

Figures 1.11 and 1.12; Chapter 1

06/06/2021

RightsLink Printable License

scan the printed edition to create an electronic version. **Posting to a repository:** Authors are permitted to post a summary of their chapter only in their institution's repository.

19. Thesis/Dissertation: If your license is for use in a thesis/dissertation your thesis may be submitted to your institution in either print or electronic form. Should your thesis be published commercially, please reapply for permission. These requirements include permission for the Library and Archives of Canada to supply single copies, on demand, of the complete thesis and include permission for Proquest/UMI to supply single copies, on demand, of the complete thesis. Should your thesis be published commercially, please reapply for permission. Theses and dissertations which contain embedded PJAs as part of the formal submission can be posted publicly by the awarding institution with DOI links back to the formal publications on ScienceDirect.

Elsevier Open Access Terms and Conditions

You can publish open access with Elsevier in hundreds of open access journals or in nearly 2000 established subscription journals that support open access publishing. Permitted third party re-use of these open access articles is defined by the author's choice of Creative Commons user license. See our [open access license policy](#) for more information.

Terms & Conditions applicable to all Open Access articles published with Elsevier:

Any reuse of the article must not represent the author as endorsing the adaptation of the article nor should the article be modified in such a way as to damage the author's honour or reputation. If any changes have been made, such changes must be clearly indicated.

The author(s) must be appropriately credited and we ask that you include the end user license and a DOI link to the formal publication on ScienceDirect.

If any part of the material to be used (for example, figures) has appeared in our publication with credit or acknowledgement to another source it is the responsibility of the user to ensure their reuse complies with the terms and conditions determined by the rights holder.

Additional Terms & Conditions applicable to each Creative Commons user license:

CC BY: The CC-BY license allows users to copy, to create extracts, abstracts and new works from the Article, to alter and revise the Article and to make commercial use of the Article (including reuse and/or resale of the Article by commercial entities), provided the user gives appropriate credit (with a link to the formal publication through the relevant DOI), provides a link to the license, indicates if changes were made and the licensor is not represented as endorsing the use made of the work. The full details of the license are available at <http://creativecommons.org/licenses/by/4.0>.

CC BY NC SA: The CC BY-NC-SA license allows users to copy, to create extracts, abstracts and new works from the Article, to alter and revise the Article, provided this is not done for commercial purposes, and that the user gives appropriate credit (with a link to the formal publication through the relevant DOI), provides a link to the license, indicates if changes were made and the licensor is not represented as endorsing the use made of the work. Further, any new works must be made available on the same conditions. The full details of the license are available at <http://creativecommons.org/licenses/by-nc-sa/4.0>.

CC BY NC ND: The CC BY-NC-ND license allows users to copy and distribute the Article, provided this is not done for commercial purposes and further does not permit distribution of the Article if it is changed or edited in any way, and provided the user gives appropriate credit (with a link to the formal publication through the relevant DOI), provides a link to the license, and that the licensor is not represented as endorsing the use made of the work. The full details of the license are available at <http://creativecommons.org/licenses/by-nc-nd/4.0>.

Figures 1.11 and 1.12; Chapter 1

06/06/2021

RightsLink Printable License

Any commercial reuse of Open Access articles published with a CC BY NC SA or CC BY NC ND license requires permission from Elsevier and will be subject to a fee.

Commercial reuse includes:

- Associating advertising with the full text of the Article
- Charging fees for document delivery or access
- Article aggregation
- Systematic distribution via e-mail lists or share buttons

Posting or linking by commercial companies for use by customers of those companies.

20. Other Conditions:

v1.10

Questions? customercare@copyright.com or +1-855-239-3415 (toll free in the US) or +1-978-646-2777.

Figures 1.15 and 1.16; Chapter 1

06/06/2021

RightsLink Printable License

ELSEVIER LICENSE TERMS AND CONDITIONS

Jun 06, 2021

This Agreement between Mustafa Hamad ("You") and Elsevier ("Elsevier") consists of your license details and the terms and conditions provided by Elsevier and Copyright Clearance Center.

License Number	5082880245487
License date	Jun 06, 2021
Licensed Content Publisher	Elsevier
Licensed Content Publication	Elsevier Books
Licensed Content Title	Introduction to Dislocations
Licensed Content Author	D. Hull,D.J. Bacon
Licensed Content Date	Jan 1, 2011
Licensed Content Pages	23
Start Page	85
End Page	107
Type of Use	reuse in a thesis/dissertation
Portion	figures/tables/illustrations
Number of figures/tables/illustrations	2
Format	both print and electronic

<https://s100.copyright.com/CustomAdmin/PLF.jsp?ref=0e9478b0-1369-41b5-bfb0-72f1bc9f31a4>

1/7

Figures 1.15 and 1.16; Chapter 1

06/06/2021

RightsLink Printable License

Are you the author of this Elsevier chapter? No

Will you be translating? No

Title In silico prediction of the physical performance of pharmaceutical crystals

Institution name Curtin University

Expected presentation date Jul 2021

Portions Figure 5.3 / page 87 Figure 5.4 / page 88

Requestor Location
Mustafa Hamad
Kent Street
Bentley
Perth, WA 6102
Australia
Attn: Mustafa Hamad

Publisher Tax ID GB 494 6272 12

Total 0.00 USD

Terms and Conditions

INTRODUCTION

1. The publisher for this copyrighted material is Elsevier. By clicking "accept" in connection with completing this licensing transaction, you agree that the following terms and conditions apply to this transaction (along with the Billing and Payment terms and conditions established by Copyright Clearance Center, Inc. ("CCC"), at the time that you opened your Rightslink account and that are available at any time at <http://myaccount.copyright.com>).

GENERAL TERMS

2. Elsevier hereby grants you permission to reproduce the aforementioned material subject to the terms and conditions indicated.

3. Acknowledgement: If any part of the material to be used (for example, figures) has appeared in our publication with credit or acknowledgement to another source, permission must also be sought from that source. If such permission is not obtained then that material may not be included in your publication/copies. Suitable acknowledgement to the source must be made, either as a footnote or in a reference list at the end of your publication, as follows:

Figures 1.15 and 1.16; Chapter 1

06/06/2021

RightsLink Printable License

"Reprinted from Publication title, Vol /edition number, Author(s), Title of article / title of chapter, Pages No., Copyright (Year), with permission from Elsevier [OR APPLICABLE SOCIETY COPYRIGHT OWNER]." Also Lancet special credit - "Reprinted from The Lancet, Vol. number, Author(s), Title of article, Pages No., Copyright (Year), with permission from Elsevier."

4. Reproduction of this material is confined to the purpose and/or media for which permission is hereby given.

5. Altering/Modifying Material: Not Permitted. However figures and illustrations may be altered/adapted minimally to serve your work. Any other abbreviations, additions, deletions and/or any other alterations shall be made only with prior written authorization of Elsevier Ltd. (Please contact Elsevier's permissions helpdesk [here](#)). No modifications can be made to any Lancet figures/tables and they must be reproduced in full.

6. If the permission fee for the requested use of our material is waived in this instance, please be advised that your future requests for Elsevier materials may attract a fee.

7. Reservation of Rights: Publisher reserves all rights not specifically granted in the combination of (i) the license details provided by you and accepted in the course of this licensing transaction, (ii) these terms and conditions and (iii) CCC's Billing and Payment terms and conditions.

8. License Contingent Upon Payment: While you may exercise the rights licensed immediately upon issuance of the license at the end of the licensing process for the transaction, provided that you have disclosed complete and accurate details of your proposed use, no license is finally effective unless and until full payment is received from you (either by publisher or by CCC) as provided in CCC's Billing and Payment terms and conditions. If full payment is not received on a timely basis, then any license preliminarily granted shall be deemed automatically revoked and shall be void as if never granted. Further, in the event that you breach any of these terms and conditions or any of CCC's Billing and Payment terms and conditions, the license is automatically revoked and shall be void as if never granted. Use of materials as described in a revoked license, as well as any use of the materials beyond the scope of an unrevoked license, may constitute copyright infringement and publisher reserves the right to take any and all action to protect its copyright in the materials.

9. Warranties: Publisher makes no representations or warranties with respect to the licensed material.

10. Indemnity: You hereby indemnify and agree to hold harmless publisher and CCC, and their respective officers, directors, employees and agents, from and against any and all claims arising out of your use of the licensed material other than as specifically authorized pursuant to this license.

11. No Transfer of License: This license is personal to you and may not be sublicensed, assigned, or transferred by you to any other person without publisher's written permission.

12. No Amendment Except in Writing: This license may not be amended except in a writing signed by both parties (or, in the case of publisher, by CCC on publisher's behalf).

13. Objection to Contrary Terms: Publisher hereby objects to any terms contained in any purchase order, acknowledgment, check endorsement or other writing prepared by you, which terms are inconsistent with these terms and conditions or CCC's Billing and Payment terms and conditions. These terms and conditions, together with CCC's Billing and Payment terms and conditions (which are incorporated herein), comprise the entire agreement between you and publisher (and CCC) concerning this licensing transaction. In the event of any conflict between your obligations established by these terms and conditions and those

Figures 1.15 and 1.16; Chapter 1

06/06/2021

RightsLink Printable License

established by CCC's Billing and Payment terms and conditions, these terms and conditions shall control.

14. **Revocation:** Elsevier or Copyright Clearance Center may deny the permissions described in this License at their sole discretion, for any reason or no reason, with a full refund payable to you. Notice of such denial will be made using the contact information provided by you. Failure to receive such notice will not alter or invalidate the denial. In no event will Elsevier or Copyright Clearance Center be responsible or liable for any costs, expenses or damage incurred by you as a result of a denial of your permission request, other than a refund of the amount(s) paid by you to Elsevier and/or Copyright Clearance Center for denied permissions.

LIMITED LICENSE

The following terms and conditions apply only to specific license types:

15. **Translation:** This permission is granted for non-exclusive world **English** rights only unless your license was granted for translation rights. If you licensed translation rights you may only translate this content into the languages you requested. A professional translator must perform all translations and reproduce the content word for word preserving the integrity of the article.

16. **Posting licensed content on any Website:** The following terms and conditions apply as follows: Licensing material from an Elsevier journal: All content posted to the web site must maintain the copyright information line on the bottom of each image; A hyper-text must be included to the Homepage of the journal from which you are licensing at <http://www.sciencedirect.com/science/journal/xxxxx> or the Elsevier homepage for books at <http://www.elsevier.com>; Central Storage: This license does not include permission for a scanned version of the material to be stored in a central repository such as that provided by Heron/XanEdu.

Licensing material from an Elsevier book: A hyper-text link must be included to the Elsevier homepage at <http://www.elsevier.com>. All content posted to the web site must maintain the copyright information line on the bottom of each image.

Posting licensed content on Electronic reserve: In addition to the above the following clauses are applicable: The web site must be password-protected and made available only to bona fide students registered on a relevant course. This permission is granted for 1 year only. You may obtain a new license for future website posting.

17. **For journal authors:** the following clauses are applicable in addition to the above:

Preprints:

A preprint is an author's own write-up of research results and analysis, it has not been peer-reviewed, nor has it had any other value added to it by a publisher (such as formatting, copyright, technical enhancement etc.).

Authors can share their preprints anywhere at any time. Preprints should not be added to or enhanced in any way in order to appear more like, or to substitute for, the final versions of articles however authors can update their preprints on arXiv or RePEc with their Accepted Author Manuscript (see below).

If accepted for publication, we encourage authors to link from the preprint to their formal publication via its DOI. Millions of researchers have access to the formal publications on ScienceDirect, and so links will help users to find, access, cite and use the best available version. Please note that Cell Press, The Lancet and some society-owned have different preprint policies. Information on these policies is available on the journal homepage.

Figures 1.15 and 1.16; Chapter 1

06/06/2021

RightsLink Printable License

Accepted Author Manuscripts: An accepted author manuscript is the manuscript of an article that has been accepted for publication and which typically includes author-incorporated changes suggested during submission, peer review and editor-author communications.

Authors can share their accepted author manuscript:

- immediately
 - via their non-commercial person homepage or blog
 - by updating a preprint in arXiv or RePEc with the accepted manuscript
 - via their research institute or institutional repository for internal institutional uses or as part of an invitation-only research collaboration work-group
 - directly by providing copies to their students or to research collaborators for their personal use
 - for private scholarly sharing as part of an invitation-only work group on commercial sites with which Elsevier has an agreement
- After the embargo period
 - via non-commercial hosting platforms such as their institutional repository
 - via commercial sites with which Elsevier has an agreement

In all cases accepted manuscripts should:

- link to the formal publication via its DOI
- bear a CC-BY-NC-ND license - this is easy to do
- if aggregated with other manuscripts, for example in a repository or other site, be shared in alignment with our hosting policy not be added to or enhanced in any way to appear more like, or to substitute for, the published journal article.

Published journal article (JPA): A published journal article (PJA) is the definitive final record of published research that appears or will appear in the journal and embodies all value-adding publishing activities including peer review co-ordination, copy-editing, formatting, (if relevant) pagination and online enrichment.

Policies for sharing publishing journal articles differ for subscription and gold open access articles:

Subscription Articles: If you are an author, please share a link to your article rather than the full-text. Millions of researchers have access to the formal publications on ScienceDirect, and so links will help your users to find, access, cite, and use the best available version.

Theses and dissertations which contain embedded PJAs as part of the formal submission can be posted publicly by the awarding institution with DOI links back to the formal publications on ScienceDirect.

If you are affiliated with a library that subscribes to ScienceDirect you have additional private sharing rights for others' research accessed under that agreement. This includes use for classroom teaching and internal training at the institution (including use in course packs and courseware programs), and inclusion of the article for grant funding purposes.

Gold Open Access Articles: May be shared according to the author-selected end-user license and should contain a [CrossMark logo](#), the end user license, and a DOI link to the formal publication on ScienceDirect.

Please refer to Elsevier's [posting policy](#) for further information.

18. **For book authors** the following clauses are applicable in addition to the above: Authors are permitted to place a brief summary of their work online only. You are not allowed to download and post the published electronic version of your chapter, nor may you

Figures 1.15 and 1.16; Chapter 1

06/06/2021

RightsLink Printable License

scan the printed edition to create an electronic version. **Posting to a repository:** Authors are permitted to post a summary of their chapter only in their institution's repository.

19. Thesis/Dissertation: If your license is for use in a thesis/dissertation your thesis may be submitted to your institution in either print or electronic form. Should your thesis be published commercially, please reapply for permission. These requirements include permission for the Library and Archives of Canada to supply single copies, on demand, of the complete thesis and include permission for Proquest/UMI to supply single copies, on demand, of the complete thesis. Should your thesis be published commercially, please reapply for permission. Theses and dissertations which contain embedded PJAs as part of the formal submission can be posted publicly by the awarding institution with DOI links back to the formal publications on ScienceDirect.

Elsevier Open Access Terms and Conditions

You can publish open access with Elsevier in hundreds of open access journals or in nearly 2000 established subscription journals that support open access publishing. Permitted third party re-use of these open access articles is defined by the author's choice of Creative Commons user license. See our [open access license policy](#) for more information.

Terms & Conditions applicable to all Open Access articles published with Elsevier:

Any reuse of the article must not represent the author as endorsing the adaptation of the article nor should the article be modified in such a way as to damage the author's honour or reputation. If any changes have been made, such changes must be clearly indicated.

The author(s) must be appropriately credited and we ask that you include the end user license and a DOI link to the formal publication on ScienceDirect.

If any part of the material to be used (for example, figures) has appeared in our publication with credit or acknowledgement to another source it is the responsibility of the user to ensure their reuse complies with the terms and conditions determined by the rights holder.

Additional Terms & Conditions applicable to each Creative Commons user license:

CC BY: The CC-BY license allows users to copy, to create extracts, abstracts and new works from the Article, to alter and revise the Article and to make commercial use of the Article (including reuse and/or resale of the Article by commercial entities), provided the user gives appropriate credit (with a link to the formal publication through the relevant DOI), provides a link to the license, indicates if changes were made and the licensor is not represented as endorsing the use made of the work. The full details of the license are available at <http://creativecommons.org/licenses/by/4.0>.

CC BY NC SA: The CC BY-NC-SA license allows users to copy, to create extracts, abstracts and new works from the Article, to alter and revise the Article, provided this is not done for commercial purposes, and that the user gives appropriate credit (with a link to the formal publication through the relevant DOI), provides a link to the license, indicates if changes were made and the licensor is not represented as endorsing the use made of the work. Further, any new works must be made available on the same conditions. The full details of the license are available at <http://creativecommons.org/licenses/by-nc-sa/4.0>.

CC BY NC ND: The CC BY-NC-ND license allows users to copy and distribute the Article, provided this is not done for commercial purposes and further does not permit distribution of the Article if it is changed or edited in any way, and provided the user gives appropriate credit (with a link to the formal publication through the relevant DOI), provides a link to the license, and that the licensor is not represented as endorsing the use made of the work. The full details of the license are available at <http://creativecommons.org/licenses/by-nc-nd/4.0>.

Figures 1.15 and 1.16; Chapter 1

06/06/2021

RightsLink Printable License

Any commercial reuse of Open Access articles published with a CC BY NC SA or CC BY NC ND license requires permission from Elsevier and will be subject to a fee.

Commercial reuse includes:

- Associating advertising with the full text of the Article
- Charging fees for document delivery or access
- Article aggregation
- Systematic distribution via e-mail lists or share buttons

Posting or linking by commercial companies for use by customers of those companies.

20. Other Conditions:

v1.10

Questions? customercare@copyright.com or +1-855-239-3415 (toll free in the US) or +1-978-646-2777.

Figures 1.17 and 1.18; Chapter 1

06/06/2021

RightsLink Printable License

ELSEVIER LICENSE TERMS AND CONDITIONS

Jun 06, 2021

This Agreement between Mustafa Hamad ("You") and Elsevier ("Elsevier") consists of your license details and the terms and conditions provided by Elsevier and Copyright Clearance Center.

License Number	5082880551861
License date	Jun 06, 2021
Licensed Content Publisher	Elsevier
Licensed Content Publication	Acta Materialia
Licensed Content Title	Sample shape and temperature strongly influence the yield strength of metallic nanopillars
Licensed Content Author	Ajing Cao,E. Ma
Licensed Content Date	Oct 1, 2008
Licensed Content Volume	56
Licensed Content Issue	17
Licensed Content Pages	13
Start Page	4816
End Page	4828
Type of Use	reuse in a thesis/dissertation
Portion	figures/tables/illustrations

<https://s100.copyright.com/CustomAdmin/PLF.jsp?ref=79b753bd-2e8f-49c3-afef-727541c711e4>

1/7

Figures 1.17 and 1.18; Chapter 1

06/06/2021

RightsLink Printable License

Number of figures/tables/illustrations	2
Format	both print and electronic
Are you the author of this Elsevier article?	No
Will you be translating?	No
Title	In silico prediction of the physical performance of pharmaceutical crystals
Institution name	Curtin University
Expected presentation date	Jul 2021
Portions	Figure 6 / page 4882 Figure 8 / page 4883
Requestor Location	Mustafa Hamad Kent Street Bentley Perth, WA 6102 Australia Attn: Mustafa Hamad
Publisher Tax ID	GB 494 6272 12
Total	0.00 USD
Terms and Conditions	

INTRODUCTION

1. The publisher for this copyrighted material is Elsevier. By clicking "accept" in connection with completing this licensing transaction, you agree that the following terms and conditions apply to this transaction (along with the Billing and Payment terms and conditions established by Copyright Clearance Center, Inc. ("CCC"), at the time that you opened your Rightslink account and that are available at any time at <http://myaccount.copyright.com>).

GENERAL TERMS

2. Elsevier hereby grants you permission to reproduce the aforementioned material subject to the terms and conditions indicated.

<https://s100.copyright.com/CustomerAdmin/PLF.jsp?ref=79b753bd-2e8f-49c3-afef-727541c711e4>

2/7

Figures 1.17 and 1.18; Chapter 1

06/06/2021

RightsLink Printable License

3. Acknowledgement: If any part of the material to be used (for example, figures) has appeared in our publication with credit or acknowledgement to another source, permission must also be sought from that source. If such permission is not obtained then that material may not be included in your publication/copies. Suitable acknowledgement to the source must be made, either as a footnote or in a reference list at the end of your publication, as follows:

"Reprinted from Publication title, Vol /edition number, Author(s), Title of article / title of chapter, Pages No., Copyright (Year), with permission from Elsevier [OR APPLICABLE SOCIETY COPYRIGHT OWNER]." Also Lancet special credit - "Reprinted from The Lancet, Vol. number, Author(s), Title of article, Pages No., Copyright (Year), with permission from Elsevier."

4. Reproduction of this material is confined to the purpose and/or media for which permission is hereby given.

5. Altering/Modifying Material: Not Permitted. However figures and illustrations may be altered/adapted minimally to serve your work. Any other abbreviations, additions, deletions and/or any other alterations shall be made only with prior written authorization of Elsevier Ltd. (Please contact Elsevier's permissions helpdesk [here](#)). No modifications can be made to any Lancet figures/tables and they must be reproduced in full.

6. If the permission fee for the requested use of our material is waived in this instance, please be advised that your future requests for Elsevier materials may attract a fee.

7. Reservation of Rights: Publisher reserves all rights not specifically granted in the combination of (i) the license details provided by you and accepted in the course of this licensing transaction, (ii) these terms and conditions and (iii) CCC's Billing and Payment terms and conditions.

8. License Contingent Upon Payment: While you may exercise the rights licensed immediately upon issuance of the license at the end of the licensing process for the transaction, provided that you have disclosed complete and accurate details of your proposed use, no license is finally effective unless and until full payment is received from you (either by publisher or by CCC) as provided in CCC's Billing and Payment terms and conditions. If full payment is not received on a timely basis, then any license preliminarily granted shall be deemed automatically revoked and shall be void as if never granted. Further, in the event that you breach any of these terms and conditions or any of CCC's Billing and Payment terms and conditions, the license is automatically revoked and shall be void as if never granted. Use of materials as described in a revoked license, as well as any use of the materials beyond the scope of an unrevoked license, may constitute copyright infringement and publisher reserves the right to take any and all action to protect its copyright in the materials.

9. Warranties: Publisher makes no representations or warranties with respect to the licensed material.

10. Indemnity: You hereby indemnify and agree to hold harmless publisher and CCC, and their respective officers, directors, employees and agents, from and against any and all claims arising out of your use of the licensed material other than as specifically authorized pursuant to this license.

11. No Transfer of License: This license is personal to you and may not be sublicensed, assigned, or transferred by you to any other person without publisher's written permission.

12. No Amendment Except in Writing: This license may not be amended except in a writing signed by both parties (or, in the case of publisher, by CCC on publisher's behalf).

Figures 1.17 and 1.18; Chapter 1

06/06/2021

RightsLink Printable License

13. **Objection to Contrary Terms:** Publisher hereby objects to any terms contained in any purchase order, acknowledgment, check endorsement or other writing prepared by you, which terms are inconsistent with these terms and conditions or CCC's Billing and Payment terms and conditions. These terms and conditions, together with CCC's Billing and Payment terms and conditions (which are incorporated herein), comprise the entire agreement between you and publisher (and CCC) concerning this licensing transaction. In the event of any conflict between your obligations established by these terms and conditions and those established by CCC's Billing and Payment terms and conditions, these terms and conditions shall control.

14. **Revocation:** Elsevier or Copyright Clearance Center may deny the permissions described in this License at their sole discretion, for any reason or no reason, with a full refund payable to you. Notice of such denial will be made using the contact information provided by you. Failure to receive such notice will not alter or invalidate the denial. In no event will Elsevier or Copyright Clearance Center be responsible or liable for any costs, expenses or damage incurred by you as a result of a denial of your permission request, other than a refund of the amount(s) paid by you to Elsevier and/or Copyright Clearance Center for denied permissions.

LIMITED LICENSE

The following terms and conditions apply only to specific license types:

15. **Translation:** This permission is granted for non-exclusive world **English** rights only unless your license was granted for translation rights. If you licensed translation rights you may only translate this content into the languages you requested. A professional translator must perform all translations and reproduce the content word for word preserving the integrity of the article.

16. **Posting licensed content on any Website:** The following terms and conditions apply as follows: Licensing material from an Elsevier journal: All content posted to the web site must maintain the copyright information line on the bottom of each image; A hyper-text must be included to the Homepage of the journal from which you are licensing at <http://www.sciencedirect.com/science/journal/xxxxx> or the Elsevier homepage for books at <http://www.elsevier.com>; Central Storage: This license does not include permission for a scanned version of the material to be stored in a central repository such as that provided by Heron/XanEdu.

Licensing material from an Elsevier book: A hyper-text link must be included to the Elsevier homepage at <http://www.elsevier.com>. All content posted to the web site must maintain the copyright information line on the bottom of each image.

Posting licensed content on Electronic reserve: In addition to the above the following clauses are applicable: The web site must be password-protected and made available only to bona fide students registered on a relevant course. This permission is granted for 1 year only. You may obtain a new license for future website posting.

17. **For journal authors:** the following clauses are applicable in addition to the above:

Preprints:

A preprint is an author's own write-up of research results and analysis, it has not been peer-reviewed, nor has it had any other value added to it by a publisher (such as formatting, copyright, technical enhancement etc.).

Authors can share their preprints anywhere at any time. Preprints should not be added to or enhanced in any way in order to appear more like, or to substitute for, the final versions of

Figures 1.17 and 1.18; Chapter 1

06/06/2021

RightsLink Printable License

articles however authors can update their preprints on arXiv or RePEc with their Accepted Author Manuscript (see below).

If accepted for publication, we encourage authors to link from the preprint to their formal publication via its DOI. Millions of researchers have access to the formal publications on ScienceDirect, and so links will help users to find, access, cite and use the best available version. Please note that Cell Press, The Lancet and some society-owned have different preprint policies. Information on these policies is available on the journal homepage.

Accepted Author Manuscripts: An accepted author manuscript is the manuscript of an article that has been accepted for publication and which typically includes author-incorporated changes suggested during submission, peer review and editor-author communications.

Authors can share their accepted author manuscript:

- immediately
 - via their non-commercial person homepage or blog
 - by updating a preprint in arXiv or RePEc with the accepted manuscript
 - via their research institute or institutional repository for internal institutional uses or as part of an invitation-only research collaboration work-group
 - directly by providing copies to their students or to research collaborators for their personal use
 - for private scholarly sharing as part of an invitation-only work group on commercial sites with which Elsevier has an agreement
- After the embargo period
 - via non-commercial hosting platforms such as their institutional repository
 - via commercial sites with which Elsevier has an agreement

In all cases accepted manuscripts should:

- link to the formal publication via its DOI
- bear a CC-BY-NC-ND license - this is easy to do
- if aggregated with other manuscripts, for example in a repository or other site, be shared in alignment with our hosting policy not be added to or enhanced in any way to appear more like, or to substitute for, the published journal article.

Published journal article (JPA): A published journal article (PJA) is the definitive final record of published research that appears or will appear in the journal and embodies all value-adding publishing activities including peer review co-ordination, copy-editing, formatting, (if relevant) pagination and online enrichment.

Policies for sharing publishing journal articles differ for subscription and gold open access articles:

Subscription Articles: If you are an author, please share a link to your article rather than the full-text. Millions of researchers have access to the formal publications on ScienceDirect, and so links will help your users to find, access, cite, and use the best available version.

Theses and dissertations which contain embedded PJAs as part of the formal submission can be posted publicly by the awarding institution with DOI links back to the formal publications on ScienceDirect.

If you are affiliated with a library that subscribes to ScienceDirect you have additional private sharing rights for others' research accessed under that agreement. This includes use for classroom teaching and internal training at the institution (including use in course packs and courseware programs), and inclusion of the article for grant funding purposes.

Figures 1.17 and 1.18; Chapter 1

06/06/2021

RightsLink Printable License

Gold Open Access Articles: May be shared according to the author-selected end-user license and should contain a [CrossMark logo](#), the end user license, and a DOI link to the formal publication on ScienceDirect.

Please refer to Elsevier's [posting policy](#) for further information.

18. For book authors the following clauses are applicable in addition to the above: Authors are permitted to place a brief summary of their work online only. You are not allowed to download and post the published electronic version of your chapter, nor may you scan the printed edition to create an electronic version. **Posting to a repository:** Authors are permitted to post a summary of their chapter only in their institution's repository.

19. Thesis/Dissertation: If your license is for use in a thesis/dissertation your thesis may be submitted to your institution in either print or electronic form. Should your thesis be published commercially, please reapply for permission. These requirements include permission for the Library and Archives of Canada to supply single copies, on demand, of the complete thesis and include permission for Proquest/UMI to supply single copies, on demand, of the complete thesis. Should your thesis be published commercially, please reapply for permission. Theses and dissertations which contain embedded PJAs as part of the formal submission can be posted publicly by the awarding institution with DOI links back to the formal publications on ScienceDirect.

Elsevier Open Access Terms and Conditions

You can publish open access with Elsevier in hundreds of open access journals or in nearly 2000 established subscription journals that support open access publishing. Permitted third party re-use of these open access articles is defined by the author's choice of Creative Commons user license. See our [open access license policy](#) for more information.

Terms & Conditions applicable to all Open Access articles published with Elsevier:

Any reuse of the article must not represent the author as endorsing the adaptation of the article nor should the article be modified in such a way as to damage the author's honour or reputation. If any changes have been made, such changes must be clearly indicated.

The author(s) must be appropriately credited and we ask that you include the end user license and a DOI link to the formal publication on ScienceDirect.

If any part of the material to be used (for example, figures) has appeared in our publication with credit or acknowledgement to another source it is the responsibility of the user to ensure their reuse complies with the terms and conditions determined by the rights holder.

Additional Terms & Conditions applicable to each Creative Commons user license:

CC BY: The CC-BY license allows users to copy, to create extracts, abstracts and new works from the Article, to alter and revise the Article and to make commercial use of the Article (including reuse and/or resale of the Article by commercial entities), provided the user gives appropriate credit (with a link to the formal publication through the relevant DOI), provides a link to the license, indicates if changes were made and the licensor is not represented as endorsing the use made of the work. The full details of the license are available at <http://creativecommons.org/licenses/by/4.0>.

CC BY NC SA: The CC BY-NC-SA license allows users to copy, to create extracts, abstracts and new works from the Article, to alter and revise the Article, provided this is not done for commercial purposes, and that the user gives appropriate credit (with a link to the formal publication through the relevant DOI), provides a link to the license, indicates if changes were made and the licensor is not represented as endorsing the use made of the

Figures 1.17 and 1.18; Chapter 1

06/06/2021

RightsLink Printable License

work. Further, any new works must be made available on the same conditions. The full details of the license are available at <http://creativecommons.org/licenses/by-nc-sa/4.0>.

CC BY NC ND: The CC BY-NC-ND license allows users to copy and distribute the Article, provided this is not done for commercial purposes and further does not permit distribution of the Article if it is changed or edited in any way, and provided the user gives appropriate credit (with a link to the formal publication through the relevant DOI), provides a link to the license, and that the licensor is not represented as endorsing the use made of the work. The full details of the license are available at <http://creativecommons.org/licenses/by-nc-nd/4.0>. Any commercial reuse of Open Access articles published with a CC BY NC SA or CC BY NC ND license requires permission from Elsevier and will be subject to a fee.

Commercial reuse includes:

- Associating advertising with the full text of the Article
- Charging fees for document delivery or access
- Article aggregation
- Systematic distribution via e-mail lists or share buttons

Posting or linking by commercial companies for use by customers of those companies.

20. Other Conditions:

v1.10

Questions? customercare@copyright.com or +1-855-239-3415 (toll free in the US) or +1-978-646-2777.

Figure 1.20; Chapter 1

06/06/2021

RightsLink Printable License

JOHN WILEY AND SONS LICENSE TERMS AND CONDITIONS

Jun 06, 2021

This Agreement between Mustafa Hamad ("You") and John Wiley and Sons ("John Wiley and Sons") consists of your license details and the terms and conditions provided by John Wiley and Sons and Copyright Clearance Center.

License Number	5082880809343
License date	Jun 06, 2021
Licensed Content Publisher	John Wiley and Sons
Licensed Content Publication	Angewandte Chemie International Edition
Licensed Content Title	Superelastic Shape Recovery of Mechanically Twinned 3,5-Difluorobenzoic Acid Crystals
Licensed Content Author	Yuichi Takasaki, Satoshi Takamizawa
Licensed Content Date	Feb 23, 2015
Licensed Content Volume	54
Licensed Content Issue	16
Licensed Content Pages	3
Type of use	Dissertation/Thesis
Requestor type	University/Academic

<https://s100.copyright.com/CustomAdmin/PLF.jsp?ref=2ec92cc8-837c-4d0f-ae7d-96dc56f8ccc1>

1/6

Figure 1.20; Chapter 1

06/06/2021

RightsLink Printable License

Format	Print and electronic
Portion	Figure/table
Number of figures/tables	1
Will you be translating?	No
Title	In silico prediction of the physical performance of pharmaceutical crystals
Institution name	Curtin University
Expected presentation date	Jul 2021
Portions	Figure 1 / page 4815
Requestor Location	Mustafa Hamad Kent Street Bentley Perth, WA 6102 Australia Attn: Mustafa Hamad
Publisher Tax ID	EU826007151
Total	0.00 USD

Terms and Conditions

TERMS AND CONDITIONS

This copyrighted material is owned by or exclusively licensed to John Wiley & Sons, Inc. or one of its group companies (each a "Wiley Company") or handled on behalf of a society with which a Wiley Company has exclusive publishing rights in relation to a particular work (collectively "WILEY"). By clicking "accept" in connection with completing this licensing transaction, you agree that the following terms and conditions apply to this transaction (along with the billing and payment terms and conditions established by the Copyright Clearance Center Inc., ("CCC's Billing and Payment terms and conditions"), at the time that

Figure 1.20; Chapter 1

06/06/2021

RightsLink Printable License

you opened your RightsLink account (these are available at any time at <http://myaccount.copyright.com>).

Terms and Conditions

- The materials you have requested permission to reproduce or reuse (the "Wiley Materials") are protected by copyright.
- You are hereby granted a personal, non-exclusive, non-sub licensable (on a stand-alone basis), non-transferable, worldwide, limited license to reproduce the Wiley Materials for the purpose specified in the licensing process. This license, **and any CONTENT (PDF or image file) purchased as part of your order**, is for a one-time use only and limited to any maximum distribution number specified in the license. The first instance of republication or reuse granted by this license must be completed within two years of the date of the grant of this license (although copies prepared before the end date may be distributed thereafter). The Wiley Materials shall not be used in any other manner or for any other purpose, beyond what is granted in the license. Permission is granted subject to an appropriate acknowledgement given to the author, title of the material/book/journal and the publisher. You shall also duplicate the copyright notice that appears in the Wiley publication in your use of the Wiley Material. Permission is also granted on the understanding that nowhere in the text is a previously published source acknowledged for all or part of this Wiley Material. Any third party content is expressly excluded from this permission.
- With respect to the Wiley Materials, all rights are reserved. Except as expressly granted by the terms of the license, no part of the Wiley Materials may be copied, modified, adapted (except for minor reformatting required by the new Publication), translated, reproduced, transferred or distributed, in any form or by any means, and no derivative works may be made based on the Wiley Materials without the prior permission of the respective copyright owner. **For STM Signatory Publishers clearing permission under the terms of the [STM Permissions Guidelines](#) only, the terms of the license are extended to include subsequent editions and for editions in other languages, provided such editions are for the work as a whole in situ and does not involve the separate exploitation of the permitted figures or extracts**, You may not alter, remove or suppress in any manner any copyright, trademark or other notices displayed by the Wiley Materials. You may not license, rent, sell, loan, lease, pledge, offer as security, transfer or assign the Wiley Materials on a stand-alone basis, or any of the rights granted to you hereunder to any other person.
- The Wiley Materials and all of the intellectual property rights therein shall at all times remain the exclusive property of John Wiley & Sons Inc, the Wiley Companies, or their respective licensors, and your interest therein is only that of having possession of and the right to reproduce the Wiley Materials pursuant to Section 2 herein during the continuance of this Agreement. You agree that you own no right, title or interest in or to the Wiley Materials or any of the intellectual property rights therein. You shall have no rights hereunder other than the license as provided for above in Section 2. No right, license or interest to any trademark, trade name, service mark or other branding ("Marks") of WILEY or its licensors is granted hereunder, and you agree that you shall not assert any such right, license or interest with respect thereto
- NEITHER WILEY NOR ITS LICENSORS MAKES ANY WARRANTY OR REPRESENTATION OF ANY KIND TO YOU OR ANY THIRD PARTY, EXPRESS, IMPLIED OR STATUTORY, WITH RESPECT TO THE MATERIALS OR THE ACCURACY OF ANY INFORMATION CONTAINED IN THE MATERIALS, INCLUDING, WITHOUT LIMITATION, ANY IMPLIED WARRANTY OF MERCHANTABILITY, ACCURACY, SATISFACTORY QUALITY, FITNESS FOR A PARTICULAR PURPOSE, USABILITY,

<https://s100.copyright.com/CustomerAdmin/PLF.jsp?ref=2ec92cc8-837c-4d0f-ae7d-96dc56f8ccc1>

3/6

Figure 1.20; Chapter 1

06/06/2021

RightsLink Printable License

INTEGRATION OR NON-INFRINGEMENT AND ALL SUCH WARRANTIES ARE HEREBY EXCLUDED BY WILEY AND ITS LICENSORS AND WAIVED BY YOU.

- WILEY shall have the right to terminate this Agreement immediately upon breach of this Agreement by you.
- You shall indemnify, defend and hold harmless WILEY, its Licensors and their respective directors, officers, agents and employees, from and against any actual or threatened claims, demands, causes of action or proceedings arising from any breach of this Agreement by you.
- IN NO EVENT SHALL WILEY OR ITS LICENSORS BE LIABLE TO YOU OR ANY OTHER PARTY OR ANY OTHER PERSON OR ENTITY FOR ANY SPECIAL, CONSEQUENTIAL, INCIDENTAL, INDIRECT, EXEMPLARY OR PUNITIVE DAMAGES, HOWEVER CAUSED, ARISING OUT OF OR IN CONNECTION WITH THE DOWNLOADING, PROVISIONING, VIEWING OR USE OF THE MATERIALS REGARDLESS OF THE FORM OF ACTION, WHETHER FOR BREACH OF CONTRACT, BREACH OF WARRANTY, TORT, NEGLIGENCE, INFRINGEMENT OR OTHERWISE (INCLUDING, WITHOUT LIMITATION, DAMAGES BASED ON LOSS OF PROFITS, DATA, FILES, USE, BUSINESS OPPORTUNITY OR CLAIMS OF THIRD PARTIES), AND WHETHER OR NOT THE PARTY HAS BEEN ADVISED OF THE POSSIBILITY OF SUCH DAMAGES. THIS LIMITATION SHALL APPLY NOTWITHSTANDING ANY FAILURE OF ESSENTIAL PURPOSE OF ANY LIMITED REMEDY PROVIDED HEREIN.
- Should any provision of this Agreement be held by a court of competent jurisdiction to be illegal, invalid, or unenforceable, that provision shall be deemed amended to achieve as nearly as possible the same economic effect as the original provision, and the legality, validity and enforceability of the remaining provisions of this Agreement shall not be affected or impaired thereby.
- The failure of either party to enforce any term or condition of this Agreement shall not constitute a waiver of either party's right to enforce each and every term and condition of this Agreement. No breach under this agreement shall be deemed waived or excused by either party unless such waiver or consent is in writing signed by the party granting such waiver or consent. The waiver by or consent of a party to a breach of any provision of this Agreement shall not operate or be construed as a waiver of or consent to any other or subsequent breach by such other party.
- This Agreement may not be assigned (including by operation of law or otherwise) by you without WILEY's prior written consent.
- Any fee required for this permission shall be non-refundable after thirty (30) days from receipt by the CCC.
- These terms and conditions together with CCC's Billing and Payment terms and conditions (which are incorporated herein) form the entire agreement between you and WILEY concerning this licensing transaction and (in the absence of fraud) supersedes all prior agreements and representations of the parties, oral or written. This Agreement may not be amended except in writing signed by both parties. This Agreement shall be binding upon and inure to the benefit of the parties' successors, legal representatives, and authorized assigns.
- In the event of any conflict between your obligations established by these terms and conditions and those established by CCC's Billing and Payment terms and conditions,

Figure 1.20; Chapter 1

06/06/2021

RightsLink Printable License

these terms and conditions shall prevail.

- WILEY expressly reserves all rights not specifically granted in the combination of (i) the license details provided by you and accepted in the course of this licensing transaction, (ii) these terms and conditions and (iii) CCC's Billing and Payment terms and conditions.
- This Agreement will be void if the Type of Use, Format, Circulation, or Requestor Type was misrepresented during the licensing process.
- This Agreement shall be governed by and construed in accordance with the laws of the State of New York, USA, without regards to such state's conflict of law rules. Any legal action, suit or proceeding arising out of or relating to these Terms and Conditions or the breach thereof shall be instituted in a court of competent jurisdiction in New York County in the State of New York in the United States of America and each party hereby consents and submits to the personal jurisdiction of such court, waives any objection to venue in such court and consents to service of process by registered or certified mail, return receipt requested, at the last known address of such party.

WILEY OPEN ACCESS TERMS AND CONDITIONS

Wiley Publishes Open Access Articles in fully Open Access Journals and in Subscription journals offering Online Open. Although most of the fully Open Access journals publish open access articles under the terms of the Creative Commons Attribution (CC BY) License only, the subscription journals and a few of the Open Access Journals offer a choice of Creative Commons Licenses. The license type is clearly identified on the article.

The Creative Commons Attribution License

The [Creative Commons Attribution License \(CC-BY\)](#) allows users to copy, distribute and transmit an article, adapt the article and make commercial use of the article. The CC-BY license permits commercial and non-

Creative Commons Attribution Non-Commercial License

The [Creative Commons Attribution Non-Commercial \(CC-BY-NC\) License](#) permits use, distribution and reproduction in any medium, provided the original work is properly cited and is not used for commercial purposes.(see below)

Creative Commons Attribution-Non-Commercial-NoDerivs License

The [Creative Commons Attribution Non-Commercial-NoDerivs License](#) (CC-BY-NC-ND) permits use, distribution and reproduction in any medium, provided the original work is properly cited, is not used for commercial purposes and no modifications or adaptations are made. (see below)

Use by commercial "for-profit" organizations

Use of Wiley Open Access articles for commercial, promotional, or marketing purposes requires further explicit permission from Wiley and will be subject to a fee.

Further details can be found on Wiley Online Library
<http://olabout.wiley.com/WileyCDA/Section/id-410895.html>

Other Terms and Conditions:

<https://s100.copyright.com/CustomAdmin/PLF.jsp?ref=2ec92cc8-837c-4d0f-ae7d-96dc56f8ccc1>

5/6

Figure 1.20; Chapter 1

06/06/2021

RightsLink Printable License

v1.10 Last updated September 2015

Questions? customercare@copyright.com or +1-855-239-3415 (toll free in the US) or +1-978-646-2777.

Figure 1.22; Chapter 1

06/06/2021

RightsLink Printable License

ELSEVIER LICENSE TERMS AND CONDITIONS

Jun 06, 2021

This Agreement between Mustafa Hamad ("You") and Elsevier ("Elsevier") consists of your license details and the terms and conditions provided by Elsevier and Copyright Clearance Center.

License Number	5083041043507
License date	Jun 06, 2021
Licensed Content Publisher	Elsevier
Licensed Content Publication	Journal of the Mechanics and Physics of Solids
Licensed Content Title	A surface stacking fault energy approach to predicting defect nucleation in surface-dominated nanostructures
Licensed Content Author	Jin-Wu Jiang,Austin M. Leach,Ken Gall,Harold S. Park,Timon Rabczuk
Licensed Content Date	Sep 1, 2013
Licensed Content Volume	61
Licensed Content Issue	9
Licensed Content Pages	20
Start Page	1915
End Page	1934
Type of Use	reuse in a thesis/dissertation

<https://s100.copyright.com/CustomAdmin/PLF.jsp?ref=888a77ae-fbb0-4e65-a72d-3d91cd52ab27>

1/7

Figure 1.22; Chapter 1

06/06/2021

RightsLink Printable License

Portion	figures/tables/illustrations
Number of figures/tables/illustrations	1
Format	both print and electronic
Are you the author of this Elsevier article?	No
Will you be translating?	No
Title	In silico prediction of the physical performance of pharmaceutical crystals
Institution name	Curtin University
Expected presentation date	Jul 2021
Portions	Figure 4 / page 1921
Requestor Location	Mustafa Hamad Kent Street Bentley Perth, WA 6102 Australia Attn: Mustafa Hamad
Publisher Tax ID	GB 494 6272 12
Total	0.00 USD
Terms and Conditions	

INTRODUCTION

1. The publisher for this copyrighted material is Elsevier. By clicking "accept" in connection with completing this licensing transaction, you agree that the following terms and conditions apply to this transaction (along with the Billing and Payment terms and conditions established by Copyright Clearance Center, Inc. ("CCC"), at the time that you opened your Rightslink account and that are available at any time at <http://myaccount.copyright.com>).

GENERAL TERMS

<https://s100.copyright.com/CustomerAdmin/PLF.jsp?ref=888a77ae-fbb0-4e65-a72d-3d91cd52ab27>

2/7

Figure 1.22; Chapter 1

06/06/2021

RightsLink Printable License

2. Elsevier hereby grants you permission to reproduce the aforementioned material subject to the terms and conditions indicated.
3. Acknowledgement: If any part of the material to be used (for example, figures) has appeared in our publication with credit or acknowledgement to another source, permission must also be sought from that source. If such permission is not obtained then that material may not be included in your publication/copies. Suitable acknowledgement to the source must be made, either as a footnote or in a reference list at the end of your publication, as follows:

"Reprinted from Publication title, Vol /edition number, Author(s), Title of article / title of chapter, Pages No., Copyright (Year), with permission from Elsevier [OR APPLICABLE SOCIETY COPYRIGHT OWNER]." Also Lancet special credit - "Reprinted from The Lancet, Vol. number, Author(s), Title of article, Pages No., Copyright (Year), with permission from Elsevier."
4. Reproduction of this material is confined to the purpose and/or media for which permission is hereby given.
5. Altering/Modifying Material: Not Permitted. However figures and illustrations may be altered/adapted minimally to serve your work. Any other abbreviations, additions, deletions and/or any other alterations shall be made only with prior written authorization of Elsevier Ltd. (Please contact Elsevier's permissions helpdesk [here](#)). No modifications can be made to any Lancet figures/tables and they must be reproduced in full.
6. If the permission fee for the requested use of our material is waived in this instance, please be advised that your future requests for Elsevier materials may attract a fee.
7. Reservation of Rights: Publisher reserves all rights not specifically granted in the combination of (i) the license details provided by you and accepted in the course of this licensing transaction, (ii) these terms and conditions and (iii) CCC's Billing and Payment terms and conditions.
8. License Contingent Upon Payment: While you may exercise the rights licensed immediately upon issuance of the license at the end of the licensing process for the transaction, provided that you have disclosed complete and accurate details of your proposed use, no license is finally effective unless and until full payment is received from you (either by publisher or by CCC) as provided in CCC's Billing and Payment terms and conditions. If full payment is not received on a timely basis, then any license preliminarily granted shall be deemed automatically revoked and shall be void as if never granted. Further, in the event that you breach any of these terms and conditions or any of CCC's Billing and Payment terms and conditions, the license is automatically revoked and shall be void as if never granted. Use of materials as described in a revoked license, as well as any use of the materials beyond the scope of an unrevoked license, may constitute copyright infringement and publisher reserves the right to take any and all action to protect its copyright in the materials.
9. Warranties: Publisher makes no representations or warranties with respect to the licensed material.
10. Indemnity: You hereby indemnify and agree to hold harmless publisher and CCC, and their respective officers, directors, employees and agents, from and against any and all claims arising out of your use of the licensed material other than as specifically authorized pursuant to this license.
11. No Transfer of License: This license is personal to you and may not be sublicensed, assigned, or transferred by you to any other person without publisher's written permission.

Figure 1.22; Chapter 1

06/06/2021

RightsLink Printable License

12. **No Amendment Except in Writing:** This license may not be amended except in a writing signed by both parties (or, in the case of publisher, by CCC on publisher's behalf).

13. **Objection to Contrary Terms:** Publisher hereby objects to any terms contained in any purchase order, acknowledgment, check endorsement or other writing prepared by you, which terms are inconsistent with these terms and conditions or CCC's Billing and Payment terms and conditions. These terms and conditions, together with CCC's Billing and Payment terms and conditions (which are incorporated herein), comprise the entire agreement between you and publisher (and CCC) concerning this licensing transaction. In the event of any conflict between your obligations established by these terms and conditions and those established by CCC's Billing and Payment terms and conditions, these terms and conditions shall control.

14. **Revocation:** Elsevier or Copyright Clearance Center may deny the permissions described in this License at their sole discretion, for any reason or no reason, with a full refund payable to you. Notice of such denial will be made using the contact information provided by you. Failure to receive such notice will not alter or invalidate the denial. In no event will Elsevier or Copyright Clearance Center be responsible or liable for any costs, expenses or damage incurred by you as a result of a denial of your permission request, other than a refund of the amount(s) paid by you to Elsevier and/or Copyright Clearance Center for denied permissions.

LIMITED LICENSE

The following terms and conditions apply only to specific license types:

15. **Translation:** This permission is granted for non-exclusive world **English** rights only unless your license was granted for translation rights. If you licensed translation rights you may only translate this content into the languages you requested. A professional translator must perform all translations and reproduce the content word for word preserving the integrity of the article.

16. **Posting licensed content on any Website:** The following terms and conditions apply as follows: Licensing material from an Elsevier journal: All content posted to the web site must maintain the copyright information line on the bottom of each image; A hyper-text must be included to the Homepage of the journal from which you are licensing at <http://www.sciencedirect.com/science/journal/xxxxx> or the Elsevier homepage for books at <http://www.elsevier.com>; Central Storage: This license does not include permission for a scanned version of the material to be stored in a central repository such as that provided by Heron/XanEdu.

Licensing material from an Elsevier book: A hyper-text link must be included to the Elsevier homepage at <http://www.elsevier.com>. All content posted to the web site must maintain the copyright information line on the bottom of each image.

Posting licensed content on Electronic reserve: In addition to the above the following clauses are applicable: The web site must be password-protected and made available only to bona fide students registered on a relevant course. This permission is granted for 1 year only. You may obtain a new license for future website posting.

17. **For journal authors:** the following clauses are applicable in addition to the above:

Preprints:

A preprint is an author's own write-up of research results and analysis, it has not been peer-reviewed, nor has it had any other value added to it by a publisher (such as formatting, copyright, technical enhancement etc.).

Figure 1.22; Chapter 1

06/06/2021

RightsLink Printable License

Authors can share their preprints anywhere at any time. Preprints should not be added to or enhanced in any way in order to appear more like, or to substitute for, the final versions of articles however authors can update their preprints on arXiv or RePEc with their Accepted Author Manuscript (see below).

If accepted for publication, we encourage authors to link from the preprint to their formal publication via its DOI. Millions of researchers have access to the formal publications on ScienceDirect, and so links will help users to find, access, cite and use the best available version. Please note that Cell Press, The Lancet and some society-owned have different preprint policies. Information on these policies is available on the journal homepage.

Accepted Author Manuscripts: An accepted author manuscript is the manuscript of an article that has been accepted for publication and which typically includes author-incorporated changes suggested during submission, peer review and editor-author communications.

Authors can share their accepted author manuscript:

- immediately
 - via their non-commercial person homepage or blog
 - by updating a preprint in arXiv or RePEc with the accepted manuscript
 - via their research institute or institutional repository for internal institutional uses or as part of an invitation-only research collaboration work-group
 - directly by providing copies to their students or to research collaborators for their personal use
 - for private scholarly sharing as part of an invitation-only work group on commercial sites with which Elsevier has an agreement
- After the embargo period
 - via non-commercial hosting platforms such as their institutional repository
 - via commercial sites with which Elsevier has an agreement

In all cases accepted manuscripts should:

- link to the formal publication via its DOI
- bear a CC-BY-NC-ND license - this is easy to do
- if aggregated with other manuscripts, for example in a repository or other site, be shared in alignment with our hosting policy not be added to or enhanced in any way to appear more like, or to substitute for, the published journal article.

Published journal article (JPA): A published journal article (PJA) is the definitive final record of published research that appears or will appear in the journal and embodies all value-adding publishing activities including peer review co-ordination, copy-editing, formatting, (if relevant) pagination and online enrichment.

Policies for sharing publishing journal articles differ for subscription and gold open access articles:

Subscription Articles: If you are an author, please share a link to your article rather than the full-text. Millions of researchers have access to the formal publications on ScienceDirect, and so links will help your users to find, access, cite, and use the best available version.

Theses and dissertations which contain embedded PJAs as part of the formal submission can be posted publicly by the awarding institution with DOI links back to the formal publications on ScienceDirect.

If you are affiliated with a library that subscribes to ScienceDirect you have additional private sharing rights for others' research accessed under that agreement. This includes use for classroom teaching and internal training at the institution (including use in course packs and courseware programs), and inclusion of the article for grant funding purposes.

Figure 1.22; Chapter 1

06/06/2021

RightsLink Printable License

Gold Open Access Articles: May be shared according to the author-selected end-user license and should contain a [CrossMark logo](#), the end user license, and a DOI link to the formal publication on ScienceDirect.

Please refer to Elsevier's [posting policy](#) for further information.

18. **For book authors** the following clauses are applicable in addition to the above: Authors are permitted to place a brief summary of their work online only. You are not allowed to download and post the published electronic version of your chapter, nor may you scan the printed edition to create an electronic version. **Posting to a repository:** Authors are permitted to post a summary of their chapter only in their institution's repository.

19. **Thesis/Dissertation:** If your license is for use in a thesis/dissertation your thesis may be submitted to your institution in either print or electronic form. Should your thesis be published commercially, please reapply for permission. These requirements include permission for the Library and Archives of Canada to supply single copies, on demand, of the complete thesis and include permission for Proquest/UMI to supply single copies, on demand, of the complete thesis. Should your thesis be published commercially, please reapply for permission. Theses and dissertations which contain embedded PJAs as part of the formal submission can be posted publicly by the awarding institution with DOI links back to the formal publications on ScienceDirect.

Elsevier Open Access Terms and Conditions

You can publish open access with Elsevier in hundreds of open access journals or in nearly 2000 established subscription journals that support open access publishing. Permitted third party re-use of these open access articles is defined by the author's choice of Creative Commons user license. See our [open access license policy](#) for more information.

Terms & Conditions applicable to all Open Access articles published with Elsevier:

Any reuse of the article must not represent the author as endorsing the adaptation of the article nor should the article be modified in such a way as to damage the author's honour or reputation. If any changes have been made, such changes must be clearly indicated.

The author(s) must be appropriately credited and we ask that you include the end user license and a DOI link to the formal publication on ScienceDirect.

If any part of the material to be used (for example, figures) has appeared in our publication with credit or acknowledgement to another source it is the responsibility of the user to ensure their reuse complies with the terms and conditions determined by the rights holder.

Additional Terms & Conditions applicable to each Creative Commons user license:

CC BY: The CC-BY license allows users to copy, to create extracts, abstracts and new works from the Article, to alter and revise the Article and to make commercial use of the Article (including reuse and/or resale of the Article by commercial entities), provided the user gives appropriate credit (with a link to the formal publication through the relevant DOI), provides a link to the license, indicates if changes were made and the licensor is not represented as endorsing the use made of the work. The full details of the license are available at <http://creativecommons.org/licenses/by/4.0>.

CC BY NC SA: The CC BY-NC-SA license allows users to copy, to create extracts, abstracts and new works from the Article, to alter and revise the Article, provided this is not done for commercial purposes, and that the user gives appropriate credit (with a link to the formal publication through the relevant DOI), provides a link to the license, indicates if changes were made and the licensor is not represented as endorsing the use made of the

Figure 1.22; Chapter 1

06/06/2021

RightsLink Printable License

work. Further, any new works must be made available on the same conditions. The full details of the license are available at <http://creativecommons.org/licenses/by-nc-sa/4.0>.

CC BY NC ND: The CC BY-NC-ND license allows users to copy and distribute the Article, provided this is not done for commercial purposes and further does not permit distribution of the Article if it is changed or edited in any way, and provided the user gives appropriate credit (with a link to the formal publication through the relevant DOI), provides a link to the license, and that the licensor is not represented as endorsing the use made of the work. The full details of the license are available at <http://creativecommons.org/licenses/by-nc-nd/4.0>. Any commercial reuse of Open Access articles published with a CC BY NC SA or CC BY NC ND license requires permission from Elsevier and will be subject to a fee.

Commercial reuse includes:

- Associating advertising with the full text of the Article
- Charging fees for document delivery or access
- Article aggregation
- Systematic distribution via e-mail lists or share buttons

Posting or linking by commercial companies for use by customers of those companies.

20. Other Conditions:

v1.10

Questions? customer@copyright.com or +1-855-239-3415 (toll free in the US) or +1-978-646-2777.

Figure 1.23; Chapter 1

06/06/2021

<https://marketplace.copyright.com/rs-ui-web/mp/license/a77a640f-76f2-46be-add2-13f8b35111a8/ebbd7705-09df-43c2-83a3-fb4124c843c7>



Marketplace™

IOP Publishing, Ltd - License Terms and Conditions

This is a License Agreement between Mustafa Hamad / Curtin University ("You") and IOP Publishing, Ltd ("Publisher") provided by Copyright Clearance Center ("CCC"). The license consists of your order details, the terms and conditions provided by IOP Publishing, Ltd, and the CCC terms and conditions.

All payments must be made in full to CCC.

Order Date	06-Jun-2021	Type of Use	Republish in a thesis/dissertation
Order License ID	1123906-1	Publisher	IOP Publishing
ISSN	1361-651X	Portion	Chart/graph/table/figure

LICENSED CONTENT

Publication Title	Modelling and Simulation in Materials Science and Engineering	Country	United Kingdom of Great Britain and Northern Ireland
Author/Editor	Institute of Physics (Great Britain)	Rightsholder	IOP Publishing, Ltd
Date	01/01/1992	Publication Type	e-Journal
Language	English	URL	http://iopscience.iop.org/0965-0393/

REQUEST DETAILS

Portion Type	Chart/graph/table/figure	Distribution	Worldwide
Number of charts / graphs / tables / figures requested	1	Translation	Original language of publication
Format (select all that apply)	Print, Electronic	Copies for the disabled?	No
Who will republish the content?	Academic institution	Minor editing privileges?	No
Duration of Use	Life of current and all future editions	Incidental promotional use?	No
Lifetime Unit Quantity	Up to 499	Currency	USD
Rights Requested	Main product		

NEW WORK DETAILS

Title	In silico prediction of the physical performance of pharmaceutical crystals	Institution name	Curtrin University
Instructor name	Professor Andrew Rohl	Expected presentation date	2021-07-16

ADDITIONAL DETAILS

Order reference number	N/A	The requesting person / organization to appear on the license	Mustafa Hamad / Curtin University
------------------------	-----	---	-----------------------------------

REUSE CONTENT DETAILS

<https://marketplace.copyright.com/rs-ui-web/mp/license/a77a640f-76f2-46be-add2-13f8b35111a8/ebbd7705-09df-43c2-83a3-fb4124c843c7>

1/5

Figure 1.23; Chapter 1

06/06/2021	https://marketplace.copyright.com/rs-ui-web/mp/license/a77a640f-76f2-46be-add2-13f8b35111a8/ebbd7705-09df-43c2-83a3-fb4124c843c7		
Title, description or numeric reference of the portion(s)	Figure 3	Title of the article/chapter the portion is from	An atomic-level model for studying the dynamics of edge dislocations in metals
Editor of portion(s)	N/A	Author of portion(s)	Institute of Physics (Great Britain)
Volume of serial or monograph	N/A	Issue, if republishing an article from a serial	N/A
Page or page range of portion	431	Publication date of portion	1992-01-01

PUBLISHER TERMS AND CONDITIONS

These special terms and conditions are in addition to the standard terms and conditions for CCC's Republication Service and, together with those standard terms and conditions, govern the use of the Works. As the User you will make all reasonable efforts to contact the author(s) of the article which the Work is to be reused from, to seek consent for your intended use. Contacting one author who is acting expressly as authorised agent for their co-author(s) is acceptable. User will reproduce the following wording prominently alongside the Work: the source of the Work, including author, article title, title of journal, volume number, issue number (if relevant), page range (or first page if this is the only information available) and date of first publication; and a link back to the article (via DOI); and if practicable, and IN ALL CASES for new works published under any of the Creative Commons licences, the words "© IOP Publishing. Reproduced with permission. All rights reserved" Without the express permission of the author(s) and the Rightsholder of the article from which the Work is to be reused, User shall not use it in any way which, in the opinion of the Rightsholder, could: (i) distort or alter the author(s)' original intention(s) and meaning; (ii) be prejudicial to the honour or reputation of the author(s); and/or (iii) imply endorsement by the author(s) and/or the Rightsholder. This licence does not apply to any article which is credited to another source and which does not have the copyright line '© IOP Publishing Ltd'. User must check the copyright line of the article from which the Work is to be reused to check that IOP Publishing Ltd has all the necessary rights to be able to grant permission. User is solely responsible for identifying and obtaining separate licences and permissions from the copyright owner for reuse of any such third party material/figures which the Rightsholder is not the copyright owner of. The Rightsholder shall not reimburse any fees which User pays for a republication license for such third party content. This licence does not apply to any material/figure which is credited to another source in the Rightsholder's publication or has been obtained from a third party. User must check the Version of Record of the article from which the Work is to be reused, to check whether any of the material in the Work is third party material. Third party citations and/or copyright notices and/or permissions statements may not be included in any other version of the article from which the Work is to be reused and so cannot be relied upon by the User. User is solely responsible for identifying and obtaining separate licences and permissions from the copyright owner for reuse of any such third party material/figures where the Rightsholder is not the copyright owner. The Rightsholder shall not reimburse any fees which User pays for a republication license for such third party content. User and CCC acknowledge that the Rightsholder may, from time to time, make changes or additions to these special terms and conditions without express notification, provided that these shall not apply to permissions already secured and paid for by User prior to such change or addition. User acknowledges that the Rightsholder (which includes companies within its group and third parties for whom it publishes its titles) may make use of personal data collected through the service in the course of their business. If User is the author of the Work, User may automatically have the right to reuse it under the rights granted back when User transferred the copyright in the article to the Rightsholder. User should check the copyright form and the relevant author rights policy to check whether permission is required. If User is the author of the Work and does require permission for proposed reuse of the Work, User should select 'Author of requested content' as the Requestor Type. The Rightsholder shall not reimburse any fees which User pays for a republication license. If User is the author of the article which User wishes to reuse in User's thesis or dissertation, the republication licence covers the right to include the Version of Record of the article, provided it is not then shared or deposited online. User must include citation details. Where User wishes to share their thesis or dissertation online, they should remove the Version of Record before uploading it. User may include a Preprint or the Accepted Manuscript (after the embargo period) in the online version of the thesis or dissertation, provided they do so in accordance with the Rightsholder's policies on sharing Preprints or Accepted Manuscripts. User may need to obtain separate permission for any third party content included within the article. User must check this with the copyright owner of such third party content. Any online or commercial use of User's thesis or dissertation containing the article, including publication via ProQuest, would need to be expressly notified in writing to the Rightsholder at the time of request and would require separate written permission from the Rightsholder. As well as CCC, the Rightsholder shall have the right to bring any legal action that it deems necessary to enforce its rights should it consider that the Work infringes those rights in any way. For content reuse requests that qualify for permission under the STM Permissions Guidelines, which may be updated from time to time, the STM Permissions Guidelines supplement the terms and conditions contained in this license.

CCC Republication Terms and Conditions

1.

Figure 1.23; Chapter 1

06/06/2021

<https://marketplace.copyright.com/rs-ui-web/mp/license/a77a640f-76f2-46be-add2-13f8b35111a8/ebbd7705-09df-43c2-83a3-fb4124c843c7>

Description of Service; Defined Terms. This Republication License enables the User to obtain licenses for republication of one or more copyrighted works as described in detail on the relevant Order Confirmation (the "Work(s)"). Copyright Clearance Center, Inc. ("CCC") grants licenses through the Service on behalf of the rightsholder identified on the Order Confirmation (the "Rightsholder"). "Republication", as used herein, generally means the inclusion of a Work, in whole or in part, in a new work or works, also as described on the Order Confirmation. "User", as used herein, means the person or entity making such republication.

2. The terms set forth in the relevant Order Confirmation, and any terms set by the Rightsholder with respect to a particular Work, govern the terms of use of Works in connection with the Service. By using the Service, the person transacting for a republication license on behalf of the User represents and warrants that he/she/it (a) has been duly authorized by the User to accept, and hereby does accept, all such terms and conditions on behalf of User, and (b) shall inform User of all such terms and conditions. In the event such person is a "freelancer" or other third party independent of User and CCC, such party shall be deemed jointly a "User" for purposes of these terms and conditions. In any event, User shall be deemed to have accepted and agreed to all such terms and conditions if User republishes the Work in any fashion.
3. Scope of License; Limitations and Obligations.
 - 3.1. All Works and all rights therein, including copyright rights, remain the sole and exclusive property of the Rightsholder. The license created by the exchange of an Order Confirmation (and/or any invoice) and payment by User of the full amount set forth on that document includes only those rights expressly set forth in the Order Confirmation and in these terms and conditions, and conveys no other rights in the Work(s) to User. All rights not expressly granted are hereby reserved.
 - 3.2. General Payment Terms: You may pay by credit card or through an account with us payable at the end of the month. If you and we agree that you may establish a standing account with CCC, then the following terms apply: Remit Payment to: Copyright Clearance Center, 29118 Network Place, Chicago, IL 60673-1291. Payments Due: Invoices are payable upon their delivery to you (or upon our notice to you that they are available to you for downloading). After 30 days, outstanding amounts will be subject to a service charge of 1-1/2% per month or, if less, the maximum rate allowed by applicable law. Unless otherwise specifically set forth in the Order Confirmation or in a separate written agreement signed by CCC, invoices are due and payable on "net 30" terms. While User may exercise the rights licensed immediately upon issuance of the Order Confirmation, the license is automatically revoked and is null and void, as if it had never been issued, if complete payment for the license is not received on a timely basis either from User directly or through a payment agent, such as a credit card company.
 - 3.3. Unless otherwise provided in the Order Confirmation, any grant of rights to User (i) is "one-time" (including the editions and product family specified in the license), (ii) is non-exclusive and non-transferable and (iii) is subject to any and all limitations and restrictions (such as, but not limited to, limitations on duration of use or circulation) included in the Order Confirmation or invoice and/or in these terms and conditions. Upon completion of the licensed use, User shall either secure a new permission for further use of the Work(s) or immediately cease any new use of the Work(s) and shall render inaccessible (such as by deleting or by removing or severing links or other locators) any further copies of the Work (except for copies printed on paper in accordance with this license and still in User's stock at the end of such period).
 - 3.4. In the event that the material for which a republication license is sought includes third party materials (such as photographs, illustrations, graphs, inserts and similar materials) which are identified in such material as having been used by permission, User is responsible for identifying, and seeking separate licenses (under this Service or otherwise) for, any of such third party materials; without a separate license, such third party materials may not be used.
 - 3.5. Use of proper copyright notice for a Work is required as a condition of any license granted under the Service. Unless otherwise provided in the Order Confirmation, a proper copyright notice will read substantially as follows: "Republished with permission of [Rightsholder's name], from [Work's title, author, volume, edition number and year of copyright]; permission conveyed through Copyright Clearance Center, Inc. " Such notice must be provided in a reasonably legible font size and must be placed either immediately adjacent to the Work as used (for example, as part of a by-line or footnote but not as a separate electronic link) or in the place where substantially all other credits or notices for the new work containing the republished Work are located. Failure to include the required notice results in loss to the Rightsholder and CCC, and the User shall be liable to pay liquidated damages for each such failure equal to twice the use fee specified in the Order Confirmation, in addition to the use fee itself and any other fees and charges specified.

<https://marketplace.copyright.com/rs-ui-web/mp/license/a77a640f-76f2-46be-add2-13f8b35111a8/ebbd7705-09df-43c2-83a3-fb4124c843c7>

3/5

Figure 1.23; Chapter 1

06/06/2021

<https://marketplace.copyright.com/rs-ui-web/mp/license/a77a640f-76f2-46be-add2-13f8b35111a8/ebbd7705-09df-43c2-83a3-fb4124c843c7>

- 3.6. User may only make alterations to the Work if and as expressly set forth in the Order Confirmation. No Work may be used in any way that is defamatory, violates the rights of third parties (including such third parties' rights of copyright, privacy, publicity, or other tangible or intangible property), or is otherwise illegal, sexually explicit or obscene. In addition, User may not conjoin a Work with any other material that may result in damage to the reputation of the Rightsholder. User agrees to inform CCC if it becomes aware of any infringement of any rights in a Work and to cooperate with any reasonable request of CCC or the Rightsholder in connection therewith.
4. Indemnity. User hereby indemnifies and agrees to defend the Rightsholder and CCC, and their respective employees and directors, against all claims, liability, damages, costs and expenses, including legal fees and expenses, arising out of any use of a Work beyond the scope of the rights granted herein, or any use of a Work which has been altered in any unauthorized way by User, including claims of defamation or infringement of rights of copyright, publicity, privacy or other tangible or intangible property.
5. Limitation of Liability. UNDER NO CIRCUMSTANCES WILL CCC OR THE RIGHTSHOLDER BE LIABLE FOR ANY DIRECT, INDIRECT, CONSEQUENTIAL OR INCIDENTAL DAMAGES (INCLUDING WITHOUT LIMITATION DAMAGES FOR LOSS OF BUSINESS PROFITS OR INFORMATION, OR FOR BUSINESS INTERRUPTION) ARISING OUT OF THE USE OR INABILITY TO USE A WORK, EVEN IF ONE OF THEM HAS BEEN ADVISED OF THE POSSIBILITY OF SUCH DAMAGES. In any event, the total liability of the Rightsholder and CCC (including their respective employees and directors) shall not exceed the total amount actually paid by User for this license. User assumes full liability for the actions and omissions of its principals, employees, agents, affiliates, successors and assigns.
6. Limited Warranties. THE WORK(S) AND RIGHT(S) ARE PROVIDED "AS IS". CCC HAS THE RIGHT TO GRANT TO USER THE RIGHTS GRANTED IN THE ORDER CONFIRMATION DOCUMENT. CCC AND THE RIGHTSHOLDER DISCLAIM ALL OTHER WARRANTIES RELATING TO THE WORK(S) AND RIGHT(S), EITHER EXPRESS OR IMPLIED, INCLUDING WITHOUT LIMITATION IMPLIED WARRANTIES OF MERCHANTABILITY OR FITNESS FOR A PARTICULAR PURPOSE. ADDITIONAL RIGHTS MAY BE REQUIRED TO USE ILLUSTRATIONS, GRAPHS, PHOTOGRAPHS, ABSTRACTS, INSERTS OR OTHER PORTIONS OF THE WORK (AS OPPOSED TO THE ENTIRE WORK) IN A MANNER CONTEMPLATED BY USER; USER UNDERSTANDS AND AGREES THAT NEITHER CCC NOR THE RIGHTSHOLDER MAY HAVE SUCH ADDITIONAL RIGHTS TO GRANT.
7. Effect of Breach. Any failure by User to pay any amount when due, or any use by User of a Work beyond the scope of the license set forth in the Order Confirmation and/or these terms and conditions, shall be a material breach of the license created by the Order Confirmation and these terms and conditions. Any breach not cured within 30 days of written notice thereof shall result in immediate termination of such license without further notice. Any unauthorized (but licensable) use of a Work that is terminated immediately upon notice thereof may be liquidated by payment of the Rightsholder's ordinary license price therefor; any unauthorized (and unlicensable) use that is not terminated immediately for any reason (including, for example, because materials containing the Work cannot reasonably be recalled) will be subject to all remedies available at law or in equity, but in no event to a payment of less than three times the Rightsholder's ordinary license price for the most closely analogous licensable use plus Rightsholder's and/or CCC's costs and expenses incurred in collecting such payment.
8. Miscellaneous.
 - 8.1. User acknowledges that CCC may, from time to time, make changes or additions to the Service or to these terms and conditions, and CCC reserves the right to send notice to the User by electronic mail or otherwise for the purposes of notifying User of such changes or additions; provided that any such changes or additions shall not apply to permissions already secured and paid for.
 - 8.2. Use of User-related information collected through the Service is governed by CCC's privacy policy, available online here:<https://marketplace.copyright.com/rs-ui-web/mp/privacy-policy>
 - 8.3. The licensing transaction described in the Order Confirmation is personal to User. Therefore, User may not assign or transfer to any other person (whether a natural person or an organization of any kind) the license created by the Order Confirmation and these terms and conditions or any rights granted hereunder; provided, however, that User may assign such license in its entirety on written notice to CCC in the event of a transfer of all or substantially all of User's rights in the new material which includes the Work(s) licensed under this Service.
 - 8.4. No amendment or waiver of any terms is binding unless set forth in writing and signed by the parties. The Rightsholder and CCC hereby object to any terms contained in any writing prepared by the User or its

<https://marketplace.copyright.com/rs-ui-web/mp/license/a77a640f-76f2-46be-add2-13f8b35111a8/ebbd7705-09df-43c2-83a3-fb4124c843c7>

4/5

Figure 1.23; Chapter 1

06/06/2021

<https://marketplace.copyright.com/rs-ui-web/mp/license/a77a640f-76f2-46be-add2-13f8b35111a8/ebbd7705-09df-43c2-83a3-fb4124c843c7>

principals, employees, agents or affiliates and purporting to govern or otherwise relate to the licensing transaction described in the Order Confirmation, which terms are in any way inconsistent with any terms set forth in the Order Confirmation and/or in these terms and conditions or CCC's standard operating procedures, whether such writing is prepared prior to, simultaneously with or subsequent to the Order Confirmation, and whether such writing appears on a copy of the Order Confirmation or in a separate instrument.

- 8.5. The licensing transaction described in the Order Confirmation document shall be governed by and construed under the law of the State of New York, USA, without regard to the principles thereof of conflicts of law. Any case, controversy, suit, action, or proceeding arising out of, in connection with, or related to such licensing transaction shall be brought, at CCC's sole discretion, in any federal or state court located in the County of New York, State of New York, USA, or in any federal or state court whose geographical jurisdiction covers the location of the Rightsholder set forth in the Order Confirmation. The parties expressly submit to the personal jurisdiction and venue of each such federal or state court. If you have any comments or questions about the Service or Copyright Clearance Center, please contact us at 978-750-8400 or send an e-mail to support@copyright.com.

v 1.1

Figure 1.24; Chapter 1



06-Jun-2021

This license agreement between the American Physical Society ("APS") and Mustafa Hamad ("You") consists of your license details and the terms and conditions provided by the American Physical Society and SciPris.

Licensed Content Information

License Number: RNP/21/JUN/040790
License date: 06-Jun-2021
DOI: 10.1103/PhysRevLett.91.135501
Title: Phonon Instabilities and the Ideal Strength of Aluminum
Author: D. M. Clatterbuck et al.
Publication: Physical Review Letters
Publisher: American Physical Society
Cost: USD \$ 0.00

Request Details

Does your reuse require significant modifications: No
Specify intended distribution locations: Worldwide
Reuse Category: Reuse in a thesis/dissertation
Requestor Type: Academic Institution
Items for Reuse: Figures/Tables
Number of Figure/Tables: 1
Figure/Tables Details: Figure 2
Format for Reuse: Electronic and Print
Total number of print copies: Up to 1000

Information about New Publication:

University/Publisher: Curtin University
Title of dissertation/thesis: In silico prediction of the physical performance of pharmaceutical crystals
Author(s):
Expected completion date: Jul. 2021

License Requestor Information

Name: Mustafa Hamad
Affiliation: Individual
Email Id: mustafa.hamad@postgrad.curtin.edu.au
Country: Australia

Figure 1.24; Chapter 1



TERMS AND CONDITIONS

The American Physical Society (APS) is pleased to grant the Requestor of this license a non-exclusive, non-transferable permission, limited to Electronic and Print format, provided all criteria outlined below are followed.

1. You must also obtain permission from at least one of the lead authors for each separate work, if you haven't done so already. The author's name and affiliation can be found on the first page of the published Article.
2. For electronic format permissions, Requestor agrees to provide a hyperlink from the reprinted APS material using the source material's DOI on the web page where the work appears. The hyperlink should use the standard DOI resolution URL, <http://dx.doi.org/{DOI}>. The hyperlink may be embedded in the copyright credit line.
3. For print format permissions, Requestor agrees to print the required copyright credit line on the first page where the material appears: "Reprinted (abstract/excerpt/figure) with permission from [(FULL REFERENCE CITATION) as follows: Author's Names, APS Journal Title, Volume Number, Page Number and Year of Publication.] Copyright (YEAR) by the American Physical Society."
4. Permission granted in this license is for a one-time use and does not include permission for any future editions, updates, databases, formats or other matters. Permission must be sought for any additional use.
5. Use of the material does not and must not imply any endorsement by APS.
6. APS does not imply, purport or intend to grant permission to reuse materials to which it does not hold copyright. It is the requestor's sole responsibility to ensure the licensed material is original to APS and does not contain the copyright of another entity, and that the copyright notice of the figure, photograph, cover or table does not indicate it was reprinted by APS with permission from another source.
7. The permission granted herein is personal to the Requestor for the use specified and is not transferable or assignable without express written permission of APS. This license may not be amended except in writing by APS.
8. You may not alter, edit or modify the material in any manner.
9. You may translate the materials only when translation rights have been granted.
10. APS is not responsible for any errors or omissions due to translation.
11. You may not use the material for promotional, sales, advertising or marketing purposes.
12. The foregoing license shall not take effect unless and until APS or its agent, Aptara, receives payment in full in accordance with Aptara Billing and Payment Terms and Conditions, which are incorporated herein by reference.
13. Should the terms of this license be violated at any time, APS or Aptara may revoke the license with no refund to you and seek relief to the fullest extent of the laws of the USA. Official written notice will be made using the contact information provided with the permission request. Failure to receive such notice will not nullify revocation of the permission.
14. APS reserves all rights not specifically granted herein.
15. This document, including the Aptara Billing and Payment Terms and Conditions, shall be the entire agreement between the parties relating to the subject matter hereof.

Figure 4.10; Chapter 4

06/06/2021

RightsLink Printable License

AIP PUBLISHING LICENSE TERMS AND CONDITIONS

Jun 06, 2021

This Agreement between Mustafa Hamad ("You") and AIP Publishing ("AIP Publishing") consists of your license details and the terms and conditions provided by AIP Publishing and Copyright Clearance Center.

License Number	5083060289015
License date	Jun 06, 2021
Licensed Content Publisher	AIP Publishing
Licensed Content Publication	Journal of Applied Physics
Licensed Content Title	Anomalous deformation twinning in fcc metals at high temperatures
Licensed Content Author	Tanushree Sinha, Yashashree Kulkarni
Licensed Content Date	Jun 1, 2011
Licensed Content Volume	109
Licensed Content Issue	11
Type of Use	Thesis/Dissertation
Requestor type	University or Educational Institution
Format	Print and electronic
Portion	Figure/Table

Figure 4.10; Chapter 4

06/06/2021

RightsLink Printable License

Number of figures/tables 1

Title In silico prediction of the physical performance of pharmaceutical crystals

Institution name Curtin University

Expected presentation date Jul 2021

Portions Figure 1 / page 114315-2

Mustafa Hamad
56/159 Hubert Street, East Victoria Park

Requestor Location
Perth, WA 6101
Australia
Attn: Mustafa Hamad

Total 0.00 USD

Terms and Conditions

AIP Publishing -- Terms and Conditions: Permissions Uses

AIP Publishing hereby grants to you the non-exclusive right and license to use and/or distribute the Material according to the use specified in your order, on a one-time basis, for the specified term, with a maximum distribution equal to the number that you have ordered. Any links or other content accompanying the Material are not the subject of this license.

1. You agree to include the following copyright and permission notice with the reproduction of the Material: "Reprinted from [FULL CITATION], with the permission of AIP Publishing." For an article, the credit line and permission notice must be printed on the first page of the article or book chapter. For photographs, covers, or tables, the notice may appear with the Material, in a footnote, or in the reference list.
2. If you have licensed reuse of a figure, photograph, cover, or table, it is your responsibility to ensure that the material is original to AIP Publishing and does not contain the copyright of another entity, and that the copyright notice of the figure, photograph, cover, or table does not indicate that it was reprinted by AIP Publishing, with permission, from another source. Under no circumstances does AIP Publishing purport or intend to grant permission to reuse material to which it does not hold appropriate rights.
You may not alter or modify the Material in any manner. You may translate the Material into another language only if you have licensed translation rights. You may not use the Material for promotional purposes.
3. The foregoing license shall not take effect unless and until AIP Publishing or its agent, Copyright Clearance Center, receives the Payment in accordance with Copyright Clearance Center Billing and Payment Terms and Conditions, which are incorporated herein by reference.

<https://s100.copyright.com/CustomerAdmin/PLF.jsp?ref=e405e889-56cd-457d-886f-358d9582be1e>

2/3

Figure 4.10; Chapter 4

06/06/2021

RightsLink Printable License

4. AIP Publishing or Copyright Clearance Center may, within two business days of granting this license, revoke the license for any reason whatsoever, with a full refund payable to you. Should you violate the terms of this license at any time, AIP Publishing, or Copyright Clearance Center may revoke the license with no refund to you. Notice of such revocation will be made using the contact information provided by you. Failure to receive such notice will not nullify the revocation.
5. AIP Publishing makes no representations or warranties with respect to the Material. You agree to indemnify and hold harmless AIP Publishing, and their officers, directors, employees or agents from and against any and all claims arising out of your use of the Material other than as specifically authorized herein.
6. The permission granted herein is personal to you and is not transferable or assignable without the prior written permission of AIP Publishing. This license may not be amended except in a writing signed by the party to be charged.
7. If purchase orders, acknowledgments or check endorsements are issued on any forms containing terms and conditions which are inconsistent with these provisions, such inconsistent terms and conditions shall be of no force and effect. This document, including the CCC Billing and Payment Terms and Conditions, shall be the entire agreement between the parties relating to the subject matter hereof.

This Agreement shall be governed by and construed in accordance with the laws of the State of New York. Both parties hereby submit to the jurisdiction of the courts of New York County for purposes of resolving any disputes that may arise hereunder.

V1.2

Questions? customercare@copyright.com or +1-855-239-3415 (toll free in the US) or +1-978-646-2777.

Figure 8.6; Chapter 8

07/07/2021

RightsLink Printable License

JOHN WILEY AND SONS LICENSE TERMS AND CONDITIONS

Jul 07, 2021

This Agreement between Mustafa Hamad ("You") and John Wiley and Sons ("John Wiley and Sons") consists of your license details and the terms and conditions provided by John Wiley and Sons and Copyright Clearance Center.

License Number	5103440163878
License date	Jul 07, 2021
Licensed Content Publisher	John Wiley and Sons
Licensed Content Publication	physica status solidi (a) applications and materials science
Licensed Content Title	Anisotropy of Microhardness in Anthracene Single Crystals
Licensed Content Author	A. Sasaki, M. Iwata
Licensed Content Date	Feb 16, 2006

Licensed Content Volume 85

<https://s100.copyright.com/CustomerAdmin/PLF.jsp?ref=14abdd64-b806-4f7d-a86f-cc20cedba4f70>

1/8

Figure 8.6; Chapter 8

07/07/2021

RightsLink Printable License

Licensed Content Issue	2
Licensed Content Pages	3
Type of use	Dissertation/Thesis
Requestor type	University/Academic
Format	Print and electronic
Portion	Figure/table
Number of figures/tables	1
Will you be translating?	No
Title	In silico prediction of the physical performance of pharmaceutical crystals
Institution name	Curtin University
Expected presentation date	Jul 2021
Portions	Figure 1 on page K106

<https://s100.copyright.com/CustomerAdmin/PLF.jsp?ref=14abdd64-b806-4f7d-a86f-cc20edba4f70>

2/8

Figure 8.6; Chapter 8

07/07/2021

RightsLink Printable License

Requestor Location	Mustafa Hamad Kent Street Bentley Perth, WA 6102 Australia Attn: Mustafa Hamad
Publisher Tax ID	EU826007151
Total	0.00 USD

Terms and Conditions

TERMS AND CONDITIONS

This copyrighted material is owned by or exclusively licensed to John Wiley & Sons, Inc. or one of its group companies (each a "Wiley Company") or handled on behalf of a society with which a Wiley Company has exclusive publishing rights in relation to a particular work (collectively "WILEY"). By clicking "accept" in connection with completing this licensing transaction, you agree that the following terms and conditions apply to this transaction (along with the billing and payment terms and conditions established by the Copyright Clearance Center Inc., ("CCC's Billing and Payment terms and conditions"), at the time that you opened your RightsLink account (these are available at any time at <http://myaccount.copyright.com>).

Terms and Conditions

- The materials you have requested permission to reproduce or reuse (the "Wiley Materials") are protected by copyright.
- You are hereby granted a personal, non-exclusive, non-sub licensable (on a stand-alone basis), non-transferable, worldwide, limited license to reproduce the Wiley Materials for the purpose specified in the licensing process. This license, **and any CONTENT (PDF or image file) purchased as part of your order**, is for a one-time

<https://s100.copyright.com/CustomAdmin/PLF.jsp?ref=14abdd64-b806-4f7d-a86f-cc20cdba4f70>

3/8

Figure 8.6; Chapter 8

07/07/2021

RightsLink Printable License

use only and limited to any maximum distribution number specified in the license. The first instance of republication or reuse granted by this license must be completed within two years of the date of the grant of this license (although copies prepared before the end date may be distributed thereafter). The Wiley Materials shall not be used in any other manner or for any other purpose, beyond what is granted in the license. Permission is granted subject to an appropriate acknowledgement given to the author, title of the material/book/journal and the publisher. You shall also duplicate the copyright notice that appears in the Wiley publication in your use of the Wiley Material. Permission is also granted on the understanding that nowhere in the text is a previously published source acknowledged for all or part of this Wiley Material. Any third party content is expressly excluded from this permission.

- With respect to the Wiley Materials, all rights are reserved. Except as expressly granted by the terms of the license, no part of the Wiley Materials may be copied, modified, adapted (except for minor reformatting required by the new Publication), translated, reproduced, transferred or distributed, in any form or by any means, and no derivative works may be made based on the Wiley Materials without the prior permission of the respective copyright owner. **For STM Signatory Publishers clearing permission under the terms of the [STM Permissions Guidelines](#) only, the terms of the license are extended to include subsequent editions and for editions in other languages, provided such editions are for the work as a whole in situ and does not involve the separate exploitation of the permitted figures or extracts,** You may not alter, remove or suppress in any manner any copyright, trademark or other notices displayed by the Wiley Materials. You may not license, rent, sell, loan, lease, pledge, offer as security, transfer or assign the Wiley Materials on a stand-alone basis, or any of the rights granted to you hereunder to any other person.
- The Wiley Materials and all of the intellectual property rights therein shall at all times remain the exclusive property of John Wiley & Sons Inc, the Wiley Companies, or their respective licensors, and your interest therein is only that of having possession of and the right to reproduce the Wiley Materials pursuant to Section 2 herein during the continuance of this Agreement. You agree that you own no right, title or interest in or to the Wiley Materials or any of the intellectual property rights therein. You shall have no rights hereunder other than the license as provided for above in Section 2. No right, license or interest to any trademark, trade name, service mark or other branding ("Marks") of WILEY or its licensors is granted hereunder, and you agree that you shall not assert any such right, license or interest with respect thereto
- NEITHER WILEY NOR ITS LICENSORS MAKES ANY WARRANTY OR REPRESENTATION OF ANY KIND TO YOU OR ANY THIRD PARTY,

<https://s100.copyright.com/CustomerAdmin/PLF.jsp?ref=14abdd64-b806-4f7d-a86f-cc20cd8a4f70>

4/8

Figure 8.6; Chapter 8

07/07/2021

RightsLink Printable License

EXPRESS, IMPLIED OR STATUTORY, WITH RESPECT TO THE MATERIALS OR THE ACCURACY OF ANY INFORMATION CONTAINED IN THE MATERIALS, INCLUDING, WITHOUT LIMITATION, ANY IMPLIED WARRANTY OF MERCHANTABILITY, ACCURACY, SATISFACTORY QUALITY, FITNESS FOR A PARTICULAR PURPOSE, USABILITY, INTEGRATION OR NON-INFRINGEMENT AND ALL SUCH WARRANTIES ARE HEREBY EXCLUDED BY WILEY AND ITS LICENSORS AND WAIVED BY YOU.

- WILEY shall have the right to terminate this Agreement immediately upon breach of this Agreement by you.
- You shall indemnify, defend and hold harmless WILEY, its Licensors and their respective directors, officers, agents and employees, from and against any actual or threatened claims, demands, causes of action or proceedings arising from any breach of this Agreement by you.
- IN NO EVENT SHALL WILEY OR ITS LICENSORS BE LIABLE TO YOU OR ANY OTHER PARTY OR ANY OTHER PERSON OR ENTITY FOR ANY SPECIAL, CONSEQUENTIAL, INCIDENTAL, INDIRECT, EXEMPLARY OR PUNITIVE DAMAGES, HOWEVER CAUSED, ARISING OUT OF OR IN CONNECTION WITH THE DOWNLOADING, PROVISIONING, VIEWING OR USE OF THE MATERIALS REGARDLESS OF THE FORM OF ACTION, WHETHER FOR BREACH OF CONTRACT, BREACH OF WARRANTY, TORT, NEGLIGENCE, INFRINGEMENT OR OTHERWISE (INCLUDING, WITHOUT LIMITATION, DAMAGES BASED ON LOSS OF PROFITS, DATA, FILES, USE, BUSINESS OPPORTUNITY OR CLAIMS OF THIRD PARTIES), AND WHETHER OR NOT THE PARTY HAS BEEN ADVISED OF THE POSSIBILITY OF SUCH DAMAGES. THIS LIMITATION SHALL APPLY NOTWITHSTANDING ANY FAILURE OF ESSENTIAL PURPOSE OF ANY LIMITED REMEDY PROVIDED HEREIN.
- Should any provision of this Agreement be held by a court of competent jurisdiction to be illegal, invalid, or unenforceable, that provision shall be deemed amended to achieve as nearly as possible the same economic effect as the original provision, and the legality, validity and enforceability of the remaining provisions of this Agreement shall not be affected or impaired thereby.
- The failure of either party to enforce any term or condition of this Agreement shall not constitute a waiver of either party's right to enforce each and every term and condition

<https://s100.copyright.com/CustomerAdmin/PLF.jsp?ref=14abdd64-b806-4f7d-a86f-cc20edba4f70>

5/8

Figure 8.6; Chapter 8

07/07/2021

RightsLink Printable License

of this Agreement. No breach under this agreement shall be deemed waived or excused by either party unless such waiver or consent is in writing signed by the party granting such waiver or consent. The waiver by or consent of a party to a breach of any provision of this Agreement shall not operate or be construed as a waiver of or consent to any other or subsequent breach by such other party.

- This Agreement may not be assigned (including by operation of law or otherwise) by you without WILEY's prior written consent.
- Any fee required for this permission shall be non-refundable after thirty (30) days from receipt by the CCC.
- These terms and conditions together with CCC's Billing and Payment terms and conditions (which are incorporated herein) form the entire agreement between you and WILEY concerning this licensing transaction and (in the absence of fraud) supersedes all prior agreements and representations of the parties, oral or written. This Agreement may not be amended except in writing signed by both parties. This Agreement shall be binding upon and inure to the benefit of the parties' successors, legal representatives, and authorized assigns.
- In the event of any conflict between your obligations established by these terms and conditions and those established by CCC's Billing and Payment terms and conditions, these terms and conditions shall prevail.
- WILEY expressly reserves all rights not specifically granted in the combination of (i) the license details provided by you and accepted in the course of this licensing transaction, (ii) these terms and conditions and (iii) CCC's Billing and Payment terms and conditions.
- This Agreement will be void if the Type of Use, Format, Circulation, or Requestor Type was misrepresented during the licensing process.
- This Agreement shall be governed by and construed in accordance with the laws of the State of New York, USA, without regards to such state's conflict of law rules. Any legal action, suit or proceeding arising out of or relating to these Terms and Conditions or the breach thereof shall be instituted in a court of competent jurisdiction in New York County in the State of New York in the United States of America and each party hereby consents and submits to the personal jurisdiction of such court, waives any objection to venue in such court and consents to service of process by registered or

<https://s100.copyright.com/CustomerAdmin/PLF.jsp?ref=14abdd64-b806-4f7d-a86f-cc20edba4f70>

6/8

Figure 8.6; Chapter 8

07/07/2021

RightsLink Printable License

certified mail, return receipt requested, at the last known address of such party.

WILEY OPEN ACCESS TERMS AND CONDITIONS

Wiley Publishes Open Access Articles in fully Open Access Journals and in Subscription journals offering Online Open. Although most of the fully Open Access journals publish open access articles under the terms of the Creative Commons Attribution (CC BY) License only, the subscription journals and a few of the Open Access Journals offer a choice of Creative Commons Licenses. The license type is clearly identified on the article.

The Creative Commons Attribution License

The [Creative Commons Attribution License \(CC-BY\)](#) allows users to copy, distribute and transmit an article, adapt the article and make commercial use of the article. The CC-BY license permits commercial and non-

Creative Commons Attribution Non-Commercial License

The [Creative Commons Attribution Non-Commercial \(CC-BY-NC\) License](#) permits use, distribution and reproduction in any medium, provided the original work is properly cited and is not used for commercial purposes.(see below)

Creative Commons Attribution-Non-Commercial-NoDerivs License

The [Creative Commons Attribution Non-Commercial-NoDerivs License \(CC-BY-NC-ND\)](#) permits use, distribution and reproduction in any medium, provided the original work is properly cited, is not used for commercial purposes and no modifications or adaptations are made. (see below)

Use by commercial "for-profit" organizations

Use of Wiley Open Access articles for commercial, promotional, or marketing purposes requires further explicit permission from Wiley and will be subject to a fee.

Further details can be found on Wiley Online Library
<http://olabout.wiley.com/WileyCDA/Section/id-410895.html>

<https://s100.copyright.com/CustomerAdmin/PLF.jsp?ref=14abdd64-b806-4f7d-a86f-cc20edba4f70>

7/8

Figure 8.6; Chapter 8

07/07/2021

RightsLink Printable License

Other Terms and Conditions:

v1.10 Last updated September 2015

Questions? customercare@copyright.com or +1-855-239-3415 (toll free in the US) or +1-978-646-2777.